The Role of the Formyl-peptide Receptor in multi-organ fibrosis mechanisms

Benjamin John Minford Millar

August 2016

A thesis submitted in fulfilment of the requirements for the degree of Doctor of Philosophy

Faculty of Medical Sciences, Institute of Cellular Medicine

Declaration

I declare that the thesis entitled ‘The Role of the Formyl-peptide Receptor in multi-organ fibrosis mechanisms’ is entirely my own work and credited collaborators.

The research was carried out from September 2011 to September 2014 at Newcastle University. All activities in this thesis are original unless acknowledged in the text or by reference. The thesis has not been previously submitted at this University or any other University.

Abstract

Mitochondrial Damage-associated molecular patterns (mtDAMPs) are an emerging source of endogenous alarmins. N-formylated peptides bind members of the formyl-peptide receptor (FPR) family. From its original role in chemotaxis of immune cells towards sites of infection the part that this G-protein coupled receptor (GPCR) plays in the human body is expanding with expression evident in cells of non-phagocyte origin as well as neutrophils and macrophage.

To investigate how FPR1 affects the development of pulmonary fibrosis the bleomycin acute injury *in vivo* model was employed as its pathogenesis shares features with Idiopathic pulmonary fibrosis (IPF). Transgenic mice lacking functional *fpr1* displayed a reduced inflammatory profile and fibrotic phenotype at acute and end-stage endpoints respectively post-bleomycin instillation. *In vivo* models of fibrosis in different organs such as the liver and kidney there was not the same protective effect with deletion of *fpr1* as with acute bleomycin lung injury mechanism. This in turn brought the pathogenesis of the *in vivo* models into question particularly due to the abundance of *fpr1* expression on neutrophils, the first line of defense of the immune system. By depleting neutrophils prior to the bleomycin injury the nature of these myeloid cells in this lung fibrosis model and through evaluation of the inflammatory and fibrotic phases post-instillation it is evident that these cells play a major role in how the disease develops.

Translation to the human disease (IPF) was a vital step to elucidate the true role of FPR1 in chronic fibrosis mechanisms. Expression was demonstrated by immunofluorescence in CD45+ leukocytes as well as in isolated fibroblasts. This was corroborated by mRNA levels in primary cultured cells when FPR1 expression was ‘primed’ by inflammatory stimuli such as lipopolysaccharide (LPS). With effects observed in a murine setting and also in primary tissue/cells the FPR1 effect may be microenvironment/neutrophil dependent.

Abbreviations

16-HBE	Human bronchial epithelial cell line
ALT	Alanine aminotransferase
ANOVA	Analysis of variance
APC	Allophycocyanin
APC-cy7	Allophycocyanin-Cyanine7
AST	Aspartate aminotransferase
ATP	Adenosine triphosphate
BAL	Bronchoalveolar lavage
BDL	Bile duct ligation
BLM	Bleomycin
BSA	Bovine serum albumin
BV421	Brilliant violet
BW	Body weight
Ca^{2+}	Calcium
CBC	Comparative Biology Centre
CCl_4	Carbon tetrachloride
CCR7	C-C chemokine receptor type 7
CD11b	Cluster of differentiation 11b
CD206	Cluster of Differentiation 206/Mannose receptor
CD3	Cluster of differentiation 3
CD45	Cluster of differentiation 45/ leukocyte common antigen
CD49	Cluster of differentiation 49
CD66a	Cluster of differentiation 66a
CD68	Cluster of Differentiation 68
CDNA	Complementary DNA
CKD	Chronic kidney disease
CLD	Chronic liver disease
COPD	Chronic obstructive pulmonary disease
CpG	5'—C—phosphate—G—3'
CsH	Cyclosporin H
CXCL1	Chemokine (C-X-C motif) ligand 1
DAG	Diacylglycerol
DAMPs	Damage-associated molecular patterns
DAPI	4',6-diamidino-2-phenylindole
DMEM	Dulbecco's Modified Eagle Medium
DNA	Deoxyribonucleic acid
ECM	Extracellular matrix
EDTA	Ethylenediaminetetraacetic acid
ELISA	Enzyme-linked immunosorbent assay
EMT	Epithelial-mesenchymal transition
ERK	Extracellular signal-regulated kinases
ESRD	End-stage renal disease
ETC	Electron transport chain
EtOH	Ethanol

F4/80	EGF-like module-containing mucin-like hormone receptor-like 1
FACS	Fluorescence-activated cell sorting
FCS	Fetal calf serum
FFPE	Formalin-fixed paraffin-embedded
FITC	Fluorescein isothiocyanate
Fizz-1	Found in inflammatory Zone 1
fMLF	Formyl-methionyl-leucyl phenylalanine
N-fMLF	N-Formylmethionyl-leucyl-phenylalanine
FPR	Formyl-peptide receptor
FPR1	Formyl-peptide receptor 1
FPR2	Formyl-peptide receptor 2
FPR3	Formyl-peptide receptor 3
FPRL1	Formyl peptide receptor-like 1
FSC-H	Forward side scatter-height
GOLD	Global initiative for chronic Obstructive Lung Disease
GPCR	G-protein coupled receptor
GR1	Granulocyte receptor-1
H&E	Haemotoxylin and Eosin
HBSS	Hank's Balanced Salt Solution
HCC	Hepatocellular carcinoma
HCRT	High-resolution computed tomography
HEK-293	Human embryonic kidney-293 epithelial cell line
HMGB1	High-mobility growth box protein 1
HSC	Hepatic stellate cell
HSPs	Heat-shock proteins
IFN-γ	Interferon-gamma
IgG	Immunoglobulin
IL-13	Interleukin 13
IL-1β	Interleukin 1beta
IL-6	Interleukin 6
IL-8	Interleukin 8
ILD	Interstitial lung disease
iNOS	Inducible nitric oxide synthases
IPF	Idiopathic pulmonary fibrosis
IVC	Inferior vena cava
KC	Keratinocyte chemoattractant
LAP	Latency associated Peptide
LK	Left kidney
LPS	Lipopolysaccharide
LW	Liver weight
Ly6G	Lymphocyte antigen 6 complex, locus G
MAPK	Mitogen-activated phosphokinase
MCP-1	Monocyte chemoattractant peptide 1
MFI	Median fluorescent intensity
MLF	Murine lung fibroblast
MMP	Matrix metalloproteinases
MOMA-2	Marginal zone metallophilic macrophages 2

mRNA	Messenger ribonucleic acid
MSD	Mesoscale Delivery
mtDAMPs	Mitochondrial DAMPs
mtDNA	Mitochondrial DNA
MΦ	Macrophage
NAC	N-acetyl Cysteine
NAD	Nicotinamide adenine
NASH	Non-alcoholic Steatohepatitis
NFKB-1	Nuclear factor NF-kappa-B
NLRs	NOD-like receptors
NSIP	Non-specific interstitial pneumonia
O.D.	Optical density
O.H.P.	Hydroxyproline
OSF-2	Periostin/Osteoblast-specific factor 2
PAMPs	Pathogen-associated molecular patterns
PAS	Periodic acid Schiff
PBECS	Primary bronchial epithelial cells
PBST	Phosphate-buffered saline Tween
PCNA	Proliferating cell nuclear antigen
PCR	Polymerase chain reaction
PE	Phycoerythrin
PE cy7	Phycoerythrin Cyanine 7
Percp	Peridinin chlorophyll
PFA	Paraformaldehyde
PKC	Phosphokinase C
PLC	Phospholipase C
PLF	Primary lung fibroblast
PMA	Phorbol 12-myristate 13-acetate
PMN	Polymorphonuclear neutrophil
PRRs	Pattern recognition receptors
PSR	PicroSiriusRed
qPCR	Quantitative polymerase chain reaction
RA	Rheumatoid arthritis
RBC	Red blood cell
RELM	Resistin-like molecule
RK	Right kidney
RNA	Ribonucleic acid
ROS	Reactive oxygen species
RRT	Renal replacement therapy
RT-PCR	Reverse-transcription PCR
SAL	Saline
SC BLM	Subcutaneous bleomycin
SigLecF	Sialic acid-binding immunoglobulin-type lectin F
SIRS	Systemic inflammatory response syndrome
SNPs	Single-nucleotide polymorphisms
SSC-A	Side scattered-area
TGFβ1	Transforming growth factor beta 1
THP-1	Human monocyte-derived cell line

TIMP	Tissue inhibitor of metalloproteinase
TLR	Toll-like receptor
TM	Transmembrane
TNF-α	Tumour necrosis factor alpha
TRAIL	TNF-related apoptosis-inducing ligand
TRITC	Tetramethylrhodamine
UIP	Usual interstitial pneumonia
UUO	Unilateral ureteral obstruction
α-SMA	Alpha-smooth muscle actin

Acknowledgements

I would like to thank everyone in Fibrosis and lung research groups that research helped throughout my project and provided some well-needed banter when required. My supervisors Derek Mann and Andrew Fisher were patient with me throughout my PhD and provided insight into the direction of my project which I am thankful for as well as ample support.

Rachel Howarth was invaluable for her help with all of my many animal models along with Chris Fox who kindly performed any necessary surgical procedures. Thanks go to Fiona Oakley and Lee Borthwick for the extensive help and guidance with the bleomycin investigations during the course of my project at Newcastle and in Cambridge (Medimmune site).

Thanks must go to the different members of the MedImmune team that helped and provided useful tools over the years including Alan Carruthers, John Ferguson and Matt Bell. Lynne Murray, Donna Finch and Matt Sleeman provided much appreciated support when I did placements at MedImmune and with studies conducted at Newcastle, running assays on samples for my project and project supervision through the industrial collaboration.

Special thanks go to Evelyn Barron who has put up with me and my unusual work habits for too long. Nothing I can say will convey how appreciative I am of her support.

Table of Contents

List of figures

1 Introduction

1.1 Damage-associated molecular patterns (DAMPs)

DAMPs are endogenous molecules released as a result of injury/damage that interact with cellular receptors. DAMPs are distinct from pathogen-associated molecular patterns (PAMPs) in that they are derived from damaged/dying cells within a host rather than an infectious agent. DAMPs share homology with exogenous PAMPs therefore initiating and controlling the immune response via affecting activation, maturation, cell trafficking, antigen presentation efficiency and function of neutrophils, macrophages, mast cells and eosinophils (Chen and Nuѭez, 2010).

Since Matzinger's postulation of the 'danger theory' concepts in immunology have had to drastically change and adapt on account of the inclusion of a vast array of new players in the innate immune response (Matzinger & Kamala., 2011). The ability of the body to recognise non-self and self-molecular determinants is another caveat of the immune system linked with evolution. These signals due to shared homology with exogenous PAMPs are recognised by pattern recognition receptors (PRRs) including toll like receptors (TLRs), nod like receptors (NLRs) and formyl peptide receptors (FPR) (Arnoult *et al*., 2011; Krysko *et al*., 2011). Initial studies demonstrated cytotoxic (CD8+ve) and T-helper (CD4+ve) mediated immune responses to DAMPs secreted by dead cells (Shi *et al*., 2003; Kono *et al*., 2014).

The innate immune response (IL-1α-mediated) in so-called 'sterile inflammation' has been tied with these intracellular 'alarmins' since the early days of their conception (Matzinger, 1994). Interleukin 1α/1β release is triggered by inflammasome-mediated Caspase-1 cleavage which constitutes the response to non-pathogenic stimulus (Kono *et al*., 2014). Endogenous DAMP release is controlled by cellular death. Apoptosis and necrosis are fundamentally similar and distinct from one another simultaneously. The spontaneous nature of cellular content release into the extracellular environment by necrotic/dying cells generates a pro-inflammatory response leading to activation of immune cells stimulating phagocytosis and neutrophil trafficking. This contrasts with the passive apoptotic pathways (Kono *et al*., 2014).

Certainly, since their conception DAMPs have become heavily associated with trauma injuries. Although not entirely aseptic (sterile) endogenous danger signals have been implicated in exacerbations of injuries triggering systemic immune responses acting as a potential mechanism for secondary infections and sepsis (Hwang *et al*., 2011).

DAMPs have previously been categorised as either extracellular matrix (ECM) components such as fibronectin, hyaluronan, heparin sulphate or cellular stress molecules including heat shock proteins (HSPs), nucleic acids, high-mobility group box 1 (HMGB1) or immunomodulatory proteins comprising β-defensins and pulmonary surfactant proteins (Tolle and Standiford, 2013). All of which have a role in acute lung injury and other inflammatory diseases (Fairchild and Bromberg, 2012). Uric acid (monosodium urate) was the first intracellular danger signal to be shown to promote a T-cell immune response (Shi *et al*., 2003) and since then many more have been discovered such as CpG-rich DNA, RNA, ATP, Adenosine, actin and myosin filaments, peroxideroxin, IL-1α and IL-33 (Piccini and Midwood, 2010; Kono *et al*., 2014).

Indeed in human disease elevated levels of endogenous alarmins have been demonstrated. Different inflammatory and autoimmune conditions such as rheumatoid arthritis (RA), inflammatory bowel disease, sarcoidosis, sclerosis, psoriasis, chronic renal disease, diabetes are all associated with increased DAMPs (Piccini and Midwood, 2010). In chronic, progressive pulmonary diseases DAMPs have been implicated in their pathogenesis. Ellson *et al*. (2014) indicate DAMP – receptor interactions in three main pathways: pro-inflammatory and apoptosis inhibition as part of the innate immune response and thirdly, the adaptive immune response. DAMPs are driving forces behind necrotic and apoptotic events in Idiopathic Pulmonary Fibrosis (IPF) with some instances of defective danger signalling have aberrant downstream effects. In Chronic obstructive pulmonary disease (COPD), a characteristically inflammatory disease there is progressive degeneration of airway tissue which is now linked to alarmin release due to elevated levels of S100 proteins, defensins and HMGB1 (Pouwels *et al*., 2014). Clearly, DAMPs are not just limited to acute injuries with as yet undefined exacerbating roles in long-term diseases.

1.2 Mitochondrial Damage-Associated Molecular Patterns

Mitochondrial DAMPs (mtDAMPs) have emerged as a reservoir of signalling molecules with unknown potential in recent years. Mitochondria are the power-house of eukaryotic cells with demonstrable roles in the respiration, apoptosis and reactive oxygen species (ROS) production as well as a source of mtDAMPs. These organelles share many properties with prokaryotes due to their concurrent evolution as put forward by the theory of 'endosymbiosis' (Vargas-Parada, 2010; Krysko *et al*., 2011) in which ancestral eukaryotic cells assimilated aerobic prokaryotes (or a proto-mitochondrion) to form a eukaryote capable of ATP production. Mitochondrial origin is logical especially when comparing mitochondrial deoxyribonucleic acid (mtDNA) and mitochondrial N-formyl-peptides with bacterial DNA and N-formylated-peptides such as fMLF respectively (Le *et al*., 2002). Some researchers have even postulated that mitochondria are a sub-species of bacteria due to distinct features shared between the organelle and prokaryotes. Indeed the outer and inner membranes and cytoplasm/mitochondrial matrix have similarities. β-barrel proteins and outer membrane protein (OMP) machinery are conserved but key features in bacterial plasma membranes are absent in the eukaryotic organelle such as LPS residues and flagella used for motility. Due to the intrinsic role of mitochondria in respiration and ATP production the arrangement of the mitochondrial inner membrane is distinctly unique by multiple folds forming cristae structures which house elements of the electron-transport chain (ETC) (Pallen, 2011).

Indeed mitochondrial N-formyl peptides, analogues of bacterial counterparts, were shown to promote interleukin-8 (IL-8) production from activated monocytes hence showing a role for the mitochondria in innate immunity (Crouser *et al*., 2009; Krysko *et al*., 2011). Mitochondrial DAMPs are frequently elevated in the serum of trauma patients due to release from damaged/dying cells during cellular and inflammatory changes. Disrupted mitochondria in damaged cells release material via the intrinsic apoptotic pathway. In this key paper mtDAMPs were determined to be immunogenic in circulation and across different organ systems potentially contributing to systemic inflammatory response syndrome (SIRS) (Raoof *et al*., 2010).

1.2.1 Mitochondrial DNA

Key mitochondrial DAMPs characterised by recent papers include mitochondrial DNA (mtDNA) such as non-methylated cytosine-phosphate-guanosine, CpG, sites which encode N-formyl peptides. MtDNA has been documented in recent data in systemic inflammatory response syndrome (SIRS) associated with acute trauma in dramatic serum concentration elevations. Non-methylated CpG motifs such as these bind the intracellular endosome pattern recognition receptor (PRR) TLR9, a highly conserved Type I membrane protein (Zhang *et al*., 2010). MtDNA is distinct from nuclear DNA by a characteristic pre-sequence only present before nuclear translocation. Ligation of TLR9 by the pro-inflammatory mtDNA triggers p38 mitogen-activated kinase protein (MAPK) phosphorylation in neutrophils.

1.2.2 N-Formyl peptides

For many years now the degradation products of bacterial and mitochondrial proteins have been distinguished by their chemoattractive behaviour (Prossnitz & Ye, 1997; Hartt *et al*., 1999). Mitochondrial DNA and their translated products are considered the major signatures of a new source of DAMPs, distinct from bacterial counterparts due to their endogenous nature (Zhang *et al*., 2010). Even thirty years ago Carp (1982) recognised that mitochondrial N-formylated proteins were important just by their similarity to bacterial products. Though defined as the original chemoattractant G-protein coupled receptor with high expression on neutrophils and monocytes, Becker *et al*. (1998) characterised FPR expression by immunohistochemistry on a variety of different cell types including those of non-phagocytic origin. Staining has been noted for FPR particularly on endothelial cells and in thyroid, adrenal, liver and nervous system tissue. Human FPR was originally characterised as a high affinity binding site for the prototypic N-formyl peptide formyl-methionine-leucyl-phenylalanine (fMLF) (Le *et al*., 2002). Recent studies have demonstrated that mitochondrial peptides/lysates are capable of eliciting an immunogenic response on neutrophils *in vitro* and *in vivo*. This has implications for human disease by increasing susceptibility to organ dysfunction and systemic inflammation through mitochondrial alarmins affecting

neutrophil physiological behaviour after trauma. The effect of mitochondrial DAMPs feeds into the idea of 'sterile inflammation' which is of concern after trauma injuries where sepsis and uncontrolled inflammation is a major problem (Raoof *et al*., 2010; Wenceslau *et al*., 2013).

1.2.3 N-formylation post-translational modification

Delving into the evolutionary importance of N-formyl peptides highlights the principal reason behind the role of the FPR in host defense. Originally, N-formylation is a post-translational modification of amino acids that marks the start site for peptide synthesis in bacteria (Gerack *et al*., 2014). In prokaryotes protein production begins with a methionine residue and the transfer of a formyl group from formyl tetrahydrofolic acid via formyl transferase activity. With activity restricted to bacteria the N-formyl peptides are firstly cleaved by methionine aminopeptidase after deformylation and then targeted by the human immune system as exogenous foreign material during bacterial infections (Mader *et al*., 2013).

1.3 Formyl-peptide receptor molecular properties

1.3.1 Genetic details of FPR gene

The three human members of the formyl-peptide receptor family: FPR1, FPR2 (69% homology to FPR1), FPR3 (58% homology to FPR1) are clustered at the locus 19q13.3 (Le *et al.*, 2002; Ye *et al*., 2009). Positions on chromosome 19q13.3 are shown in Figure 1.1 perhaps alluding to the different expression and binding behaviours of these receptors. Several groups have cloned the *fpr* genes in an attempt to elucidate its molecular role in the cell (Boulay *et al.*, 1990; Murphy *et al*., 1993; Rabiet *et al*., 2005). Early work concluded that the expression of the *fpr1* receptor arises from two alternatively spliced mRNAs hence the presence of two transcript variants (NM_001193306.1 and NM_002029.3 respectively). The lower affinity receptors FPRL1 and FPRL2 like FPR1 were isolated by gene cloning techniques with the only

difference being the probes' stringency threshold (Murphy *et al*., 1992; Prossnitz & Ye, 1997). Key features shown in Figure 1.1 mark the *fpr* gene cluster apart from others are its 6kb single copy coding region and three Alu repeats (Le *et al*., 2000; Murphy *et al*., 1992 & 1993). Luciferase assays also elucidated that there is no need for a CCAAT box in order for gene transcription (Miettinen, 2011) therefore the promoter consists of a non-consensus TATA element.

Phylogenetic analysis has shown that humans and other members of the primate family display a high degree of sequence homology especially when compared to gorilla and chimpanzee counterparts. This can clearly be seen in Figure 1.2 (b) even more so with the divergent FPR genes of the other mammalian species. This is particularly evident in murine genetic makeup which consists of seven related sequences. Mouse FPR1 is essentially orthologous to human FPR but due to a 76% identity its ligand affinity is drastically reduced (Le *et al*., 2000). The other Fpr-related amino-acid sequences split even further with regards to their extracellular loops. Mouse *fpr-rs1* and *fpr-rs2* both equate to the multi-ligand receptor FPR2/LXA4 receptor. The other Fpr-related amino-acid sequences have been deemed functional but are not orthologous to human receptors. Recently in fact another gene has been characterised despite previously classified as Fpr-rs2 pseudogene, *fpr-rs8* (Tiffany *et al*., 2011). The divergence of this family is clearly evident when subject to sequence similarity analysis (Figure 1.2 (a)).

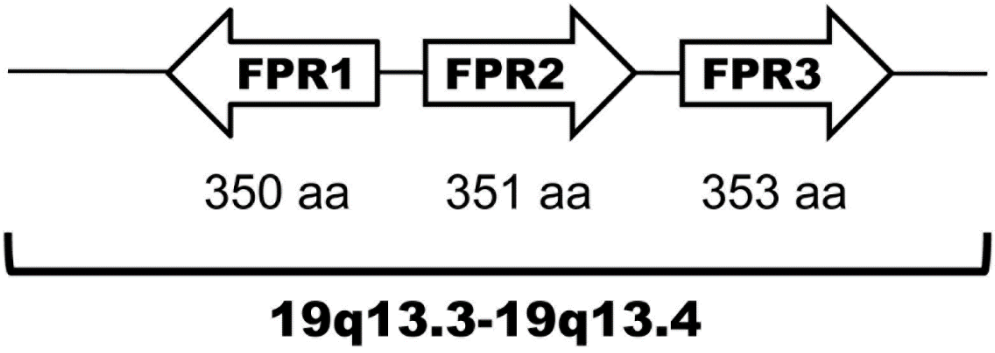

Figure 1.1: The loci of the three FPR genes as organised on chromosome 19q13.3. FPR1 is encoded by a 6kb copy gene with an intronless open-reading frame translating to a 350 amino acid (aa) product. Human FPR2 gene encodes a 351 aa 7 transmembrane receptor with 68% sequence identity to FPR1. FPR3 gene translates to a 353 aa product with 58% homology to FPR1 (adapted from Ye *et al*., 2009).

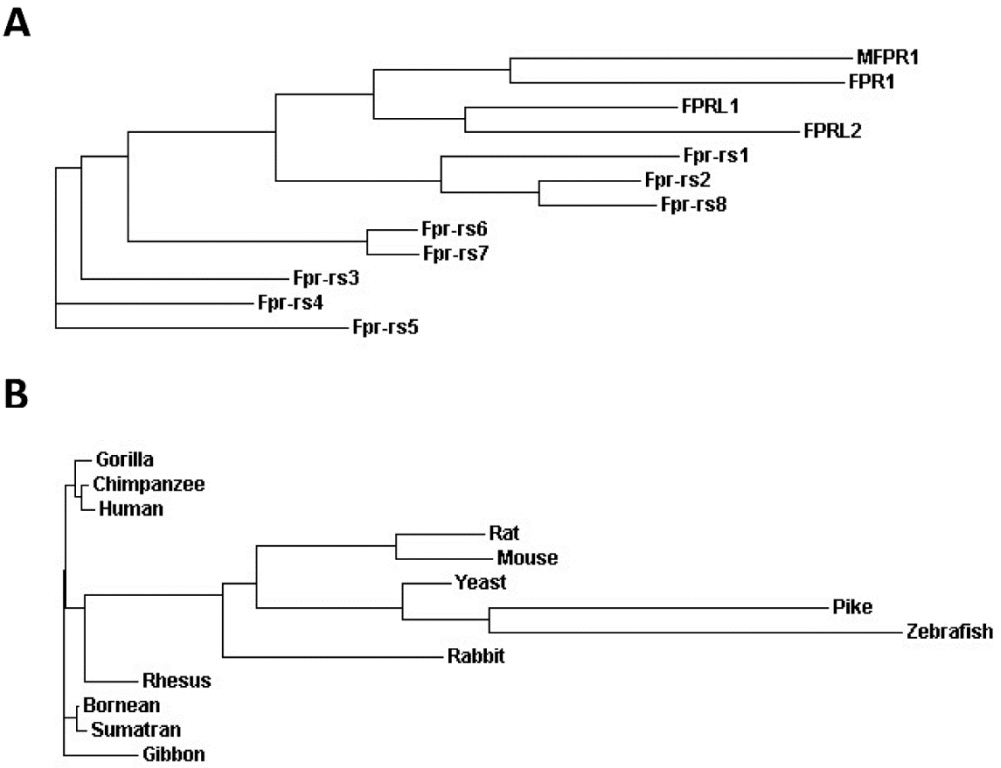

Figure 1.2: Phylogenetic analysis of the FPR gene family between (a) the three human functional isoforms and murine functional/pseudogenes; (b) FPR1 sequences across the evolutionary scale from higher mammals to simple eukaryotes. Phylogram generated using ClustalW2 online sequence alignment software on http://www.ebi.ac.uk/Tools/msa/clustalw2/ .

With regards to the polymorphic nature of the FPR family, human FPR1 has many different single-nucleotide polymorphisms (SNPs) associated with its gene resulting multiple different isoforms (Le *et al*., 2002). In some cases this variability in sequence has been linked to certain diseases such as juvenile periodontis arising from defective immune responses (Sahagun-Ruiz *et al*., 2001). Differences in the activity of these FPR1/FPRL1 receptors may potentially trace back to their common evolutionary origin which was followed by a distinct heritage.

FPR family genes have been investigated and characterised in mammals only to date (Panaro *et al*., 2007). Panaro *et al*. (2007) employed a conservation/mutation pattern-based strategy and for conservation indexes it appears mutations are likely to occur from G to A and C to T. Evolutionary analysis of FPR gene sequences has revealed that certain bases are less susceptible to selective pressure. Conservation/mutation indexes of $1^{st}/2^{nd}$ nucleotides of codons share a strong, proportional linkage but the conservation index of the 2^{nd} is significantly elevated compared to the first codon base. This chemokine receptor conservation/mutation trend is shared by the FPR family and Chemokine CXC Receptor 4 (Panaro *et al*., 2008). The divergent phylogeny observed in all mammals and the SNPs in human FPR1 present evidence for distinct evolutionary events directing its development (Sahagun-Ruiz *et al*., 2001).

1.3.2 FPR ligands

1.3.2.1 Agonists

Due to its originally defined role as one of the first chemoattractant receptors a majority of the ligands which bind FPRs are bacterial (exogenous) but in recent years N-formylated peptides encoded by the mitochondrial genome (endogenous antigens) have demonstrated the ability to bind in a similar fashion (Zhang *et al*., 2010).

Studies investigating mitochondrial DAMPs and their effect on the cell typically involve the application of the subcellular fraction of disrupted organelles. Rabiet *et al*. (2005) have carried out such investigations revealing that members of the electron transport chain may indeed activate the FPR family (Raoof *et al., 2010).* The former group utilised N-formylated hexapeptides equivalent to the N-termini of NADH

dehydrogenase and cytochrome c oxidase subunits which trigger signalling through both FPR1and FPRL1.

Human formyl-peptide receptor (FPR) is essentially a high affinity binding site on the surface of neutrophils for the bacterial formyl-methionine-leucyl-phenylalanine (fMLF). Human FPR constitutes a high affinity binding site on the surface of neutrophils for the formylated complex N-fMLF. In terms of kinetics fMLF is capable of activating FPR1 with as little as picomolar concentrations. FPR2 bind various different ligands including bacterial formylated peptides, annexin 1, cathespin G and HIV gp41 peptides (Le *et al*., 2002). FPR1 stimulation is thought to trigger surface marker expression, reactive oxygen species (ROS) production, pro-inflammatory cytokine/chemokine production and degranulation (Migeotte *et al*., 2006). Emerging evidence suggests the importance of formyl peptide receptor (FPR) ligands in lung epithelium, with established expression of the receptors in monocytes and neutrophils. Particularly of note is its role in chemotaxis and migration of cells to sites of injury (Shao *et al*., 2011; Rescher *et al*., 2002; Crouser *et al*., 2009).

FPR2 stimulation is somewhat more complicated by the fact not only does it bind fMLF (at micromolar concentrations) but also non-formylated ligands, not unlike FPRL2 (Ye *et al*., 2009). Due to its wide and variable repertoire of ligands, complicated even further by the discovery of small-molecule agonists for FPR1 and FPR2 (Kirpotina *et al*., 2010; Khlebnikov *et al*., 2010), this inflammatory GPCR family is aptly described as ‘promiscuous’ by the scientific community (Huet *et al*., 2007). Full determination of the FPR family's role can only come with elucidation of all the possible receptor-ligand interactions (Migeotte *et al*., 2006).

1.3.2.2 Antagonists

Certain inhibitory agents are capable of binding this GPCR family desensitising and preventing further interactions with the receptor. The promiscuous nature of the FPR family has only been elucidated by the use of antagonists such as cyclosporins, Boc-MLF and Boc-FLFLF (Stenfeldt *et al*., 2007). For many years the cyclosporine family

of compounds have been characterised as inhibitors of FPR signalling, acting as selective antagonists (Loor *et al*., 2002). Cyclosporin H (CsH) are classified as high affinity 'inverse agonists' locking the receptor into an inactive conformation caused by an ion pair localised key residues in the seven putative transmembrane domains of FPR1 (Loor *et al*., 2002; Stenfeldt *et al*., 2007). The binding and efficacy of N-formylmethionyl-leucyl-phenylalanine (fMLF) peptide depends upon residues in the human formyl peptide receptor structure. These include conserved and non-conserved amino acids Arg84, Lys85, Arg163, Arg205 and Asp284 situated on the extracellular loops of TM domains (Lala *et al*., 1999).

The high affinity bacterial fMLF, the same peptide that has been utilised to assess FPR functionality in numerous cell types (Rabiet *et al*., 2005) was altered by the removal of the N-formyl group and replaced with a tert-butyloxycarbonyl (Boc) group creating a nonselective antagonist (Freer *et al*., 1980; Stenfeldt *et al*., 2007). Studies of different inhibitors have characterised CsH as the most potent. Asides from antagonists discovered more than thirty years ago not many inhibitors are available although recent high throughput screening (HTS) of compound libraries have pointed towards two novel, potent candidates: benzimidazole and diamide as small molecule FPR inhibitors (Unitt *et al*., 2011; Arterburn *et al*., 2009). Clearly these flow cytometry-based screening methods merit further investigation due to potential, highly selective binders for the different members of the FPR family as yet unidentified and uncharacterised.

There was scope for use of FPR antagonists *in vitro* or *in vivo* but the specificity of cyclosporin H and small molecule inhibitors is not optimal therefore they were not utilised in my project. In recent months a human FPR1-specific antibody was optimised in-house by MedImmune (Cambridge, UK) with improved enzyme kinetics and binding affinities over other receptor inhibitory agents (Douthwaite *et al*., 2014). Since this antibody is specific for human immunogens it is ideal for evaluation of receptor expression at a protein level but not for mouse *in vivo* experiments. The crux of this is that a knockout mouse must be used for *in vivo* research as there is no specific mouse FPR1 antibody that could be used for blockage of FPR1.

1.3.3 Structure of the FPR1 GPCR

Typically, this receptor family is characterised as a seven trans-membrane (TM) G-protein coupled receptor as depicted in Figure 1.3 (adapted from Ye *et al*., 2009). The transmembrane segments are hydrophobic and connect to each other by hydrophilic components composed of 3 intracellular cytoplasmic and 3 extracellular loops. Two N-glycosylation sites are present at the amino terminus and in the 2nd extracellular loop (Prossnitz and Ye, 1997). Different amino acid residues equate to a variety of functions within in this receptor's structure as indicated in Figure 1.3. FPR1 is highly polymorphic as previously described with several substitutions as at number of positions including 11 (Ile/Thr), 47 (Val/Ala), 101 (Leu/Val), 190 (Arg/Trp), 192 (Asn/Lys) and 346 (Ala/Glu). Shaded circular residues Arg84, Lys85, and Asp284 are key for maximal binding of N-formylated ligands (Mills *et al*., 1998). Other residues play a role in generic G-protein interactions with Asp122, Arg123, and Cys124 forming this conserved motif. Also of note is the NPMLY sequence in the 7th TM segment required for receptor internalisation (He *et al*., 2001).

At the Carboxy-terminus Ser/Thr phosphorylation occurs at 11 distinct sites which are functionally activated depending on FPR isoform in the cytoplasmic tail. These phosphopeptides were determined by mass spectrometry of tryptic digests (Maaty *et al*., 2013). Differential phosphorylation on neutrophil FPRs appears to correlate with the affinity of the receptors (FPR1 has high fMLF affinity as opposed to low affinity with FPRL1). Evaluation of this important receptor regulation process could be key in the development of a therapeutic approach for tailoring the innate immune response driven by neutrophils.

1.3.4 GPCR signalling

All three human FPR1, FPR2 and FPR3 receptors are intrinsically associated with the Gi protein subunit. FPR1 is specifically coupled to Gi1, Gi2 and Gi3. The heterotrimeric G protein breaks into alpha and beta-gamma subunits. This dissociation of this multicomponent complex triggers stimulation of downstream effectors such

phosphatidylinositol-3-kinase (PI3K), phospholipase C (PLC), protein kinase C (PKC) and a number of mitogen-activated protein kinases (MAPKs). PLC activation allows the generation of the second messenger IP3, ultimately causing a calcium flux and diacyglycerol (DAG) accumulation. (Amatruda *et al*., 1995; Le *et al*., 2002; Selvatici *et al*., 2006).

GPCR activation is intrinsically linked to the control of vital cellular events such as growth, proliferation, differentiation and apoptosis (Roux and Blenis, 2004). Typically signalling through these heterotrimeric complexes triggers downstream cascades, most notably MAPK activation. Principal members of this important family of kinases include ERK1/2 (p44/p42), ATP and p38 which ultimately feed into the master transcription factor, NF-kB pathway (Caunt *et al*., 2006; Huet *et al*., 2007; Crouser *et al*., 2009; Zhang *et al*., 2010). As for the mechanisms of GPCR signalling with regards to receptor kinetics most of these seven transmembrane (TM) putative domain structures undergo desensitisation with repeated ligand exposure. In order to prevent saturation adaptor molecules called ‘arrestins’ are in place to sterically hinder G protein activation and even to trigger internalisation of chronically stimulated receptors (Caunt *et al*., 2006; Le *et al*., 2000).

In terms of the formyl peptide receptor family only FPRL1 signalling requires the action of these beta-arrestins (Huet *et al*., 2007). The variety of ligands which bind FPR2 adds to the complexity of this receptor family's function and consequences of activation. Across the board in mammalian species the seven transmembrane coding regions is distinctive of GPCRs. Cross-talk of FPR with other signalling pathways seems to be a common trait as interactions with CCR5, EGFR and SUPAR pathways have been reported (Zein *et al*., 2010).

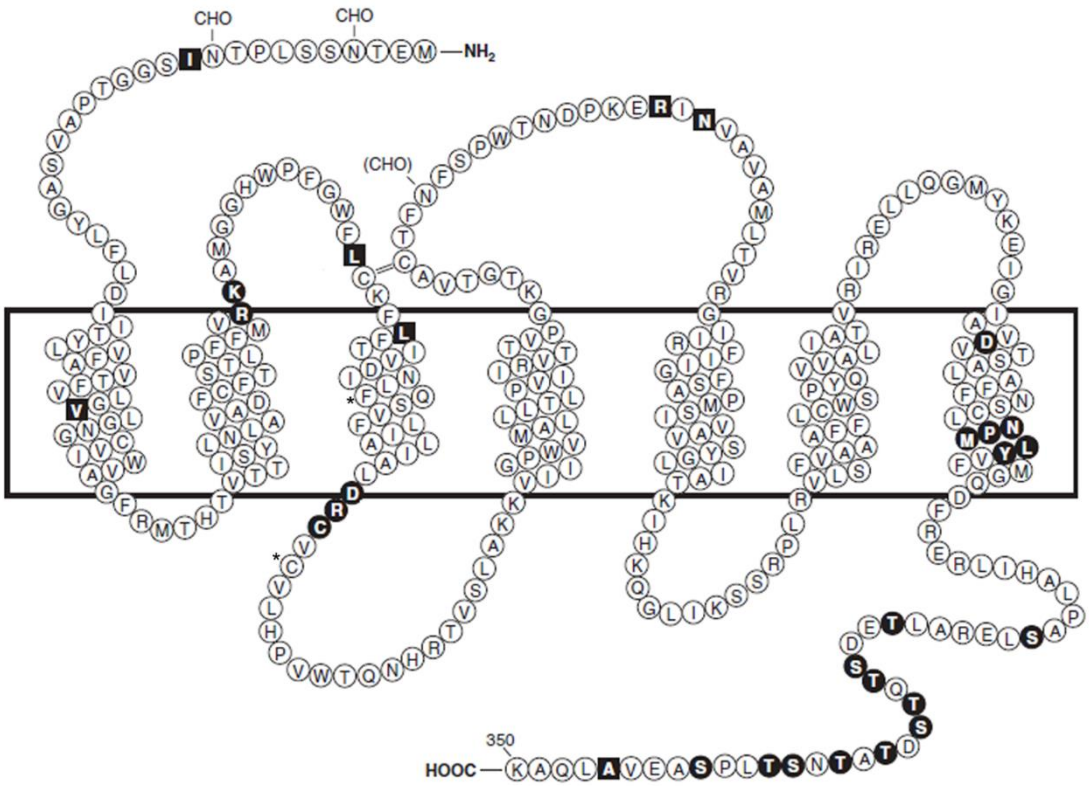

Figure 1.3: Human FPR1 G-protein coupled receptor amino acid (aa) arrangement across the transmembrane (predicted). 350 aa are encoded by the *fpr1* gene. Throughout its structure are sites important for SNP formation (black squares), high-affinity binding of potent ligands (fMLF), G-protein interaction, receptor internalisation, N-glycosylation sites and Ser/Thr phosphorylation sites (black circles). Asterisks indicate residue positions implicated in SNPs associated with juvenile periodontis (adapted from Ye *et al*., 2009).

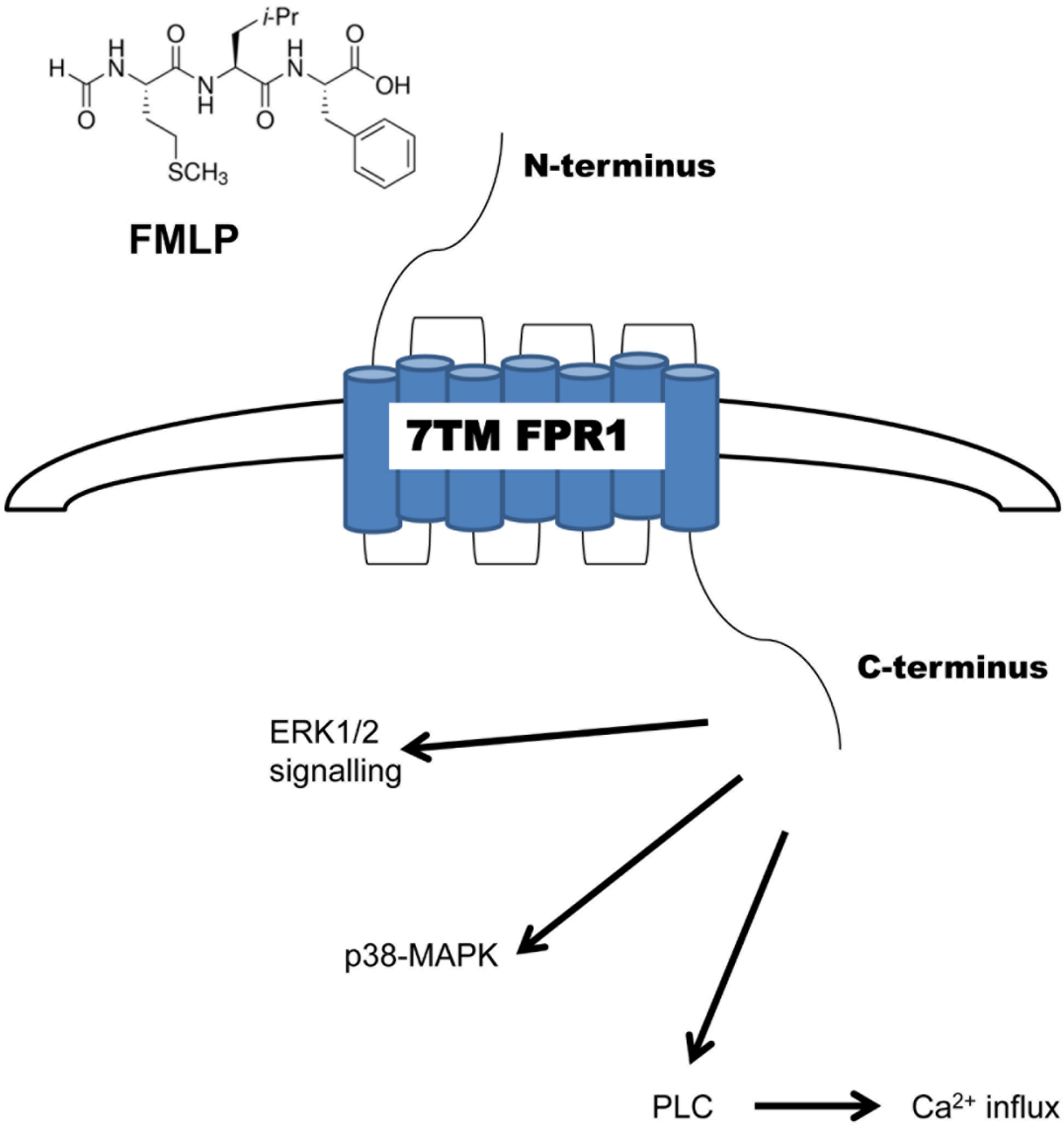

Figure 1.4: Schematic representation of receptor-ligand (fMLF) interaction with FPR upon the plasma membrane detailing activation of different downstream processes by the GPCR-binding of a ligand (fMLF) (adapted from Selvatici *et al*., 2006).

1.3.5 FPR functionality in disease

Originally characterised as one the first chemoattractant GPCRs in humans FPR function and physiological role has evolved over the years. The importance of this family in host defense has long been known but new tools in recent years have further elucidated its effects on this vital process. *Fpr* null -/- mice demonstrate ablated immune responses and this evident in different *in vivo* models. Susceptibility to bacterial infection and immunogenicity changed with loss of functional *fpr1* expression due to altered infiltration and migration of leukocytes to sites of infections (Gao *et al*., 1999). Due to lack of bacterial clearance by the innate immune response spleen and liver bacterial loads were dramatically elevated 2 days post infection correlating with impaired neutrophils in *fpr1*-deficient mice. In neutrophils FPR1 stimulation is responsible for a myriad of different processes such superoxide production, chemotaxis, CD11b, CD66b, CD62L surface marker expression changes, granule contents secretion including MMP-8, MMP-9, Cathepsins B, D, G, Myeloperoxidase, elastase activity and release of cytokine/chemokines (IL-8, MIP-1β, TNF-α). Decreased PMN function is demonstrated in FPR1 blocked mice similar to depleted migrating wildtype neutrophils in CsH treated cells (McDonald *et al*., 2010).

With bacterial and mitochondrial products capable of catalysing identical signalling pathways the significance of the DAMPs should not be underplayed with regards to trauma (Hauser *et al*., 2010). As trauma is essentially a sterile inflammation event is not surprising that mtDAMPs have been readily associated with it. Increased mtDNA levels in serum was confirmed in patients following trauma injuries, potentially acting to promote migration of leukocytes to damage sites via binding of TLR9. Indeed Hauser *et al*. (2010) detected thousand fold increases in femur fracture reamings (FFx) where tissue was disrupted as a result of lung injury. MtDAMPs isolated from patients were found to phosphorylate p44/p42 MAPK kinases, promote IL-8 and MMP9 secretion as well inducing calcium (Ca^{2+}) influx. Obviously trauma-induced alarmins are capable of activating neutrophil function. This is indeed a common theme due to role of the formyl-peptide receptor family in host defense. Monocytes are activated in a similar manner to neutrophils by the necrosis/damage-induced release of mitochondrial peptides which bind FPRs (Crouser *et al*., 2009). Due to evolutionary similarities FPR1 is able

to detect formyl peptides from both gram negative bacteria and dysfunctional endogenous cells.

Recent studies suggest the importance of FPR interactions promoting an innate immune response specifically by their expression in non-immune cells such as human fibroblasts of lung/skin origin (Van Compernolle *et al*., 2003). As an endogenous source of inflammatory agents N-formyl-peptide activation of FPRs has been shown to be integral in the migration of neutrophils and monocytes to sites of sterile inflammation (McDonald *et al.*, 2010). In effect FPR signalling is aiding the wound healing mechanism which has been further corroborated by Shao *et al*. (2011) in a linear scratch injury model using human lung epithelium. Interestingly, this paper has confirmed that FPR expression is integral to the wound healing response in non-haemopoietic cells. Another function mediated by human FPR1 is the induction of mesenchymal stem cell differentiation to osteoblast lineages presenting this GPCR as having a role in dynamic bone remodelling (Shin *et al*., 2011; Viswanathan *et al*., 2007). Another factor to consider is that different ligands exert a variety of effects through the FPR receptor. Formyl-peptides are certainly immunogenic but not necessarily pro-inflammmatory. Synthetic FPR agonists such as compound 43 (Cpd43) inhibit inflammation by downregulating interleukin 6 (IL-6) and dampening osteoclastogenesis (bone damage) in a murine rheumatoid arthritis (RA) K/BxN model as well as suppressing IL-6 release in translational human cells (Kao *et al*., 2014).

FPRs are relatively uncharacterised in non-inflammatory diseases but recent staining in malignant tumours of the central nervous system may suggest a role in cancer status (Huang *et al*., 2008). Before that even FPR expression was confirmed in human glioma cell line (U-87) by reverse transcription-polymerase chain reaction (RT-PCR) (Zhou *et al*., 2005). Furthermore Huang *et al*. (2010) have determined that the chemotactic behaviour of FPR1 is not limited to immune cells but is present in glioblastoma tumours thus increasing the chances of malignancy distribution. This was demonstrated by reduced malignancy and its associated features through *in vitro* and *in vivo* experiments, Receptor-ligand interactions were found to induce proliferation, angiogenesis and migration of tumours. Interestingly, these effects are similar to those demonstrated by leukocytes upon fMLF challenge (Zhou *et al*., 2005; Ye *et al*., 2009;

McDonald *et al*., 2010). Recent findings by Snapkov *et al*. (2014) indicate that N-formyl-peptides of mitochondrial origin are involved in the tumorigenesis of neuroblastoma cell lines at least *in vitro*. This correlates with its role in immune cells particularly neutrophils.

Interestingly emerging research may indicate contrasting roles for FPR activity in cancer as FPR1 was determined to downregulate angiogenic processes in human gastric cancer opposite to its effect in glioblastoma (Prevete *et al*., 2014). With expression on gastric epithelia cells and confirmed roles in wound repair in this setting it appears that FPR1 ligation limits key tumorigenic processes by acting as a suppressor in this specific setting. Clearly in certain types of cancer the FPR family may present a novel therapeutic target for future therapy interventions.

1.3.6 Neutrophil biology

Regarded as the first line of defense against pathogenic attack and acting as a link between the innate and adaptive immune response mechanisms, the neutrophil has many unique features that gear it towards its multiple functions. Due to their short lifespan neutrophils (Farahi *et al.*, 2012) are an obvious effectors to fight against opportunistic infections with the ability to secrete a myriad of cytokines and chemokines. These include CXC-chemokines, CC-chemokines, pro-inflammatory cytokines, anti-inflammatory cytokines, immunoregulatory cytokines, colony-stimulating factors, fibrogenic factors, and TNF superfamily members (Mantovani *et al*., 2011).

Neutrophils in the bloodstream are captured by the endothelium via selectin-mediated interactions. P-selectins and E-selectins bind P-selectin glycoprotein ligand-1 (PSGL-1) and L-selectins. The movement of neutrophils along the endothelial wall is by a rolling mechanism along a chemoattractant gradient until firm adhesion is achieved. This next stage is facilitated by integrins (ICAM/VCAM) and is followed by diapedesis whereby the cell translocates across the barrier to migrate to the infection site (Amulic *et al*., 2012).

After chemotaxis to the sites of inflammation and infection neutrophil elicit a myriad of different functions including release of pro-inflammatory cytokines, NET formation and

phagocytosis of microbes and infected cells. The latter is effected by NADPH (nicotinamide adenine dinucleotide phosphate-oxidase) oxidase activity which generates superoxide free radicals and triggers degranulation of intracellular organelles. Degranulation allows the release of anti-microbial proteins with enzymatic functions. Azurophilic granules contain stores of cathespin G, elastase, proteinase 3, defensins and myeloperoxidases with other granules containing lactoferrin, cathelicidin, collagenase and gelatinases. These granular effectors are the implementors of foreign cell/material breakdown in phagocytic activity (Witko-Sarsat, *et al*., 2000) Immunodeficiency Chronic granulomatous disease (CGD) is caused by NADPH subunit mutations in which infections are prolonged and with poor phagocytic ability (Heyworth *et al*., 2003). Upon clearance of bacteria neutrophils are rapidly depleted by apoptosis in order to resolve the inflammation associated with infection (Mocsai, 2013).

Neutrophil extracellular traps (NETs) are one of many methods that neutrophils mediate the removal of bacteria and compromised cells. NETs are a branched network of chromatin, granules and cytoplasm peptides. Only subpopulations of neutrophils manufacture NETs by a process called NETosis, a type of programmed cell death (Mantovani *et al*., 2011). The decondensation of chromatin fibres triggers the destruction of the nucleus. Another process, superoxide (reactive oxygen species, ROS) production is fundamental for NETs to be formed. Typically, NETs are released upon cell disintegration. These events are stimulated by bacteria recognition or stimulation with PMA which triggers remodelling of nuclear chromatin and dissolution of the nuclear membrane (Kobayashi, 2015).

From the millennium onwards it has become clear that neutrophils have a myriad of different roles in modulating the immune response both innate and adaptive. Through interactions with other immune cells such as T-lymphocytes, B-cells, dendritic cells and Natural Killer (NK) cells, a fully-equipped anti-bacterial/fungal response is mounted. Neutrophils facilitate cell activation through antigen presentation and polarising, pro-inflammatory cytokine production.

1.4 The heterogeneous environment of the lung

The structure of the human respiratory system is designed to provide an efficient delivery mechanism for oxygen into the body. Air travels through the nasal cavity or mouth passing down through the trachea (windpipe) and ultimately through its respective branches or bronchi. The divisions in the airways continue forming a tree-like structure until the bronchioles lead to their termini, gas-exchanging surfaces called alveoli. The alveolar airspaces present a large surface area for respiration numbering over ~300 million in healthy, non-diseased lungs (American Thoracic Society, 2014).

Epithelial cells constitute a major cell type in the human lung but depending on the location functions may vary from large to small airways to alveolar airspaces. Large airways cell types are involved in host defense against infection with ciliated and secretory cells as well as undifferentiated basal types. Small airways, further into the lung architecture (2^6 branches), have significantly increased proportion of ciliated cells with Clara cells differentiating from secretory cells. At the terminal branches (2^{23}) of the lung, the alveolar structures, airway and alveolar epithelium combine with type I/II cells (Crystal *et al*., 2008). Depending on the amount of branching epithelium constituents are subject to changes with ciliated columnar cells giving way to cuboidal epithelium which then branch further to squamous epithelium (the alveolar airspaces). The heterogeneous nature of lung epithelium and its co-ordination with endothelial, mesenchymal and fibroblasts cells is a key factor in the pathogenesis of most of the chronic pulmonary diseases commonplace today.

In a normal alveolus (air-sac) functionality is optimal with gas-exchange processes occurring due to close localisation with blood capillaries. Within this large surface area a resident population of alveolar macrophages represent the primary line of defense against opportunistic infection. Surfactant production by type II pneumocytes maintains the surface tension of the alveoli in a healthy pulmonary setting but with neutrophil recruitment and damage the alveolar membrane is compromised. The gas-exchange structures of the lung composed of type I pneumocyte cells are irrevocably altered with injury (acute and chronic) undergoing programmed and uncontrolled cell death (Figure 1.5).

Upon injury granulocytes (neutrophils) transmigrate into the lung across the capillary and alveolar cell membranes. Bloodstream neutrophils move along a chemokine gradient secreted by activated platelets rolling on selectins. Following neutrophil infiltration of the lung injury/infection is resolved by action of the immune cells. Epithelium/endothelium layers drastically increase their permeability resulting in leakage of protein-rich oedema material into the interstitium. This in turn alters the stability of the alveolar wall and the oxygen/carbon dioxide exchanging capability of the lung (Grommes and Soehnlein, 2010).

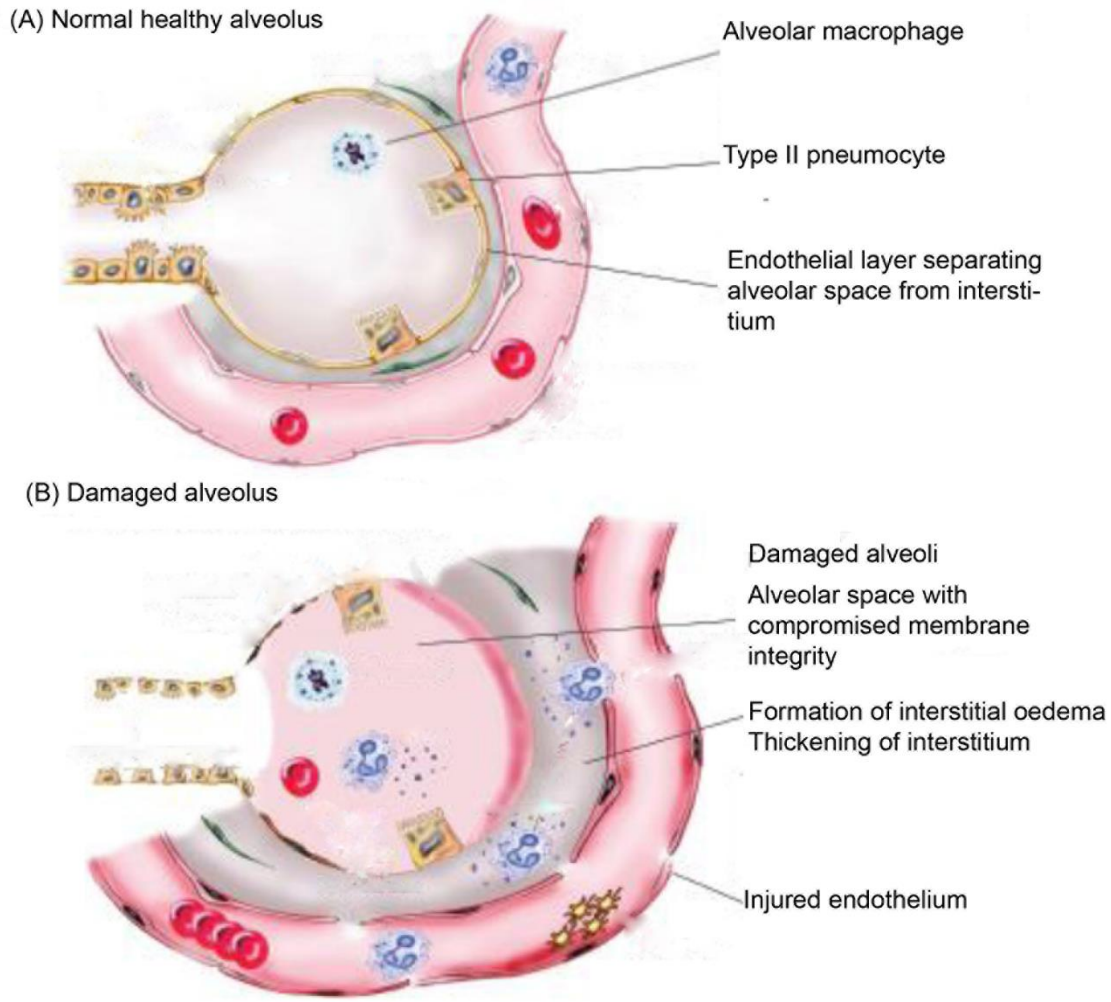

Figure 1.5: Diagram of healthy normal alveolus (A) versus a similar structure following neutrophil recruitment and damage to the lung (B). Schematic altered from Grommes and Soehnlein (2010) in which acute lung injury was characterised.

1.5 Fibrosis: an overview of fibrogenesis and wound-healing

Fibrosis is the result of unchecked wound-healing and fibrogenesis associated with the loss of functional tissue and the formation of dense scar tissue composed of collagenous depositions (Araya *et al*., 2010). Tissue fibrosis in different organs has many commonalities partly due to the similarity of the wound healing process. In the kidney, heart and liver particularly similar patterns are demonstrated with parenchymal injury, inflammatory response, vascular leakage and fibroblast proliferation (Zeisberg and Kalluri, 2012). Fibrosis occurs in many different organs such as the lung, liver, skin and kidney. Typically this involves an injury and damage which triggers a wound-healing response. Fibrogenesis mediators act upon immune cells but unchecked this leads to fibrosis and the replacement of tissue with non-functional scars. Pathogenesis of fibrosis in different organs is not identical due to differing microenvironments and cell interactions but a common mechanistic pattern is evident.

As is usually the case chronic insults impair the normal wound-healing response leading to progression from fibrogenesis to fibrosis such as cirrhosis – the end stage of chronic liver disease (CLD) (Hold *et al*., 2009). Disruption of the ECM production and turnover is a key feature of fibrosis in different organs. Type I collagen as well as other collagens (Type III and IV) are elevated with excessive deposition affecting tissue architecture and ultimately function. Tissue inhibitor of metalloproteinases (TIMP) and matrix metalloproteinases (MMP) work to maintain the equilibrium the ECM content. TIMP-1 and TIMP-2, the primary ECM regulatory elements bind MMP in an inhibitory fashion. The breakdown of this regulatory mechanism is an inherent part of the fibrotic process as production of collagen exceeds the rate of degradation (Friedman, 2008).

Fibrogenic processes that drive organ fibrosis and subsequent degeneration have been extensively characterised. Several mediators have been shown to induce an activated phenotype at a molecular level with differential effects between organs. Transforming growth factor-βeta (TGF-β1), a pleiotropic growth factor is responsible for fibroblast activation to an activated myofibroblast phenotype. All isotypes of TGF-β (1/2/3) in mammals have similar ECM regulatory activity. In particular it stimulates ECM production/deposition. Traditionally, sequestered in its latent form as a disulphide-bonded homodimer, by linkage to latency-associated protein (LAP) TGF-β undergoes

proteolytic cleavage to become activated triggering the Smad signalling pathway upon binding of its receptors. Phosphorylation of Smad and serine/threonine kinase activation results in stimulation of COL1A1 transcription (Wynn. 2008; Hold *et al*., 2009).

Transforming growth factor-Beta elicits a multitude of effects: inflammatory immune cell infiltration and secretion of different mediators which trigger hyperproliferation and deposition of collagen and other ECM components (Pohlers *et al*., 2009). TGF-β has long been associated with fibrogenesis and aberrant wound-healing responses. This cytokine is involved in maintenance of the extracellular matrix balance with increased secretion prior to tissue remodelling. In terms of tissue fibrosis TGF-β-mediated ECM production is demonstrated in chronic human diseases as well as experimental animal models in a variety of different organs including lung, liver, kidney, heart, skin and pancreas (Branton and Kopp, 1999). Key effects in wound-healing and fibrosis development are ECM accumulation, fibroblast proliferation, migration and myofibroblast differentiation (Pohlers *et al*., 2009).

The different members of this cytokine superfamily: TGFβ1/2/3 are all processed in a similar manner from latent proteins forming a complex with latent binding proteins. Upon cleavage of the LTBP from the C-terminus the precursor is activated allowing binding by a heterodimeric receptor composed of TGF-BRI and TGF-βRII. Subsequently the Smad signalling pathway is activated, with Smad4 is translocated to the nucleus for transcriptional regulation of gene expression (Leask and Abraham, 2004). As in human disease TGFβ is elevated with bleomycin-induced pulmonary fibrosis, with the selected duoset ELISA (R&D systems) detecting total cytokine level in bronchoalveolar lavage (BAL) fluid.

Normal wound healing responses are required to maintain tissue homeostasis and repair damage. Injury to epithelial/endothelial layers of tissue in the different organs leads to apoptosis of dysfunctional cells. These dying cells signal the release of pro-inflammatory mediators which in turn triggers coagulation. Platelet aggregates form and blood vessels undergo vasodilation with an increase in permeability. The effector cells of fibrogenesis, myofibroblasts are activated due to inflammatory events developing a collagen producing and α-smooth muscle actin (α-SMA) phenotype. These fibroblasts secrete MMPs as well as a variety of inflammatory mediators and

growth factors. Normal wound-healing processes are composed of 4 main stages: homeostasis, inflammation, proliferation (fibrogenesis) and remodelling. In homeostasis certain bio-physiologic events take place triggering vascular constriction as well as platelet aggregation, degranulation and the formation of fibrin. Inflammation consists of leukocyte infiltration via innate and adaptive immune responses localised to the injury site. Neutrophils, macrophages and lymphocytes migrate and secrete pro-inflammatory and pro-fibrogenic mediators which interact with tissue architecture. The cascade of co-ordination events leads to the proliferative phase consisting of re-epithelialisation, angiogenesis, collagen synthesis and ECM deposition. The resolution of the inflammatory phase is finished via tissue remodelling where the maintenance of the collagen synthesis/turnover balance and maturation of vascular architecture is effected (Guo and DiPietro, 2010; Wynn *et al*., 2008).

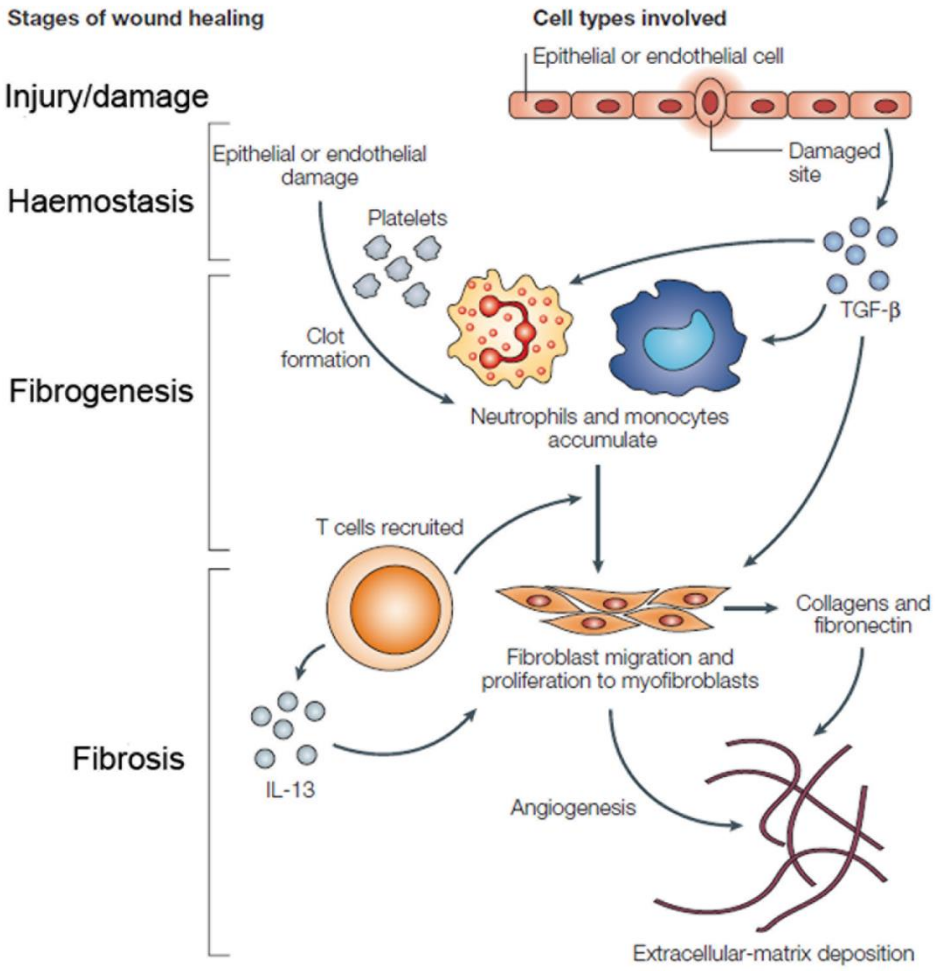

Figure 1.6: Schematic showing the stages of wound healing and cell types involved in the development of fibrogenesis and the fibrotic phase. Initial injury leads to triggering of haemostatic mechanisms causing accumulation of immune cells. During fibrogenesis proliferation of fibroblasts occurs to replace damaged tissue which if dysregulated will lead to the fibrotic phase (adapted from Wynn *et al.*, 2010).

Neutrophils and macrophages the principle immune cells involved in the innate response to damage play a vital part in potentiating the fibrogenic response. They facilitate inflammatory mediator release, chemotactic signalling, activation of effector cells and ultimately tissue remodelling. Macrophages are potent producers of TGF-β promoting ECM production by myofibroblasts. TGF-β has also been found to directly affect cell populations in fibrosis by promotion of epithelial-mesenchymal transdifferentiation (EMT) leading to an increase in activated myofibroblasts (Wynn, 2008). Depletion of TGF-β1 mRNA was a key effect with macrophage-deficient mice highlighting the centrality of growth factor production by wound macrophages in lung injury models (Brancato and Albina, 2011). Long established is the idea of differential responses by macrophages in response to stimuli. Distinct subsets have been characterised as 'classically (M1) and alternatively activated (M2) macrophages' resulting from LPS/IFN-γ or IL-4/IL-13 triggers respectively. A certain degree of controversy surrounds the concept of macrophage polarisation and whether or not subsets exist or is it down to spatial temporal differential regulatory mechanisms (Brancato and Albina, 2011). The plasticity of the macrophage allows it to have multiple roles in the development of fibrosis. In mouse models of wound healing wound macrophages have traits of both M1 and M2 phenotypes strengthening the idea of temporal regulation of activation status. Cytotoxic M1 cells are expressed by inducible nitric oxide synthase (iNOS), a phenotypic marker responsible for superoxide production. Wound-healing macrophages (alternatively activated) induce expression of arginase as well as key heparin-binding Ym1/Ym2 protein during well-characterised Th2 immune responses. The expression of arginase correlates directly with M2 macrophage role in fibrosis due to their effect on collagen turnover. FIZZ-1 (found in inflammatory zone 1) is another marker of M2 macrophages found specifically in these differentiated cells (Brancato and Albina, 2011).

1.6 Chronic fibrotic conditions

Human fibroproliferative disorders are a major health concern causing a massive drain on the economy. Major chronic diseases include interstitial lung disease (ILD), liver cirrhosis, chronic kidney disease (CKD), heart disease, eye macular degeneration. Research routinely uses different methods to replicate fibrosis in multiple organs relating to a variety of different insults such as trauma, toxic injury, impaired immune mechanisms, chronic infectivity and transgenic modelling (Wynn, 2004).

1.6.1 Chronic pulmonary disease

Pulmonary fibrosis is an umbrella term for interstitial lung diseases (ILDs) of which there are different grades and varying aetiologies despite similar clinical presentations. The classification of ILD depends on the causative factors such as exposure-related triggers, connective tissue disorder-related, genetic predisposition and its idiopathic nature.

Three main examples of human lung disease are COPD, emphysema and Idiopathic Pulmonary Fibrosis (IPF). IPF is a common ILD but is arguably the most devastating; with a high mortality 3-5 years post diagnosis (Mura *et al*., 2005; Lee *et al*., 2014) and transplantation of a healthy lung is probably the best chance of surviving (Moeller *et al*., 2006). This progressive fibrotic ILD is the most distinguishable idiopathic interstitial pneumonias and is characterised by massive tissue damage, development of fibrotic foci with excessive fibroblast proliferation and collagen deposition resulting in a ‘honeycombing pattern’ as pleural surface changes in a bosselated fashion (Devaraj, 2014; Wolters, Collard and Jones., 2014). Definitions of honeycombing are not standardised but the Fleischner Society has worked to bring together a consensus. Cystic air spaces group to form clusters in severely damaged tissue in ILDs with disrupted architectural structures (Devaraj, 2014). A classical HRCT presentation of IPF consists of honeycombing, reticular opacities, basal and subpleural predominance which essentially is a typical usual interstitial pneumonia (UIP) pattern (Figure 1.7).

Pathogenesis of IPF is quintessentially 3 main phases: (1) Damage/injury; (2) Inflammatory response; (3) Resolution/Repair that comprise an aberrant wound-

healing response. Repeated injury leads to chronic inflammation disrupting cytokine/chemokine equilibrium. This perpetual pro-inflammatory response and pro-fibrotic factors, IL-13 and TGF-β1 combine to generate a fibrotic phenotype. A multitude of different factors, known and unknown, coordinate in uncontrolled myofibroblast activity with increased proliferation and ECM production (Wilson and Wynn, 2009) resulting in this severe disease (Figure 1.8).

Primary diagnosis of IPF is by exclusionary criteria and subsequent classification is basic compared to other lung diseases (Chakraborty *et al*., 2014). COPD, unlike IPF, has established guidelines and measures for prognosis purposes in the form of Global Initiative for Chronic Obstructive Lung Disease (GOLD) system which increases therapeutic scope and patient surveillance (Kolb and Collard, 2014). The unknown nature of IPF in terms of pathogenesis, severity and heterogeneous classification presents a real challenge to developing a similar system. Its aggressive and complicated pathogenesis has made it difficult for clinicians to adequately treat this condition. Unlike other chronic lung diseases, generally characterised by progressive decline in lung function, IPF is irreversible with little treatment options while COPD is much more treatable, albeit dependent on whether or not exacerbations present and to what degree (Murray, 2011).

Potential therapeutic intervention strategies for interstitial lung disease include anti-inflammatory and anti-fibrotic drug regimens. Non-steroidal anti-inflammatory drugs (NSAIDs) comprise the analgesic/antipyretic group of medications. Key members of this non-steroidal group are paracetamol, aspirin and ibuprofen which act mainly by blockage of cyclooxygenase-1/-2 (COX-1/-2) activity and ultimately prostaglandin and thromboxane production (Vane and Botting, 1998).

Corticosteroids are another class of steroid anti-inflammatory drugs, derived from cholesterol through cytochrome P450 enzymatic activity. There are 4 main groups: Hydrocortisone, Acetonides, Betamethasone and Esters. Two notable steroids are prednisolone, the IPF therapeutic agent and dexamethasone. Dexamethasone has anti-inflammatory and immunosuppressant properties when used in humans and mice (Weichhart *et al*., 2010) with significant depletion of LPS effects in C57Bl6 mice in an acute model.

The most successful option for combating IPF is Pirfenidone (anti-fibrotic agent) which inhibits growth factors and collagen deposition through reduced TGF-β production as well as anti-inflammatory effects including reduction of TNF-α, interferon-γ and IL-6 (Nakazato *et al*., 2002). The actual benefit to the patient is only within a certain window dependent of stage of disease. Many researchers have questioned the validity of the use of this drug due to the prevailing opinion that IPF is not inflammatory driven (Oku *et al*., 2007; British Lung Foundation, 2014). Other drugs are being piloted such as anti-fibrotic agents Nintedanib and N-acetyl-cysteine (NAC) but the unknown pathogenesis and cause present problems development of therapeutic options (Chakraborty *et al*., 2014). Some evidence indicates IPF progression from non-specific interstitial pneumonia (NSIP) where chronic injury and inflammation at different stages trigger alveolitis, widespread damage and tissue remodelling.

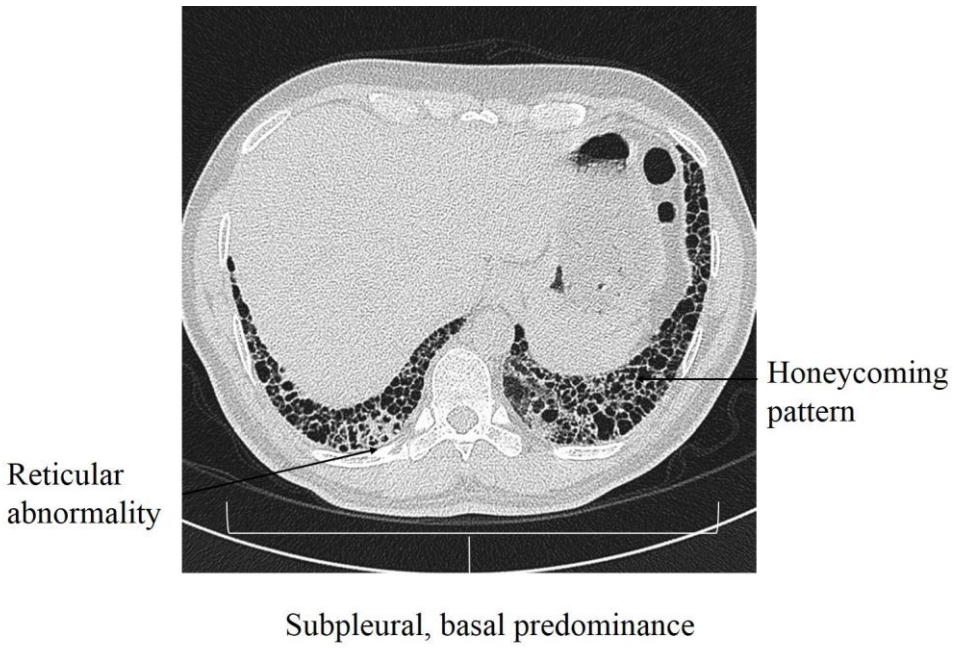

Figure 1.7: High-resolution computed tomography (HCRT) is standard method of diagnosing IPF with basal and peripheral honeycombing distribution (adapted from Devaraj, 2014) comprising a typical UIP pattern.

In normal tissue this would be a normal wound-healing response but in IPF impaired regulation of the repair process leads to an aberrant, uncontrolled response. This leads to the formation of type II pneumocytes, epithelium dysfunction, fibroblast hyper-proliferation, metaplasic squamous cells and honeycomb structure formation (Mura *et al*., 2005).

Alternatively activated macrophages are commonly associated with fibrosis development. Fibrotic responses resolve inflammatory responses to tissue damage. Increased immunomodulatory TGFβ cytokine levels triggers fibrogenesis and in response fibroblast proliferate. The change in phenotype correlates with a switch to Th2 cell cytokine profile comprising of IL-4, IL-13 and IL-10. Heterogeneous alveolar macrophages are fibrotic mediators contrasting with 'classically activated' M1 macrophages (Pechkovsky *et al*., 2010).

As for potential targets for therapeutic intervention in IPF there are many avenues that are currently being pursued. The dysregulated wound-healing response, chronic injury and inflammation and fibrotic processes are a by-product of multiple signalling pathways occurring simultaneously in a synergic and non-synergic fashion. Pathways that have been investigated in the past have been determined to have no effect by themselves indicating a complicated micro-environment within an IPF lung with redundant/coordinated processes and variation in different phenotypic groups presenting with IPF (Chakraborty *et al*., 2014). Studies into IPF so far have determined that in the course of this progressive disease there are three main pathogenic stages: predisposition, initiation and uncontrolled progression (Wolters, Collard and Jones, 2014). The initial stage consists of chronic dysfunctional epithelium due to SNPs and environmental factors predisposing a lung towards a fibrotic phenotype. Tissue remodelling is largely prevalent in the latter stages of IPF but exacerbations may flare in ILD-suffering individuals leading to an IPF presentation (Selman *et al*., 2001).

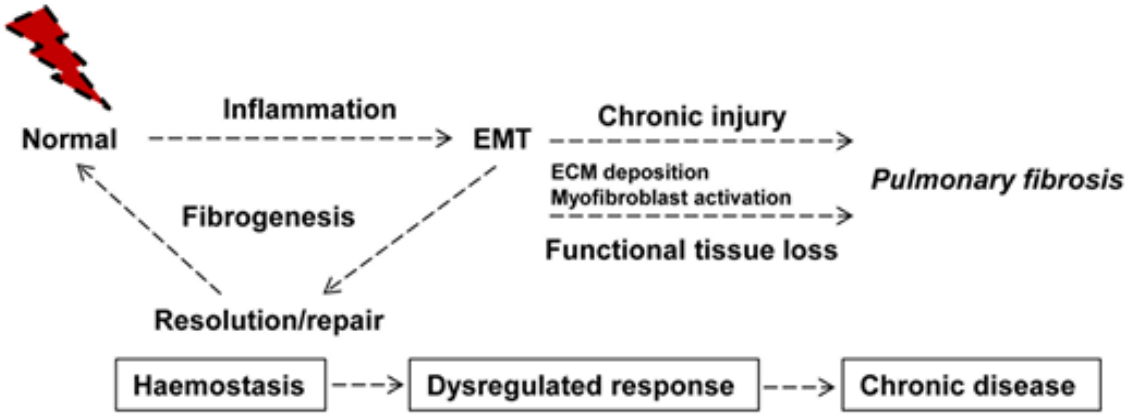

Figure 1.8: Schematic showing a simplified pathway for the development of pulmonary fibrosis from injury against normal tissue and the dysregulation of the haemostatic response to the progression to non-functional scar tissue (adapted from Drug Discovery Models:Today).

1.6.2 Chronic liver disease

Chronic liver disease (CLD) is a serious health implication with over 800,000 people worldwide dying each year (WHO) from end stage liver cirrhosis. Cirrhosis is irreversible due to a loss of the majority of functional tissue. Therapeutic interventions are largely focussed on liver fibrosis before it reaches the cirrhotic stage as the organ's regenerative capacity is able to be utilised in treatment (Marques *et al*., 2012). As with other organs CLD is associated with loss of parenchymal tissue leading to non-functionality. Parenchyma obliteration pre-empts either reversible fibrosis or irreversible cirrhosis. Cirrhosis is a chronic condition resulting from multiple bouts of damage and apoptosis from consecutive acute episodes. The difference between the two conditions is the ability to resolve the damage triggering the wound-healing response (Liu *et al*., 2012). Tissue homeostasis is maintained by apoptotic pathways which if unbalanced leads to disease. Damage to healthy liver cells triggers programmed cell death and inflammation is induced.

Liver fibrosis is preceded by injury or damage to tissue which initiates a pro-inflammatory immune response. Fibrogenesis is triggered and the immune response is resolved, proliferation replaces defunct tissue and liver can function normally again. With chronic liver injury the damage is never fully resolved resulting in an uncontrolled, fibrogenic response (Friedman, 2008).

Hepatocyte damage generally occurs in the form of membrane damage and lipid peroxidation. This generates reactive oxygen species (ROS) which perpetuate the injury phase. Apoptosis via the FAS-mediated TRAIL pathway has been shown to activate stellate cells. Essentially the initiation of an inflammatory response via hepatocyte destruction stimulates the liver microenvironment in a paracrine manner. Constant injury to hepatocytes drives hepatic stellate cell (HSC) activation from their quiescent form. Fibrogenesis leads to the proliferation, migration, contraction and ECM equilibrium shift within the stellate cell populations (Friedman, 2008). Trans-differentiation causes matrix degradation via production of tissue inhibitors of metalloproteinases (TIMPs). In response to TIMP enzymatic function collagen accumulates from positive enforcement of the feedback loop promoting liver fibrosis and cell survival. Cell death is a key factor in the wound-healing response. Resolution of fibrotic scar tissue and isolated hepatocytes is facilitated by hepatic myofibroblast

apoptosis. Gliotoxin, an epipolythiodioxoperazine fungal toxin has pro-apoptotic effects via its inhibition of NFκB. This destabilises the membrane enabling release of cytochrome C. Experimental *in vitro* studies have demonstrated gliotoxin-induced HSC apoptosis which when applied *in vivo* in rats stimulates fibrosis reversion in CCl_4 model (Wright *et al*., 2001). Activated stellate cell apoptosis alters the balance of MMP and TIMP action to favour matrix degradation ultimately leading to tissue remodelling and reversing of liver fibrosis (Elsharkawy *et al*., 2001).

HSCs are normally located in the sub-endothelial space of Disse between hepatocytes and sinusoidal endothelium where they are the main reservoir of extracellular matrix (ECM). With liver damage HSCs undergo a hyper-proliferative response losing their retinoid (Vitamin A) stores in their differentiation to activated myofibroblasts, the drivers of the fibrotic responses (Friedman, 2003; Jang *et al*., 2008).

Human liver disease is attributed to a variety of different causative agents with different aetiologies across conditions. These include viral infections such as hepatitis B and C (HBV & HCV), cholestasis, genetic susceptibility due to occurrence of single nucleotide polymorphisms (SNPs), portal hypertension, leptin accumulation (Non-alcoholic steatohepatitis; NASH), cancer (hepatocellular carcinoma, HCC), parasitic and opportunistic infections as well as drug abuse and alcoholism (Friedman, 2004; Liu *et al*., 2012; Liedtke *et al*., 2013).

In humans the main read-outs for chronic liver damage/fibrosis are serum damage enzyme levels: Aspartate aminotransferase (AST), Alanine aminotransferase (ALT), bilirubin and hyaluronan. ALT and AST are intracellular enzymes localised in the cytoplasm levels of which is able to be measured in plasma of patients due to cellular turnover. They are particularly indicative of hepatic liver damage and are used as a ‘liver function test’ with individuals diagnosed with clinical features of CLD or those at risk of CLD (Nyblom *et al*., 2004). Typically liver biopsy samples are analysed by histological means allowing grading (depending on amount of bridging collagen deposition patterns). In recent years non-invasive imaging such as IVIS methodologies have been employed to gauge level of damage/fibrotic tissue. These techniques involve fluorescent probes which label cells, ideally this is the way to analyse patients as it allows a real-time study of CLD (Liedtke *et al*., 2013).

1.6.3 Chronic kidney disease

Chronic kidney disease (CKD) encompasses a wide variety of conditions with complicated aetiologies which have damaged renal architecture and function. With CKD incidence on the rise, from a mere 7,000 patients in 1982 to over 50,000 reported cases in 2009, in the UK and rates increasing globally this is not a disease to be ignored (Zoccali *et al*., 2010; Caskey *et al*., 2011). Often involved with other diseases such as diabetes mellitus, hypertensions, and glomerulonephritis and also with aging (Levey *et al*., 2010; Zeisberg and Kalluri, 2013) there is demonstrable co-ordination in different aetiologies with increased cardiovascular and mortality risk with CKD.

CKD is difficult to diagnose in early stages with detection often coming too late for successful therapeutic intervention. Typically renal functions proteinuria and haematuria are assessed by serum creatine levels to determine the estimated glomerular filtration rate (eGFR) which is subsequently used to rank patients in order of severity (Levey and Coresh, 2012). The National Kidney Foundation has set out KDOQI staging of CKD comprising five severity ranks ranging from normal – mildly reduced – moderately reduced – severely reduced – renal failure correspond to progressive structural/functional alterations which ultimately result in impaired functional capability (Stevens *et al*., 2007; Cirillo, 2010).

End-stage renal disease (ESRD) is the last point for therapeutic treatment but at this stage renal replacement therapy (RRT) is involved in the form of either dialysis or transplantation. Increasing incidence of CKD has in turn raised numbers of patients requiring RRT according to UK Renal Registry 13th Annual Report (2010) which is a major cost equating to over £30,000/patient/year (Caskey *et al*., 2011). Tightly organised tubules in the cortical region located in the extracellular matrix (ECM) with basal deposition levels are subject to drastic changes in ESRD. An interstitial fibrotic phenotype is exhibited with ECM equilibrium dysregulation, myofibroblast activation, proliferation, nephron destruction, leukocyte infiltration and tubular atrophy (Zocalli *et al*., 2010).

Key factors that distinguish renal fibrosis over other organs are its architecture and cell types in the microenvironment. Development of fibrosis and loss of functionality typically occurs in two main areas: glomeruli and tubular interstitium. Depending on

region in kidney fibroblasts have differing functions. Erythropoietin is exclusively produced by medulla region lipid-rich fibroblast unlike cortical counterparts. A major feature of chronic renal fibrosis is the nullified expression of this anaemia inhibitor in activated myofibroblasts. Indeed fibroblasts have a degree of heterogeneity within this setting but they also differ significantly with other organs. Proliferation and regenerative capability are severely compromised in CKD but unlike the liver it is largely irreversible (Zeisberg and Kalluri, 2013). The cortical region is largely tubulointerstitium (~90) as well as glomeruli (~10%). Other cell types include tubular epithelial cells, quiescent fibroblasts and immune cells (macrophages and lymphocytes). In terms of human CKD the key region affected by renal fibrosis is the cortical region (Harris and Nelson, 2006).

The progressive nature of the disease is devastating in terms of function and kidney mass with little hope of therapeutic intervention. Regression has noted in cases of diabetic nephropathy with pancreas transplantation and with clinical drug trials of ACE inhibitors but research is still a significant way from making a difference in therapeutic treatment. Avoidance of renal failure (eGFR<15mL/min/1.73m^2) by improvement of available tools available for early diagnosis is a priority of current research.

2 Hypothesis

FPR activity through the ligation of its vast repertoire including mitochondrial DAMPs is important in the pathogenesis of fibrosis. As the microenvironment in different organs varies in terms of architecture and cellular infiltration particularly neutrophil recruitment the fibrotic mechanism will vary in turn.

Neutrophil involvement will vary in different mechanisms of fibrosis in different organs which may be, due to an abundance of FPR expression, related to FPR activity. Pulmonary fibrosis mechanisms are neutrophil-dependent with regards to the bleomycin-injury *in vivo* model. In other settings, hepatic and renal FPR expression loss will have a marginal effect on the development of fibrosis.

Aims (i)

To elucidate FPR1's role in the development of fibrosis in the pulmonary setting

Objectives

- Utilisation of bleomycin-induced injury *in vivo* model with evaluation inflammatory and fibrotic phases
- Evaluation of the bleomycin model as a method of investigating pulmonary fibrosis with regards to its pathogenesis

Aim (ii)

To determine role of FPR1 in the pathogenesis of other *in vivo* organ fibrosis models such as the kidney, liver and skin

Objectives

- Utilisation of obstruction renal model (UUO) to determine effect of *fpr* deletion on kidney fibrosis
- Utilisation of chronic toxic injury model (CCl_4) to gauge effect on liver fibrosis and fibrogenesis

Aim (iii)

Characterisation of FPR receptor family expression in *in vitro* cultured cells and primary human tissue

Objectives

- Utilisation of different methodologies to assess levels of receptor expression in terms of messenger RNA (mRNA) and translated protein in cultured cells, cell lines and primary human and murine cells.
- Evaluation of FPR1 receptor in primary diseased human tissue combined with other cellular markers. This in turn will allow assessment of importance in architectural and/or immune cells.

3 Methods

3.1 Cell culture

3.1.1 Primary human tissue culture

Primary bronchial epithelial cells (PBECs) were obtained from bronchial brushings of unused donor normal or explant IPF/COPD. Cells were grown in specialised small airway growth medium (SABM, Gibco) supplemented with Bovine Pituitary Extract (BPE), 2.0ml; Hydrocortisone, 0.5ml; human Epidermal Growth Factor (hEGF), 0.5ml; Epinephrine, 0.5ml; Transferrin, 0.5ml; Insulin, 0.5ml; Retinoic Acid, 0.5ml; Triiodothyronine, 0.5ml; GA, 0.5ml; Bovine Serum Albumin-Fatty Acid Free (BSA-FAF), 5.0ml. All flasks and plates used for culture were coated with 0.5% Purecol (Invitrogen, UK) diluted in PBS prior to seeding. Primary lung fibroblasts were grown in minimal eagle medium (MEM, Sigma) supplemented with 10% Fetal Bovine Serum (FBS), 100µg/ml penicillin, 100U/ml streptomycin (P/S) and 1% L-glutamine (L-GLUT). Regardless of cell type consistent seeding densities were used, for RNA experiments 200,000 cells per well of a 6-well plate with serum-starving upon attainment of ~70% confluence. Primary cells were utilised from passages 1-4 as with later generations of isolated populations cells begin to change their characteristics losing physiological relevance.

3.1.2 Isolation of human immune cells

3.1.2.1 Peripheral blood neutrophils

All isolations performed by Simpson group at Newcastle University by Jonathan Scott or other members of the lab accordingly to a method described in Dransfield *et al.* (1994). Neutrophils were isolated from whole blood obtained from healthy, normal volunteers via dextran sedimentation and Percoll gradient fractionation steps. As part of the same protocol primary macrophages/monocytes were obtained from similar samples for use in gene expression investigations.

3.1.2.2 Peripheral T cell populations

Primary T lymphocytes were obtained from healthy, normal volunteers in PBMC populations isolated from peripheral blood. Isolation of PBMCs and positive selection for CD3 expression using microbeads (Milteny Biotec) was undertaken by Monika Suwara.

3.1.3 Cell line tissue culture

Human embryonic kidney (HEK) cells were maintained in Dulbecco's Modified Eagle Media (DMEM, Sigma) media supplemented with 10% FBS, 1mM glucose-pyruvate and 100µg/ml penicillin, 100U/ml streptomycin (P/S). HEK cells transfected with FPR1 and FPR2 clonal constructs were grown also in 10% FBS DMEM but with supplement differences. Media supplements included 1mg/ml Geneticin (G418, Invitrogen), 350µg/ml Zeocin (Invitrogen, UK) and x5 Non-essential amino acids (NEAA, Invitrogen) for FPR1-overexpressing HEK cells and 1mg/ml Geneticin (G418) only for FPR2-overexpressing HEK cells. These semi-adherent cell lines did not require trypsinisation for passage events instead washes with phosphate-buffered saline (PBS) were sufficient. With regards to assessing FPR expression either at a protein or transcript level these stably transfected cell lines acted as positive controls for formyl-peptide receptors, FPR1 and FPRL1. Both transfected cell lines were obtained as part of the collaboration with MedImmune (Cambridge, UK) and were used in the optimisation of a human FPR1-specific antibody developed by Douthwaite *et al*. (2014).

THP-1 monocytic cells ($1x10^6$ cells/ml) were activated to an adherent phenotype in 6 well plates containing 2ml of RPMI 1640 medium (Sigma, UK) supplemented with 5ng/ml phorbol 12-myristate 13-acetate (PMA) over 24 hours. Doses of PMA used to differentiate THP-1 cells among different groups range from 5-400ng/ml (Greenberger *et al*., 1980; Park *et al*. (2006) ascertained that THP-1 monocytes were converted to functional macrophages (CD14+ve) with an optimal dose of 5ng/ml. For differentiation to inflammatory (M1) and anti-inflammatory (M2) phenotypes PMA-activated cells were

treated with IFNγ or an IL-4/IL-13 mixture all 20ng/ml (R&D Systems, UK) for 18 hours respectively. Following RPMI media was replaced to remove any non-adherent cells and LPS (1µg/ml) was then added at various time points.

16-HBE14o- (a gift of D. Grinert), a differentiated SV-40 transformed bronchial epithelial cell line were maintained in HyClone media supplemented with 10% FBS, 1% L-GLUT and P/S.

MRC5, a fibroblast cell line were cultured in 10% FBS MEM media with 1% L-GLUT and P/S.

3.2 Polymerase chain reaction (PCR)

3.2.1 RNA isolation and cDNA synthesis

Total ribonucleic acid (RNA) was extracted from cultured cells aswell as tissue samples and neutrophil preparations using the RNeasy Kit (Qiagen) starting with lysis in RLT buffer-β-mercaptoethanol (10µL per 1ml RLT). Following RNA isolation in RNase-free water (Qiagen) a nanodrop 2000 machine was used to quantify RNA (ng/µl). Purity was ascertained by 260/280 ratio with samples <1.8 excluded. Subsequently, between 0.25-1.0µg was used to prepare cDNA templates with Moloney murine leukemia virus reverse transcriptase (MMLV-RT). A suitable quantity of RNA was incubated at 37°C for 30mins along with 1µl DNAse and 1µl DNase buffer. Application of a DNase Stop solution consisting of 0.5M EGTA stopped DNAse activity and was followed by 0.5µl Random Hexamers (Primers) plus 2µl of nuclease water. After a 5 minute incubation at 70°C, samples were kept on ice till a reaction mixture of 0.5µl RNAsin, 1µl MMLV-RT, 1µl dNTPs oligonucleotides and 4µl MMLV-RT buffer was added (all reagents Promega, UK). Sample templates were diluted to 10ng/µl following 60min incubation at 42°C.

3.2.2 RT-PCR

Reverse Transcriptase Polymerase Chain Reaction (RT-PCR) was performed under the following thermocycling conditions: 3 minutes at 94°C, followed by 40 cycles of 20 seconds at 94°C, annealing at 50-60°C for 30 seconds and elongation at 72°C for

30seconds followed by a final 7 minutes at 72°C. Reaction mixtures contained Dreamtaq master mix (Promega, UK), 20ng cDNA template 0.1umM of primers made up to 25µl final volume with RNase-free water. Following PCR run, products were run with 3µl of 10x OrangeG running buffer on a 2% agarose gel for one hour at 0.15A. Upon completion of gel electrophoresis PCR bands were visualised alongside a PCR marker DNA ladder under UV.

3.2.3 Quantitative PCR (qPCR)

Quantitative polymerase chain reaction (qPCR) was performed using a 7500 Fast System (Applied Biosciences). Standard reactions in each well of a 96-well plate consisted of 6.5µl SYBR Green Master Mix (Sigma-Aldrich, UK), 10ng of cDNA and 0.1µM of primers made up to a total volume of 13µl. Reaction mixtures underwent 40 cycles of denaturation for 10 seconds at 95°C, annealing at 50-60°C (depending on primer pair) for 30 seconds and elongation at 72°C for 30 seconds, followed by a final dissociation curve cycle of 95°C for 15 seconds, 60°C for 60 seconds and 95°C for 30 seconds. All results were normalised to a control housekeeping gene (GAPDH).

3.2.3.1 Primer design and optimisation

All primers were designed using NCBI nucleotide sequences. The coding sequences were analysed with OLIGO ™ primer generator software to produce short oligonucleotide sequences for forward and reverse primers. Primer pairs capable of amplifying unique genetic sequences 150-250bp in length were then ordered from Sigma-Aldrich (UK). Using this approach primers were generated for human FPR1 (hFPR1), human FPR2 (hFPR2), mouse FPR1 (mFPR1), mouse FPR2 (mFPR2) and the human TLRs (Table 1). These oligonucleotides were tested for specificity and efficiency via RT-PCR and qPCR respectively. A dilution series for each primer's control cDNA allows primer efficiency to be calculated by linear regression (Figure 3.1). The higher the efficiency percentage the better the affinity and PCR product yield. Another test of any primers designed with OLIGO software was qualitative assessment of qPCR melt curve at the end of the run. This enabled elimination of primers which formed excessive primer-dimer and mis-primed product signal.

3.2.3.2 Normalisation of gene expression

All results were normalised to a housekeeping control gene: GAPDH (Human/Mouse) to assess accuracy. Gene expression was calculated relative to untreated controls by using the formula: (1/2A) x100.

3.3 Protein isolation and Western blotting

Following *in vitro* treatment cultured cells were harvested using Radio Immuno-Precipitation Assay (RIPA) lysis buffer. Homogenization of samples was achieved by sonication for 6 minutes under ice conditions. Samples were then subjected to high-speed centrifugation at 4°C for 15 mins at 13,000xg. The supernatant was decanted into another eppendorff, discarding the resulting pellet of cellular debris. Samples were then quantified using the Bradford DC Protein assay. Absorbance at 750nm measurement using a spectrophotometer enabled 50µg of protein sample to be aliquoted and stored at -80°C. Equal amounts of protein samples were added to 5x Laemmli buffer and denatured for 5 minutes at 95°C. 10% sodium dodecylsulfate (SDS)-polyacrylamide gels were run for approximately 2 hours at 100V followed by 100V nitrocellulose membrane transfer. Membranes were then stained with Ponceau Red to confirm accurate sample loading and blocked with 5% milk in Tris-buffered Saline (TBS)/0.01% Tween 20 (TBS-T) to prevent non-specific binding.

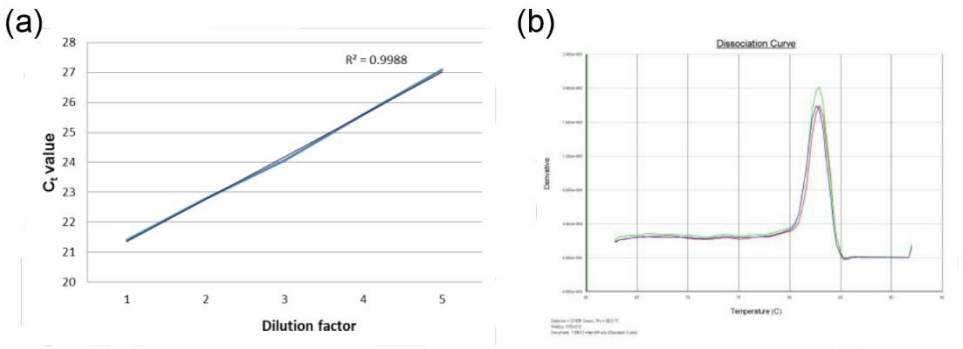

Figure 3.1: Primer optimisation evaluated by (a) primer efficiency following doubling dilution of template cDNA (initial quantity: 20ng). Linear regression of line of best fit allows calculation of R^2 value which should be above 0.95 for optimal results. (b) Optimal melt dissociation curve showing a single, clear peak with no secondary peaks (indicative of primer-dimer formation).

Table 3.1: Oligonucleotide 5'-3' sequences for functional primers of human and mouse genes

Gene target	Forward primer sequence	Reverse primer sequence
Mouse GAPDH	GCACAGTCAAGGCCGAGAAT	GCCTTCTCCATGGTGGTGAA
Mouse FPR1	ACACCAACATGTCTCTCCTC	TAAAATGGCAAAGTGGAAGT
Mouse FPR2	GATTCTCACTTTGCCCATTTTTA	CAGCAATGAGTCCATAGCAAACA
Mouse FPR3	TGTGGTGATCTATGATTCTACCA	TCATAGCCATTTCAACAAGAAGG
Mouse Fibronectin	GAGCAAGAAGGACAACAGAG	GGTCTGGGGTTGGTAAATAG
Mouse Elastin	CCCTGTCCCTGTTCCTTCTG	CGCTCCCTATCCTCTTGTTG
Mouse TIMP1	GCAACTCGGACCTGGTCATAA	CGGCCCGTGATGAGAAACT
Mouse MCP-1	AGGTCCCTGTCATGCTTCTG	TCTGGACCCATTCCTTCTTG
Mouse KC	CTGGGATTCACCTCAAGAACATC	CAGG-GTCAAGGCAAGCCTC
Mouse α-SMA	TCAGCGCCTCCAGTTCCT	AAAAAAAACCACGTAACAAATCAA
Mouse Collagen 1A1	TTCACCTACAGCACGCTTGTG	GATGACTGTCTTGCCCCAAGTT
Mouse IL-6	TAGTCCTTCCTACCCCAATTTCC	TTGGTCCTTAGCCACTCCTTC
Mouse S100A9	CACCCTGAGCAAGAAGGAAT	TGTCATTTATGAGGGCTTCATTT
Human GAPDH	GAGTCAACGGATTTGGTCGT	GACAAGCTTCCCGTTCTCAG
Human FPR1	CCTGATCGCCCTCATTGCTC	GTTGGTCCAGGGCGAAAAGT
Human FPR2	TACCATGCTGACAGCCAGAG	CCAGTTGAAAGGGAAACCAA
Human TLR1	CCTAAAGACCTATCCCAGAA	ACAGTAGGGTGGCAAGAAAT
Human TLR2	TTGTGGATGGTGTGGGTCTT	AGGTCACTGTTGCTAATGTA
Human TLR3	TATTTCCCTTGCCTCACTCC	TGGTTAGGTTGAGTATGTGT
Human TLR4	TTTTTCTAATCTGACCAATC	TCATAGGGTTCAGGGACAGG
Human TLR5	TACCCCCTTGACTATTGACA	ATAACCATCTTTCAATACAG
Human TLR6	TTCCATTTTGTTTGCCTTAT	TTATGGGAAAGTCTCAAAAC
Human TLR7	GATTTACTCCATTCAACAGC	TGTCGTTCATCATCAGTTTC
Human TLR8	ATGTTCCTTCAGTCGTCAAT	TTTTGCTTTTTCTCATCACA
Human TLR9	TACCTTGCCTGCCTTCCTAC	TGTCACCAGCCTTTCCTTGT
Human TLR10	TTATGACAGCAGAGGGTGATG	GGAGTTGAAAAAGGAGGTTA

Milk contains casein, a phosphoprotein hence if looking at phosphorylated proteins 5% bovine serum-derived albumin (BSA) should be utilised to block membranes. Upon 1 hour room temperature incubation primary antibodies in 5% milk or 5% BSA were applied to membranes which were then incubated overnight at 4°C. Membranes were washed in TBS-T solution for 5 minutes three times preceding 1/5000 diluted horseradish peroxidise (HRP) conjugated secondary antibody 1 hour incubation at room temperature. Blots were again washed with TBS-T before development using Pierce ECL kit. Antibody-substrate complexes ascertained via usage chemi-luminescent detection reagents and X-ray film cassettes according to manufacturer's instructions.

ERK1/2 phosphorylation status was assessed via western blot analysis utilising FPR-transfected HEK cells. ERK activation was measured using an anti-Pp44/p42 mAb (1:1000, Cell Signalling Technology) and equal loading with a total ERK (p44/p42) (1:1000. Cell Signalling Technology).

3.4 Immunohistochemistry

3.4.1 Haemotoxylin and Eosin (H&E) staining

Formalin-fixed paraffin embedded sections were dewaxed in Xylene (10 minutes), and then 100% alcohol (2 minutes) followed by 95% alcohol. For staining sections were washed in running tap water before 4 minute incubation in Mayers Haemotoxylin. This was followed by tap water wash for 1 minute then 30 seconds in Scott's Water for nuclei counterstain. Another 1 minute wash was performed succeeded by an Eosin 1 minute incubation. A final thorough wash in running tap water was performed for 4 minutes. This was followed by dehydration steps through graded alcohols: 50%, 75%, 95%, 100% Ethanol (EtOH) 2 seconds each then 100% EtOH 2 minutes. Two Xylene treatments for 4 minutes were performed until clear. Sections were then mounted with coverslips using DPX.

3.4.2 Pico-Sirius Red (PSR)

Formalin-fixed paraffin embedded sections (4µm thick) were dewaxed via 5 minute incubation in the following solutions: Clearene I, Clearene II, 100% Ethanol and 70% Ethanol (EtOH). Distilled water washes 3 minute/washes directly preceded incubation in phosphomolybdic acid (0.2% PMA) for five minutes. Distilled water washes were as described previously. Subsequently sections were incubated with 0.1% Sirius red F3B in saturated picric acid for 2 hours. This was followed by 0.01M HCl wash (2 minutes) and dehydration of sections through alcohols: 70%, 90%, 100% for 20 seconds each then 2 minutes in 100% EtOH and finally Clearene for 5 minutes prior to mounting in Pertex.

3.4.3 Murine formalin-fixed tissue

Formalin-fixed paraffin embedded (FFPE) sections (4µm thick) were dewaxed as previously described. Non-specific endogenous peroxidase activity was blocked by 0.2% hydrogen peroxide (H_2O_2)/methanol incubation. Antigen retrieval varied depending on antibody methodology (see table 1). Subsequent blocking was achieved by Avidin/Biotin Blocking Kit (Vector Laboratories) followed by 20% porcine serum block in PBS. Sections were incubated with primary antibodies to alpha-SMA, PCNA, CD68, NIMP and CD3 overnight at 4°C. Sections were in turn applied with the appropriate secondary antibody for 2 hours, washed and incubated with ABC tertiary agent (Vector Laboratories) and visualised for positivity using 3,3′-diaminobenzidine tetrahydrochloride (DAB, Vector Laboratories). Sections were counterstained using Mayers-Haemotoxylin (for 10-30 seconds) and Scott's water (30 seconds). All antigen retrieval methods and concentration of antibodies used (primary and secondary) are described in Table 3.2.

3.4.4 Human formalin-fixed tissue stained for FPR1 expression

Human IPF paraffin-embedded formalin-fixed sections were pre-heated to 60°C for 1 hour. Sections were then de-waxed in xylene for 10 minutes and re-hydrated through graded alcohols: 99%, 99% and 95% IMS for 1 minute. Endogenous peroxidases were blocked in 0.3% methanol/H_2O_2 for 30mins. Sections were then washed for 10 minutes in running tap water followed by rinsing in TBS buffer. Antigen retrieval was achieved by microwaving in boiling citrate buffer (pH= 6.0) for 15 minutes. Subsequently sections were left to cool for 20 minutes and then rinsed in TBS prior to primary monoclonal antibody incubation. Human FPR1–HRP direct conjugated antibody was diluted in 3 % BSA to a concentration of 2µg/ml for staining the tissue. Antibody was linked to HRP conjugate as per manufacturer's instructions (Innova Biosciences). 100µl monoclonal antibody was added to sections and incubated at 4°C for 48 hours. After this primary incubation sections were washed three times in TBS buffer for 5 minutes per wash. For the final immuno-reactivity step a working solution of DAB was applied for 5 minutes with positive areas turning brown. Following this incubation DAB was neutralised in a bleach/water solution and sections were washed for 5 minutes in running tap water. Haematoxylin counterstain was then applied for 1 minute and subsequently washed in tap water. Stained sections were finally dehydrated through ethanol: 95%, 99% and 99% for 30 seconds, cleared in Xylene solution and mounted using DPX solvent. Staining protocol was developed extensively from the beginning by Kasim Jiwa (Biomedical Scientist, Freeman Hospital, Histopathology Department).

3.4.5 Periodic Acid-Schiff (PAS) stain

Specifically stains carbohydrate residues in proteoglycan components of the basement membranes. Paraffin-embedded formalin-fixed 2-4µm thick tissue sections were dewaxed in xylene (10 minutes) and rehydrated in EtOH (100% and 95% each 30 seconds) then distilled water (5 minutes). Sections were then incubated in Periodic Acid (1%) for 6 minutes then washed in distilled water (3x 2 minutes). Sections were incubated in Schiff's reagent for 10 minutes followed by 10 minutes under running distilled water. Tissue was then counterstained with haematoxylin for 1 minute and washed thoroughly for 5 minutes under the tap. Dehydration was performed in

increasing strengths of Ethanol (60% 80% 95% 100%), each for 30 seconds and then into xylene for 30 seconds. Finally sections were mounted with coverslips using DPX (Sigma, UK).

3.4.6 Image analysis

Bright-field image analysis was carried out using Nikon Eclipse Upright microscope proprietary Elements™ software. Cell counts were performed to give an average number of positive cells per field. Typically for counting cells 20 fields (at x20 magnification) were taken and analysed. For densitometry of ECM components (collagens and α-smooth muscle actin) a threshold was defined and applied to images acquired of IHC stains at x10 magnification. From this a percentage area was calculated allowing treatment groups to be compared using GraphPad Prism 5.0 software.

Fluorescent image analysis was carried out using Zeiss Axio Observer Inverted and Laser Scanning Confocal Microscopy (LSCM) equipment.

3.4.7 Histological scoring

3.4.7.1 Liver

Picro-Sirius Red (PSR) stained sections from chronic CCl_4 / Olive oil 8 week model were scored on a scale of 0-4 by Dr Fiona Oakley (Fibrosis Research Group). Ranking was assigned according to the degree of fibrosis indicated by collagen staining and scar formation. Ranks are as follows: 0 – No fibrosis evident, 1- Mild, 2-Moderate, 3-Severe (>2 vessels linked and multi-layered deposition), 4-Cirrhosis (multiple instances of bridging fibrosis and nodule formation).

3.4.7.2 Kidney

Histological scoring of UUO model was determined by examination of sections stained according Periodic Acid Schiff's (PAS) protocol by bright field microscopy using the aforementioned Nikon Eclipse Upright microscope. For each contralateral and obstructed kidney section, 20 fields in the cortical region were acquired at x20 magnification. Using Photoshop software, a 10 x 10 grid was superimposed onto each image and the number of grid intersections overlaying interstitial areas and tubular luminae were counted and expressed as a percentage of the total 81 grid intersections (excluding glomeruli), for each image (Figure 3.2). All counts were performed in a blinded manner. Depending on where in the particular field intersections were observed the percentage interstitial expansion (A) or tubular dilatation (B) was calculated.

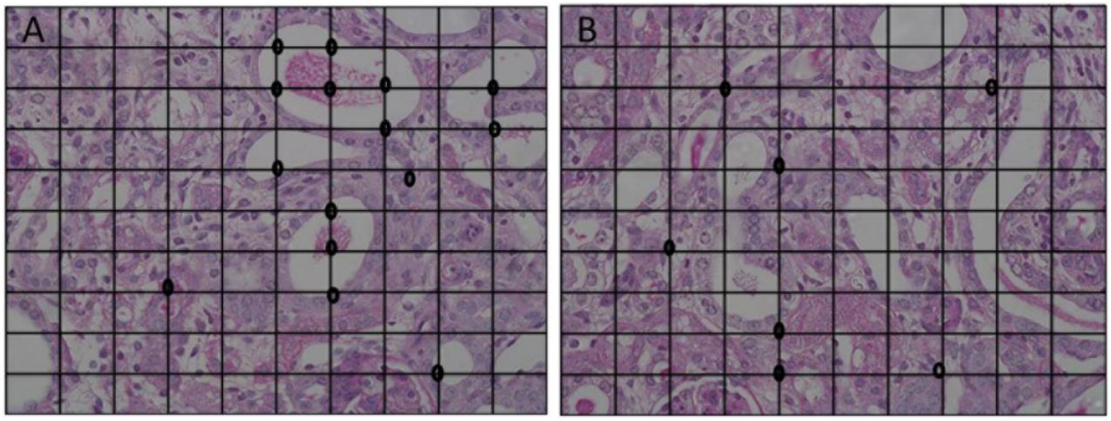

Figure 3.2: Manual scoring of periodic acid Schiff's stained renal tissues for tubular dilatation and interstitial expansion. Counting of grid intersections over areas of interest to measure tubular dilatation (A), and interstitial expansion (B). Scores calculated by converting counts to percentages of the total number of grid intersections (81) per high powered field minus intersections located on glomeruli structures. (B). Magnification of acquired images is x20.

Table 3.2: Immunohistochemistry antibodies used on murine FFPE-sections for different cellular markers. Commercial supplier, antigen retrieval and secondary antibody for each antibody detailed.

Antigen	**Supplier**	**Cellular target**	**Antigen retrieval**	**Secondary antibody**
NIMP, Rat monoclonal	Abcam, UK/ ab2557-50/ NIMP-R14	Neutrophils	0.01% Pronase, humidified atmosphere 37°C	Goat anti-rat biotin conjugated Ac (STAR80B Serotec, 1/200 dilution)
CD3, Rat anti-human	AbDSerotec, UK/ MCA1477/ CD3-12	Lymphocytes	EDTA pH 8.0, microwave	Goat anti-rat biotin conjugated Ac (STAR80B Serotec, 1/200 dilution)
CD68, Rabbit polyclonal	Aviva Biosystems, UK/ OABB00472	Macrophages	Sodium citrate buffer (H3300, Vector), microwave	Swine anti-rabbit biotinylated antibody (E0353 Dako, 1/200 dilution)
PCNA, Rabbit polyclonal	Abcam, UK/ ab2426	Proliferation	Trypsin, waterbath 37°C	Swine Anti-Rabbit Immunoglobulins/Biotinylated (E0353 Dako, UK)
α-SMA, Monoclonal anti-FITC	Sigma, UK/ F3777	α-Smooth Muscle Actin, ECM	Sodium citrate buffer (H3300, Vector), microwave	Goat Biotinylated anti-fluorescein (BA-0601 Vector, 1:3000 dilution) 1% piggy serum

3.5 Immunofluorescence

3.5.1 Fixation and staining of cultured cells

Cultured cells were grown to confluence in chamber slides (4 well) and subsequently fixed with 4% Paraformaldehyde (PFA) in a 10 minute incubation. Fixative was then quenched using 100mM Glycine solution and permeabilised with 0.1% Trition-X-100 following a 30 minute incubation. Cells were blocked with 5% BSA 0.01% Tween Phosphate Buffered Saline (PBST) for 1 hour. IgG APC control antibody and FPR1 APC direct conjugate were incubated in the dark at room temperature for 2 hours at 1:100 concentration. Coverslips were mounted in DAPI-containing fluorescent mounting medium (VectaShield) for at least 2 hours in the dark at 4◦C.

3.5.2 Human FPR1 staining of fixed cells/paraffin-embedded tissue (FFPE)

Formalin-fixed paraffin embedded tissue was dewaxed and rehydrated in Clearene and decreasing concentrations of ethanol. Endogenous peroxidase was blocked to eliminate non-specific binding prior to antigen retrieval in 1mM EDTA (pH=8.0) solution (15 minutes full power microwave incubation). Elimination of non-specific binding achieved by 1 hour block at room temperature with 5% BSA PBST. E-Cadherin (epithelial marker), alpha-smooth muscle actin (alpha-SMA), CD45 and CD68 primary antibodies were incubated overnight at 4◦C at 1:100 concentration diluted in blocking solution. All washes were performed in PBST. FITC, TRITC, IgG APC control antibody and FPR1 APC direct conjugate were incubated in the dark at room temperature for 2 hours at 1:100 dilution. Coverslips were mounted in DAPI-containing fluorescent mounting medium (VectaShield) for at least 2 hours in the dark at 4◦C.

Table 3.3: Immunofluorescence antibodies used on human FFPE-sections for different cellular markers. Commercial supplier, antigen retrieval and secondary antibody for each antibody detailed.

Antigen	**Supplier**	**Cellular target**	**Secondary antibody**
CD45	Abcam Ab10558, UK	Leukocytes	Goat anti-rabbit TRITC conjugated, Sigma T6778 (UK)
E-CADHERIN	BD Biosciences 61081, UK	Epithelium	Goat anti-mouse FITC conjugated, Sigma F2012 (UK)
VIMENTIN	Abcam, Ab92547 UK	Fibroblasts	Goat anti-rabbit TRITC conjugated, Sigma T6778 (UK)
CD68	Abcam Ab955, UK	Macrophages/ Moncytes	Goat anti-mouse FITC conjugated, Sigma F2012 (UK)

3.6 Flow cytometry

3.6.1 Principle of assay

Flow cytometry is a process by which dyes and fluorochromes absorb light and emit a higher wavelength. Dichroic mirrors are responsible for the reflection of light at specific wavelengths. These emissions are detected and converted to an electrical current with a proportional voltage relative to the amount of light resulting in a digital signal in the form of median fluorescence intensity (MFI).

Side and forward scatter equate to the two main measurements of the physicality of the cells being analysed. Forward scatter is the diffracted light from the laser is proportional to size. Side scatter is the refracted (plus reflected) light from the different lasers allowing intracellular complexity to be gauged.

In the event of multi-parameter analysis when multiple antibodies are used to stain the same sample a variety of different channels are required. In the case of multiple fluorophore utilisation spectral overlap is a concern as conjugates with emission ranges that are close together may result in false positive signals. Electronic compensation is required to correct signal 'bleeding' between different channels. Ideally fluorophores should be chosen with separate emission ranges such as FITC and PerCp.

Each experiment will have several different controls such as unstained cells, compensation controls and isotype controls. The latter control will define the non-specific background. A threshold can be generated by defining a cut-off for negative and positive staining when using a multi-parameter panel.

3.6.2 Human FPR1-based flow cytometry of cultured cells: fibroblasts, epithelial cells and neutrophils

Cultured cells were grown to confluence in 12-well tissue culture plates, serum starved in 0.4% FCS MEM media overnight at 37◦C. Cells were then harvested by trypsinisation, pelleted by centrifugation and resuspended in FACs buffer (1% FCS in PBS) at an appropriate dilution. Cell suspensions were then added to 96-well round bottom plates, spun at 850 x g to pellet cells and resuspended in antibody-containing

FACs buffer. Antibody mixture consists of 3.67µl of antibody (human FPR1 / IgG isotype control) and 1µl Live/Dead viability dye in 250µl FACs buffer. Concentration of the antibodies was adjusted upon reconstitution with APC-linking agent to 0.67 µg/µl. 50µl of antibody mixtures were added to pelleted cells. Control and HFPR1 antibody were adjusted to 400µg for linkage to allophycocyanin (APC) conjugate as per manufacturer's instructions (InnovaBiosciences). Incubation for 30 minutes in the dark at 4◦C followed resuspension. Cells were then washed by adding 200µl FACs buffer to each well, followed by resuspension and pelleting by centrifugation. 200µl FACs buffer added to each well and cells were transferred to FACs tubes for reading by the flow cytometer.

3.6.3 Gating strategy for human cultured cells using FlowJo

Upon acquisition with FACSCantoII flow cytometer machine raw data was then exported and analysed with FlowJo software. Firstly, cell populations were gated to exclude debris and dead cells by plotting FSC-H against SSC-A. Then cells were gated accordingly to include single cells only (doublet exclusion) by plotting FSC-H versus FSC-A. Live/dead gating was employed by utilising the wavelength of the dye (405-450nm) to give a population of live single cells. A histogram was then generated by plotting count against 635-660nm channel (APC range) to give the signal by unstained, IgG isotype control APC and hFPR1 APC stained cells. Median Fluorescent Intensity (MFI) was then calculated for statistical purposes. The gating strategy employed for these flow cytometry experiments demonstrated in Figure 3.3.

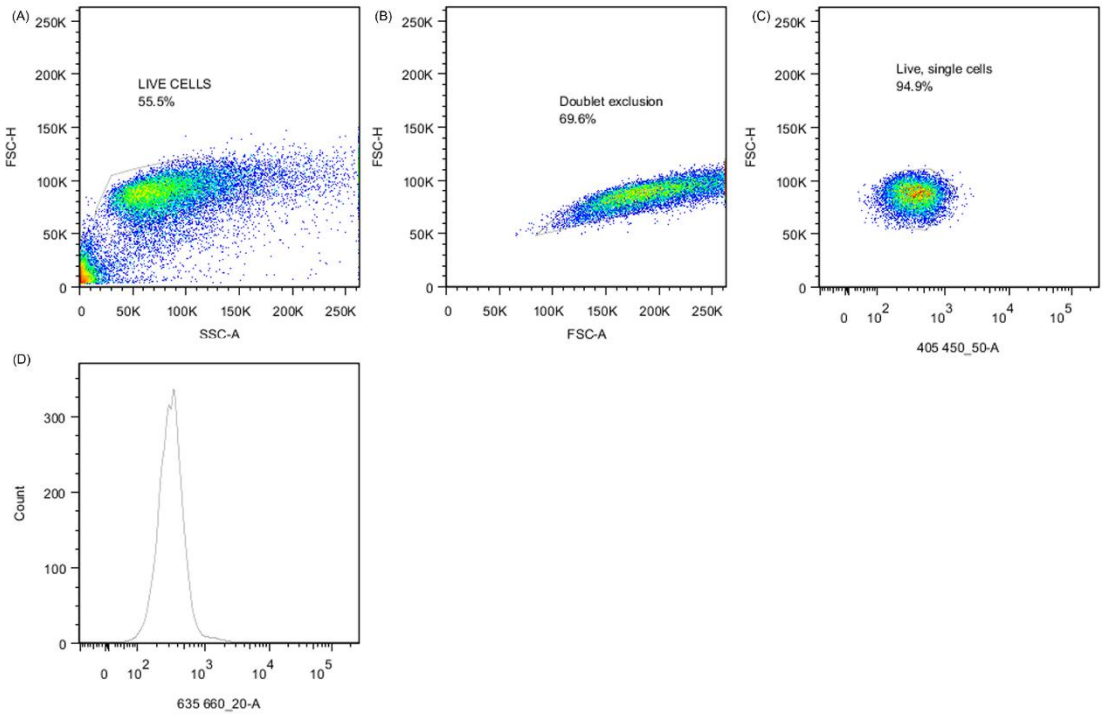

Figure 3.3: Gating strategy for FPR1 expression. Cell populations were separated according to the following gating strategy. Cellular debris, doublets and dead cells were excluded before being gated for FPR1-APC positivity. Flow cytometry runs were analysed with FlowJo software.

3.6.4 Flow cytometry analysis of inflammatory infiltrate of bleomycin/saline treated mice

Lung lobes from WT and FPR1KO mice from day 5 and day 21 time points were chopped finely for rough homogenisation. Processed tissue was digested in complete RPMI (Sigma, UK) containing 10% FCS and L-Glucose and supplements 25µg/ml DNase 18µg/ml Liberase TM for 1 hour at 37°C in shaker. Following digestion incubation sample was mixed and filtered through 70µm cell strainer into a 50ml falcon tube. A 1/3ml syringe plunger was used to mash remainder lung tissue into filter and washed subsequently with complete media. Filtrate supernatant transferred to a new tube and the centrifuged at 850 x g for 10 minutes. RBC Lysis step was included to make sure all erythrocytes were removed by 1 minute incubation with 1ml RBC Lysis solution (Sigma, UK). 10ml complete media added to digest and subsequently washed by 850 x g centrifugation at 4°C and resuspension in PBS twice. Cells in each digest sample was then counted by flow cytometry at a 1/10 dilution (30µl sample plus 270µl PBS) with flow rate used to estimate the number of cells in a 1 minute run.

In total five panels of antibodies were used in this experiment for the determination of the cell populations present in the inflammatory infiltrate following bleomycin/saline instillation. All antibodies were prepared in 1% BSA FACs buffer (500ml PBS, 5g BSA, 1ml Sodium Azide) with a total of 1µg used in each reaction. The primary and isotype antibodies and their corresponding panel are detailed in Table 3.3. Compensation controls were set up with 2.5 x mix solution in a 1:1 ratio of lung sample: bone marrow cell suspension.

For this experiment a 96-well format for staining and subsequent flow cytometer runs. Upon cell count suspensions were adjusted for $4x10^5$ cells per well. 150µl cell suspension per well spun to pellet cells then resuspended in 1:1 PBS: Aqua mixture. Viability live/dead dye diluted 1/150 in PBS from stock solution (50µl DMSO vial). Plates incubated on ice for 30 minutes. Washed once in FACs buffer and resuspended in 100µl of FC block (stops non-specific binding). Samples were incubated on ice for 10 minutes. Depending on antibody panel appropriate primary mix was added to each well (100µl) for 30 minutes on ice. Subsequently washed with FACs buffer and centrifuged twice. Fixation with 4% PFA required prior to cell permeabilisation with appropriate buffer for antibody panels 4a and 5a. Cells were washed twice in

Permeabilisation buffer (P buffer) followed by resuspension in 100µl buffer and 100µl antibody mix. Followed by a 30 minute incubation and two washes in P buffer. Plates stored overnight at 4°C and read on FACSCanto. This experiment was run on-site at MedImmune (Cambridge, UK) with the help and co-ordination of Dr John Ferguson.

Table 3.4: Panels of Flow cytometry antibodies for different markers of inflammatory cells such as neutrophils (PMNs), eosinophils, lymphocytes and M1/M2 macrophage (Mϕ) lineages.

Panel	Antibody	Source/Product code	Marker	Isotype control
1	CD45 APC-cy7	Biolegend, 103116	Leukocytes	Rat IgG2b APC-Cy7
	GR1-APC	Biolegend, 560599	Granulocytes	Rat IgG2a APC
	CD11b Percp	Biolegend, 101230	Activated PMNs	Rat IgG2a PerCP
	CD66a PE	Biolegend, 134505	Activated PMNs	Mouse IgG1 PE
	F4/80 BV421	Biolegend, 123132	Mϕ	Rat IgG2a BV421
2	CD45 APC-cy7	Biolegend, 103116	Leukocytes	Rat IgG2b APC-Cy7
	GR1-APC	Biolegend, 560599	Granulocytes	Rat IgG2a APC
	SiglecF-PE	BD Biosciences, 552126	Eosinophils	Rat IgG2a PE
	F4/80 BV421	Biolegend, 123132	Mϕ	Rat IgG2a BV421
3	CD45 APC-cy7	Biolegend, 103116	Leukocytes	Rat IgG2b APC-Cy7
	CD3 percp	Biolegend, 100326	CD3+ve T-cells	Armenian Hamster IgG PerCP
	CD4-BV421	Biolegend, 100544	CD4+ve T-cells	Rat IgG2a BV421
	CD8 FITC	Biolegend, 100706	CD8+ve T-cells	Rat IgG2a FITC
	CD49b APC	eBioscience, 17-0691-52	Natural Killer cells	Rat IgM APC
	NK1.1 PE	eBioscience, 12-5941-83	Natural Killer cells	Mouse IgG2a PE
	B220 Pe Cy7	eBioscience, 25-0452-82	B-cells	Rat IgG2a Pe Cy7
4	CD45 APC-cy7	Biolegend, 103116	Leukocytes	Rat IgG2b APC Cy7
	F480 BV421	Biolegend, 123132	Mϕ	Rat IgG2a BV421
	CCR7 PE cy7	eBioscience, 25-1971-82	M1 Mϕ	Rat IgG2a PE Cy7
	MOMA-2 PE	ABDserotec, MCA519PET	Mϕ	Rat IgG2b PE
	CD68 Percp cy5.5	Biolegend, 137009	Mϕ	Rat IgG2a PerCp Cy5.5
	CD206-APC	Biolegend, 141708	M2 Mϕ	Rat IgG2a APC
5	CD11b Percp	Biolegend, 101230	Activated Mϕ	Rat IgG2b PerCP
	CD45 APC-cy7	Biolegend, 103116	Leukocytes	Rat IgG2b APC Cy7
	F480 BV421	Biolegend, 123132	Macrophages	Rat IgG2a BV421
	iNOS-APC	Biorybt, orb113211	M1 macrophages	iNOS-APC
	FIZZ-1 _RPE	N/A	M2 macrophages	FIZZ-1 _RPE

3.7 *In* vivo procedures

3.7.1 Mouse strains

C57BL/6 (WT) mice were obtained from an in house breeding colony (Comparative Biology Centre, CBC). FPR1KO mice (from a C57Bl/6 background) were firstly obtained from Medimmune (Cambridge, UK) and then housed/bred by CBC facility. All animals were treated humanely in accordance with the UK Animals scientific Procedures Act, 1986. All procedures were performed under the UK Home Office licence.

FPR1KO (643) mice were generated using a targeted genetrap-mediated mechanism to produce a truncated non-functional gene. Functionality testing on neutrophils at MedImmune (Cambridge, UK) with FPR1 agonists showed knockout of FPR1 in the transgenic mice colony. For the purposes of this thesis knockouts are referred to as FPR1KO or simply KO throughout.

3.7.2 Genotyping of FPR1-deficient mice

Ear punches were digested in 250µl of lysis buffer (2ml NaCl (5M), 2ml EDTA 0.5M, 2ml Tris-HCl pH: 7.5 (1M), 2.5ml 10% SDS, 41.5ml DNAse-free water) in a heat-block at 55°C overnight. An equal volume of phenol was then added to each digestion mixture, vortexed and spun at full speed for 5 minutes. Top layer was then removed and added to 2-3 volumes of ethanol (100%) and 2µl 3M sodium acetate. Following this mixture was incubated at -80°C for 2 hours. Genomic DNA was then pelleted by centrifuging at full speed for 10 minutes. Supernatant decanted off and pellet was then left to air dry prior to resuspension in 50µl 1x Trypsin-EDTA (TE, Sigma-Aldrich UK) buffer. DNA was then diluted 1:50 for genotyping PCR reactions.
Due to the genetrap deletion the fpr*643* knockouts have a deletion in the *FPR1* gene codon (proprietary to Deltagene, source of FPR1 knockout mice). Interestingly Abcam and other commercial antibodies have immunogenic sequences that are located in codons within and outside this deletion sequence therefore FPR1 will still be detected

in KO mice via western blot-based methodology. The endogenous gene product is only detected in WT C57Bl6 mice with the deletion in the knockouts resulting in an absence of this gene product following RT-PCR.

3.7.3 Isolation of different cell populations

3.7.3.1 Hepatic stellate cells (HSC) from mouse livers

At least 2-4 livers from wild type (C57bl6) and FPR1 knockout mice were washed in PBS following perfusion via the Inferior vena cava (IVC). Chopped livers were digested for 25-30 minutes with collagenase II (2mg/ml, Roche Laboratories) and pronase I (10mg/ml, Roche Laboratories) diluted in 40mls of Ca^{2+}HBSS at 37◦C. The livers were then mashed into fragments in ~5mls of DNase (0.25mg/ml, Roche Laboratories) DNase 0.1mg/ml in Ca^{2+}HBSS (Sigma-Alrdrich, UK). After digestion they were passed through nylon mesh with a pipette into a beaker. The liver was washed through with Ca^{2+}HBSS and made up to 50mls. Filtrate was then centrifuged for 7 minutes at 850 x g. The supernatant was removed and resuspended in 1ml DNase to prevent the cells from clumping. The mixture was made up to 50mls with Ca^{2+}HBSS and centrifuged at 850 x g for 7 minutes. The supernatant was removed and the cells resuspended in 1ml DNase. An Optiprep (Nycomed, Sigma Aldrich) sucrose gradient was prepared to separate the stellate cells by density. When centrifuged the sucrose separates and the heavy cells (hepatocytes) spin down and buoyant cell (hepatic stellates) form an upper layer. The lower layer contains 4.7ml working Optiprep and 3.2ml HBSSCa^{2+} and the upper layer 5.9ml working Optiprep and 8.9ml cell suspension. (Working Optiprep contained 25ml Optiprep / 26ml Ca^{2+}HBSS). The digestion mixes were made up to 8.9ml with Ca^{2+}HBSS. The density gradient was subsequently overlaid with 1ml Ca^{2+}HBSS. The gradient was then centrifuged at 1400 x g with no break for 18 minutes. The HSCs were removed from the gradient with a pipette from either side of the blood layer. The cells were put in a falcon tube with ~1ml DNase and Ca^{2+}HBSS added up to 50mls. This was centrifuged for 6 minutes at 850 x g. The supernatant was removed and the cells resuspended in complete media consisting of Dulbecco's Modified Eagle Medium (DMEM; Gibco, Life Technologies), 16% FCS (Sigma-Aldrich, UK), 1mM pyruvate-glutamine (Sigma-Aldrich, UK), penicillin-streptomycin antibiotic (Sigma-Aldrich, UK). The population was then seeded onto T75 flasks (Greiner) at an

appropriate density. Cells were incubated at 37◦C in the presence of 5% CO_2 until ready in terms of confluence for experiments.

3.7.3.2 Murine lung fibroblasts

Following harvesting of organ from mice, tissue was washed in DMEM (10% FCS, 1% penicillin/streptomycin and 1% L-glutamine) and chopped into small pieces using scissors. Pieces were then washed on a 40µm filter to remove debris and red cells and resuspended in 10ml serum free DMEM containing 0.1% BSA and 0.2% collagenase type 2. This digestion mix was incubated at room temperature on a roller for 2 hours with occasional agitation. Suspension was then filtered through large gauze mesh (sterile tea strainer) followed by passage through a 100µm filter. The filtrate was then centrifuged at 400 x g for 5 minutes. Following multiple washes with DMEM cells were plated on collagen-coated plates at approximately 80000 cells/cm^2.

After 10mins the cell suspension was transferred to another collagen-coated plate and left to attach for 1hr. After 1hr the cells that did not attach were transferred again to another dish. Cells were subsequently maintained in complete DMEM with 10% FCS, 1% penicillin/streptomycin and 1% L-glutamine at 37◦C in the presence of 5% CO_2

3.7.3.3 Bone-marrow derived macrophages

Mice were sacrificed by cervical dislocation and hind leg bones were excised by cutting away all muscle tissue. Bones were then flushed through with HBSS (minus Calcium) using a syringe attached to a 21G needle. The entire bone marrow cell population was then plated on 10 cm^2 dishes and incubated for 6-7 days with 5% CO_2 at 37◦C. All growth media was supplemented with L929-conditioned medium. Supernatant was collected from L929 cells grown at normal conditions essentially acting as a source of GM-CSF, a differentiating factor for macrophages.

3.7.4 Bleomycin (BLM) –induced pulmonary fibrosis model

3.7.4.1 Intratracheal BLM model protocol

100µl sedative ketamine/xyzaline (2:1) diluted 1:1 in water for intraperitoneal (i.p.) injection to anaesthetise the animal prior to intratracheal administration. Using bookends connected with suture wire the mouse was positioned via front teeth between the two supports with a P1000 tip box beneath to keep animal flat. The tongue was pulled slightly out with forceps and a 200ul pipette with gel loading tip was positioned into bottom right corner of mouth. The tip was manoeuvred until resistance lessened (opening to the trachea) and the plunger of pipette was pushed several times due to mucus in lungs. Dosage was 0.007U intratracheal (i.t.) instillation in a 30µl volume (this was a previously titered dose used routinely at MedImmune, Cambridge). A successful dose resulted in (1) rate of breathing increase and (2) a hiccup response as drug is taken into the trachea. Instillation was followed by 50µl anti-sedan injection diluted 1:1 in saline (recovery agent) and placement into hot box in surgery room until recovery. Lobes were taken for RNA, protein, lung homogenate, histology and hydroxyproline along with serum and bronchoalveolar lavage (BAL) upon harvesting of animals at study endpoints 1, 5 and 21 days post-bleomycin administration. Bleomycin-injured and saline-treated mice were an equally weighted mix of both genders.

Initial studies at MedImmune utilised power calculations for optimal numbers of animals for day 5 and day 21 endpoints post-bleomycin injury. From sample size analysis 4 mice were deemed necessary to adjust for response variability in saline vs bleomycin.

Further studies at Newcastle University used at least the same number but due to using both males and females in some studies (Ly6G and 1 day BLM) more were included to account for variability in response to bleomycin on an exploratory rationale.

3.7.4.2 Bronchoalveoloar lavage (BAL) processing

BAL fluid was isolated from animals following saline/bleomycin instillation. Between 700-950µl PBS (5mM EDTA) retrieved from the 1000µl pumped in via rat canula inserted into the trachea. BAL fluid was kept on ice until centrifugation at 1400 x g for 5 minutes. Subsequently supernatant was stored at -80°C for future use in ELISA/MSD multiplex assays. The cell pellet was resuspended in 200µl PBS for counting and cytospin preparation. 10µl of suspension was pipetted into a disposable haemocytometer slide and scanned/read using automatic EVE cell counter (NanoEntek™). For preparation of cytospins $5x10^4$cells were pelleted onto glass slides using a cytocentrifuge and Shandon disposable filter funnels. Slides were air-dried for approximately 10 minutes and fixed for 20 minutes in acetone solution. Cytospins were then stained with Wright-Giemsa solution (Sigma, UK; 1% diluted 1/10 in PBST) for 20 minutes. Differential cell counts were performed on randomly selected fields by counting at least 300 cells to determine the percentage of eosinophils, lymphocyte/mononuclear cells, neutrophils and macrophages (Figure 3.4).

3.7.4.3 TGF-β1 and Periostin (OSF-2) cytokine quantitation

Secreted cytokine levels were determined in BAL fluid utilising TGF-β1 ELISA duoset kits according to manufacturer's instructions (R&D Systems, UK). All BAL samples ran in triplicate in a 96-well format with absorbance read at 450nm. Background signal was corrected for by reading at 540nm. Using linear regression from the standard curve unknown concentrations (samples) were interpolated. Periostin, OSF-2 levels were determined the use of an MSD single-plex platform according to manufacturer's instructions (Mesoscale Discovery, USA). ELISAs were either performed at Newcastle or on-site at MedImmune (Cambridge, UK) by myself, Matt Bell or Jayesh Majithiya.

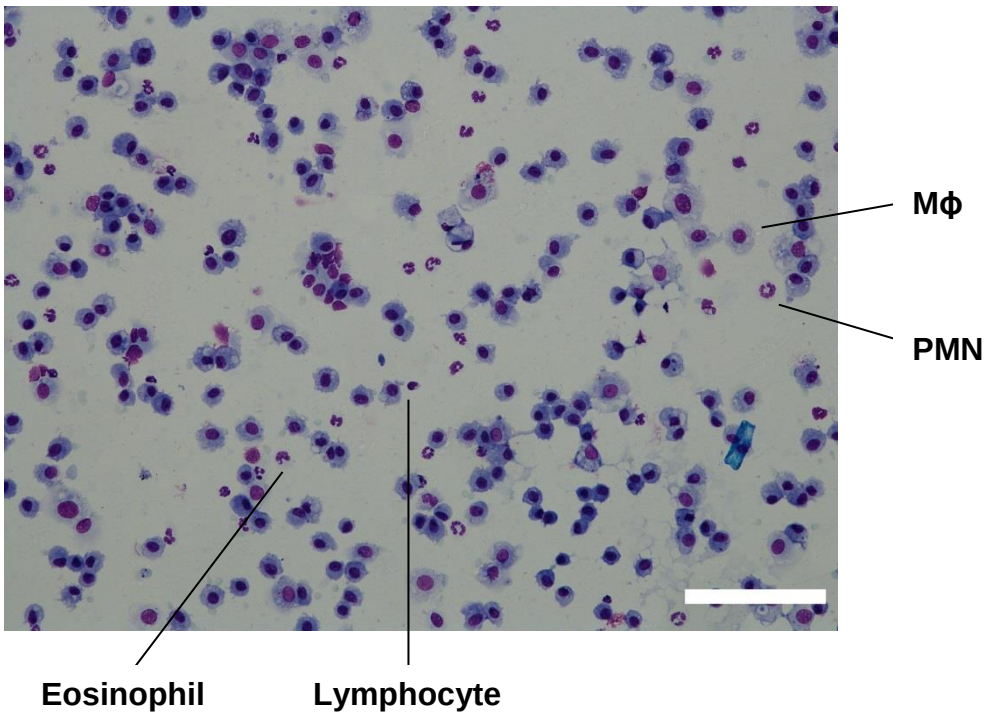

Figure 3.4: Bronchoalveolar lavage (BAL) cytospin stained with Wrights-Giemsa solution from which differential cell counts for neutrophils (PMN), macrophages (Mϕ), lymphocytes and eosinophils were performed. Examples are highlighted on the above sample field. Scale bar represents 100µm. 300 cells were counted in total and percentages of different cell populations were calculated.

3.7.4.4 Hydroxyproline content colorimetric assay

Tissue samples (lung lobe) were hydrolysed in Kimex Corning glass tubes in 1ml 6N HCl acid overnight at 110°C in heat-block located in fumehood. At least 18 hours is required for adequate hydrolysis of tissue weighing between 100-200mg. At time of animal harvesting tissue is stable in hydrochloric acid indefinitely and following acid hydrolysis samples are again stable indefinitely. Hydroxyproline standards made up from 4mg/ml Calbiochem (EMD) stock. Stock was diluted 1:10 in sterile water to 400µg/ml and subsequently 1:2 several times to generate a 12-point standard curve. 20µl standard was pipetted to flat-bottomed 96-well plate (Greiner) and then 20µl sample in triplicate. Solutions A and B were made up as follows: A – 0.282g Chloramine T-hydrate (Sigma, UK), 2ml water, 2ml isopropanol, 16ml Citrate Acetate buffer. Citrate acetate buffer consisted of 5% w/v Citric Acid, 1.2% w/v Glacial Acetic Acid, 7.24% w/v Sodium Acetate, 3.4% w/v Sodium Hydroxide with sterile water added for a complete volume of 200ml (heated buffer solution at 37°C for 15 minutes to ensure dissolving); B – 2.5g p-dimethylaminobenzaldehyde (Sigma, UK), 9.3ml Isopropanol (Sigma, UK), 7.3ml Perchloric acid (Sigma, UK). Perchloric acid was added last at a slow rate due to an exothermic reaction. Plate was tapped to mix samples before 100µl Solution A was added to each well. For oxidation to occur samples were incubated for 20 minutes at room temperature. Solution B was then added to each well (100µl) for the colorimetric reaction to take place. Plates were then tapped to ensure mixing before incubation at 60°C for 30 minutes. Measurements were made using a 570nm spectrophotometer reader yielding optical density (O.D.) values to be interpolated from the hydroxyproline standard curve (Figure 3.5).

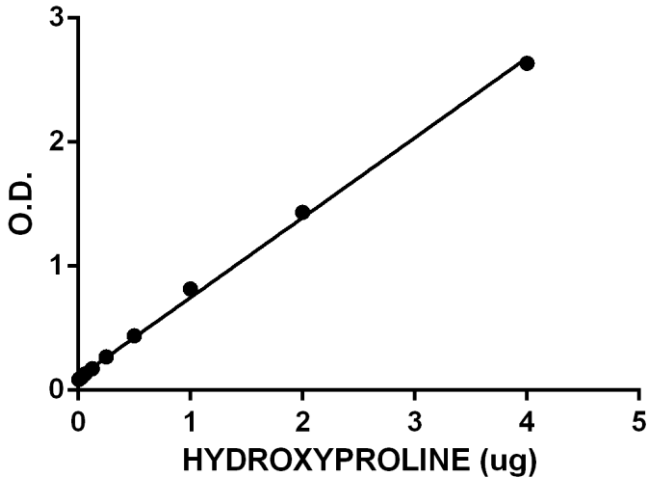

Figure 3.5: Hydroxyproline (O.H.P.) standard curve graph with O.D. (absorbance at 570 nm) vs hydroxyproline (µg). Unknown values were interpolated using this standard curve in GraphPad Prism 5.0 by linear regression.

3.7.4.5 Analysis of pro-inflammatory cytokine release from lung homogenate via multiplex ELISA MesoScale Discovery (MSD) platform

Secretion of interleukin 6 (IL-6), chemokine (C-X-C motif) ligand 1 (CXCL1, KC), interleukin 1-beta (IL-1β), macrophage chemoattractant peptide 1 (MCP-1) and interleukin 13 (IL-13) were measured in lung homogenates (prepared in PBS using homogeniser) from saline/bleomycin-treated mice using MesoScale Discovery® mouse pro-inflammatory 5-plex base kit (MesoScale Discovery, Gaithersburg, MD, USA). Protocol was carried out according to manufacturer's instructions using appropriate buffers and diluents (supplied with kit). Electrochemical signals from the multiplex plates were analysed on SECTOR Imager 6000 instrument to measure cytokine levels. Light emission detected by the instrument is directly related to the amount of protein in lung homogenate samples. Dependent on the analyte the signal ranges from 10 to 1 x 10^6 counts with negative values equating to background noise (Figure 3.6). All MSD plates were performed and analysed on-site at MedImmune, Cambridge by myself, Alan Carruthers, Matt Bell and Jayesh Majithiya.

3.7.5 Ly6G-mediated neutrophil depletion

ALZET osmotic mini-pumps were implanted in C57BL6 WT and FPR1KO mice aged 8-10 weeks old under surgical anaesthesia (induced by isoflurane) allowing systemic and continuous agent administration. The principle of the delivery system is based on the difference in osmotic pressure between the salt sleeve compartment within the mini-pump and the site of implantation in the animal. ALZET 4 week pumps (model 2004) used for the 21 day bleomycin endpoint dosing animals with a release rate of 0.25µl/hour. ALZET 7 day pumps (model 1007D) were used for the acute 1 day bleomycin endpoint with a release rate of 0.5µl/hour. Anti-Ly6G (2A3) and the rat IgG2a control (1A8) antibodies (BioXcell, USA) were used to deplete/maintain PMNs at an approximate concentration of 30µg/mouse/day.

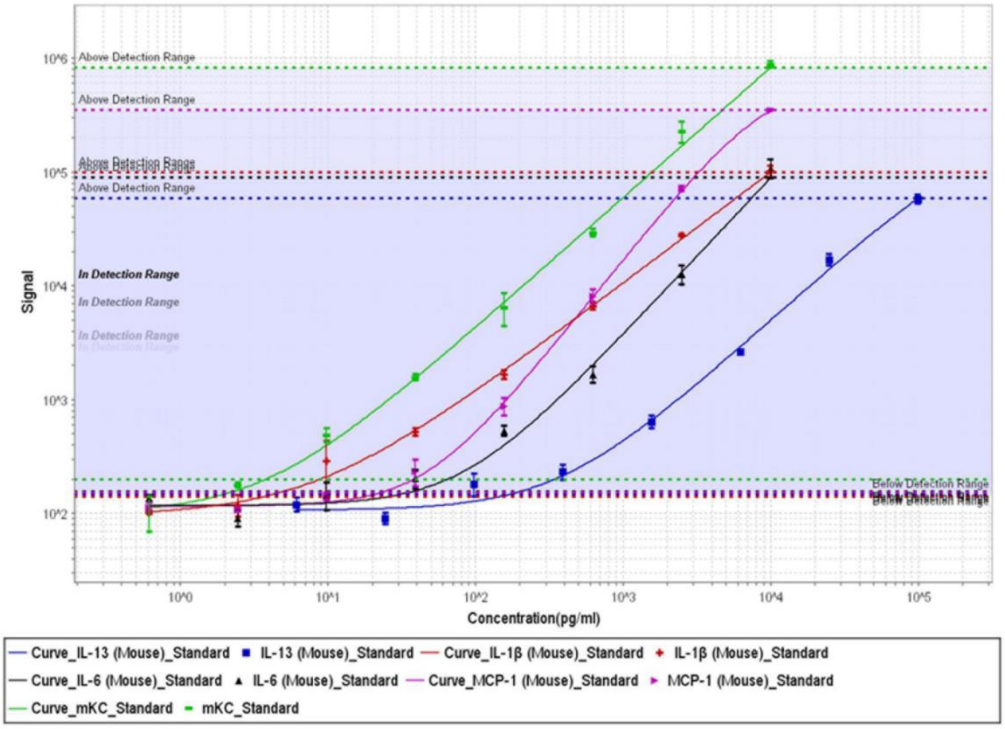

Figure 3.6: MSD analytes: IL-6, KC, MCP-1, IL-1β and IL-13 standard curves of signal strength against concentration (pg/ml). IL-13 signal was too low to be detected to give meaningful signal (<100). Standard curves were used to interpolate cytokine concentrations (pg/ml) from electrochemical signal readings.

3.7.6 Chimera bone marrow immune cell transplantation

Experiment consisted of 4 distinct groups:

(1) WT recipient mice with WT donor bone marrow
(2) KO recipient mice with WT donor bone marrow
(3) WT recipient mice with KO donor bone marrow
(4) KO recipient mice with KO donor bone marrow

Donor mice were all female. All recipient mice (40 wildtype and 35 *fpr* knockout) were irradiated at 6.8Sv, for 6 minutes per 2 cages (carried out by Rachel Howarth). Machine required a long warm-up time, with the potential for miscalibration which could have affected overall experiment. Leg bones were dissected off donor mice and washed in isotonic 1% FCS PBS. Muscle/fat was trimmed off femurs/tibias and flushed with 19G needle with 1% FCS to generate bone marrow cell suspensions. Cell suspensions were all filtered through 100µm cell strainer to remove any debris. All tubes were then centrifuged at 400xg for 4 minutes. Pooled donor cell populations of WT and KO bone marrow were then centrifuged and resuspended in 5ml 1% PBS. A Red blood cell (RBC) lysis step was included to remove erythrocytes. Samples were resuspended in ACK (Ammonium-Chloride-Potassium) Lysing Buffer, 5ml for 2 minutes. Tubes were filled to 50ml with 1% FCS PBS to stop cell lysis and cell count was subsequently performed by an automatic EVE cell counter (NanoEntek™). 10µl cell suspension and 10µl Tryphan Blue were mixed together and added to a disposable slide. Cell suspensions were analysed on Eve cell counter using Tryphan Blue setting to determine viability.

Cell counts were as follows: WT pooled suspensions, 6.6 x 10^6 live cells/ml (81% viability) and KO pooled suspensions, 7.7 x 10^6 live cells/ml (87% viability). A total of 330 x 10^6 WT bone marrow cells in 50ml were then resuspended in 6.6ml sterile saline for a concentration of 50 x 10^6 per ml. A total of 385 x 10^6 KO bone marrow cells were then resuspended in 7.7ml sterile saline for a concentration of 50 x 10^6 per ml. 1 x 10^7 cells were then injected intravenously (IV) in a 100µl volume through tail vein. All intravenous injections carried out by Saimir Luli, Gillian Patterson and Jacqueline Wilson. Following re-constitution of the immune system for 6-7 weeks mice were treated with bleomycin/saline as previously described.

3.7.7 Carbon-tetrachloride (CCl_4) liver fibrosis model

3.7.7.1 Acute liver injury and fibrogenesis

Wild-type (WT) C57BL6 and FPR1KO male mice were provided by Comparative Biology Centre (CBC, Newcastle University) and MedImmune (Cambridge, UK). Single intraperitoneal (i.p.) injection of carbon tetrachloride (CCl_4) at a dose of 2 µl (CCl4: olive oil, 1:1 [v:v])/g body weight was administered for 24, 48, and 72 hours to 8–10 week old male littermates. For statistical significance and to generate sufficient power for each time point 4-5 animals were used per treatment group.

3.7.7.2 Chronic liver injury and fibrogenesis

8–10 week old male FPR1KO and WT C57BL6 mice were injected with CCl_4 intraperitoneal (i.p.) biweekly at a dose of 2 µl (CCl_4:olive oil, 1:3, [v:v])/g body weight during 8 weeks. For the chronic CCl_4 model, animals were culled 1 day (peak) after the last CCl_4 injection. For statistical significance and to generate sufficient power for each time point at least 5 animals were used per treatment group.

Upon sacrifice of animals subjected to CCl_4 treatment the liver was harvested as depicted in Figure 3.7 with different RNA and protein tissue originating from the large lobe and all three lobes comprising tissue fixed for histology.

3.7.7.3 Serum damage enzyme aminotransferase level

Following culling, animals were exsanguinated and blood was collect in 1.5ml Eppendorf tubes. Prior to centrifugation tubes were incubated at room temperature for 20 minutes. After this period blood samples were centrifuged at 4500 x g for 10 minutes at room temperature. This will separate cellular debris from serum which is then decanted to a new Eppendorf for subsequent storage at -80°C. For analysis of aminotransferase levels in serum samples were defrosted and diluted 1:4 prior to despatch to NHS Biochemistry RVI Department. All samples processed by Susan

Douglas (NHS Biochemistry) for Alanine Transaminase (ALT) and Aspartate Aminotransferase (AST) content, two common liver damage enzymes.

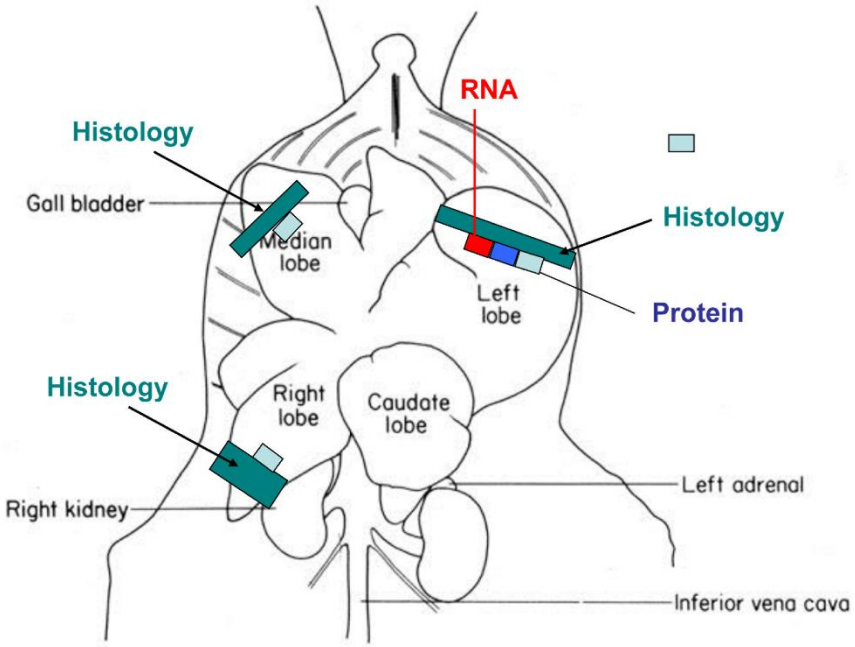

Figure 3.7: Liver histology sampling upon sacrifice of animals following acute or chronic CCl_4 model. Diagram shows areas of median, right and left large lobes sampled for fixation in formalin and processing for histological staining. Red and blue squares depict small areas of large lobe tissue to be harvested for RNA and protein.

3.7.8 Unilateral ureter obstruction (UUO) kidney fibrosis model

Surgical procedure carried out according to aseptic protocol approved by Comparative Biology Centre (CBC) and Animal Scientific guidelines implemented by the home office. Following anaesthesia by isoflurane plus oxygen the left ureter was exposed

via a surgical incision within shaved area on flank. For the UUO procedure, the left kidney was obstructed by ligation of the corresponding ureter with 5-0 nylon suture sterile wire. The incision site was then sutured and glued shut. Right ureters were left without ligating sutures acting as contralateral right kidney controls for each animal. Female mice from WT and FPR1KO litters underwent surgery. UUO model was examined at 5 day (n=7 WT; n=7 KO) and 12 day (n=6 WT; n=7 KO) endpoints to evaluate cortical immune cell infiltration and renal fibrosis respectively. Previous UUO studies carried out in-house used similar numbers for a significant difference to be observed between right kidney controls and left ligated kidneys. All surgeries carried out by Christopher Fox (Research Assistant) with myself and Rachel Howarth (Technician) assisting.

3.7.9 Subcutaneous bleomycin skin/lung fibrosis model

WT and FPR1KO mice were shaved, scruffed and 100µl 0.5mg/ml bleomycin/saline (Apollo Scientific) administered via subcutaneous injections to an area on the back approximately 1cm^2. Daily injections continued for 4 weeks at which point animals were sacrificed and skin/lung samples were harvested for RNA, protein and histology. Numbers used for this experiment were derived on a purely exploratory basis with at least n=5 per saline group and n=7 per bleomycin group to account for variability in response.

3.7.10 Statistical analysis

Data from experiments was analysed using Prism 5.0 (GraphPad, USA) statistical software and expressed as mean± standard error of the mean (SEM). Statistical significance was analysed using Prism and compared by Student t-tests or by one way Analysis of Variance (ANOVA) with Bonferroni's post-hoc correction. Significance denoted by p value; >0.05 (ns), <0.05 (*), <0.01 (**), <0.0001 (***).

4 Role of FPR1 in bleomycin-mediated pulmonary fibrosis

4.1 Models of lung disease

Development of lung disease models, whether *in vivo* or *in vitro* has played a major role in furthering our understanding of these conditions and their complex aetiologies & pathogenesis. Mice and human respiratory systems are luckily quite similar and the methods available for inducing pulmonary fibrosis are relatively easy to do.

Despite similarities between mice and humans there are significant differences in their pulmonary anatomical features including airway branching and lung epithelium. Murine respiratory system is composed of 3 main areas: tracheobronchial, intralobular bronchioles and bronchioalveolar junctional duct. In the bronchial areas columnar epithelial types consist of basal, ciliated and Clara cells. Bronchioles branching from the bronchi contain ciliated, Clara and mucus-producing Goblet cells, the latter in low numbers in mice colonies. Alveolar airspaces are composed of type I and II epithelial cells (Rock and Hogan, 2011).

Both mouse and human present efficient gas exchange surfaces in the form of their alveolar air spaces but the architecture has key differences despite shared features. In the human lung, inner tracheal width is approximately 12 mm with numerous intrapulmonary divisions with the both characteristics greatly increased than that of rodent species. Pseudostratified epithelial layers are composed of basal undifferentiated progenitor cells, ciliated and mucus-producing cells. One key feature is minimal proportion of secretory goblet cells in research mice species compared to humans (Rock, Randell and Hogan, 2010).

For murine species the trachea inner diameter spans roughly 1.5 mm with basal, ciliated, secretory and neuroendocrine epithelial positioned along its length. With as little as 6-8 divisions of the airway branches in a tree-like manner the mouse lung expands its surface area with bronchioles leading directly to alveolar airspaces. A clear distinction in these branchings is the expression of SCGB1A1, a secretoglobin, the marker of a true Clara cell (luminal in mice, cuboidal in humans). With a clear lack this marker in human Clara cells their identity is not definitive (Rock, Randell and Hogan, 2010). Due to these differences in cellular composition and architecture airway

remodelling following injury may differ between these two species therefore as with the *in vivo* models the data generated must be evaluated accordingly.

The main question for each methodology is whether the model is translatable to the human disease due to the diverse nature of interstitial lung diseases (ILDs). COPD, IPF and emphysema are three of the most debilitating disorders but each present in different ways and have had vast amounts of research performed in their respective areas distinguishing them. The nature of Idiopathic Pulmonary Fibrosis (IPF) has resulted in the question being asked: are the current *in vivo* models available for inducing pulmonary fibrosis a valid tool when looking for therapeutic interventions in human disease?

None of the current models of lung fibrosis directly reproduce all IPF features in mice as observed in the human condition (Mutsaers *et al*., 2004). Of tools used in research, murine models have presented themselves as highly translatable compared to *in vitro* methods. Cell culture-based methods including gene knockdowns, microarrays and co-culture experiments have limited value as cellular responses in developed assays may be completely different to the cellular responses within the microenvironment. Cells grown on plastic are phenotypically different as opposed to when the different cell types are organised in the tissue, with external factors affecting growth, proliferation and ultimately cellular processes such as migration, differentiation, apoptosis and extracellular matrix (ECM) production. Primary cell culture is an inherently flawed process hence the development of more representative co-culture systems but this is made difficult due to the limit on passage number of cell populations. Generally, it is regarded that primary cells should be used prior to their 4^{th} passage as past this point they tend to lose their physiological relevance as a result of changing their proliferative state (ATCC Cell culture guidelines; Shay & Wright, 2000).

Pulmonary fibrosis murine models are designed on the injury-based induction of fibrosis where damage-causing agent triggers inflammation, fibrogenesis and repair. Unchecked the process leads to an uncontrolled fibrotic response with replacement of functional tissue with useless scar formation. Depending on the drug action and route of administration the degree of reflection to the human disease will vary but the models

are commonly used as they highlight/display the main features of the pulmonary fibrotic phenotype (Mutsaers *et al*., 2004; Moeller *et al*., 2008; Moeller *et al*., 2006).

4.1.1 Modelling pulmonary fibrosis in rodents

In the course of pulmonary fibrosis research many different agents have been utilised to model lung fibrosis to determine the effect of anti-fibrotic agents and role of genetic defects on the overall process. Most of these studies have enabled the progression of disease within a few weeks as opposed to years in humans. Methods that have proven effective in *in vivo* research are fluorescein isothiocyanate (FITC), phorbol myristate acetate (PMA), silica, Transforming Growth Factor (TGF-β) adenoviral-mediated gene transfer, Th2-mediated responses, irradiation and bleomycin-induced injury (Moeller *et al*., 2006; 2008). TGF-β is heavily implicated in the fibrogenic process with release of this cytokine triggering pro-fibrotic events and hence is natural choice for inducing lung fibrosis. Sime *et al*. (1997) demonstrated that adenoviral-mediated TGF-β1 gene transfer led to a fibrotic phenotype via induction of over-expression. Compared to other models it is more representative of the relentless, dysregulated progression of IPF as it is does not require an injury phase to induce fibrosis (Moeller *et al*., 2006, Wilson *et al*., 2010).

4.1.2 FITC-induced fibrosis

FITC-induced lung fibrosis visualised the degree of fibrosis as a result of fluorescent label (Roberts *et al*., 1995). The intratracheal instillation triggers an immune response leading to infiltration and a fibrotic response (Moore and Hogaboam, 2008). This persistent fibrotic phenotype (up to 6 months) has allowed the study of novel anti-fibrotic agents and viral exacerbations which is not possible in other studies (Moore and Hogaboam, 2008; Fisher *et al*., 2005; Vanella *et al*., 2007).

4.1.3 Bleomycin-induced injury fibrosis

Bleomycin-induced pulmonary fibrosis is probably the best characterised and most used model to investigate IPF. Bleomycin, a successful chemotherapeutic drug, was found to induce pulmonary fibrosis in 20% of cancer patients treated (Limper, 2004; Moeller *et al*., 2008) therefore it appeared a natural candidate for the modelling fibrosis in rodents. Originally isolated from *Streptomyces verticillis* by Umezawa *et al*. (1966) this antibiotic family consists of two main forms: A_2 and B_2 with potent antitumour activity (Hay *et al*., 1991). This drug remains a key part of chemotherapy courses particularly in the treatment of tumours and Hodgkin's lymphoma. The structure of this small peptide (Figure 4.1) is specifically linked to its DNA damage function with its DNA-binding region and iron-binding region for cofactor complex formation, with activity limited to the cell cycle stage particularly G2 and M phases (Reinhert *et al*., 2013). This reproducible method promotes the development of lung fibrosis which has phenotype that shares common features with the human condition. With both FITC and bleomycin-mediated routes there is a distinct lack of fibroblastic foci development (Moore and Hogaboam, 2008). The drug administration can be via a myriad of different methods: intratracheal, intranasal, subcutaneous or oropharyngeal and is responsible for DNA-damage triggering fibrogenesis (Chua *et al*., 2005). Bleomycin causes double-strand targeting, among other things, telemetric DNA sequences (Nguyen and Murray, 2012). This widespread damage triggers cell cycle dysfunction, accumulation of reactive oxygen species (ROS) and decrease in NAD (nicotinamide adenine-dinucleotide) and ATP (Grande *et al*., 1998). Effects in an *in vitro* setting are well characterised but the tissue pathogenesis of this small molecule's actions are only partially elucidated. This in turn elicits an acute inflammatory response followed by a fibrotic phase between 14-28 days in the murine model. From the cellular dysfunction caused by the build-up of ROS pulmonary epithelium undergoes dramatic changes with mass signalling events, damage and cell death. Release of cellular contents and vascular leakage triggers the upregulation of pro-inflammatory cytokines and chemokines in an acute immune response. Mass infiltration of macrophages, neutrophils and lymphocytes into the lung occurs as a result of the injury localised to the pulmonary setting is essentially a wound-healing response but due to the extent of the damage a fibrotic phenotype results (Scotton and Chambers, 2010). One key facet of the bleomycin-induced pulmonary fibrosis model is the acute injury dependence. Oxidative damage mediated by bleomycin and the bleomycin-induced pneumonitis

(BIP) pulmonary toxicity has common effects in humans and mice (Reinert *et al*., 2013). Timetabling the initial inflammatory stages in terms of the peak responses of the immune cells is difficult with the ‘acute’ phase spanning up to 9 days. Initially the bronchiolocentric injury caused by intratracheal instillation leads to perivascular oedema, vascular dysfunction and alveolar wall thickening (Hay *et al*., 2013). Characterisation of the inflammatory infiltrate has been done previously in hamsters by Chandler *et al*. (1983) with significant 8-fold and 10-fold increases with neutrophil and macrophage cell populations.

This in turn draws into question the viability of this model when investigating lung fibrosis in humans but murine model does in fact present similarly to the human disease apart from the initial stages. Structural effects in the model correlate between humans and rodents thus the pattern of fibrosis matches. Cellular changes brought on by bleomycin administration lead to alveolar macrophage activation, hyaluronan synthesis, apoptosis induced by intracellular HSPs synthesis inhibition and upregulation of extracellular matrix genes including collagen Type I, III and VI. The injury causes the formation of oedema as fluid accumulates in the interstitial tissue which is lethal is left unchecked.

Typically the fibrotic response takes hold after 10 days resolving the damage and vascular leakage by scar tissue generation by hyper-proliferation of fibroblasts and excessive collagen deposition. The resolution of the inflammation comes at a heavy price with alveolar space obliteration and reduced lung oxygen-carbon dioxide exchange activity (Grande *et al*., 1998).

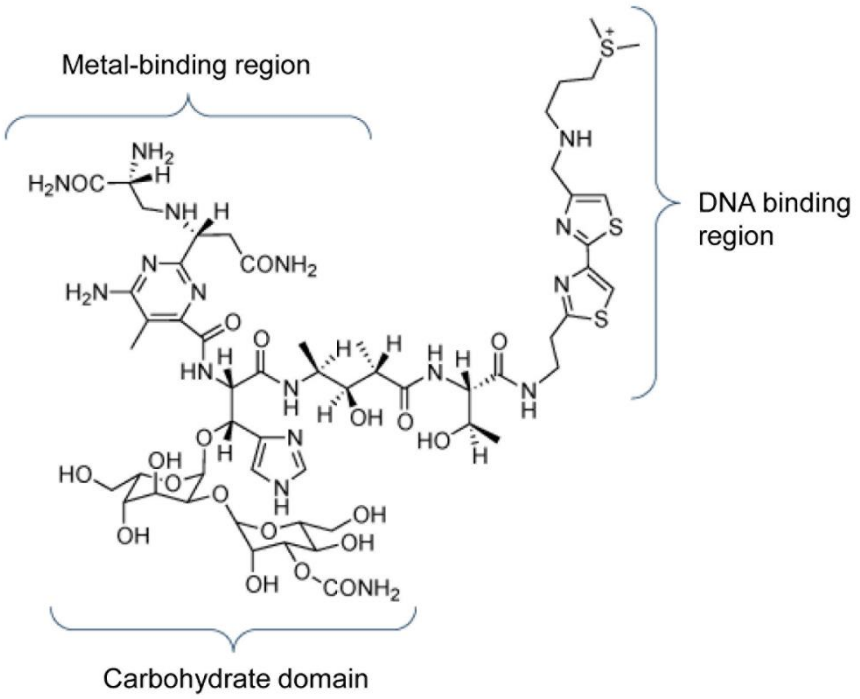

Figure 4.1: Bleomycin glycopeptide chemical structure showing all the functional components required to induce DNA-damage and acute lung injury which leads to inflammatory then fibrotic phases. Three principal features of bleomycin A2 include a metal-binding domain, a DNA-binding domain and a carbohydrate domain. Adapted from *atdbio* nucleic acid-drug interactions; http://www.atdbio.com/content/16/Nucleic-acid-drug-interactions#figure-bleomycin)

4.2 Characterisation of Bleomycin-induced acute injury pulmonary fibrosis in *C57Bl6* WT and *FPR1* KO mice at inflammatory and fibrotic phases

4.2.1 Hypothesis

The genetic ablation of FPR1 will result in a depleted pulmonary response to bleomycin-mediated injury both in an inflammatory and fibrotic fashion.

4.2.2 Rationale

Due to this receptor's characterised role in the ligation of chemoattractant and migration of immune cells towards injury sites the bleomycin fibrosis model presents an opportunity to investigate both inflammatory and fibrotic effects when the expression of this receptor is nullified in knockout mice. According to the Figure 4.2 following administration of bleomycin sulphate via the intratracheal (i.t.) route a targeted bronchiolocentric injury will result leading to an acute inflammatory response in the first week post i.t. After a chronic wound-healing response to resolve the widespread damage (induced by the drug) fibrosis will begin to develop after approximately 14 days. 3 weeks after the initial injury established lung fibrosis should be evident with increased fibrotic markers and loss of functional airspaces when used routinely by other research groups.

Pulmonary fibrosis induced by bleomycin in FPR1KO and C57BL6 mice (aged 6-8 weeks) was used to model IPF to ascertain effect of FPR1-deficiency at day 5 (inflammatory phase) and day 21 (fibrotic phase) endpoints respectively.

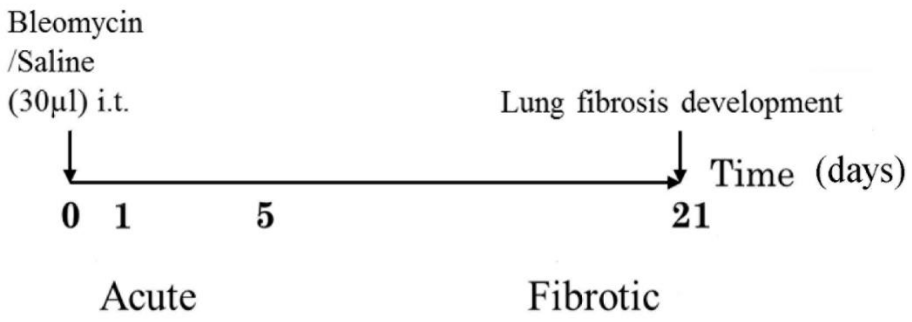

Figure 4.2: Schematic of bleomycin-induced pulmonary fibrosis model detailing the two distinct phases: acute inflammatory and fibrosis development beginning with 30µl dose of saline or 0.007U Bleomycin Sulphate.

4.2.3 Differences in weight gain/loss over 21 day time course post-bleomycin instillation

The bleomycin-induced pulmonary fibrosis model is traditionally accompanied by a significant weight loss over by the time the fibrotic phase is reached (El-Medany *et al*., 2005). WT bleomycin-treated mice lose up to 15% weight over the course of the experiment while the knockout mice maintain a consistent weight during the acute phase between 0% and -10%. FPR1KO mice gain weight over time up to 20% (Figure 4.3). In two repeat studies the weights recorded over 21 days show that the knockout mice are protected from this weight loss seen in wild type bleomycin-treated mice. This suggests a potential systemic effect; other fibrosis models should be looked at in other organs to determine what effect this promiscuous GPCR family is having.

4.2.4 Immunohistochemistry of inflammatory cellular markers 5 days post bleomycin (acute phase)

Initial bleomycin injury studies undertaken at MedImmune (Cambridge, UK) had lungs harvested from animals treated with drug or saline control vehicle. Lobes were taken for histology and IHC staining with the remainder of lung tissue prepared for RNA and protein isolation by tissue homogenisation. WT and FPR1KO mice were sacrificed 5 days post-i.t. to ascertain effect of FPR1 deletion on inflammatory phase intrinsic to this model's pathogenesis.

To identify and quantify the inflammatory infiltrate within the injured tissue IHC was employed to stain NIMP+ neutrophils (Figure 4.4), CD68+ monocytes/macrophages (Figure 4.5) and CD3+ T cells (Figure 4.6). Upon injury with bleomycin (BLM) WT and KO did not elicit a significant response in NIMP+ cells with mean counts of 4.471 ±1.049 S.E.M. and 2 ±0.6945 S.E.M. respectively. Due to variability in the group NIMP+ counts there is no clear effect demonstrable by the bleomycin but a trend of increased WT neutrophils is displayed in comparison to KO mice (both saline controls and BLM injured). Although significance was not reached this may be an indication for a general decrease in neutrophil migration on account of the gene knockout (Figure 4.4).

IHC staining for CD68 5 days post-i.t. (Figure 4.5) to quantify macrophage/monocyte levels in the lung tissue showed detectable elevations from control to BLM groups. This model is characterised by a macrophage involvement in the initial inflammatory phase. WT CD68+ cells increased from mean value 9.188 to 17.42 per high power field (±3.729 and ±2.108 S.E.M. respectively; $p>0.05$) but this did not reach significance. KO mice demonstrated a BLM macrophage response to an extent with an elevation from 2.963 to 9.157 CD68+ cells per field (±1.062 and ±1.854 S.E.M. respectively; $p>0.05$). A significant reduction ($p<0.05$) was observed between BLM treated WT and KO mice potentially indicating an altered migration function due to loss of the chemoattractant receptor.

CD3+ staining for lymphocytes (Figure 4.6) showed no significant differences between WT and KO mice but displayed a slight increase upon bleomycin-treatment (means 45.13 ±8.999 and 43.04 ±4.201 S.E.M. respectively).

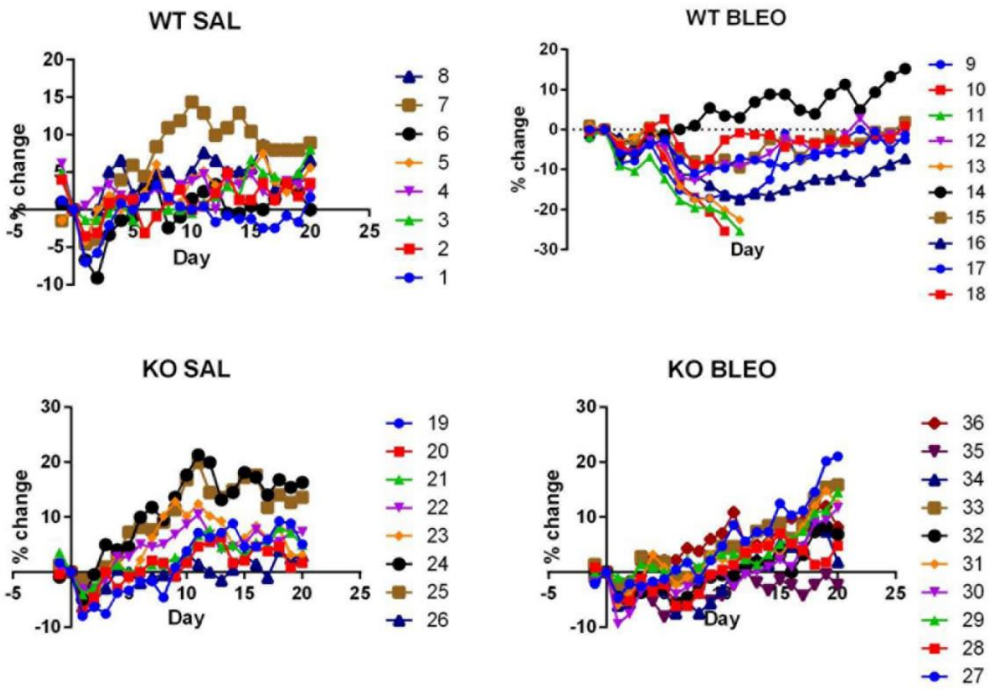

Figure 4.3: Percentage weight gain/loss post-bleomycin injury over the course of 21 days. Treatment groups include WT SAL (n=8), KO SAL (n=8), WT BLM (n=9) and KO BLM (n=10). SAL and BLEO groups equate to saline controls and bleomycin treated mice respectively.

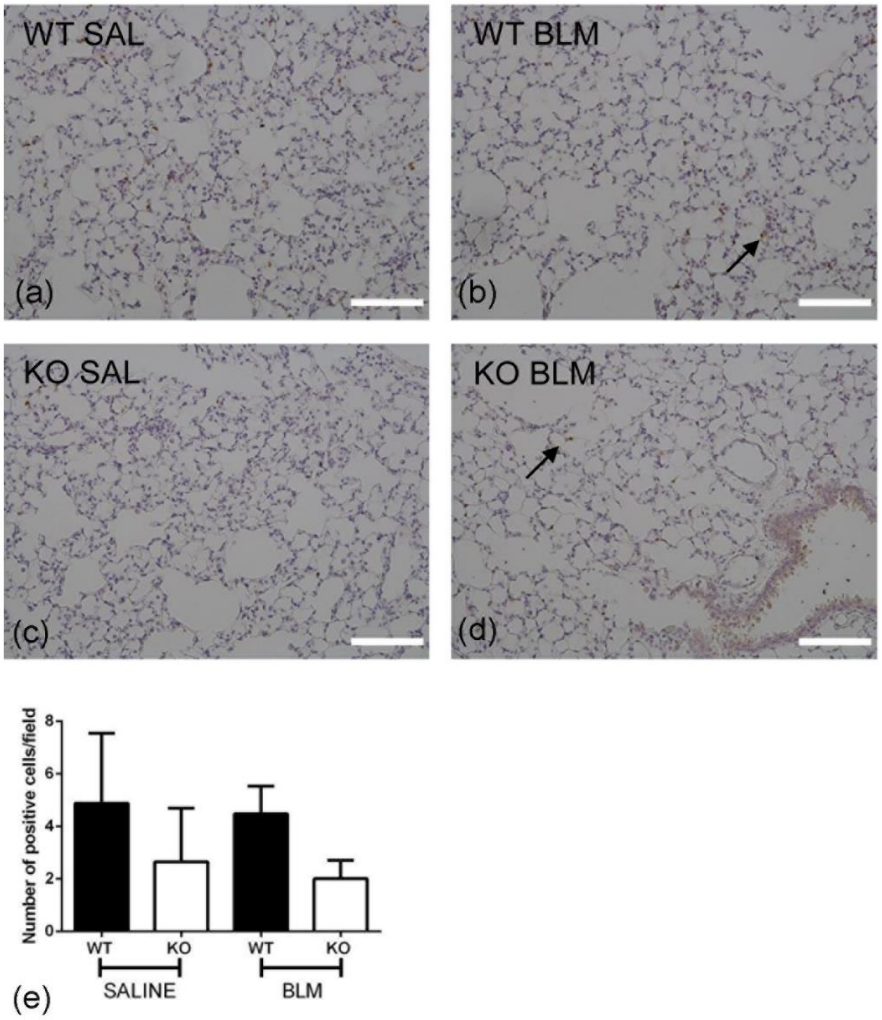

Figure 4.4: NIMP IHC counts of bleomycin-treated lungs 5 days post-injury. Relative photomicrographs of neutrophils within (a) WT SAL, (b) WT BLM, (c) KO SAL and (d) KO BLM lungs with scale bars representing 100μm (x20 magnification). (e) Results are expressed as mean positive cells per high power field (hpf) SEM. Day 5 groups were as follows: WT SAL, n=4; KO SAL, n=4; WT BLM, n=7; KO BLM, n=7. All P values were calculated using a one-way analysis of variance (ANOVA) ns $p<0.05$. Arrows highlight positive cells.

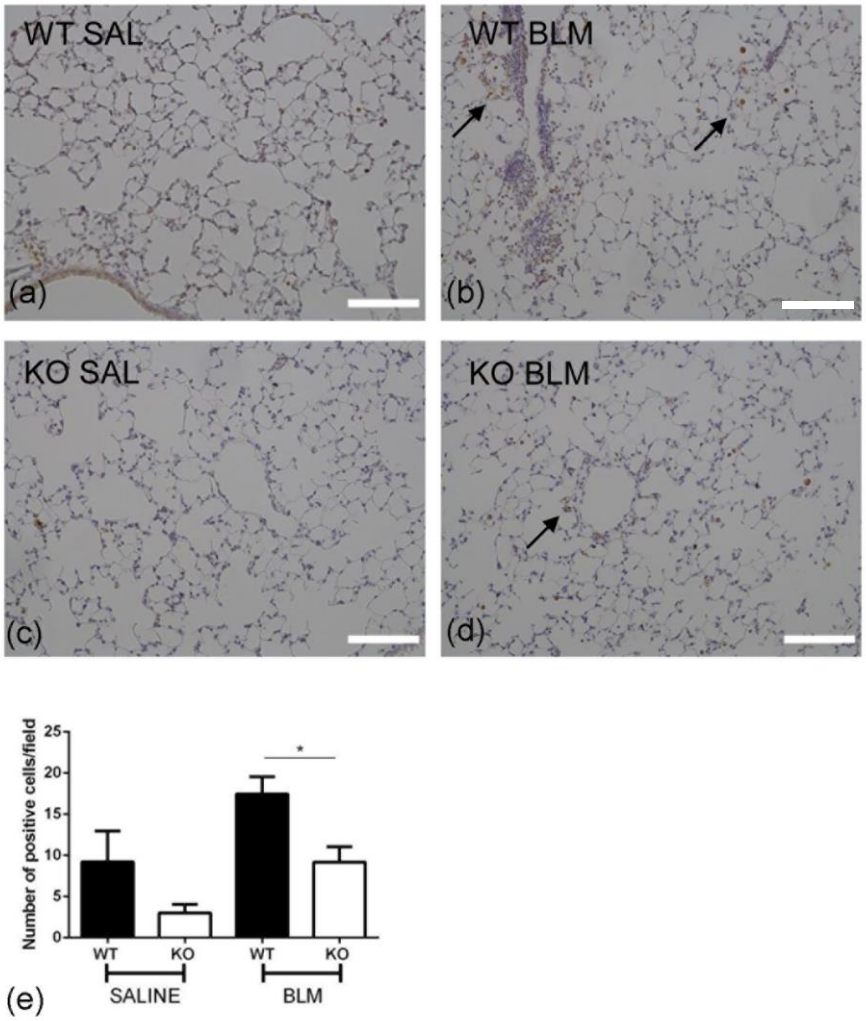

Figure 4.5: CD68 IHC counts of bleomycin-treated lungs 5 days post-injury. Relative photomicrographs of macrophages within (a) WT SAL, (b) WT BLM, (c) KO SAL and (d) KO BLM lungs with scale bars representing 100µm (x20 magnification). (e) Results are expressed as mean positive cells per high power field (hpf) SEM. Day 5 groups were as follows: WT SAL, n=4; KO SAL, n=4; WT BLM, n=7; KO BLM, n=7. All P values were calculated using a one-way analysis of variance (ANOVA) *$p<0.05$; ns $p>0.05$. Arrows highlight positive cells.

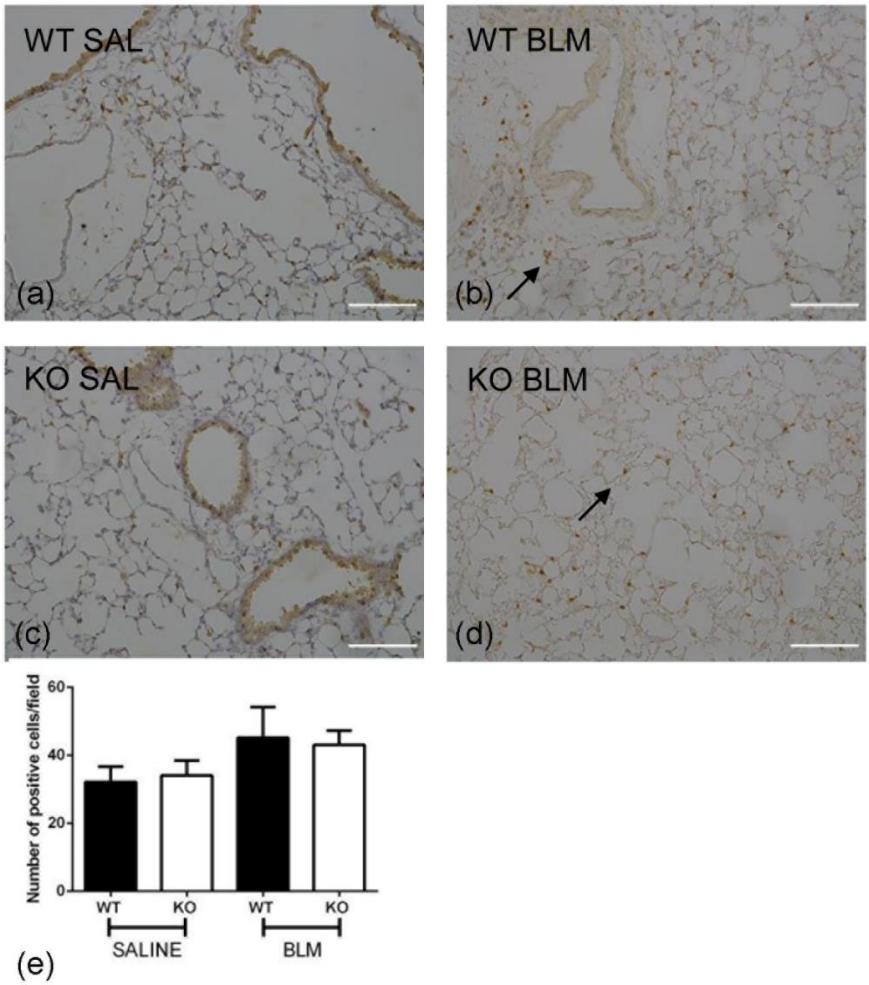

Figure 4.6: CD3 IHC counts of bleomycin-treated lungs 5 days post-injury. Relative photomicrographs of lymphocytes within (a) WT SAL, (b) WT BLM, (c) KO SAL and (d) KO BLM lungs with scale bars representing 100µm (x20 magnification). (e) Results are expressed as mean positive cells per high power field (hpf) SEM. Day 5 groups were as follows: WT SAL, n=4; KO SAL, n=4; WT BLM, n=7; KO BLM, n=7. All P values were calculated using a one-way analysis of variance (ANOVA) ns $p<0.05$. Arrows highlight positive cells.

4.2.5 Bronchoalveolar lavage (BAL) evaluation at inflammatory and fibrotic phases

4.2.5.1 Differential cell count 5 and 21 days post-injury

Analysis of bronchoalveolar lavage (BAL) composition has long been used as a measure of the lung's inflammatory status in human ILD cases and *in vivo* model counterparts. Following BAL fluid retrieval at time of harvesting animals at respective endpoints differential cell counts were performed in a blinded fashion on subsequently prepared BAL cytospins stained with Wright-Giemsa. Numbers of neutrophils, macrophages, lymphocytes and eosinophils were counted and expressed as percentages of the total (Figure 4.7). After 5 days (Figure 4.7 (a)) the predominant cell type in each group irrespective of genotype or treatment was the macrophage accounting for 85.47%, 75.71%, 63.54% and 77.51% in WT saline, KO saline, WT BLM and KO BLM groups respectively. Interestingly there was a dramatic highly significant drop of ~20% with bleomycin treatment of WT mice ($p<0.0001$) compared to that of saline treated. KO injured mice demonstrated an increase in macrophage proportion ($p<0.001$). Of particular note at day 5 in BAL counts is that there was a significant increase ($p<0.05$) from control to injured WT mice in % neutrophils identified (means of 0.0529 ±0.0301 to 3.042 ±0.9586 respectively). No change in eosinophils or lymphocytes were observed ($p>0.05$) between any of the groups.

At 21 days the differential cell count (Figure 4.7 (b)) looks remarkably similar to its day 5 counterpart with the macrophages equating to the major resident cell population in the different treatment groups (71.13%, 69.53%, 72.8%, 78.02% WT saline, KO saline, WT BLM and KO BLM respectively). WT mice were not affected by bleomycin treatment with regards to % macrophage but there was significant increase upon injury to KO lungs from saline to BLM ($p<0.001$). Minimal neutrophils and eosinophils present at this endpoint indicating cessation of lung infiltration by immune cells. T cells displayed no difference between any of the groups regardless of genotype/treatment potentially indicating that they do not have a strong role in this model if taken in hand with the modest non-significant increase determined by CD3+ IHC on tissue sections (Figure 4.6).

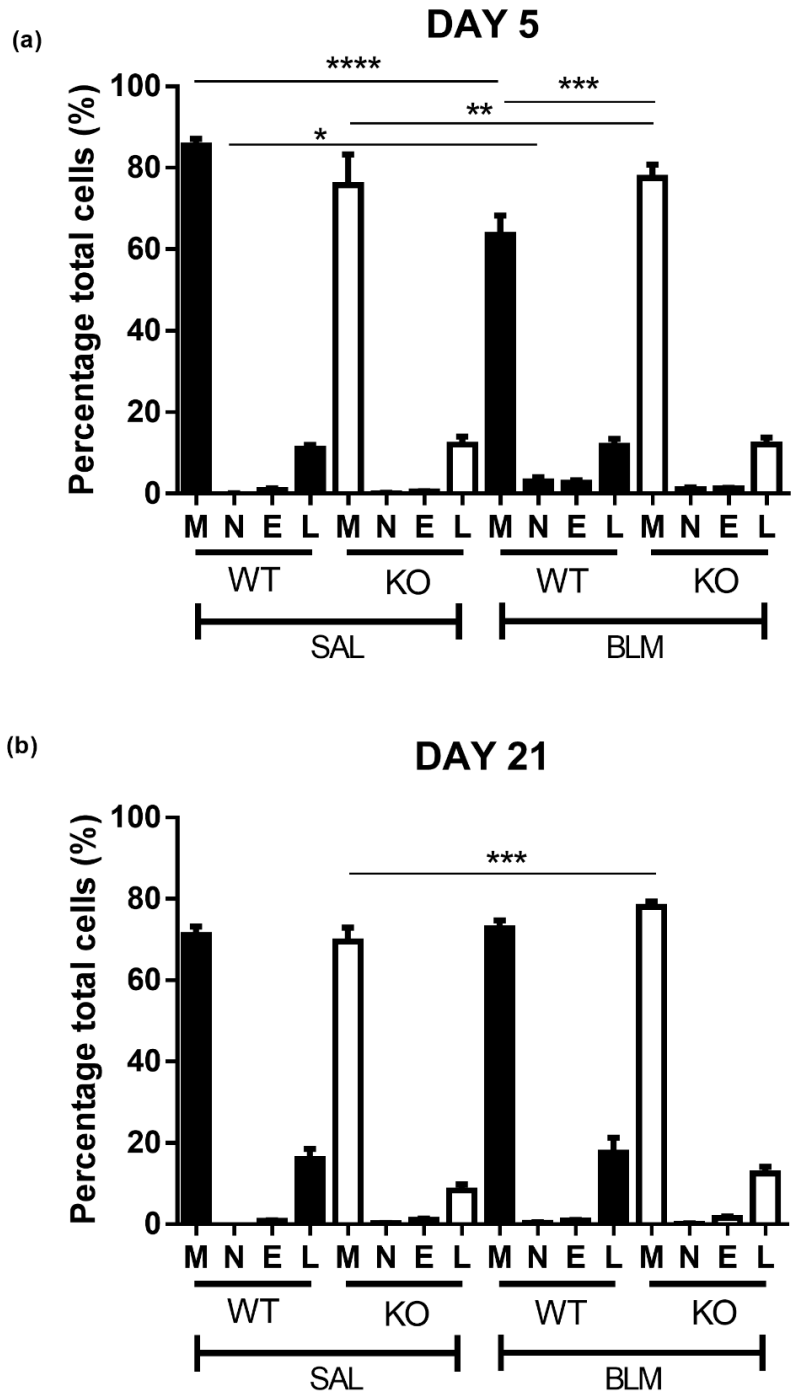

Figure 4.7: Differential cell count of bleomycin/saline treated *c57bl6* WT and *fpr643* KO mice of BAL cytospins stained with Giemsa. (a) 5 days post-bleomycin injury; (b) 21 days post-bleomycin injury (D5: WT SAL, n=4; KO SAL, n=4; WT BLM, n=7; KO BLM, n=7 and D21: WT SAL, n=5; KO SAL, n=4; WT BLM, n=8; KO BLM, n=10) Macrophages (M), neutrophils (N), eosinophils (E) and lymphocytes (L) were counted on BAL cytospins in a blinded fashion and percentages were calculated once ~300 cells were counted. All P values were calculated using a one-way analysis of variance (ANOVA) *** $p<0.001$; ** $p<0.01$; * $p<0.05$; ns $p>0.05$.

With this model an increase in inflammatory infiltrate is associated with lung subject to injury. The number of BAL leukocytes increased in a significant manner ($p<0.001$) comparing saline control groups to bleomycin-treated at 5 and 21 days post-injury for each genotype (Figure 4.8). 21 days post-injury C57Bl6 BAL leukocytes increased from a mean of $3.12x10^5$±90466 to $2.747x10^6$±455417 cells with treatment. FPR1KO BAL leukocytes increased from a mean of $2.401x10^5$±35724 to $1.834x10^6$±459100 cells (Figure 4.8 (a)). In terms of total cell counts (cells/ml) at day 5 and day 21 the BAL component increased in bleomycin-injured groups. In the acute phase of this model the total cell count elevated in WT mice from saline control group (mean $4.115x10^5$±59644 cells/ml) to $2.62x10^6$±376900 cells/ml 5 days post-injury ($p<0.05$). KO mice demonstrated an increase but not to significance. At 21 days post-BLM injury BAL total cell counts were dramatically increased ($p<0.0001$) from saline controls to fibrotic mice in a significant manner. WT BAL reached a total of $6.88x10^6$±$5.187x10^6$ cells/ml and KO BAL total elevated to $5.29x10^6$±$2.637x10^6$ cells/ml (Figure 4.8 (b)).

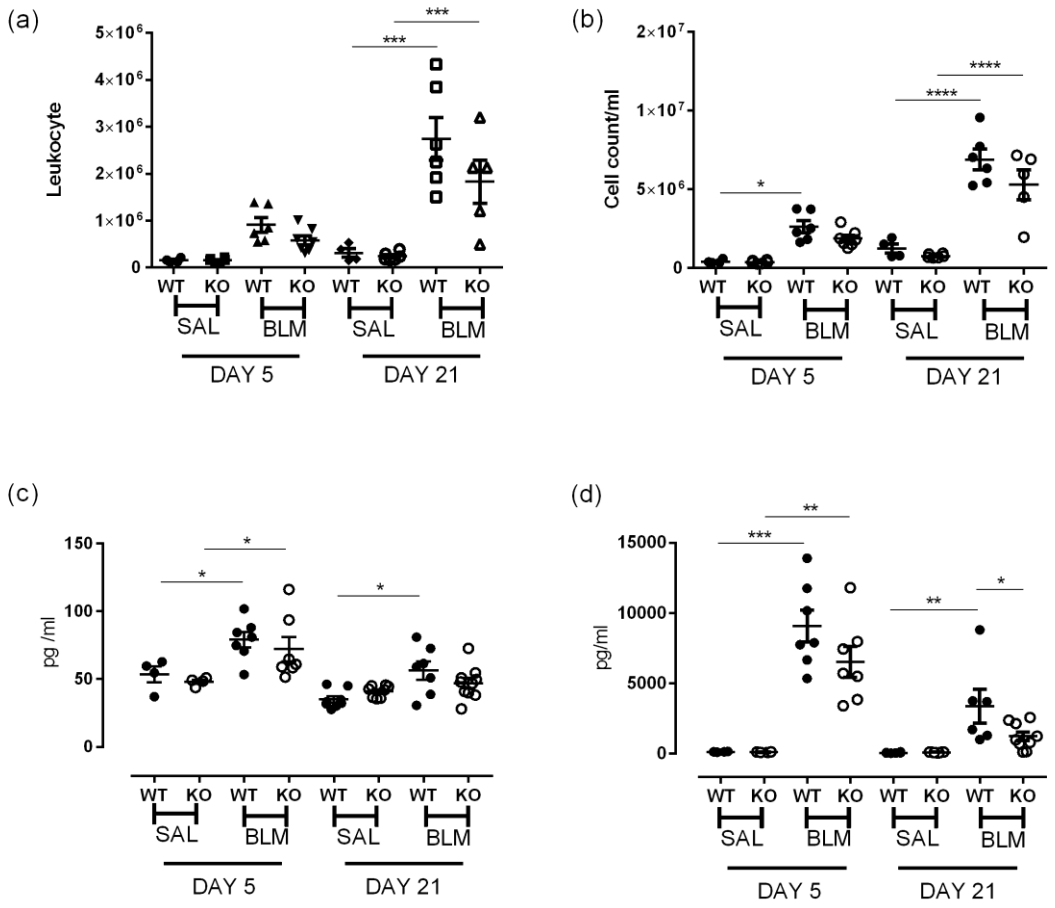

Figure 4.8: Characterisation of BAL fluid day 5 and day 21 post-bleomycin instillation *c57bl6* WT and *fpr643* KO mice. (a) Total leukocyte counts in BAL, (b) Total cells in BAL, (c) TGF-β1 cytokine secretion levels and (d) Periostin cytokine levels post-bleomycin injury. Results are expressed as a mean reading (from duplicate wells) displaying SEM (D5: WT SAL, n=4; KO SAL, n=4; WT BLM, n=7; KO BLM, n=7 and D21: WT SAL, n=5; KO SAL, n=4; WT BLM, n=8; KO BLM, n=10). All P values were calculated using a one-way analysis of variance (ANOVA) ns $p>0.05$, * $p<0.05$.

4.2.5.2 BAL levels of TGFβ and Periostin in the bleomycin model at inflammatory and fibrotic phases

Bronchoalveolar lavage (BAL) was taken at day 5 and day 21 and the supernatant obtained when preparing the cytospins was utilised for the analysis of cytokine levels. The total amount of transforming growth factor β1 isoform (TGF-β1) in the BAL of WT and KO treated with either saline or bleomycin was measured by ELISA. TGF-β1 is heavily implicated in the fibrotic mechanism by driving the differentiation of myofibroblasts not just in the chronic lung disease but in other organs such as liver, kidney and skin.

As expected TGF-β1 signal was significantly elevated with bleomycin injury at 5 and 21 day endpoints (Figure 4.8 (c)). At day 5 levels increased from 53.54±5.74 pg/ml to 79.11±5.715 pg/ml ($p<0.05$) comparing WT control and injured mice respectively. KO control and injured mice displayed an identical response ($p<0.05$) to injury with cytokine levels rising from 48.13±1.514 pg/ml to 72.05±8.943 pg/ml but no difference was observed between WT and KO injured groups. 21 days post treatment cytokine signal appears to have dropped with an ablated response evident. Injury to WT causes a significant increase ($p<0.05$) but levels are lower than at 5 day endpoint, clear by control mean of 35.15±2.405 pg/ml rising to 56.36±6.731 pg/ml in BLM-treated mice. No significant TGF-β1 cytokine response was evident in KO mice at day 21 with levels remaining at basal amounts of 40.98±1.517 pg/ml and 46.99±3.747 pg/ml in saline and BLM groups respectively ($p>0.05$). Perhaps by day 21 TGF-β1 is no longer required to potentiate the fibrotic phase and only has its major role at the beginning in fibrogenesis.

Periostin (OSF-2), another important cytokine with defined roles in pulmonary fibrosis was measured in BAL by MSD singleplex (Figure 4.8 (d)). WT periostin levels at day 5 showed a significant increase from saline to BLM-injured samples rising from 119.1±12.57 pg/ml to 9063±1139 pg/ml respectively (mean values, $p<0.001$). Similar to the TGF-β1 response at the same endpoint the knockout mice secreted periostin in response to BLM-injury increasing from 93.65±10.37 pg/ml in saline controls to 6518±1085 pg/ml in BLM-treated animals (mean values, $p<0.01$). Even with a sizable variability in cytokine level the WT BLM group the increase with injury was clear and there was a significant blunting of the response to bleomycin in the KO group ($p<0.01$).

As with the TGF-β1 cytokine response the levels of periostin elevated as the pathogenesis of the acute injury model progresses. Comparison of cytokine levels at

the different endpoints is not possible but a trend was able to be identified. At day 21 there was a significant increase in OSF-2 secretion between WT saline and BLM groups (mean values of 51.24±13.95 pg/ml to 3369±1189 pg/ml respectively; $p<0.01$). BLM-injury did not produce significant response in the KO-injured mice where only a modest increase was determined (mean values of 80.38±8.511 pg/ml to 1222±309.4 pg/ml respectively). Due to the differing responses by animals of different genotypes there is evidence to indicate an ablated response between injured mice groups ($p<0.05$) similar to the response observed at day 5.

4.2.5.3 Chemokine/cytokine secreted levels in lung homogenate of Day 5/ Day 21 post-saline/bleomycin-treated mice

As previously described upon harvesting of lung at respective endpoints a whole large lobe was homogenised in 1ml isotonic PBS buffer. The resulting homogenate was split into two 500µl aliquots for use in hydroxyproline (see subsequent section) and MSD cytokine assays. The high sensitivity of the custom-made plates means they are ideal for analysing low levels of cytokines present in tissue samples and due to the multi-spot plates a variety of different analytes can be determined from low volumes of sample. MSD technology has been optimised for use of different sample types such as cell culture media, serum and complex matrices such as tissue homogenate (MSD, USA). The cytokine composition of the lung homogenate at day 5 and 21 endpoints (Figure 4.9) enabled characterisation of the microenvironment at basal (saline control) and injured (BLM) states.

Interleukin-1β (IL-1β) cytokine has a well characterised role in pulmonary fibrosis and is recognised as key player in pro-inflammatory events hence its inclusion on the MSD multiplex plate (Figure 4.9 (a)). In day 5 groups the response equated to a significant increase from 7.329±0.842 pg/ml to 26.26±2.718 pg/ml ($p<0.01$) with injury to wild-type c57bl6. FPR1KO mice had no such response to injury with a close to saline control level (10.53±1.226 pg/ml) of 14.71±1.829 pg/ml when analysed at 5 days post-i.t. ($p>0.05$). However, between these two BLM-injured groups: WT and KO there was a significant dampening of the response ($p<0.05$). Interestingly, unlike other pro-inflammatory cytokines the IL-1β production appears to be cumulative over the pathogenesis of the bleomycin model from the acute phase to the fibrotic phase. With a known role in fibrosis the data showed a significant increase in cytokine level in WT

mice to 54.62±9.076 pg/ml at 21 days ($p<0.0001$) and this was not an unexpected result. Other bleomycin studies performed at MedImmune (Cambridge, UK) have noted a similar pattern of IL-1β sustained production (data not available). As with day 5 endpoint KO BLM–injured did not exert a notable response producing almost basal level of10.22±0.7351 pg/ml and as with the previous phase this equates to a significant (somewhat higher) reduction ($p<0.0001$).

Monocyte chemotactic peptide-1 (MCP-1) was another analyte measured by the MSD plate (Figure 4.9 (b)). As with KC and IL-6 cytokines the pro-inflammatory response was limited to within the acute injury phase, day 5 with only basal readings at 21 days ($p>0.05$). There was a significant level produced in WT mice upon injury, increasing from 109.8±8.339 pg/ml dramatically to 857.3±58.86 pg/ml ($p<0.0001$). KO mice also elicited a significant increase of 172.7±7.023 pg/ml to 565.4±71.80 pg/ml comparing saline to BLM-injured but to a lesser extent ($p<0.01$). Comparison of the two injury responses with regards to MCP-1 production reveals a clear blunting ($p<0.01$).

Chemokine (C-X-C motif) ligand 1 (CXCL1) or Keratinocyte chemoattractant (KC) has chemotactic functions promoting the migration of neutrophils and other immune cells. With the much smaller quantities of KC secreted than MCP-1 the MSD format is ideal (Figure 4.9 (c)). As with the other analytes KC level increased from saline to BLM-injury at day 5 (13.28±1.27 pg/ml to 46.65±2.032 pg/ml respectively; $p<0.0001$) and upon ablation of the *fpr1* gene the level reduced to 31.64±3.509 pg/ml ($p<0.01$). KO mice exhibited a similar injury reaction to WT counterparts going from 13.08±0.8934 pg/ml to 31.64±3.509 pg/ml ($p<0.001$).

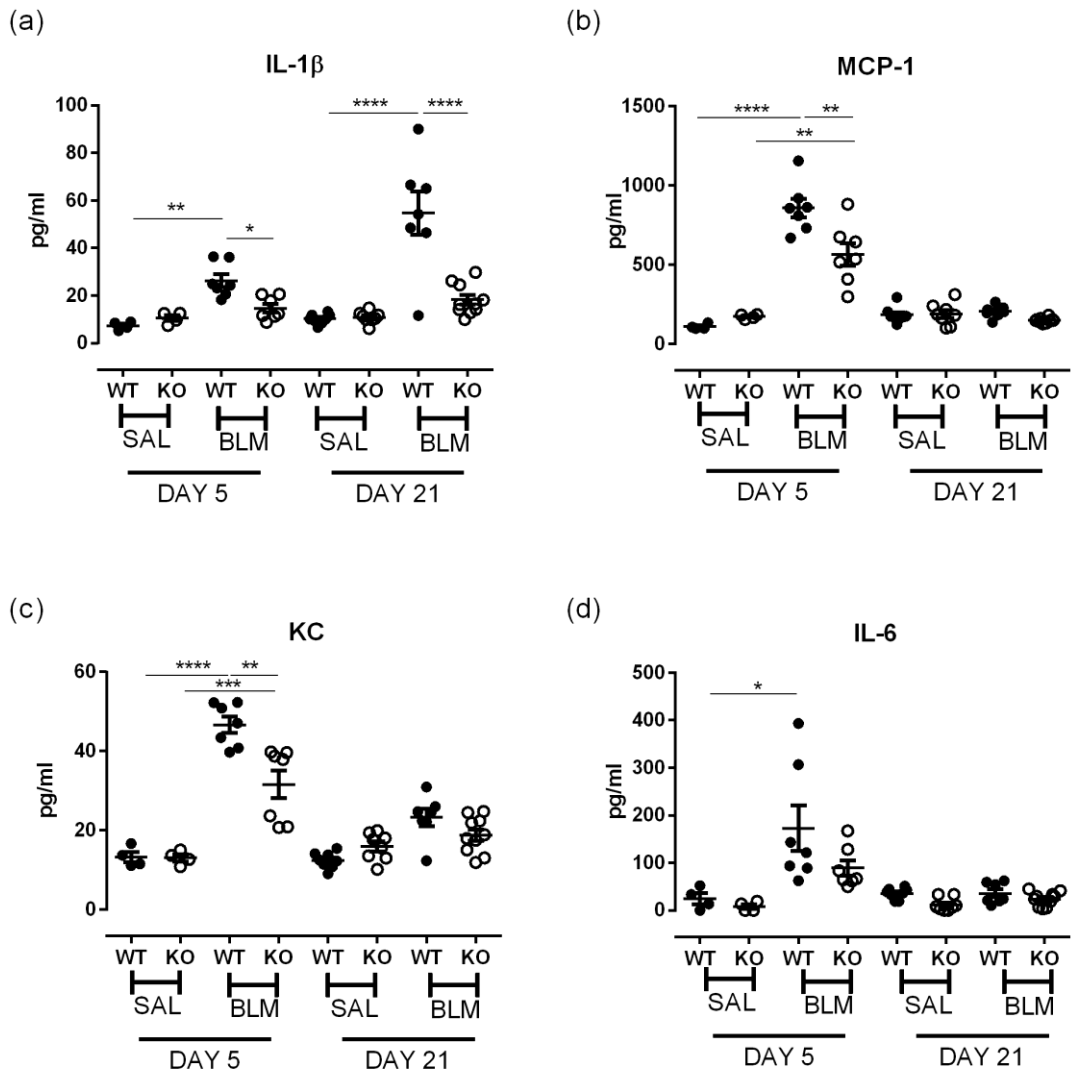

Figure 4.9: Chemokine/cytokine secreted levels in lung homogenate of D5/D21 saline/bleomycin-treated mice. Multiplex ELISA using Mesoscale Discovery (MSD) platform analysing (a) Interleukin-1β (IL-1β), (b) Monocyte Chemoattractant Peptide-1 (MCP-1), (c) KC (chemokine (C-X-C motif) ligand 1; CXCL1) and (d) Interleukin-6 (IL-6) levels in lung homogenate prepared from right lobes except post-caval. Results are expressed as a mean reading (from duplicate wells) SEM (D5: WT SAL, n=4; KO SAL, n=4; WT BLM, n=7; KO BLM, n=7 and D21: WT SAL, n=5; KO SAL, n=4; WT BLM, n=8; KO BLM, n=10). All P values were calculated using a one-way analysis of variance (ANOVA) ns $p>0.05$, * $p<0.05$, ** $p<0.01$, ***$p<0.001$.

Fitting with the trend of the previous pro-inflammatory cytokine response to the bleomycin injury Interleukin-6 (IL-6) demonstrated a significant elevation from 24.85±11.43 pg/ml to 173.0±47.67 pg/ml ($p<0.05$). KO groups did not elicit a significant response as part of the dampened immune response at day 5 evident with loss of a functional *fpr1* gene in these mice (Figure 4.9 (d)).

4.2.6 Analysis of pulmonary fibrosis phenotype 21 days post-saline/bleomycin administration

4.2.6.1 Hydroxyproline content

To ascertain the total lung collagen content in control and injured WT and KO mice homogenised samples were taken at time of harvesting (Day 5 and 21) for use in a hydroxyproline assay (Figure 4.10). Following protein synthesis proline is subject to post-translational modification in the form of hydroxylation generating 4-hydroxyproline, a principal component of collagen. Oxidation of hydroxyproline by 4-(Dimethylamino) benzaldehyde enables a colorimetric reaction can take place proportional to collagen/hydroxyproline content in acid-hydrolysed samples.

During the acute phase, the main response to the injury is infiltration and recruitment of immune cells to the area following by inflammation. This then leads to fibrogenesis in which a wound-healing response is initiated. Proliferation and activation of myofibroblasts ultimately generates a fibrotic phenotype which is established by day 21 following bleomycin dosing. At day 5 (acute phase) hydroxyproline content is at basal levels in WT and KO groups: 1.767±0.0856 µg and 2.145±0.1294 µg respectively (saline-treated); 2.356±0.1388 µg and 2.451±0.1656µg respectively (BLM-injured). Evidently, no collagen deposition at this stage in KO groups but in WT groups there was a slight increase as fibrogenesis begins post-injury.

Day 21 hydrolysed samples showed a significant increase in hydroxyproline content in WT mice treated with bleomycin (day 0). Levels increased from 2.156±0.09092 µg (saline) to 4.105±0.3623 µg (BLM) demonstrating typical collagen deposition ($p<0.001$). As with the blunted cytokine responses at day 5 hydroxyproline content did not show any change with loss of the *fpr1* gene (day 21) remaining at a basal level even with injured mice. KO bleomycin-treated group had a mean value of 2.89±0.207 µg hence no significant response compared to control group (2.568±0.1914 µg;

p>0.05). Comparison of the injury groups at day 21 clearly shows reduced collagen deposition with loss of fpr1 expression (p<0.01).

4.2.6.2 Fibrotic markers: Collagen and α-smooth muscle actin deposition analysed via IHC (Day 21)

FFPE tissue sections were stained with PicroSiriusRed (PSR) to highlight collagen I/III deposition in order to complement previous lung collagen content data (Figure 4.11 (a-e)). KO Saline group lungs revealed a raised collagen level compared to WT counterparts (p<0.01). Fixed lung tissue demonstrated an increase in percentage area (%) comparing saline and BLM WT groups (p<0.001) going from 3.277±0.3124 % to a high 14.76±2.449 % respectively. FPR1KO mice did not show this increase in percentage area (saline; 6.149±0.8314 % to BLM; 7.863±0.7424 %) with a significantly ablated response compared to wild-type counterparts (p<0.01).

To confirm the reduced collagen deposition with ablation of the *fpr1* gene RNA was isolated from post-caudal lobe segments and cDNA synthesised. Each sample was subsequently tested for pro-collagen 1 mRNA level via real-time PCR (Figure 4.11 (f)). WT expression rose from 0.9708±0.2868 to 5.495±1.097 relative fold change in saline and BLM groups respectively (p<0.01) with KO expression altering minimally upon injury (p>0.05). Pro-collagen 1 mRNA levels were indeed significantly depleted from WT BLM group to KO BLM group (2.534±0.4066 relative fold change; p<0.05).

Alpha-smooth muscle actin (α-SMA) is a marker of activated myofibroblasts, its production an indicator of fibrotic tissue. Staining via indirect IHC (Figure 4.12 (a-d)) and subsequent densitometry analysis (Figure 4.12 (e)) yielded a percentage area as with PSR-stained sections. In WT mice percentage area increased from 2.858±0.3143 % (saline) to 6.562±0.8606 % (BLM) in a significant manner (p<0.0001). KO mice displayed no such effect and the reduction between the respective BLM-injured groups (WT above and 3.605±0.2242 %) was significant (p<0.0001).

4.2.6.3 Histological evaluation of fibrotic sections

In this fibrotic phase of the bleomycin model the damage is extensive with destruction of alveolar airspaces and loss of functionality. With hyperproliferation of myofibroblasts and excessive ECM production scar tissue is generated as demonstrated by Figure 4.13. H&E immunostaining of FFPE lung sections clearly showed increased injury and fibrosis development in WT BLM over KO BLM group. Ideally a comprehensive scoring method should have been applied these sections but the criteria involved meant that time-limiting factors impinged upon histological evaluation.

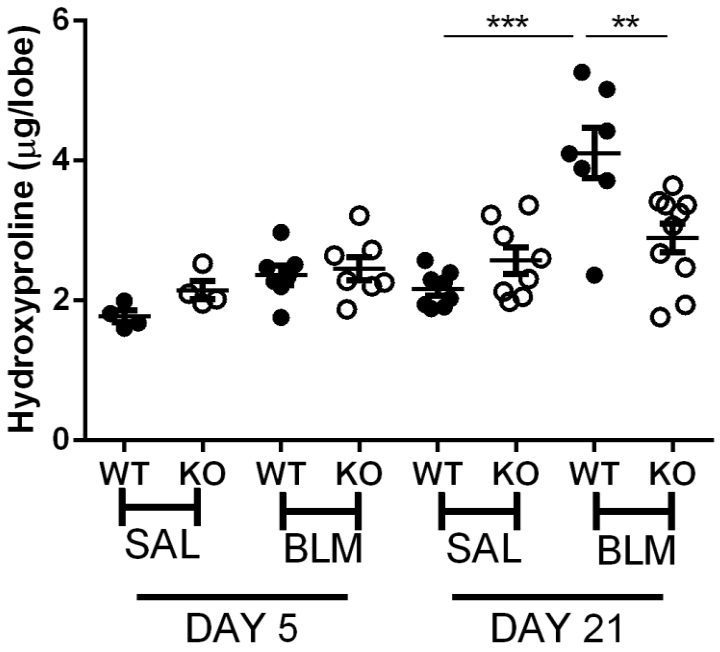

Figure 4.10: Total lung collagen content ascertained by hydroxyproline colorimetric assay. Lung homogenate samples were prepared from right lung lobes and unknown quantities were interpolated from standard curve by linear regression. Results are expressed as a mean reading (from duplicate wells) SEM (D5: WT SAL, n=4; KO SAL, n=4; WT BLM, n=7; KO BLM, n=7 and D21: WT SAL, n=5; KO SAL, n=4; WT BLM, n=8; KO BLM, n=10). All significance values were calculated using a one-way analysis of variance (ANOVA); ns $p>0.05$, * $p<0.05$, ** $p<0.01$, ***$p<0.001$.

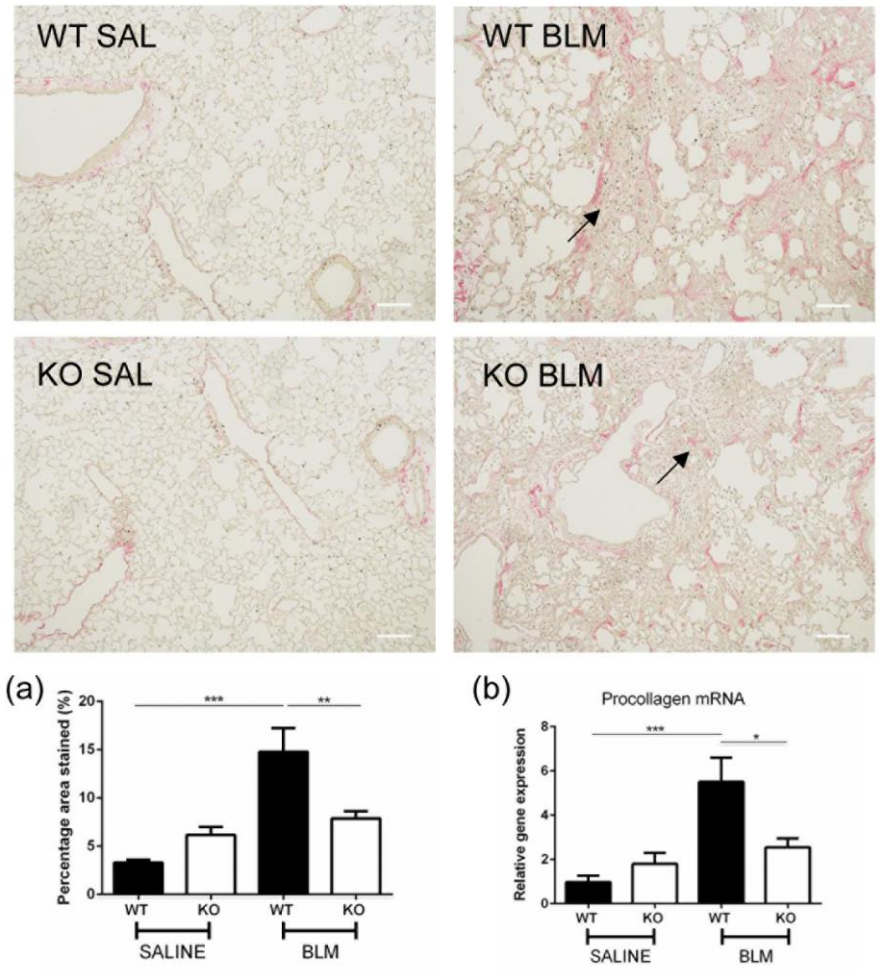

Figure 4.11: Collagen extracellular matrix (ECM) component deposition IHC percentage areas. (a) WT SAL, (b) WT BLM, (c) KO SAL and (d) KO BLM PSR stained FFPE lung sections were analysed by densitometry to yield (e) percentage area for collagen I/III. Percentage area stained of α-smooth muscle actin in FFPE sections via IHC. D21: WT SAL, n=5; KO SAL, n=4; WT BLM, n=8; KO BLM, n=10). Scale bars represent 100μm. (f) Relative expression of Procollagen 1 mRNA levels determined in lung tissue of saline and bleomycin-injured mice. All significance values were calculated using a one-way analysis of variance (ANOVA) ns $p>0.05$, * $p<0.05$.

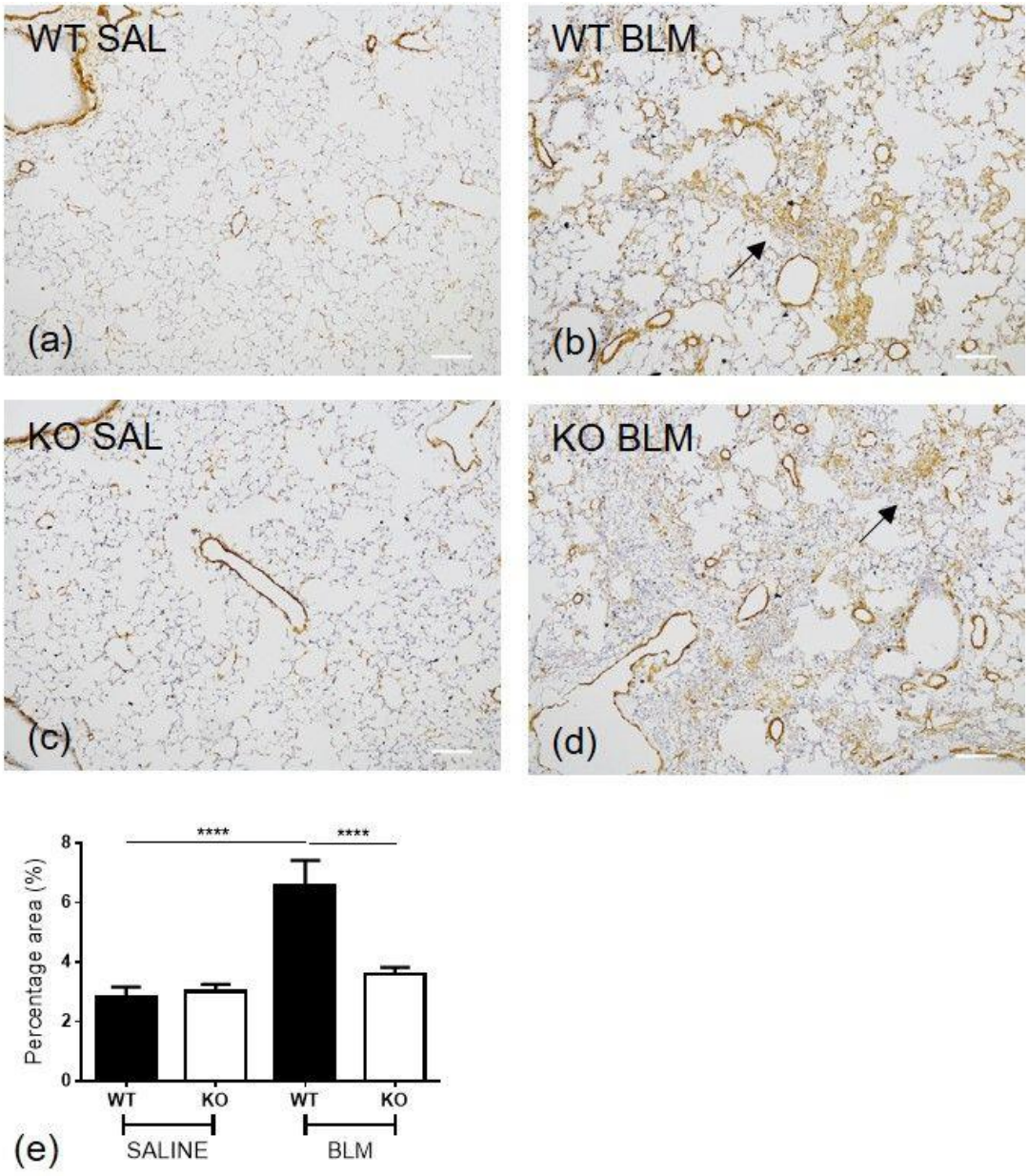

Figure 4.12: Extracellular matrix (ECM) producing myofibroblasts determined by alpha-smooth muscle actin expression. (a) WT SAL, (b) WT BLM, (c) KO SAL and (d) KO BLM IHC indirectly stained FFPE lung sections were analysed by densitometry to yield (e) percentage area ±SEM. D21: WT SAL, n=5; KO SAL, n=4; WT BLM, n=8; KO BLM, n=10). Scale bars represent 100µm. All significance values were calculated using a one-way analysis of variance (ANOVA) ns $p>0.05$, * $p<0.05$.

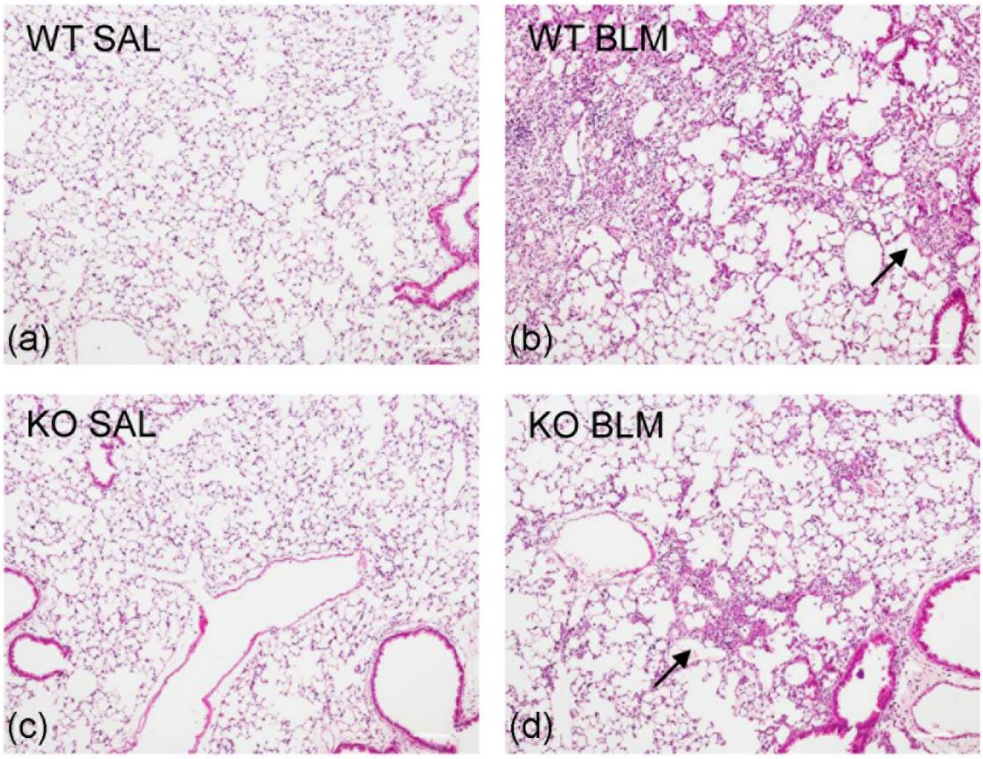

Figure 4.13: H&E histological staining of lungs 21 days post-bleomycin. Day 21 wild-type C57Bl6 (WT) and FPR1KO (KO) were treated with saline (SAL) and bleomycin (BLM): (a) WT SAL, n=5; (b) WT BLM, n=8; (c) KO SAL, n=4; (d) KO BLM, n=10). Scale bars represent 100µm.

4.2.6.4 Fibrogenic gene expression during fibrotic phase (day 21)

As fibrogenesis is intrinsic to the wound-healing response and the development of the fibrotic phenotype, determining gene expression changes is important. The turnover and balance of extracellular matrix (ECM) is a key indicator of fibrosis development as skew in a particular direction by upregulation will shift the equilibrium leading to an altered ECM and the formation of scar tissue.

Tissue inhibitor of metalloproteinases (TIMP1) mRNA expression (Figure 4.14 (a)) was upregulated in BLM-treated WT mice to 2.804±0.3638 fold change compared to saline control group, 0.9285±0.3185 ($p<0.05$). With loss of FPR functionality in KO mice there is marked reduction in TIMP1 message but not significantly. Similarly, MMP2 matrix metalloproteinase-2 (MMP-2) exhibited a stark increase in fold change expression from 1.005±0.3008 basal to 13.89±3.619 compared WT saline controls ($p<0.05$). As with TIMP1 expression, MMP2 was not significantly elevated in KO mice (Figure 4.14 (b)).

Other extracellular matrix components are deposited during fibrosis apart from collagens; elastin and fibronectin (Figure 4.14 (c-d) respectively) equilibrium may also be affected by the wound-healing response. Elastin expression was markedly increased in WT bleomycin groups compared to controls (mean value of 2.618±0.47 fold change, $p<0.05$). As with other fibrogenic genes transcription is consistent in KO groups. Fibronectin, another extracellular component also showed a significant up-regulation (4.539±0.8063 mean fold change) with BLM-injury in WT mice ($p<0.01$) and due to this higher increase above basal it was apparent that the KO-BLM group fibronectin gene expression (1.679±0.6882 mean fold change) was reduced compared to WT equivalent ($p<0.05$).

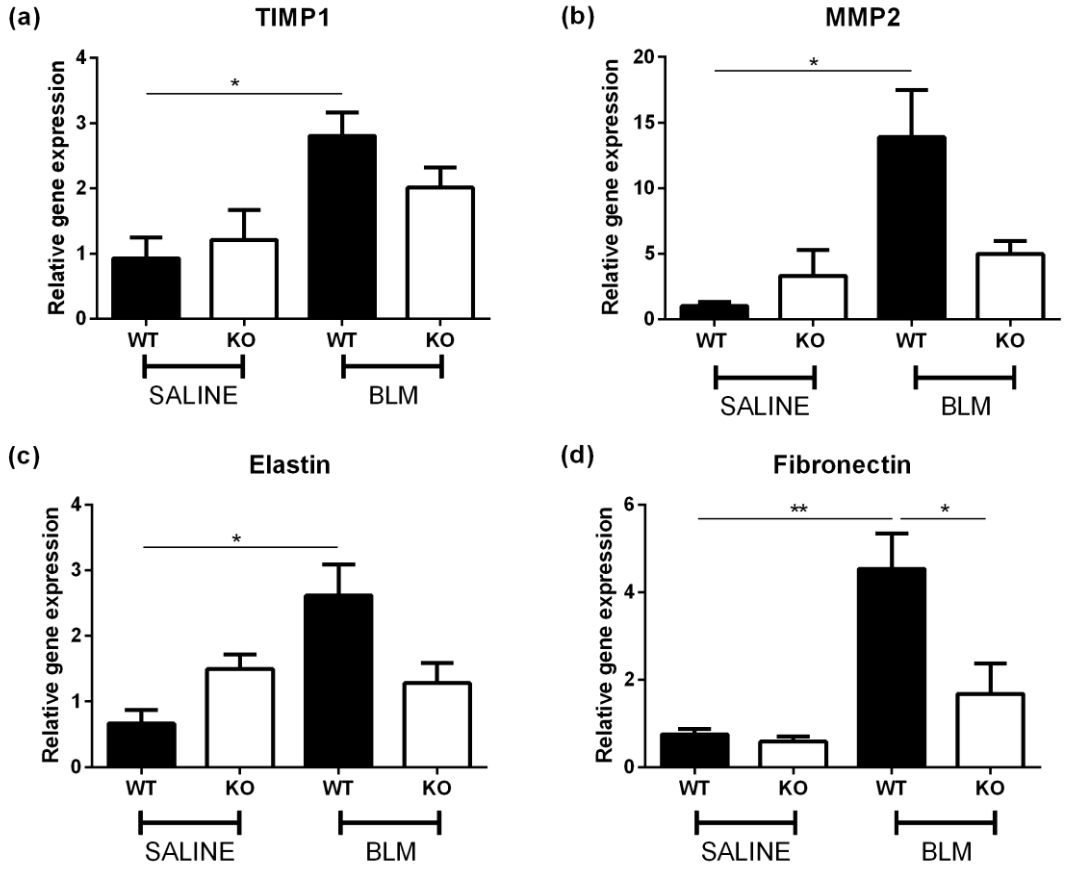

Figure 4.14: Real-time mRNA expression levels of fibrogenic markers. (a) TIMP1, (b) MMP2, (c) Elastin and (d) Fibronectin at 21 days post-bleomycin. Mean fold change calculated relative to wild-type saline control treated mice displaying SEM. D21: WT SAL, n=5; KO SAL, n=4; WT BLM, n=8; KO BLM, n=10). All significance P values were calculated using a one-way analysis of variance (ANOVA) ns $p>0.05$, * $p<0.05$.

4.2.7 Inflammatory infiltrate cell populations in bleomycin-induced pulmonary fibrosis

4.2.7.1 Hypothesis

Protective effect in FPR1 knockouts is elicited by a change in inflammatory infiltrate populations in the bleomycin-mediated pulmonary fibrosis model.

4.2.7.2 Rationale of follow-up study

Rationale behind this follow-up study to the first day 5 and day 21 endpoints was to further investigate the protective effect observed in both phases. An extensive range of cellular markers in different panels of fluorescent antibodies was employed to determine the nature of the inflammatory cell infiltrate following bleomycin insult in lung digests by FACs analyses.

4.2.7.3 Neutrophil activation

Panel 1 consisted of neutrophil activation markers, CD66a and CD11b (Figure 4.15 (a-b)). Since there was no clear effect on neutrophil infiltration in tissue via IHC the activation status of white blood cells was investigated to gauge if this was affecting the inflammatory phase of the model. Once live cells were gated to exclude debris and doublets, neutrophils were gated for CD66a and CD11b expression. Cells CD45+ (APC-Cy7) and F4/80- (Pacific Blue) were then gated for viability allowing gating for Gr-1, a neutrophil-specific marker. Gr-1, myeloid differentiation antigen is also known as Ly6G with well characterised expression on bone marrow granulocytes and peripheral neutrophils. The bone marrow taken at time of harvest is hence an ideal compensation control. For proportions of activated cells the data for this panel is expression as percentage of total neutrophils. The FACs analyses showed that a majority of the neutrophils were activated expressing CD66a and CD11b. The only marked change in the activation status was between WT and KO saline controls at day 5 dropping from 86.63±2.275 % to 70.58±5.532 % respectively ($p<0.05$) for CD66a and from 88.63±1.121 % to 70.17±4.652 % respectively ($p<0.01$). This indeed correlates with a depletion of Ly6G/Gr-1+ CD45+ leukocytes with the same groups in panel 2 (Figure 4.16 (b)) from 14.50±1.745 % to 8.96±0.053 % (mean values, $p<0.01$). For the

most part the number of neutrophils infiltrating the lung upon bleomycin injury is consistent in terms of proportion and activation status, at least at these endpoints.

4.2.7.4 Neutrophil and eosinophil populations

Panel 2 had the focus of distinguishing distinct populations of neutrophils (Ly6G+) and eosinophils (SigLecF+). These are widely regarded as specific markers making them ideal for our purposes. Lung digests were counted and gated excluding debris and doublets followed by gating for CD45+ (APC-Cy7), live cells (AmCyan-A) and low F4/80 expression (Pacific Blue-A). Cells were then gated according to SigLecF (PE) and Ly6G (APC-A) expression as shown in Figure 4.16 (a-b). High SigLecF+ low Ly6G+ cells constitute a small proportion of the infiltrate with consistently low levels in the lung digests and no change between treatment groups. Percentages appear slightly higher at 21 days but with no significant change ($p>0.05$).

4.2.7.5 Lymphocytes

A 3rd panel of antibodies was utilised to ascertain any effect on lymphocyte populations in the infiltrate (Figure 4.17). As with other panels cells were initially gated to exclude debris, doublets and to identify CD45+ (APC-Cy7) leukocytes. After checking for viability with AmCyan-A channel, live cells were gated for CD3+ expression (PerCP) then highly positive cells separated into two distinct populations of CD4+ (BV421) and CD8+ (FITC) T-cells. At day 5 high CD4+ low CD8+ cells remained at a consistent basal level ($p>0.05$) but at day 21 this subset % increased significantly ($p<0.001$) in WT BLM compared to WT saline (mean % of 7.318±0.4252 to 12.41±0.9353 respectively). With no such response in the KO groups there is a significant reduction between BLM-injury groups dropping to 8.792±1.227 % ($p<0.05$). High CD8+ low CD4+ populations showed no difference between any of the groups regardless of genotype, treatment or endpoint.

Cells gated by low CD3+ expression were subsequently gated for B-cells and Natural Killer (NK) cells positive for B220 (Pe-Cy7) and NK1.1 (PE)/CD49b (APC) expression respectively. This allowed quantification of all the T cell lineages present in the bleomycin-injury model. CD3-NK1.1+CD49b+ subsets showed no response to bleomycin at either endpoint with no difference between WT and KO. One point of note

was the percentage % total CD45+ cells were at a higher baseline at day 21 than at day 5. This is probably due to antibody staining being performed on different days. The B-lymphocyte (CD3-B220+) population demonstrated a wide degree of variability in the different groups with no discernible trend or statistically significant responses to bleomycin or genotype.

4.2.7.6 Macrophage M1/M2 subsets

As for the macrophage component of the inflammatory infiltrate FACs antibody panels were composed of M1 (classically activated) and M2 (alternatively activated) markers to determine the M1/M2 balance in the acute and fibrotic phases of the murine model. Macrophages were first gated to exclude debris and doublets then subsequently gated for expression of CD45 (APC-Cy7). Live CD45+ cells were selected according to MOMA-2 (PE) and CD68 (Percp-Cy5.5) gate to identify the total macrophage population. This was followed by viability checking through use of live/dead dye Aqua (AmCyan) to determine live cell populations of total macrophages. In the subsequent gates M1/M2 phenotype was then distinguished via CCR7 (M1) and CD206 (M2) expression. For the high CD206+ cells the selection was preceded by gating for FITC A/F (auto-fluorescence) to exclude dendritic cells (DCs) as alveolar resident macrophages have a well characterised high A/F. DCs are also selected out by CD68 but splitting cells according to A/F correlates with CD206 expression. High A/F cells are exclusively CD206+ve which may indicate that alveolar macrophages are in fact being increased by bleomycin ($p<0.05$). Upon injury in day 21 groups WT macrophage CD206+ cells increased from 11.53±0.6057 % to 34.16±6.877 %. No such ramping up of CD206+ cells occurs in KO bleomycin-treated mice (19.12±6.182 %, $p<0.05$) compared to wild-type. These cells are also highly expressing CCR7 hinting at a mixed M1/M2 phenotype (Figure 4.18 (a) and (b)).

Typically, Arginase-1 (Arg-1) is the best characterised M2 marker but the antibodies available were not suitable due to issues with their specificity. On account of these antibodies being chosen for the macrophage panels the staining strategy had to be amended as iNOS and Fizz-1 have intracellular antigens. For their inclusion an extra fix and permeabilisation step was required in the staining protocol with other antibodies specific for surface antigens. This significantly increased the protocol time but provided

the best characterisation of the M1/M2 balance *in vivo*. Following debris and doublet exclusion cells were gated from CD45+ (APC-Cy7) and live/dead status (AmCyan). These live CD45+ cells were gated for auto-fluorescence (A/F) then for F4/80+ (BV421) CD11b+ (PerCp) to give the population of activated macrophages. Finally for this panel CD45+F4/80+CD11b+ macrophages were separated into distinct FIZZ-1+ (RPE) and iNOS+ (APC) populations to yield M2 and M1 macrophages (Figure 4.19).

Inducible nitric oxide synthase (iNOS) expression by macrophages was determined to have no response to saline/bleomycin treatment or genotype change in terms of overall CD45+ve leukocytes (Figure 4.19 (a)). Interestingly, when cells were gated against Fizz-1+ expression a similar pattern as with CD206+ cells were elucidated, shown in Figure 4.19 (b). C57Bl6 groups at day 5 showed no response above basal levels but at day 21 there was a clear response to BLM with regards to Fizz-1+ percentage ($p<0.01$) increasing from 13.93±0.9681 % to 36.5±6.036 % respectively. This response is ablated in KO mice with a significant reduction to 20.37±5.761 % in the BLM group compared to WT counterpart ($p<0.05$).

The effect is distinct with CD206 but a similar pattern is seen with Fizz-1. Separation between this antibody's positive and negative controls wasn't perfect but a true signal was exhibited by this stain. Probably the best strategy is to be cautious with this result but the fact that it correlates the other marker (CD206) supports the theory that M2 macrophages are reduced in KO mice with bleomycin-induced pulmonary fibrosis compared to WT mice.

If this study was to be repeated a refined panel of antibodies for macrophage staining should be used to further elucidate the M1/M2 balance in the inflammatory infiltrate. This could be achieved by the use of an 8 colour panel consisting of CD45, Aqua (viability dye), F4/80, CD11b, FITC A/F, CD206, iNOS and Fizz-1. For the latter secondary antibodies would be used to boost the signal to make it more distinguishable. For the neutrophil activation markers CD11b and CD66a the gate began when the bone marrow compensation control and the lung digest PMN peaks cross. Rather than expression as a percentage of the parent population the data was expressed as percentage in relation to total CD45+ve leukocyte live cells. Due to the high auto-fluorescence exhibited by macrophages manual gating was required on account of the different strategy for gating on live dead cells. One shortcoming of this

study was the fact that both time points: day 5 and day 21 did not occur on the same day. Ideally both endpoints should have been done on the same day to prevent differences that occur in the processing and staining of lung samples and the bone marrow compensation controls. This may account for different baseline levels in saline controls between the two endpoints.

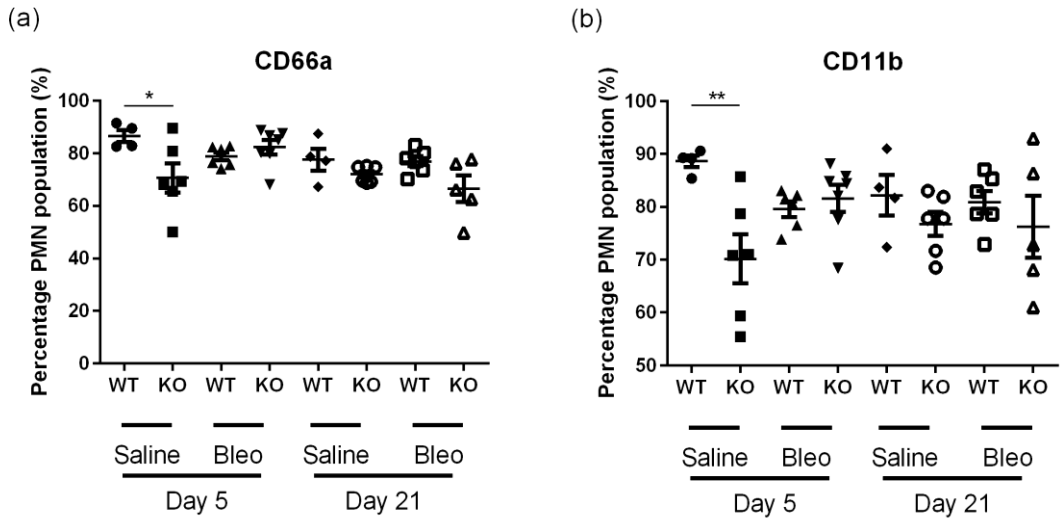

Figure 4.15: Activated neutrophil populations post-bleomycin injury at day 5/21 ascertained by multi-colour flow cytometry. (a) CD66a and (b) CD11b expression (see appendix A (i)). Results are expressed as a mean % of total Gr1+ve leukocytes (PMN) ±SEM (D5: WT SAL, n=4; KO SAL, n=6; WT BLM, n=6; KO BLM, n=7 and D21: WT SAL, n=4; KO SAL, n=6; WT BLM, n=6; KO BLM, n=5). All p values were calculated using a one-way analysis of variance (ANOVA) ns $p>0.05$, * $p<0.05$ and ** $p<0.01$.

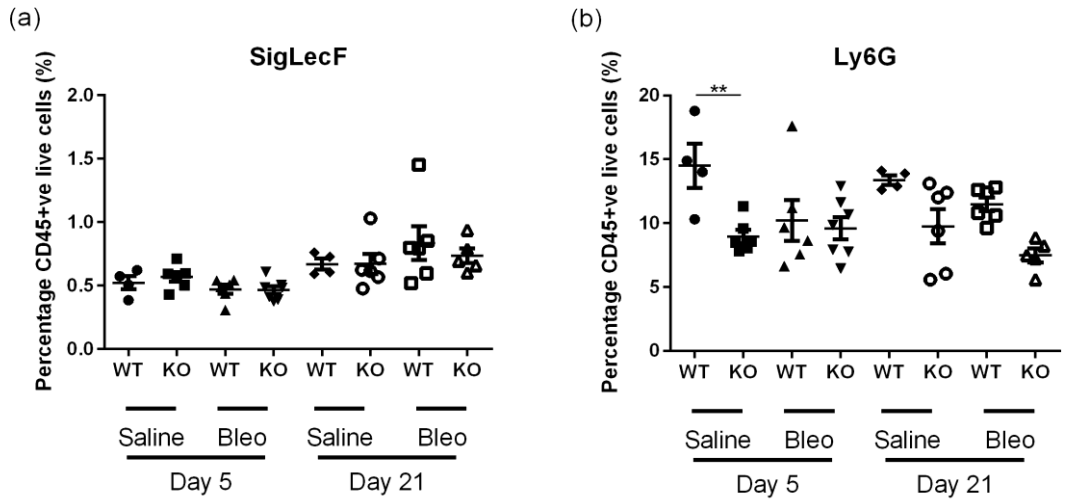

Figure 4.16: Neutrophil vs Eosinophil populations post-bleomycin injury at day 5/21 ascertained by multi-colour flow cytometry. (a) SigLecF and (b) Ly6G expression (see appendix A (ii)). Results are expressed as a mean % of total CD45+ve leukocytes ±SEM (D5: WT SAL, n=4; KO SAL, n=6; WT BLM, n=6; KO BLM, n=7 and D21: WT SAL, n=4; KO SAL, n=6; WT BLM, n=6; KO BLM, n=5). All p values were calculated using a one-way analysis of variance (ANOVA) ns $p>0.05$, * $p<0.05$ and ** $p<0.01$.

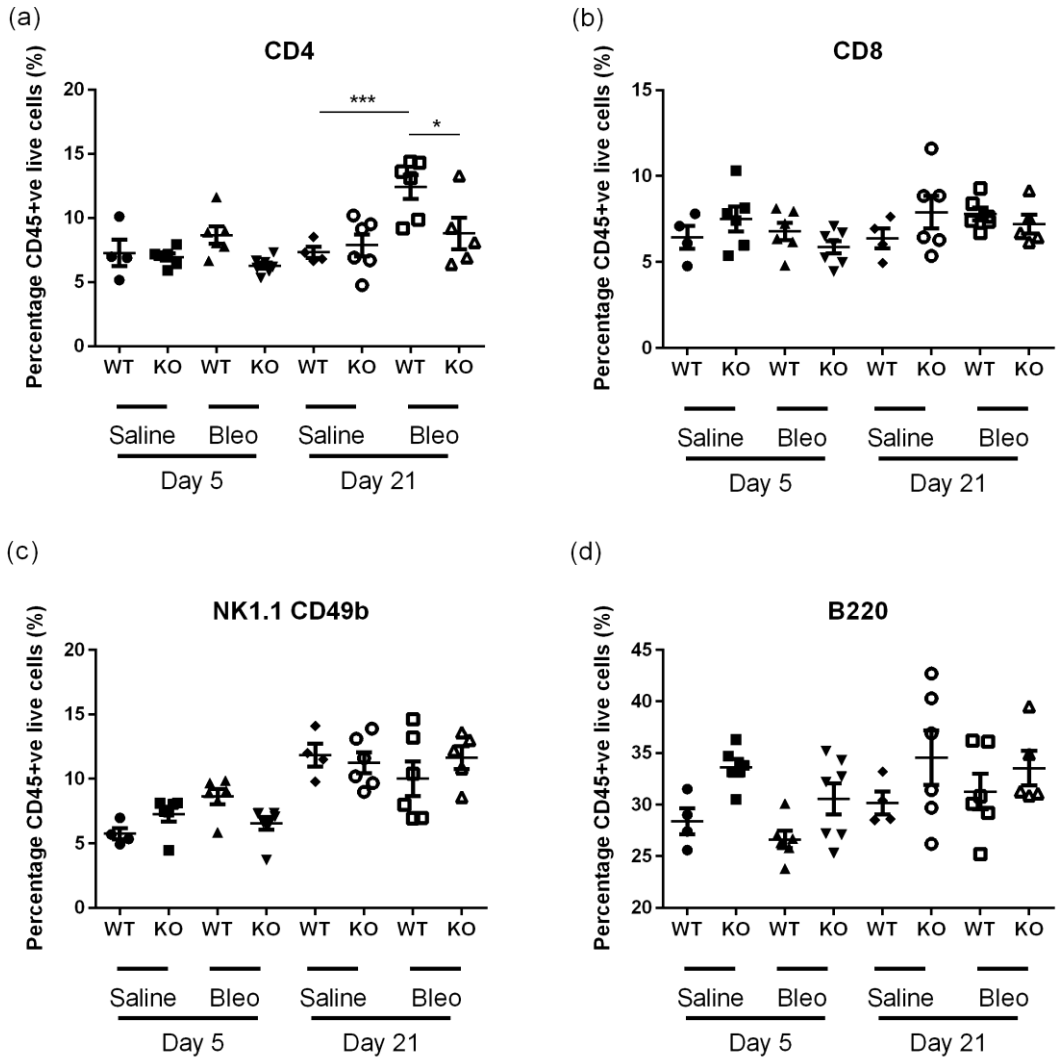

Figure 4.17: Lymphocyte populations post-bleomycin injury at day 5/21 ascertained by multi-colour flow cytometry. (a) CD4, (b) CD8, (c) NK1.1 CD49b and (d) B220 expression (see appendix A (iii)). Results are expressed as a mean % of total CD45+ve leukocytes ±SEM (D5: WT SAL, n=4; KO SAL, n=6; WT BLM, n=6; KO BLM, n=7 and D21: WT SAL, n=4; KO SAL, n=6; WT BLM, n=6; KO BLM, n=5). All p values were calculated using a one-way analysis of variance (ANOVA) ns $p>0.05$, * $p<0.05$ and *** $p<0.001$.

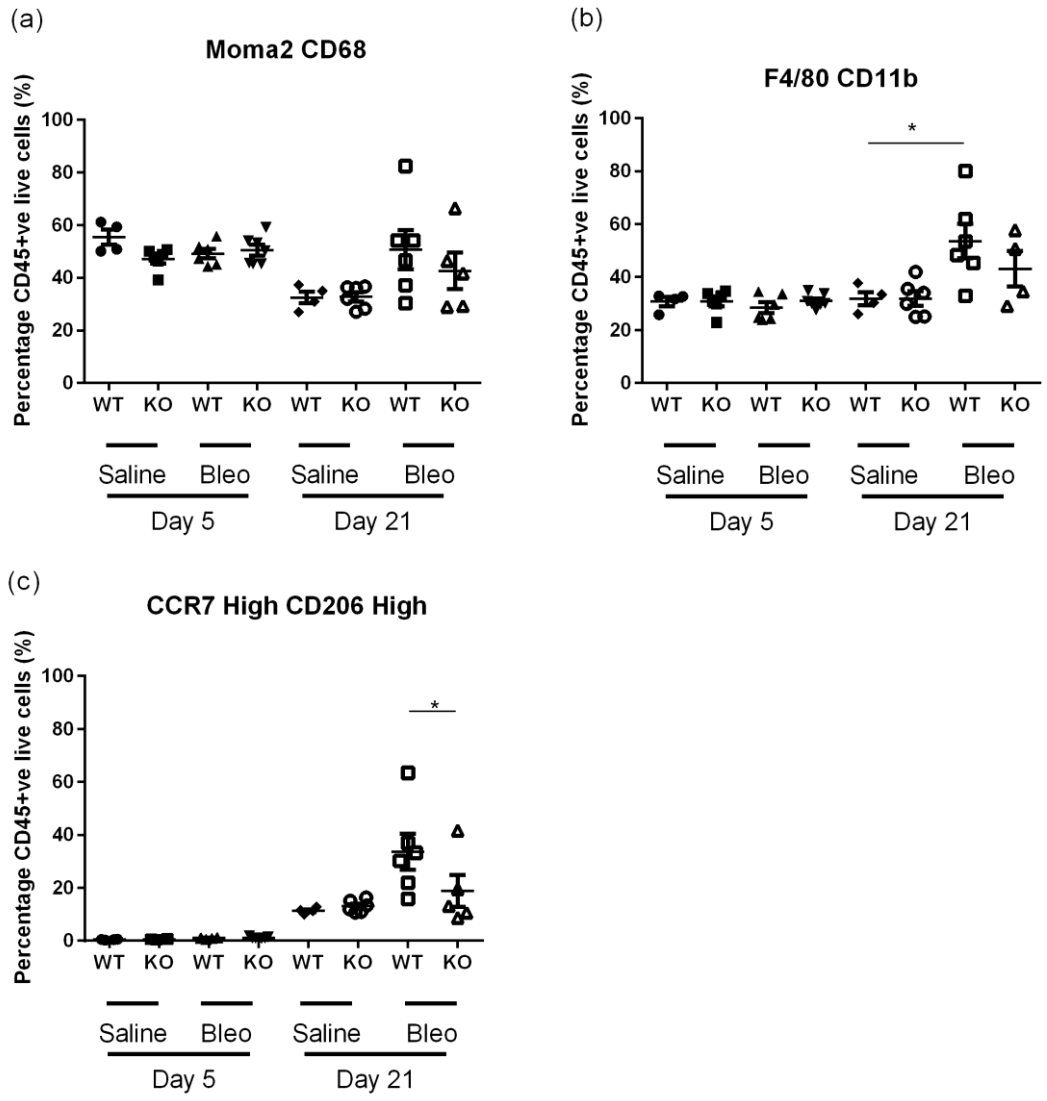

Figure 4.18: Macrophage panel 1 post-bleomycin injury at day 5/21 ascertained by multi-colour flow cytometry. (a) Moma2 CD68 (b) F4/80 CD11b, (c) High CCR7 High CD206 expression (see appendix A (iv)). Results are expressed as a mean % of total CD45+ve leukocytes ±SEM (D5: WT SAL, n=4; KO SAL, n=6; WT BLM, n=6; KO BLM, n=7 and D21: WT SAL, n=4; KO SAL, n=6; WT BLM, n=6; KO BLM, n=5). All p values were calculated using a one-way analysis of variance (ANOVA) ns $p>0.05$, * $p<0.05$.

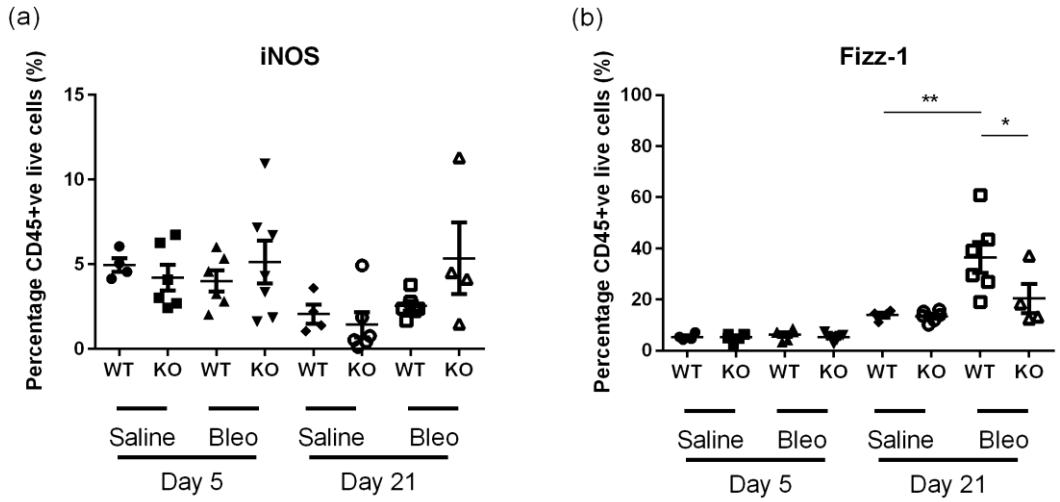

Figure 4.19: Macrophage panel 2 post-bleomycin injury at day 5/21 ascertained by multi-colour flow cytometry. (a) iNOS (b) Fizz-1 expression (see appendix A (v)). Results are expressed as a mean % of total CD45+ve leukocytes ±SEM (D5: WT SAL, n=4; KO SAL, n=6; WT BLM, n=6; KO BLM, n=7 and D21: WT SAL, n=4; KO SAL, n=6; WT BLM, n=6; KO BLM, n=5). All p values were calculated using a one-way analysis of variance (ANOVA) ns $p>0.05$, * $p<0.05$ and ** $p<0.01$.

4.2.8 Ly6G-mediated neutrophil depletion and the bleomycin model

4.2.8.1 Rationale

Research regarding the bleomycin model and the mechanism of its pathogenesis in the pulmonary setting is still incomplete. Following its induced pneumonitis activity upon the acute injury there is a notable influx of inflammatory cells particularly neutrophils, macrophages and lymphocytes. Neutrophilia as well as eosinophilia and macrophage activation all play roles in IPF-like patterns of fibrosis and perpetuating the bleomycin-induced oxidative damage (Grande *et al*., 1998). No specific study has ascertained the effect of neutrophils in this model but depletion-mediated investigations of macrophages with agents such as clodronate have proven their effects (Murray *et al*., 2011). The dysfunction of neutrophils has been investigated in other organs including the liver. Neutrophils play a pivotal role in inflammatory responses but depending on the organ setting fibrosis may not require this. Recent research by Moles *et al*. (2013) has elucidated that neutrophils are redundant in liver fibrosis. S100A9 -/- knockouts with severely impaired PMN recruitment have no effect on the activation of myofibroblasts and their deposition of collagen and other ECM markers. In fact in the liver setting, neutrophils are being shown to have an important in the pathogenesis of cancer specifically hepatocellular carcinoma (HCC, Wilson *et al*., 2015). Induction of lung injury is associated with neutrophil influx with other immune cells but little evidence is documented to support pathogenesis in the bleomycin model.

In order to determine the role of neutrophils in this model a mini-pump based strategy was employed to deplete PMNs at acute and fibrotic phase time points of 1 and 21 days respectively. Anti-Ly6G antibody is specifically engineered to target neutrophils which express the marker. Unlike other depletion antibodies such as anti-granulocyte receptor-1 (Gr-1) mAb (RB6-8C5) anti-Ly6G only binds Ly6G as opposed to Ly6C, a marker present on a wider set of different cell populations such as dendritic cells, lymphocytes and monocytes (Daley *et al*., 2008). Being able to specifically knockout neutrophils via this strategy is important in determining their effect in this acute injury-driven model. As for the implantation of the antibody via a mini-pump system, this different from many cases in the literature where repeated intraperitoneal (i.p.) injections are common place (Daley *et al*., 2008; Moles *et al*., 2013). Regardless of the endpoint used mini-pumps were surgically installed two days prior to drug/saline instillation. The rationale behind this was to deplete the neutrophils in the animal before

the initial acute phase following the BLM i.t. while allowing enough time for any viable neutrophils at the time of the depletion regimen to complete their circulatory life span. Our two days of neutrophil depletion was essentially overkill to make sure no neutrophils were present either in the blood or in the lung environment. Studies investigating neutrophil dynamics and trafficking in the SPECT-CT imaging of PMN (radiolabelled) trafficking of bone marrow neutrophils (10^{11}) allowed quantification of the marginated and circulating pools as they move through the lung showing that circulating neutrophils have a 10 hours lifespan (Farahi *et al.*, 2012). Therefore, prior to the start of my study neutrophils will no longer be viable and no new cell populations will be induced as a result of the injury agent.

Basic features of neutrophils and other immune cells have long been subject to assumptions about their functional capabilities and characteristics. Investigations are accurately defining key components of this immune cells including cell trafficking ability, lifespan and even size. Indeed Guck *et al*. (2001) determined that the approximate diameter of a live, un-manipulated PMN was 5µm by a laser-capture-based method. Before then quantification of a neutrophil had only been done on fixed tissue. Clearly there is still much to learn about this key mediator of the adaptive immune response with respect to its own characteristics and role in disease.

4.2.8.2 Hypothesis

Neutrophils expressing abundant proportions of FPR1 play an integral part in the pathogenesis of the bleomycin-mediated pulmonary fibrosis *in vivo* model. Ly6G-induced depletion of neutrophils prior to bleomycin injury will attenuate the inflammatory and fibrotic responses.

4.2.8.2.1 Aims

Elucidation of bleomycin model with regards to its pathogenesis and the role of neutrophils were evaluated by systemic administration of control IgG/Ly6G antibody via surgically implanted ALZET osmotic mini-pumps. Depletion 2 days prior to bleomycin injury at day 0 will remove short-lived Ly6G+ neutrophils and the effect on the pathogenesis of the *in vivo* model will be determined.

4.2.8.3 Acute 1 day injury for proof of PMN concept

4.2.8.3.1 Histology

As a proof of concept study for the neutrophil depletion an acute time point was used to make certain Ly6G+ granulocytes were indeed ablated. FFPE tissue sections stained for neutrophils via IHC demonstrated a significant reduction in NIMP+ cells from a mean of 54.4±9.5 (IgG-treated mice) to a mere 9.04±2.076 in Ly6G-depleted lungs ($p<0.001$). From basal untreated (U/T) lungs a mean count of 20.82±1.774 cells was determined, dramatically increasing with bleomycin instillation even after one day ($p<0.01$) in control IgG-pretreated mice (Figure 4.20).

CD68+ staining through IHC showed comparable numbers in U/T, IgG BLM and Ly6G BLM groups with no significant increase/decrease ($p>0.05$). Ly6G-mediated depletion of neutrophils did not affect macrophage recruitment in the lungs of injured WT mice or due to early endpoint the infiltration of CD68+ cells had not reached its peak (Figure 4.21).

CD3+ lymphocytes displayed a gradual decrease with bleomycin treated mini-pump administered mice (Figure 4.22). In Ly6G+ neutrophil depleted mice injured with BLM CD3+ mean counts were significantly reduced to 28.61±3.161 compared to U/T (44.6±0.813; $p<0.001$) and IgG BLM (37.77±1.722; $p<0.05$) groups. Reduction of neutrophils involved in the innate immune response to the acute bleomycin injury appeared to directly influence lymphocyte infiltration.

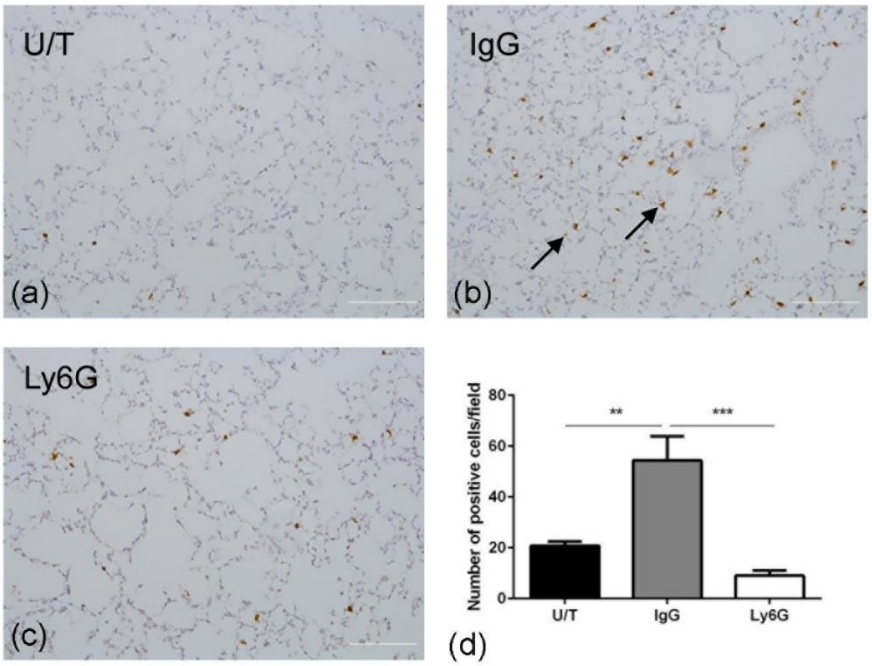

Figure 4.20: Neutrophils for neutrophil depletion of acute bleomycin-treated mice. Relative photomicrographs of NIMP+ve neutrophils within WT bleomycin IgG/Ly6G PMN depleted and untreated control treated lungs (x20 magnification). Groups were (a) U/T (n=5), (b) IgG BLM (n=5) and (c) Ly6G BLM (n=5) with scale bars representing 100µm. Positive cells indicated by arrows. Results are expressed as (d) mean positive cells per high power field (hpf) displaying SEM. All P values were calculated using a one-way analysis of variance (ANOVA) **p<0.01; ns p<0.05.

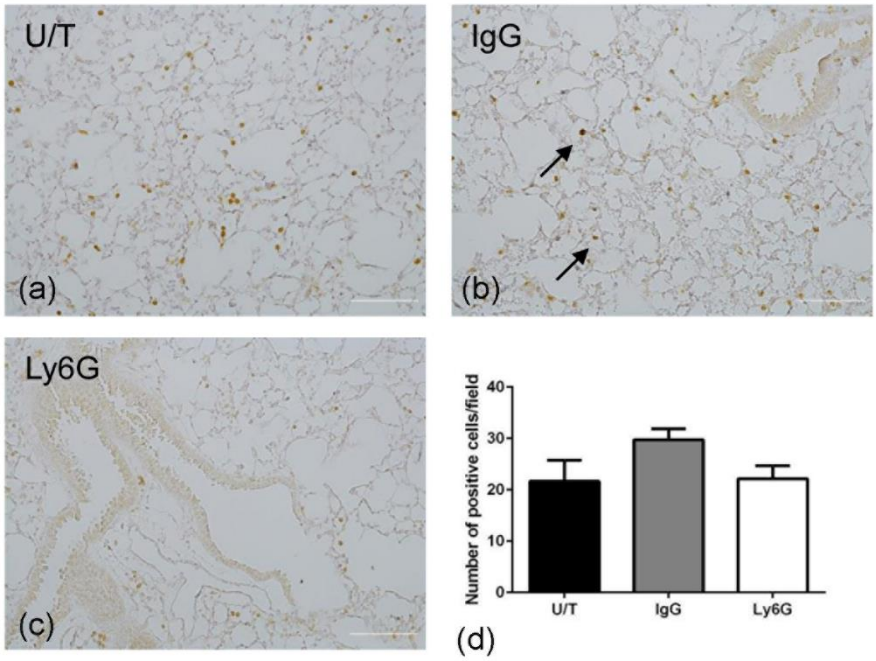

Figure 4.21: Macrophage counts for neutrophil depletion of acute bleomycin-treated mice. Relative photomicrographs of CD68+ve macrophages within WT bleomycin IgG/Ly6G PMN depleted and untreated control treated lungs (x20 magnification). Groups were (a) U/T (n=5), (b) IgG BLM (n=5) and (c) Ly6G BLM (n=5) with scale bars representing 100µm. Positive cells indicated by arrows. Results are expressed as (d) mean positive cells per high power field (hpf) displaying SEM. All P values were calculated using a one-way analysis of variance (ANOVA) ns $p<0.05$.

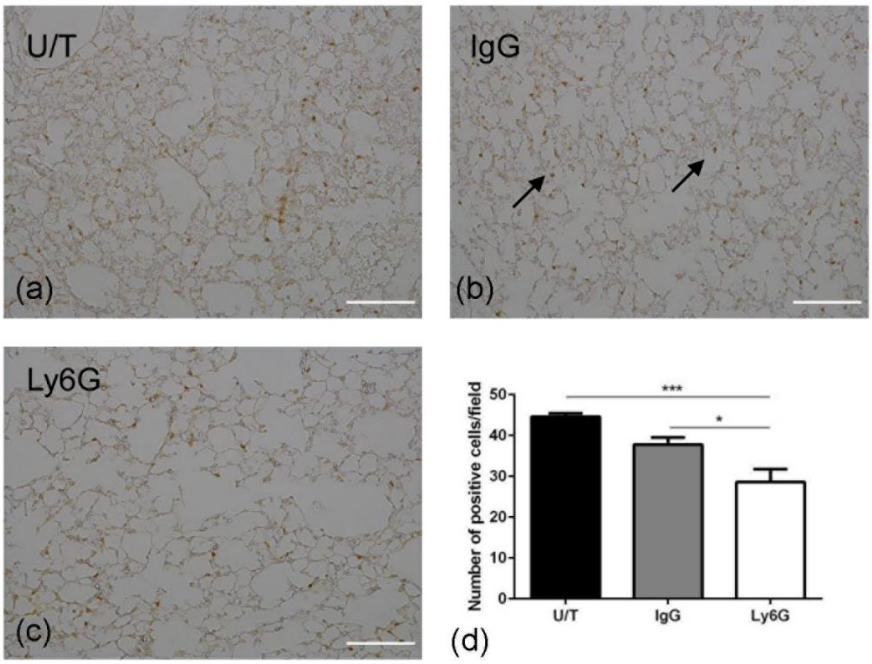

Figure 4.22: Lymphocyte counts for neutrophil depletion of acute bleomycin-treated mice. Relative photomicrographs of CD3+ve lymphocytes within WT bleomycin IgG/Ly6G PMN depleted and untreated control treated lungs (x20 magnification). Groups were (a) U/T (n=5), (b) IgG BLM (n=5) and (c) Ly6G BLM (n=5) with scale bars representing 100µm. Positive cells indicated by arrows. Results are expressed as (d) mean positive cells per high power field (hpf) displaying SEM. All P values were calculated using a one-way analysis of variance (ANOVA) **p<0.01; *p<0.05 and ns p<0.05.

4.2.8.4 BAL cytospin counts of acute bleomycin Ly6G model

Total BALF cellular count performed by Automatic EVE cell counter (NanoEntek) demonstrated clear immune cell infiltration with bleomycin 1 day endpoint. Mean U/T total cells/ml increased from 222000±43290 to 417500±23936 (IgG, $p<0.01$) and 400000±10000 (Ly6G, $p<0.01$) showing a clear response (Figure 4.23 (a)).

Differential cell counts as with others performed showed a heavy proportion of macrophages (over 80%). Using the total cell counts above the number of cells per millilitre was calculated for U/T, IgG BLM and Ly6G BLM groups (Figure 4.23 (b)). Macrophage mean counts increased in BLM-injury groups from untreated groups (2.742±0.2397 $x10^5$ cells/ml) significantly. Control group instilled with IgG antibody developed a normal response to bleomycin doubling their macrophage numbers, 5.848±1.29 $x10^5$ cells/ml ($p<0.0001$). Due to small numbers there was variability in these differential counts perhaps leading to this vast increase. Ly6G-depleted mice also showed increased numbers of macrophages, 4.537±0.1146 $x10^5$ cells/ml ($p<0.05$) compared to U/T group). Eosinophils and lymphocytes were not counted in great numbers from BAL cytospins with no detectable changes with respect to antibody treatment or bleomycin. The key difference evident in the BAL counts was the upregulation of the neutrophil population from 0.00799±0.004717 $x10^5$ cells/ml in U/T group to 0.5971±0.3288 $x10^5$ cells/ml in control BLM pretreated with IgG antibody ($p<0.01$). No such increase occurred with comparison of U/T and Ly6G-BLM groups (0.1309±0.04454 $x10^5$ cells/ml) but the responses by the bleomycin-injured groups was clearly compromised ($p<0.05$). As with the tissue infiltration of the BAL within the lungs was depleted of neutrophils by mini-pump osmotic transfer of Ly6G antibody.

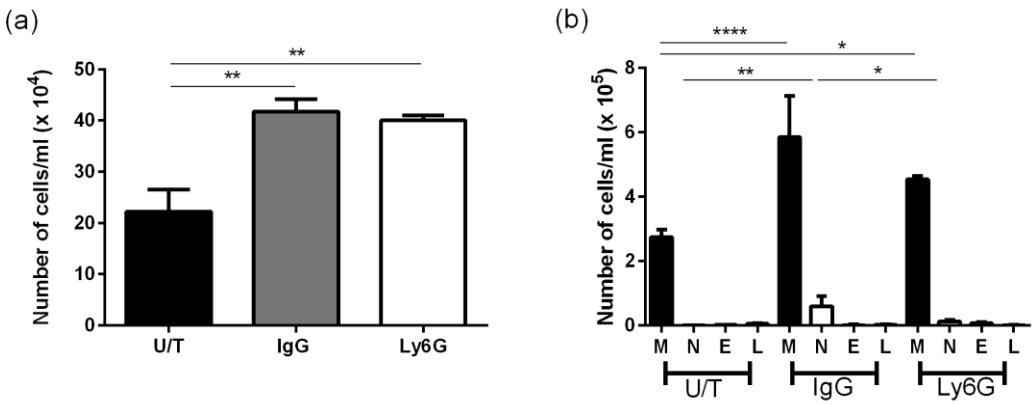

Figure 4.23: Total and differential BAL cell counts from neutrophil depleted 1 day bleomycin-treated mice. (a) Total cell count and (b) differential cell count from Ly6G 1 day bleomycin (BLM) model with untreated (U/T; n=5), isotype (IgG) mini-pump bleomycin-treated mice (n=5) and neutrophil-depleted (Ly6G) mini-pump bleomycin-treated mice (n=5). Data represented by cells/ml±SEM. All P values were calculated using a one-way analysis of variance (ANOVA) ns $p>0.05$, * $p<0.05$, ** $p<0.01$, ***$p<0.001$.

4.2.8.5 Gene expression of inflammatory markers with Ly6G-treated acute bleomycin-injured animals

mRNA gene expression levels of different cytokines are evaluated to assess effect of depletion treatment (Figure 4.24). S100A9, a myeloid cell marker was diminished in Ly6G antibody treated group relative to IgG bleomycin injured controls. Relative gene expression was decreased from a mean fold change of 0.5724±0.169 to 0.1411±0.061 with Ly6G-mediated neutrophil depletion ($p<0.05$). IL-6 and MCP-1 mRNA levels were similar with both antibody treatments and subsequent bleomycin injuries ($p>0.05$). IL-10 expression was amplified in IgG bleomycin group two-fold over that in Ly6G bleomycin group but not significantly ($p>0.05$). KC (murine IL-8 equivalent), an inflammatory cytokine, mRNA levels were increased in control IgG group compared to neutrophil-depleted mice ($p>0.05$).

4.2.8.6 Inflammatory cytokine levels in Ly6G/IgG acute bleomycin-injured mice as determined by MSD analysis

Comparison of IL-1β, MCP-1, KC and IL-6 pro-inflammatory cytokines in Ly6G and IgG-BLM injured lung homogenate demonstrated no differences (Figure 4.26; $p>0.05$). This pro-inflammatory panel was designed to evaluate key cytokines secreted by immune cells upon infiltration of the lung and translocation to sites of acute bleomycin injury. Antibody incubation prior to bleomycin administration had no effect on production of cytokines at this 24 hour endpoint, perhaps indicating that cytokine response does not occur in earnest till day 5 (Figure 4.25).

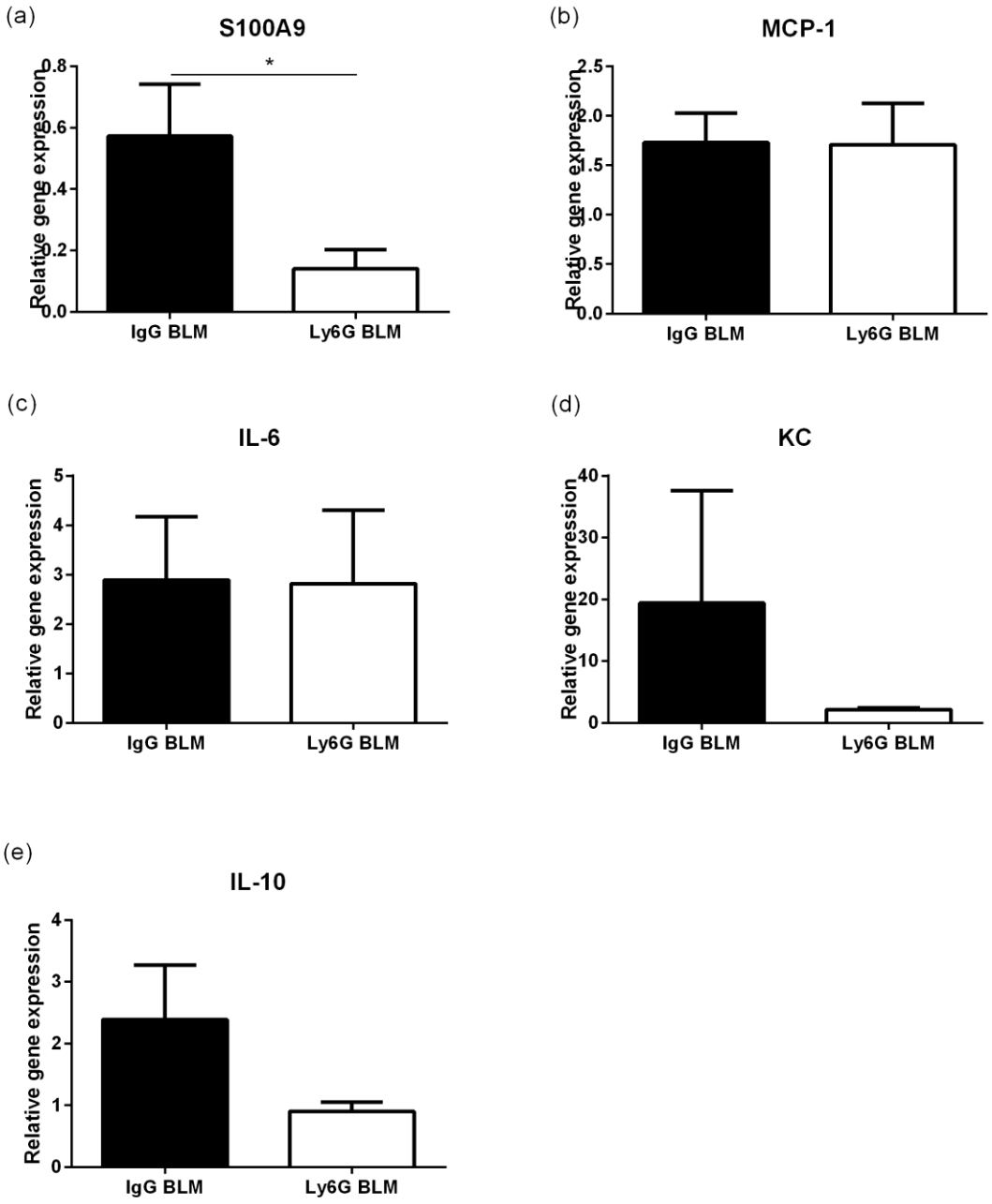

Figure 4.24: Real-time mRNA expression levels of myeloid markers and cytokines in acute Ly6G-bleomycin versus IgG controls. (a) S100A9, (b) IL-10, (c) IL-6, (d) KC and (e) MCP-1 cytokine/chemokine genes. Groups were as follows U/T (n=5), IgG BLM (n=5) and Ly6G BLM (n=5).Mean fold change normalised to GAPDH was calculated relative to control IgG treated mice displaying SEM. All P values were calculated using unpaired t-tests. ns $p>0.05$ and * $p<0.05$.

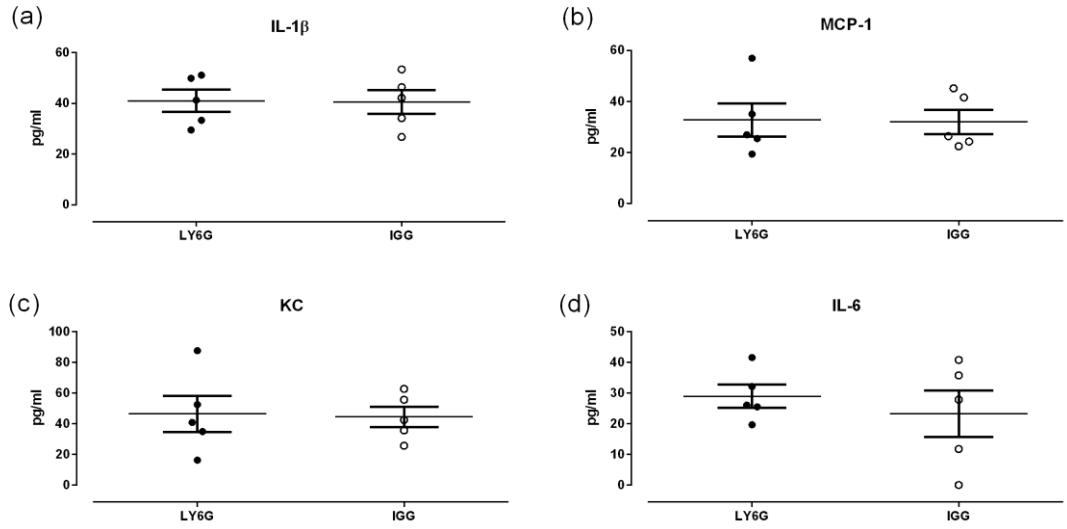

Figure 4.25: Chemokine/cytokine secreted levels in lung homogenate of Ly6G/IgG pre-treated mice subject to bleomycin injury. Multiplex ELISA using Mesoscale Discovery (MSD) platform analysed (a) Interleukin-1β (IL-1β), (b) Monocyte Chemoattractant Peptide-1 (MCP-1), (c) KC (chemokine (C-X-C motif) ligand 1; CXCL1) and (d) Interleukin-6 (IL-6) levels in lung homogenate prepared from right lobes except post-caval. Results are expressed as a mean reading (from duplicate wells) SEM (IgG BLM, n=5; Ly6G BLM, n=5). All P values were calculated using unpaired t-tests. ns $p>0.05$.

4.2.8.7 Fibrotic 21 day endpoint preceded by IgG/Ly6G mini-pump installation

Staining by PSR for collagen I/III deposition in control and neutrophil-depleted mice was calculated as percentage area (Figure 4.26). IgG-BLM and Ly6G-BLM groups demonstrated a clear reduction in collagen staining ($p<0.05$) from a mean of 5.187±1.138 % to 2.072±0.4422 %. Neutrophil depletion as proved by the acute study ablated collagen deposition at 21 day endpoint. Alpha-SMA, marker of activated myofibroblasts displayed low levels of percentage area staining (Figure 4.27). A minor increase was observed in control IgG bleomycin-treated mice from saline levels ($p>0.05$). Ly6G-BLM group (mean percentage of 1.872±0.08675 %) demonstrated lower levels of staining compared to IgG-BLM group, 2.993±0.5079 %) but it was non-significant ($p>0.05$).

4.2.8.8 Immune cells with neutrophil-depletion of bleomycin-injured mice

NIMP+ staining via IHC of FFPE sections revealed minimal positive staining with approximately 0.5 cells per high power field (Figure 4.28). This fibrotic endpoint would have low levels of neutrophils typically as immune cell response to acute injury is long completed hence low numbers in control IgG groups. Low levels of NIMP positive cells at this endpoint may indicate decreased pump efficiency towards end of study and recovery of neutrophil population.

CD3+ staining of formalin-fixed tissue sections allowed the determination that lymphocytes showed no significant changes across antibody treatments or injury (Figure 4.29). Numbers increased with neutrophil depletion perhaps indicating a downstream effect on lymphocyte recruitment ($p>0.05$).

Macrophages were stained by CD68 via IHC illuminating an increase with bleomycin treated mice implanted with control IgG antibody to 23.69±3.061 mean cells/field (Figure 4.30). With ablation of neutrophils in Ly6G-bleomycin treated group there was a significant reduction in macrophage infiltration, 16.04±2.019 cells/field ($p<0.05$). Only so much can be interpreted from this data due to the non-significant response from saline to bleomycin groups.

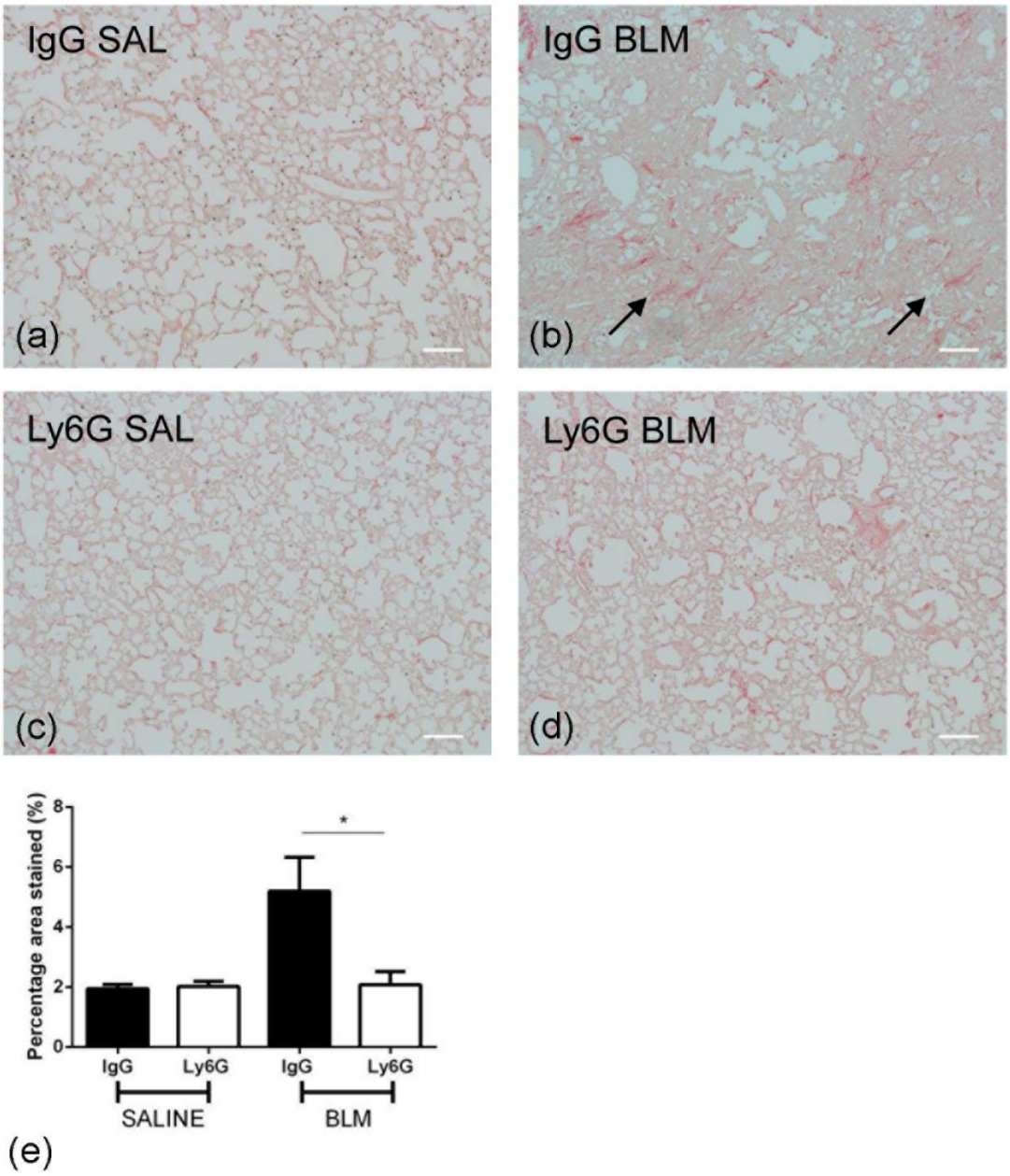

Figure 4.26: Collagen deposition in Ly6G-treated bleomycin-injured mice. Relative photomicrographs of PSR stained tissue sections of WT bleomycin IgG/Ly6G PMN depleted and saline control treated lungs (x20 magnification). (a) IgG Saline (n=4), (b) Ly6G Saline (n=4), (c) IgG BLM (n=9) and (d) Ly6G BLM (n=8) sections were analysed by densitometry. Results are expressed as (e) mean percentage area (%) per high power field (hpf) SEM. Scale bars represent 100µm. All P values were calculated using a one-way analysis of variance (ANOVA) ns $p>0.05$, * $p<0.05$.

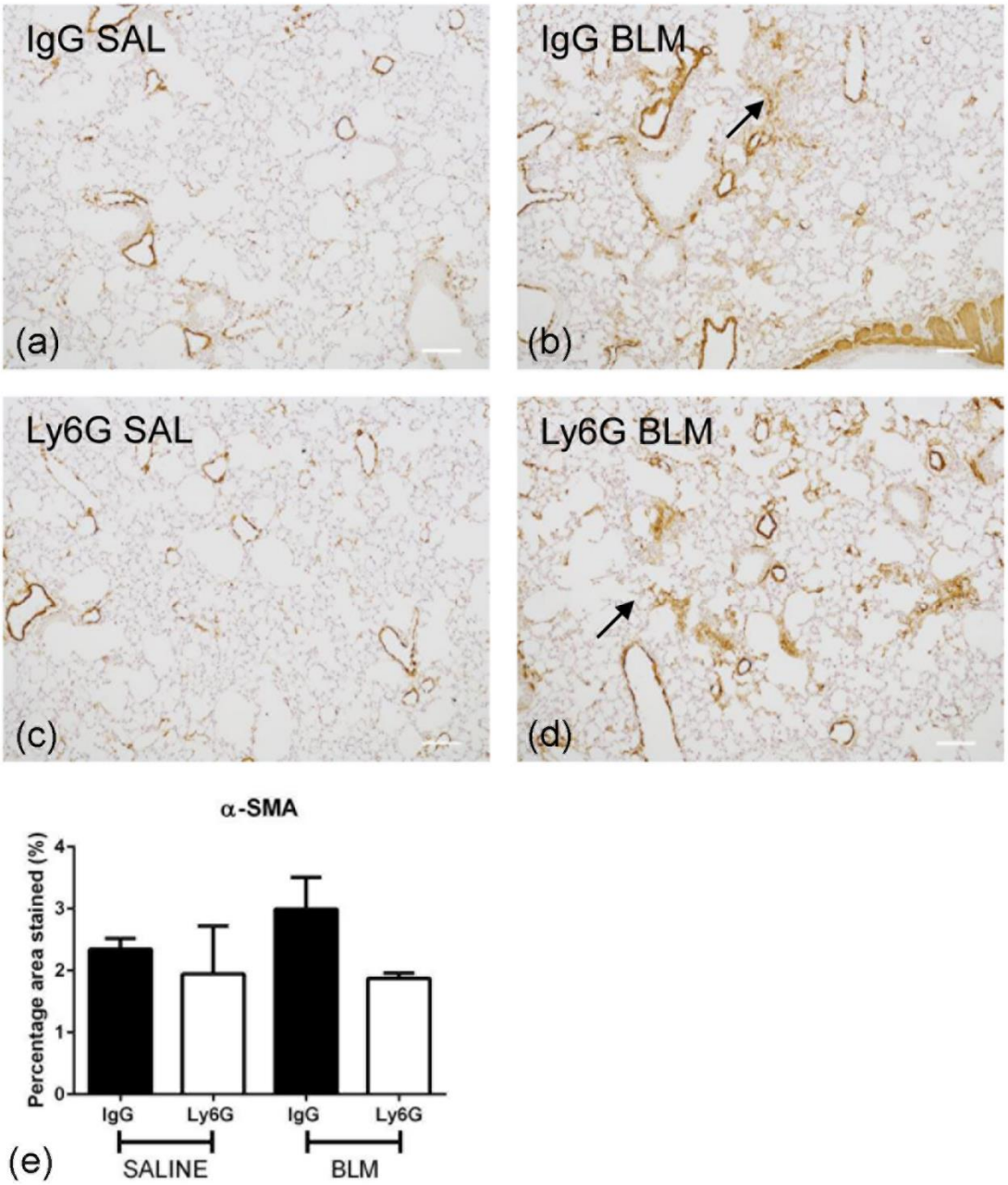

Figure 4.27: α-SMA deposition in Ly6G-treated bleomycin-injured mice. Relative photomicrographs of α-SMA indirectly stained tissue sections of WT bleomycin IgG/Ly6G PMN depleted and saline control treated lungs (x20 magnification). (a) IgG Saline (n=4), (b) Ly6G Saline (n=4), (c) IgG BLM (n=9) and (d) Ly6G BLM (n=8) sections were analysed by densitometry. Results are expressed as (e) mean percentage area (%) per high power field (hpf) SEM. Scale bars represent 100μm. All P values were calculated using a one-way analysis of variance (ANOVA) ns $p>0.05$, * $p<0.05$.

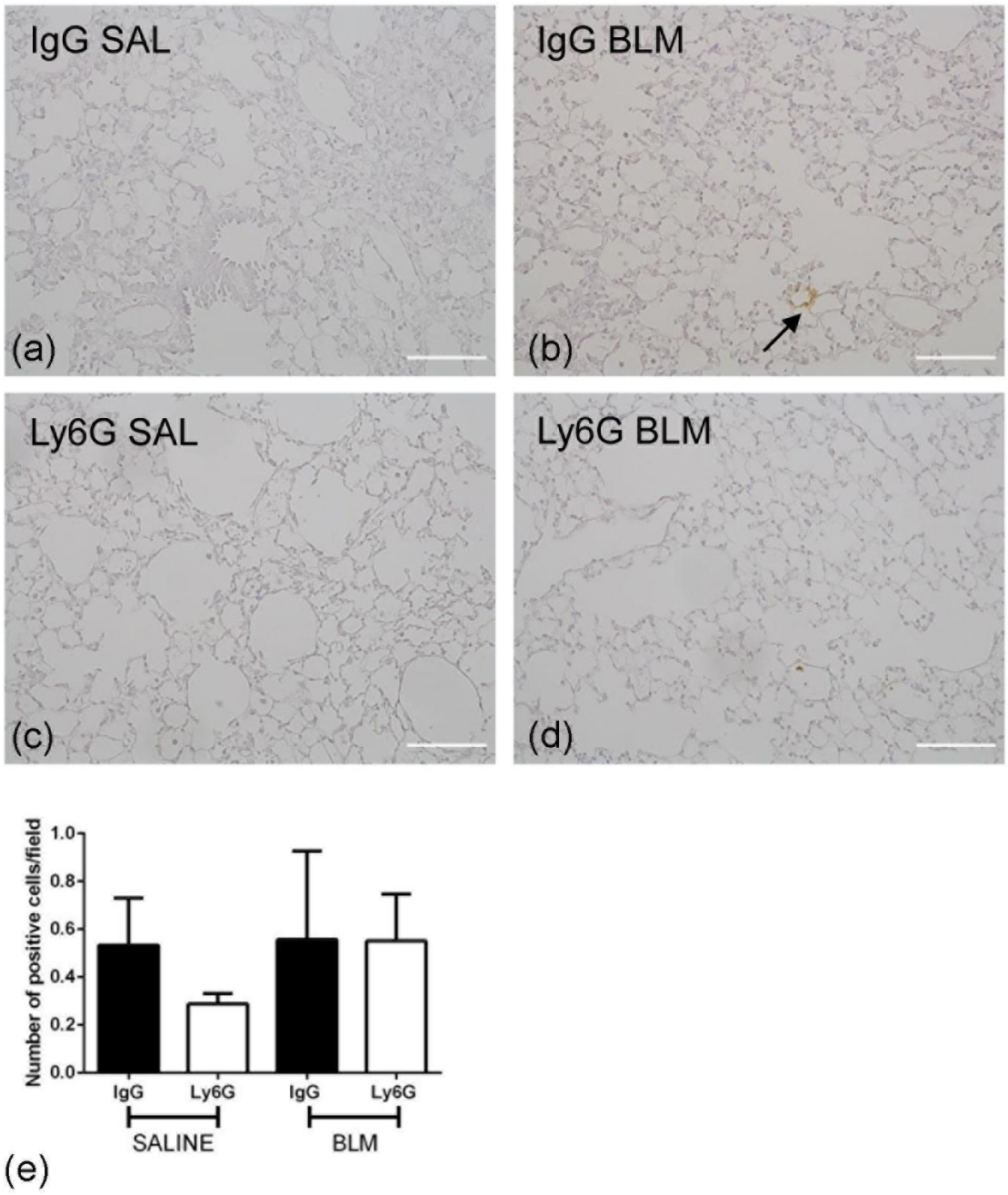

Figure 4.28: Neutrophil population in Ly6G-treated bleomycin-injured mice. Relative photomicrographs of NIMP indirectly stained tissue sections of WT bleomycin IgG/Ly6G PMN depleted and saline control treated lungs (x20 magnification); (a) IgG Saline (n=4), (b) Ly6G Saline (n=4), (c) IgG BLM (n=9) and (d) Ly6G BLM (n=8) sections were analysed for positive cells. Results are expressed as (e) mean cells/field (hpf) ±SEM. Scale bars represent 100µm. All P values were calculated using a one-way analysis of variance (ANOVA); ns $p>0.05$.

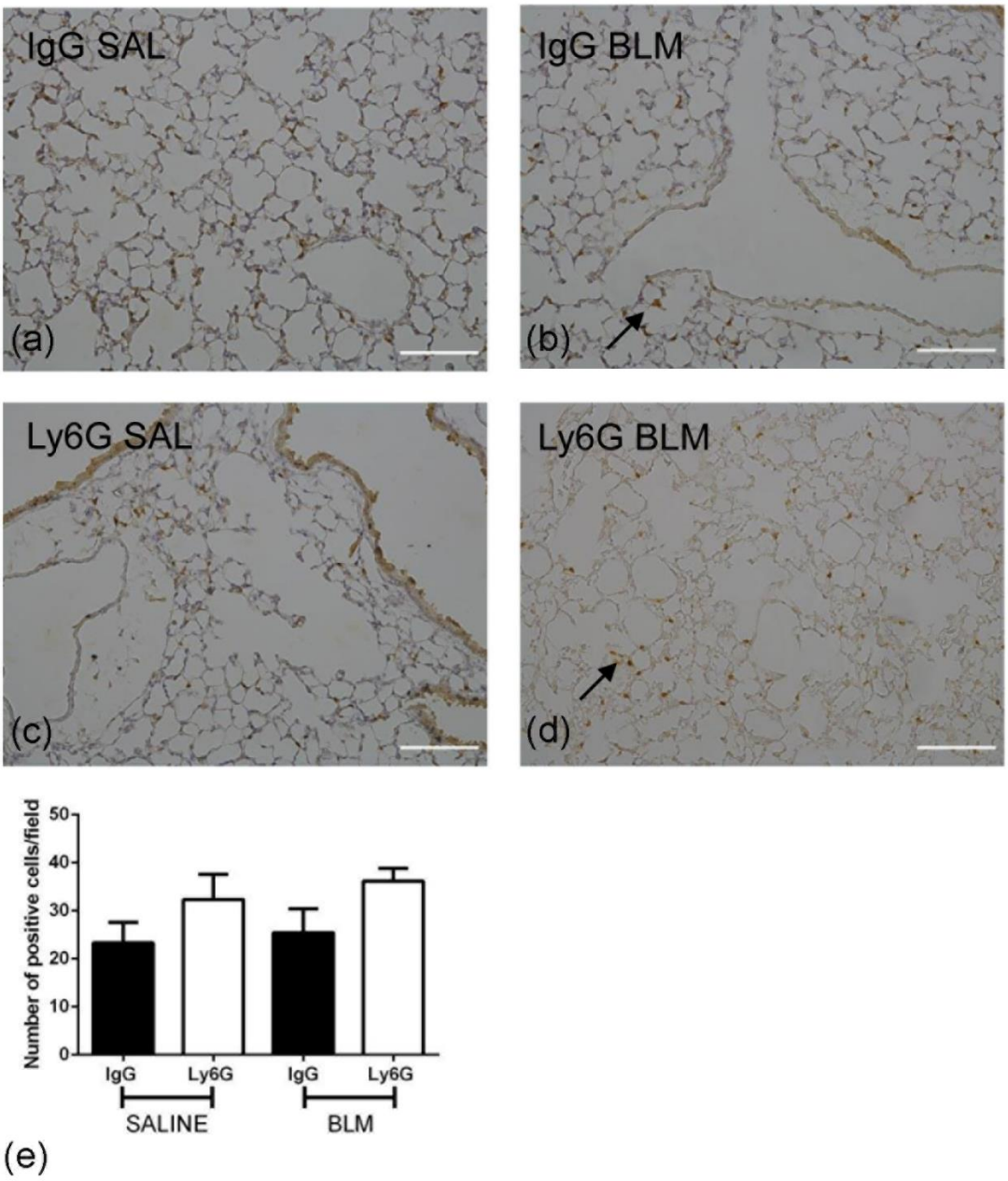

Figure 4.29: Lymphocyte population in Ly6G-treated bleomycin-injured mice. Relative photomicrographs of CD3 indirectly stained tissue sections of WT bleomycin IgG/Ly6G PMN depleted and saline control treated lungs (x20 magnification); (a) IgG Saline (n=4), (b) Ly6G Saline (n=4), (c) IgG BLM (n=9) and (d) Ly6G BLM (n=8) sections were analysed for positive cells. Results are expressed as (e) mean cells/field (hpf) ±SEM. Scale bars represent 100µm. All P values were calculated using a one-way analysis of variance (ANOVA) ns $p>0.05$.

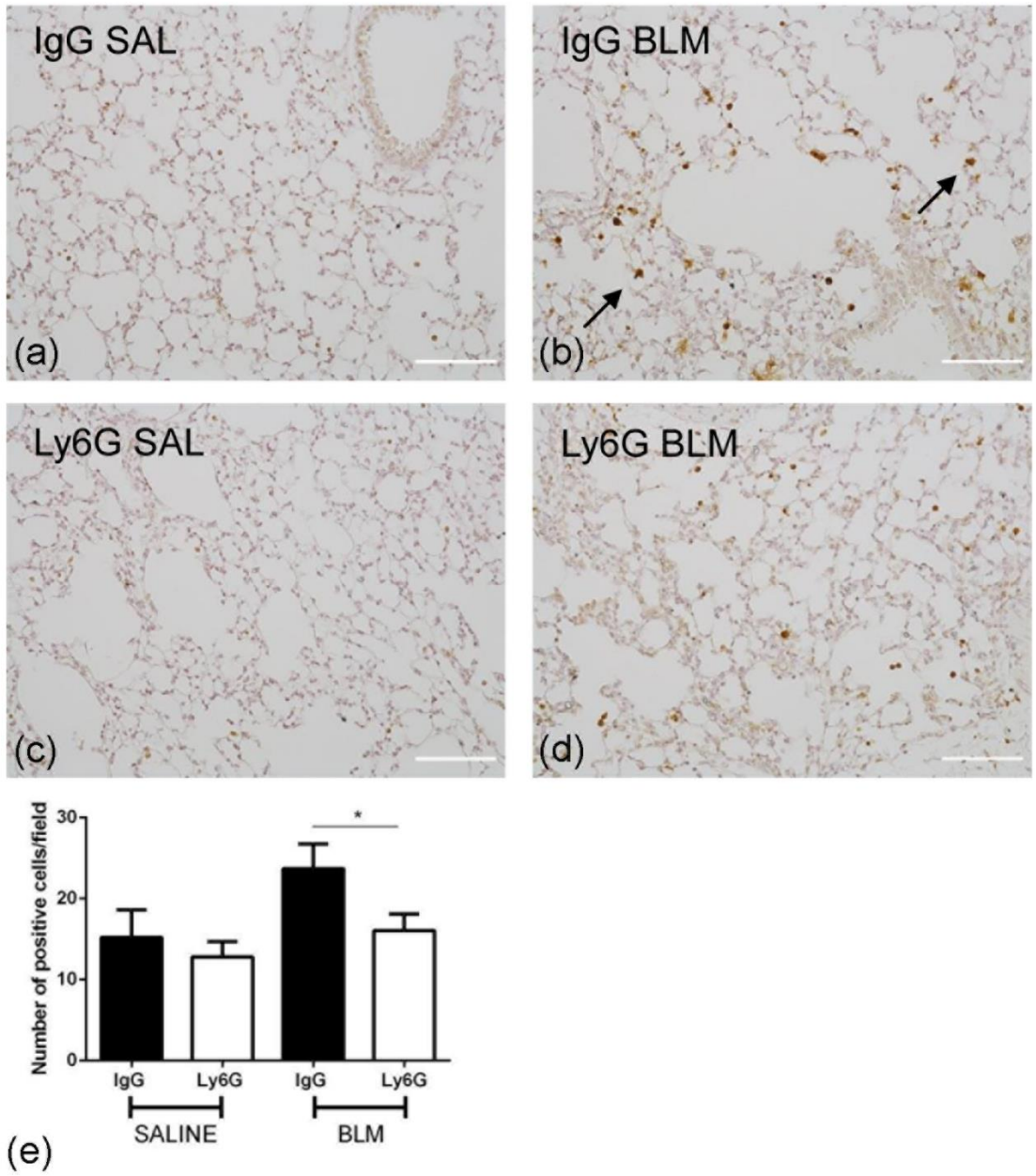

Figure 4.30: Macrophage population in Ly6G-treated bleomycin-injured mice. Relative photomicrographs of CD68 indirectly stained tissue sections of WT bleomycin IgG/Ly6G PMN depleted and saline control treated lungs (x20 magnification); (a) IgG Saline (n=4), (b) Ly6G Saline (n=4), (c) IgG BLM (n=9) and (d) Ly6G BLM (n=8) sections were analysed for positive cells. Results are expressed as (e) mean cells/field (hpf) ±SEM. Scale bars represent 100µm. All P values were calculated using a one-way analysis of variance (ANOVA) ns $p>0.05$, * $p<0.05$.

4.2.8.9 BAL TGFβ1 cytokine level in IgG/Ly6G pretreated bleomycin-injured C57Bl6 mice

Detectable levels of TGFβ1 at the day 21 endpoint preceded by Ly6G-mediated neutrophil depletion were determined by performing a duoset ELISA on BAL supernatant (Figure 4.31). Low levels were expected at this later endpoint as the signal is elevated during acute inflammation stage of model (Figure 4.9). There was a possible reduction in the level of TGFβ1 in the Ly6G-treated bleomycin group compared to isotype control-treated mice. TGFβ1 cytokine level increased significantly from 43.32±8.419 pg/ml to 68.44±6.445 pg/ml with bleomycin injury ($p<0.05$). This up-regulation was not present in Ly6G-treated mice and BLM-injured mice at day 21 produced a lower level of TGFβ1, mean of 47.37±7.127 pg/ml significantly reduced from IgG pre-treated BLM group ($p<0.05$). Loss of neutrophils appears to be directly affecting fibrogenic cytokine secretion.

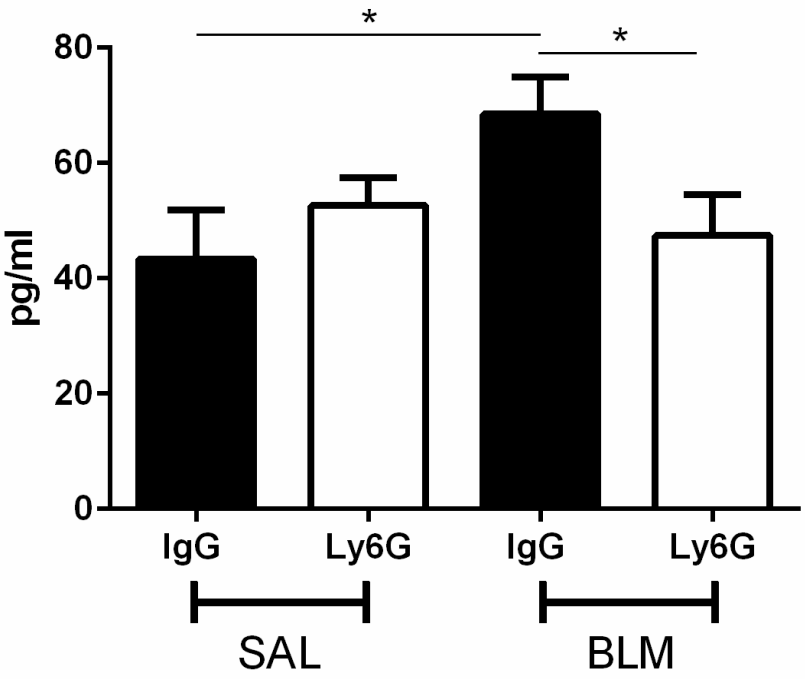

Figure 4.31: TGFβ1 levels (pg/ml) detectable in bronchoalveolar (BAL) fluid in Ly6G 21 Day bleomycin neutrophil depletion study. Basal levels of TGFβ1 in saline IgG/LY6G-treated controls ~60pg/ml. IgG bleomycin-treated group levels increased minimally to ~100pg/ml while Ly6G-treated mice demonstrated no increase in analyte. Groups were as follows: IgG Saline (n=4), (b) Ly6G Saline (n=4), (c) IgG BLM (n=9) and (d) Ly6G BLM (n=8). All P values were calculated using a one-way analysis of variance (ANOVA) ns $p>0.05$; * $p<0.05$.

4.2.8.10 MSD pro-inflammatory cytokine levels in IgG/Ly6G pre-treated bleomycin-injured C57Bl6 mice at day 21

Lung homogenate was prepared from lung lobes as previously with other bleomycin endpoints for analysis for multiple pro-inflammatory analytes using an MSD format (Figure 4.32). Due to time point assessed cytokine levels were low but still detectable. At this day 21 endpoint BLM groups had slightly elevated levels of IL-1β cytokine (Figure 4.32 (a)) which increased from 1.83±0.1156 pg/ml to 5.278±0.8865 pg/ml ($p>0.05$) with injury to control IgG antibody mini-pump mice. FPR1KO mice had a similar response to injury rising from mean level of 2.321±0.2493 pg/ml to 4.466±1.364 pg/ml ($p>0.05$).

Monocyte chemotactic peptide-1 (MCP-1) was another analyte measured by the MSD plate (Figure 4.32 (b)). WT mice, regardless of pre-treatment with IgG/Ly6G antibodies (Day -2) and saline/bleomycin dosing at day 0, exhibited consistent levels of MCP-1 in their lung homogenates ($p>0.05$). The absence of MCP-1 cytokine upregulation is probably due to the endpoint based in the fibrotic phase in which inflammation is completed.

Chemokine (C-X-C motif) ligand 1 (CXCL1) or Keratinocyte chemoattractant (KC) was secreted by mice in this study in low quantities (Figure 4.32 (c)). Apart from one outlier in Ly6G BLM group all mice secreted low basal levels of cytokine in each study group with no differences determined ($p>0.05$).

Interleukin-6 (IL-6) demonstrated a significant elevation from 7.123±2.658 pg/ml to 22.77±3.02 pg/ml ($p<0.01$) in control IgG pre-treated mice from saline to bleomycin groups respectively. Ly6G pre-treated groups did not elicit a significant response with a reduced 11.42±1.973 pg/ml IL-6 level in Ly6G-BLM group compared with IgG-BLM control injury group ($p<0.05$). The secretion of IL-6 is sustained in this study at day 21 and loss of neutrophils with Ly6G-mediated depletion appeared to directly affect this process (Figure 4.32 (d)).

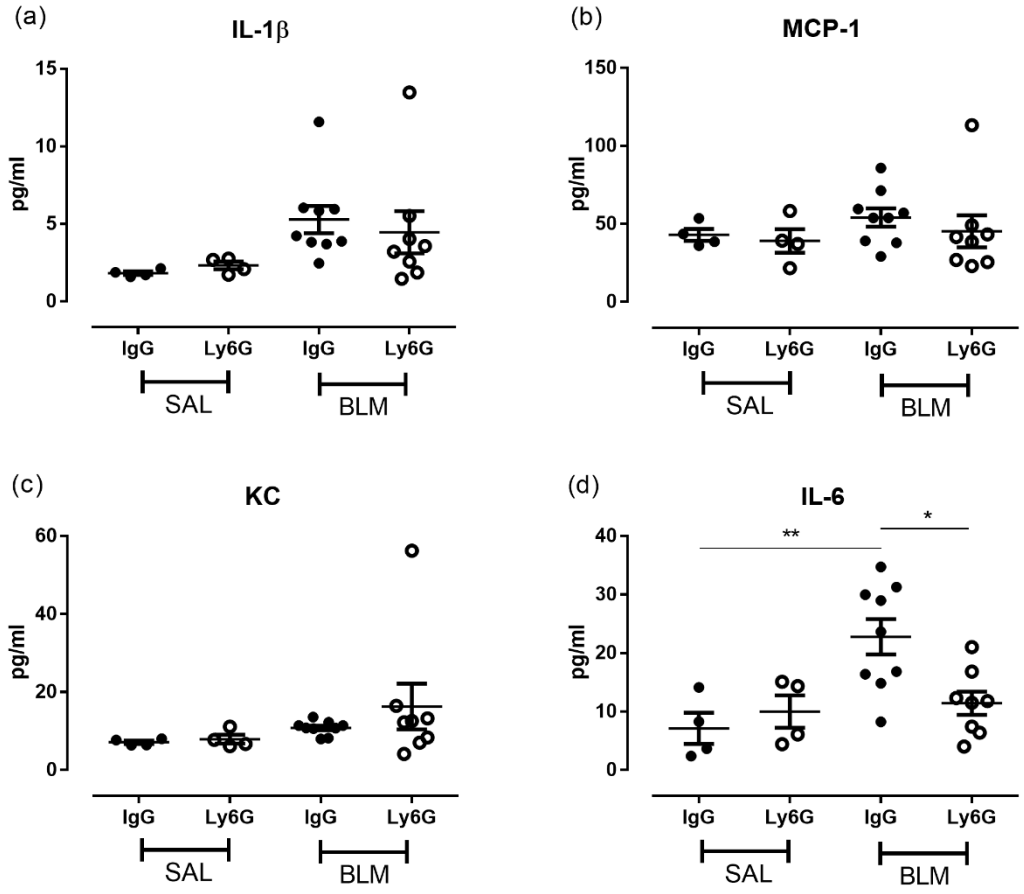

Figure 4.32: Inflammatory mediator levels in lung homogenate in Ly6G-neutrophil depleted mice harvested at 21 days post-bleomycin. Lung homogenate from IgG Saline (n=4), Ly6G Saline (n=4), IgG BLM (n=9) and Ly6G BLM (n=8) groups were assayed by MSD. Results are expressed as a mean reading from duplicate wells displaying SEM. All P values were calculated using a one-way analysis of variance (ANOVA) ** $p<0.01$; *$p<0.05$; ns $p>0.05$.

4.2.9 24 hour BLM-injured mice and determination of effect on PMNs at response peak

4.2.9.1 Hypothesis

At 24 hours post-bleomycin injury the inflammatory response in terms of immune cell recruitment to sites of damage will be at its peak.

4.2.9.2 Aims

A minimal immune cell profile was demonstrated at day 5 therefore a shorter endpoint was used in order to potentially determine a peak response with respect to neutrophils and the inflammation phase. 24 hours was used as neutrophils are the first wave of the innate immune response so upon treatment with bleomycin these cells will be the first to localise to the site of injury and due to their short lived nature.

4.2.9.3 Rationale

By evaluation of the different immune cells via differential cell counts of BAL cytospins and distinct cellular markers: CD68, NIMP and CD3 immunohistochemistry there will be evidence as to whether a bleomycin response is occurring after 24 hours post i.t. and whether this is greater than at later endpoints within the acute inflammatory phase of the bleomycin-injury model.

4.2.9.4 Immunohistochemistry of immune cellular markers in FFPE tissue sections

NIMP+ staining by IHC revealed relatively low numbers of granulocytes at day 1 (Figure 4.33). Between WT SAL and WT BLM groups a slight increase from a mean count of 6.910±1.731 cells/field to 9.725±1.437 cells/field respectively ($p>0.05$). KO control saline group and bleomycin-treated displayed a marked reduction in NIMP+ cells compared to wild type mice. KO BLM group had an average count of 3.212±0.8461 cells/field demonstrating significant reduction compared to bleomycin-treated WT mice ($p<0.01$).

CD68 positive cells were clearly elevated with bleomycin administration in WT mice (Figure 4.34). WT SAL group mean count was increased from 6.68±1.834 cells/field to 15.52±1.157 cells/field with acute injury at day 0 ($p<0.001$). This response was blunted in the KO groups with no significant increase between saline and bleomycin injured

mice (p>0.05). In terms of cell population proportion macrophages are the major cell type upregulated in the inflammatory infiltrate 24 hours post injury rather neutrophils as previously assumed.

Lymphocyte staining with anti-CD3 (Figure 4.35) showed no difference in the number of T-cells per high power field between treatments or genotype (p>0.05). This endpoint appears to be premature for T-cell infiltration into the lung microenvironment following acute injury.

4.2.9.5 BAL cytospin differential cell counts

Differential cell counts of cell populations present in BALF were typically predominantly macrophages with no difference between groups (Fig 4.36). Macrophage levels remained consistent across the different groups exhibiting no change (p>0.05). No significant increase or decrease in percentage eosinophils/lymphocytes relative to total cell count (cells $x10^5$/ml) was calculated. Neutrophils showed no significant change in count at this endpoint (p>0.05).

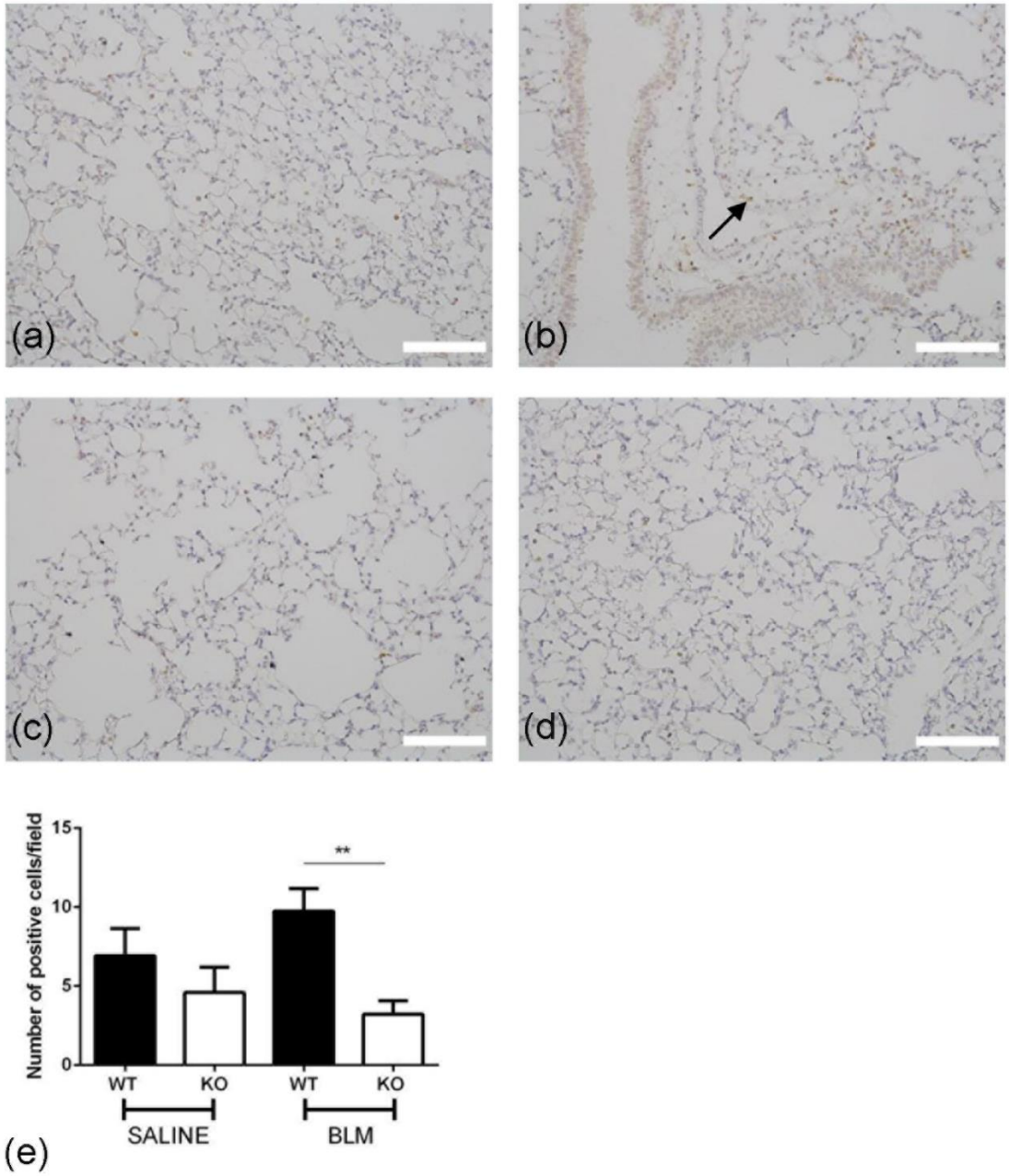

Figure 4.33: Neutrophil infiltration of bleomycin-injured lungs 24 hours post i.t. FFPE sections were stained indirectly for NIMP via IHC and positive cells per high power field were calculated (x20 magnification). (a) WT SAL (n=5), (b) WT BLM (n=12), (c) KO SAL (n=4) and (d) KO BLM (n=8) sections were analysed for positive cells. Results are expressed as (e) mean cells/field (hpf) ±SEM. Scale bars represent 100µm. Results were analysed by one-way ANOVA ** $p<0.01$.

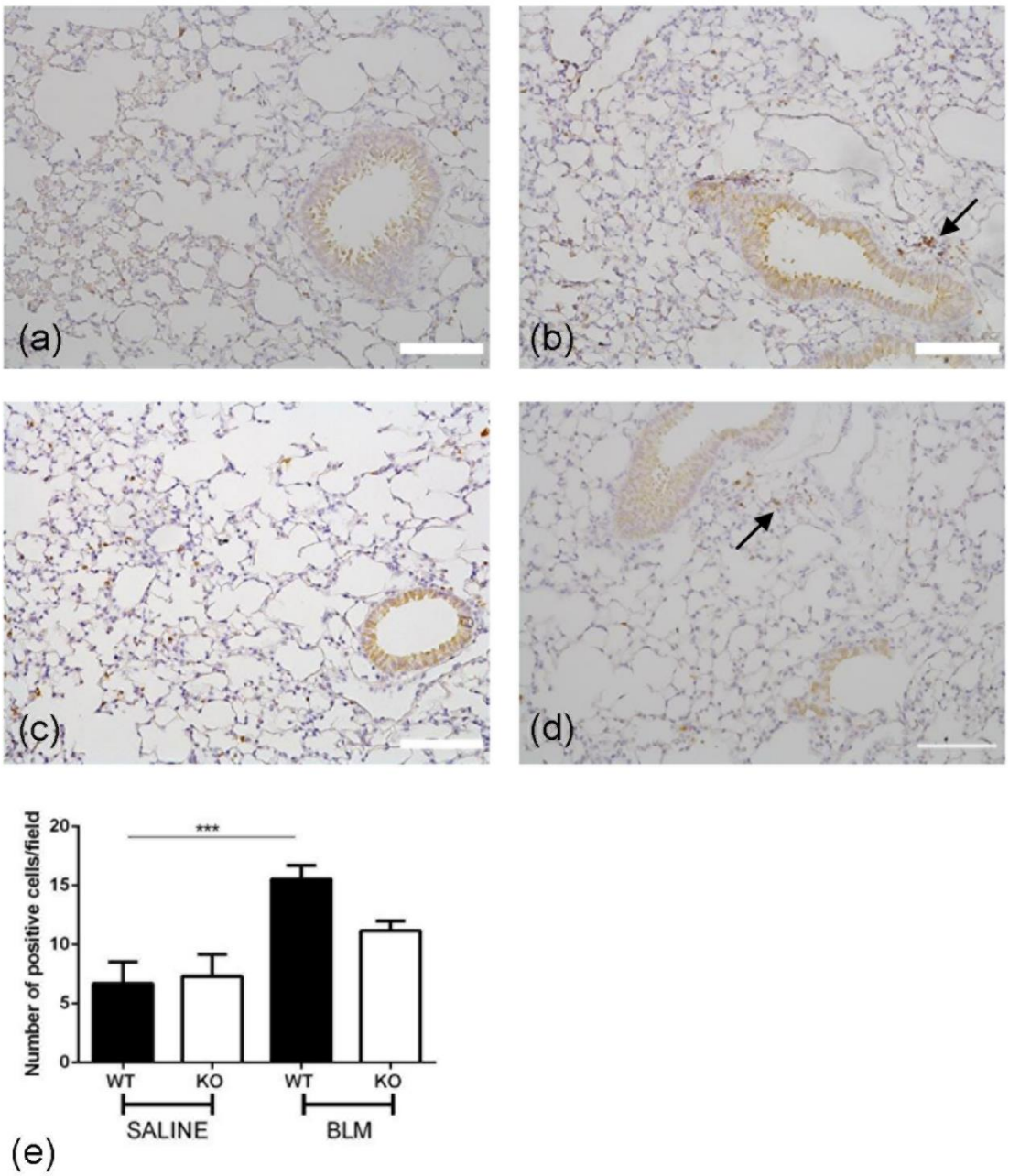

Figure 4.34: Macrophage infiltration of bleomycin-injured lungs 24 hours post i.t. FFPE sections were stained indirectly for CD68 via IHC and positive cells per high power field were calculated (x20 magnification). (a) WT SAL (n=5), (b) WT BLM (n=12), (c) KO SAL (n=4) and (d) KO BLM (n=8) sections were analysed for positive cells. Results are expressed as (e) mean cells/field (hpf) ±SEM. Scale bars represent 100µm. Results were analysed by one-way ANOVA *** $p<0.001$.

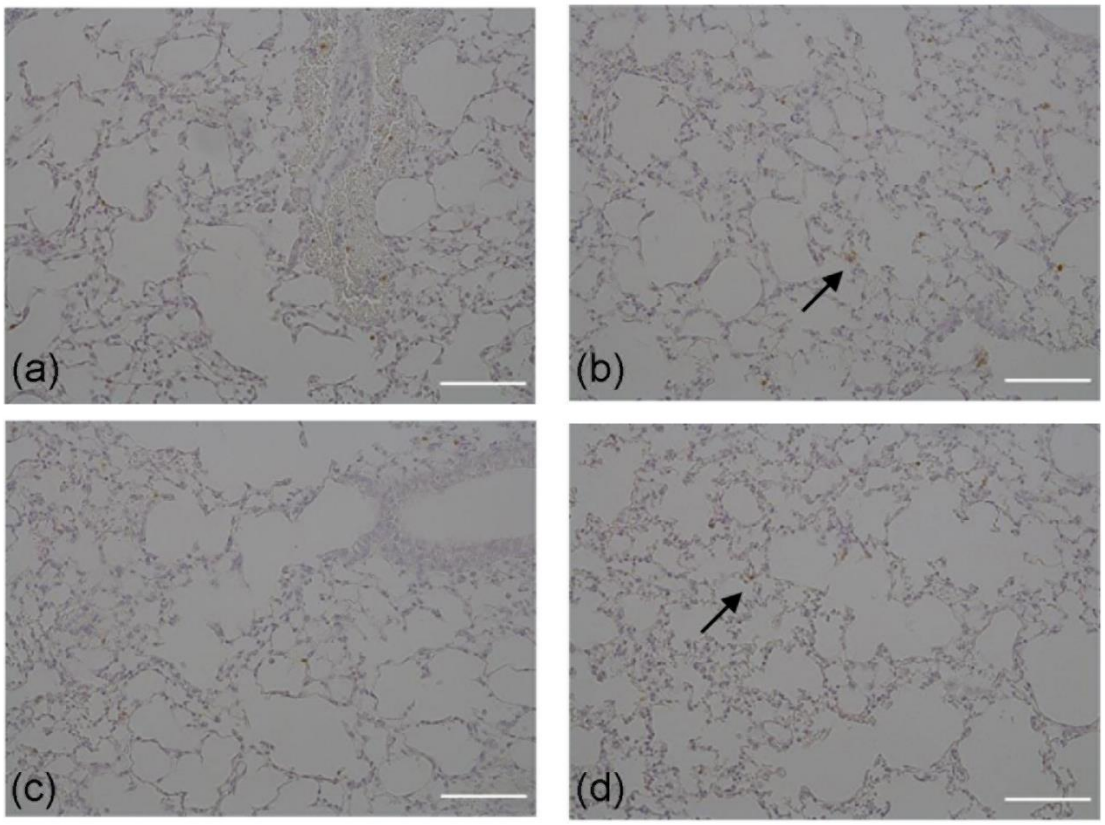

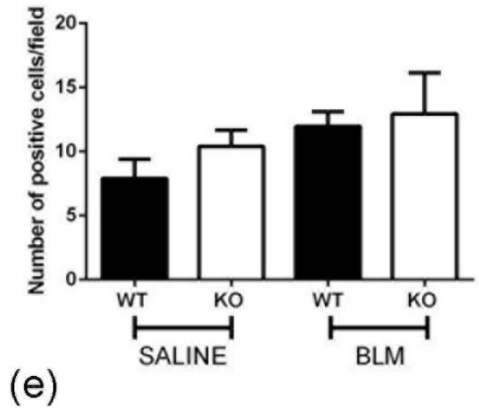

Figure 4.35: Lymphocyte infiltration of bleomycin-injured lungs 24 hours post i.t. FFPE sections were stained indirectly for CD3 via IHC and positive cells per high power field were calculated (x20 magnification). (a) WT SAL (n=5), (b) WT BLM (n=12), (c) KO SAL (n=4) and (d) KO BLM (n=8) were analysed for positive cells. Results are expressed as (e) mean cells/field (hpf) ±SEM. Scale bars represent 100µm. Results were analysed by one-way ANOVA ns $p>0.05$.

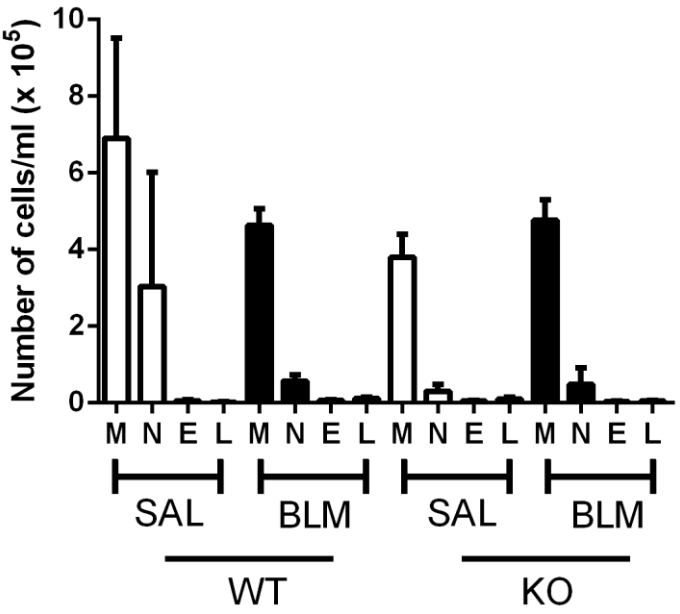

Figure 4.36: Differential cell count of BAL cytospins prepared from 24 hour bleomycin/saline treated c57bl6 WT and FPR1 KO mice. Macrophages, neutrophils, eosinophils and lymphocytes were counted on BAL cytospins in a blinded fashion and percentages were calculated once ~300 cells were counted. Groups were as follows: (a) WT SAL (n=5), (b) WT BLM (n=12), (c) KO SAL (n=4) and (d) KO BLM (n=8). All P values were calculated using a one-way analysis of variance (ANOVA) ns $p>0.05$.

4.2.9.6 BAL TGF-β1 level as a measure of injury response

Total cytokine level (pg/ml) was measured by duoset ELISA (R&D) in BAL samples harvested from each animal 24 hours post-i.t. (Figure 4.37). Elevations in level were observed in both WT and KO groups from saline to bleomycin treatments but these responses were non-significant ($p>0.05$). At this stage in the inflammatory phase is commencing with macrophage infiltration into the injured area starting, during the acute phase initiation of fibrogenesis occurs with accumulation of TGF-β1. After 24 hours there is not a dramatic increase in fibrogenic cytokine levels suggesting that further accumulation is required in order for a significant TGF-β1.

4.2.9.7 Inflammatory cytokine profile determined by multiplex MSD analysis

As with the other endpoints of 5 and 21 days lung homogenate was prepared from the large lobes harvested from mice (WT and KO) treated with saline/bleomycin. Samples were run on sensitive MSD plates pre-coated with multiple antibodies for detection of multiple analytes: IL-1β, MCP-1, KC and IL-6; a selection of pro-inflammatory cytokines known to upregulated with bleomycin injury. As shown in Figure 4.38 the levels of these analytes did not change with injury or genotype ($p>0.05$). Probably by day 5, in which a clear response was shown, accumulation of cytokines has occurred due to prolonged secretion by infiltrating immune cells which at day 1 are only commencing their response to injury.

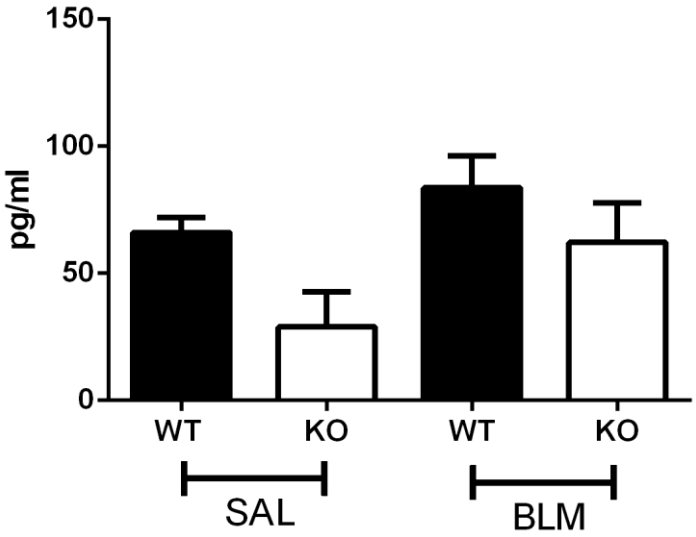

Figure 4.37: TGF-β1 cytokine release 24 hours post—bleomycin injury. Levels of TGFβ1 in saline/bleomycin treated WT/KO mice assayed in BAL fluid via an indirect ELISA in different groups of mice as follows: WT SAL (n=5), (b) WT BLM (n=12), (c) KO SAL (n=4) and (d) KO BLM (n=8). Mean pg/ml was generated from duplicate wells±SEM by linear regression against a standard curve. All P values were calculated using a one-way analysis of variance (ANOVA) ns $p>0.05$.

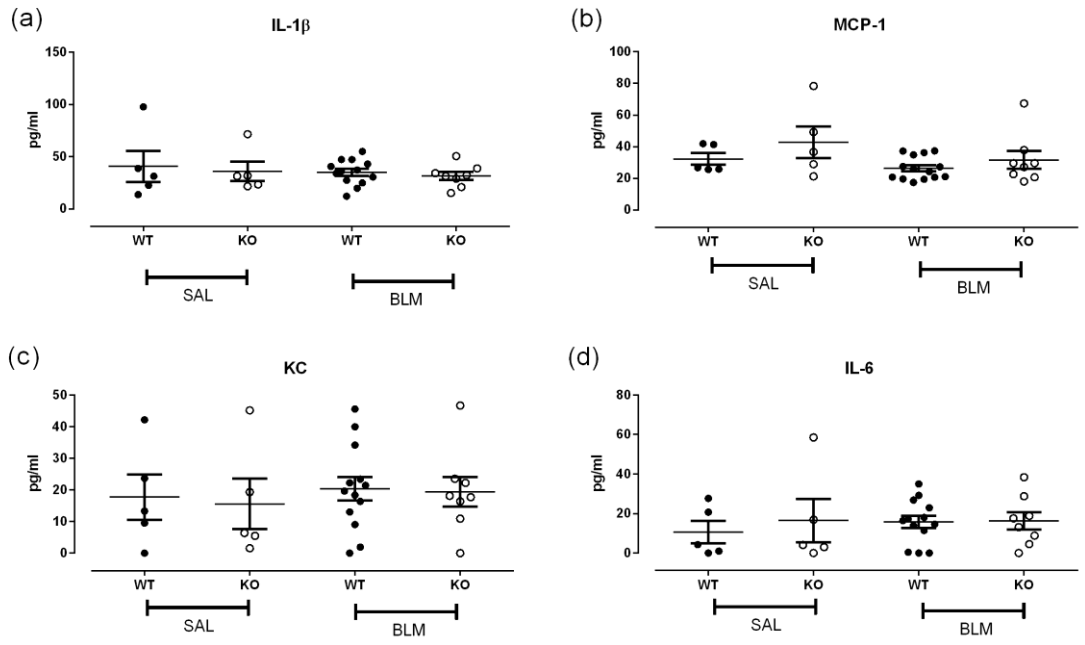

Figure 4.38: Chemokine/cytokine secreted levels in lung homogenate of 24 hour saline/bleomycin-treated mice. Multiplex ELISA using Mesoscale Discovery (MSD) platform analysing (a) Interleukin-1β (IL-1β), (b) Monocyte Chemoattractant Peptide-1 (MCP-1), (c) KC (chemokine (C-X-C motif) ligand 1; CXCL1) and (d) Interleukin-6 (IL-6) levels in lung homogenate prepared from right lobes except post-caval. Results are expressed as a mean reading (from duplicate wells) SEM (WT SAL, n=4; KO SAL, n=4; WT BLM, n=7; KO BLM, n=8). All P values were calculated using a one-way analysis of variance (ANOVA) ns $p>0.05$.

4.2.9.8 Oropharyngeal administration as an alternative method to bleomycin treatment

For reproduction of the model carried out at MedImmune (Cambridge) a different method of delivery was investigated. The oropharyngeal (OA) route has been shown previously in lung injury models to be a viable way of administrating drug agents. To determine which the optimal method for bleomycin administration was routes were researched. Among other drug the OA method has been utilised previously for bleomycin instillation (Lakatos *et al*., 2006). Consequently, the OA route was investigated at time points of 24, 48 and 72 hours were utilised to gauge initial acute injury and the inflammatory profile associated with this model. Evaluation of these early time points would give the best indication of an inflammatory response to the bleomycin injury if delivery was successfully achieved.

4.2.9.8.1 Differential cell counts at acute time points for assessment of neutrophilia

Determination of bronchoalveolar lavage (BAL) immune cell profiles (Figure 4.39) was key in identifying the success of this model. In all three time points macrophages were the major component of the BALF cellular profile, all above 90% of the total cell count. Neutrophils were elevated in (a) 24 hours post-bleomycin administration to approximately 5.634% ($p<0.05$) which subsequently reduced (b) 48 hours post-bleomycin (2.37%; $p>0.05$) and reduced to 0% after (c) 72 hours. The other immune cells (eosinophils and lymphocytes) showed minimal responsiveness to control saline and bleomycin treatment via this method.

4.2.9.8.2 Gene expression at acute bleomycin endpoints

Gene expression was assessed at 24, 48 and 72 hours post-bleomycin instillation via quantitative real-time PCR (Figure 4.40). S100A9 expression (a) increased at 24 hours post-instillation from a mean fold change 2.909 to 7.848 comparing saline control and bleomycin-treated mice respectively. By 48 hours and 72 hours expression of this myeloid marker decreased to baseline levels (0.9172 and 1.642 mean fold change respectively) suggesting a peak response within 24 hours. Interleukin-6 (IL-6) cytokine mRNA levels (b) at the respective endpoints demonstrated increases at 24 hours (1.123 to 6.971 mean fold change), 48 hours (0.5326 to 7.439 mean fold change) and 72 hours (6.767 to 20.33 mean fold change) when comparing saline and bleomycin-

treated mice. Results indicate a cumulative secretory effect as levels appear to increase over the 3 days. KC, mouse equivalent of human IL-8 (c) shows no increase at 24 or 48 hours post-bleomycin instillation between control or bleomycin groups. At 72 hours KC levels increase in both controls and bleomycin groups with no significant difference.

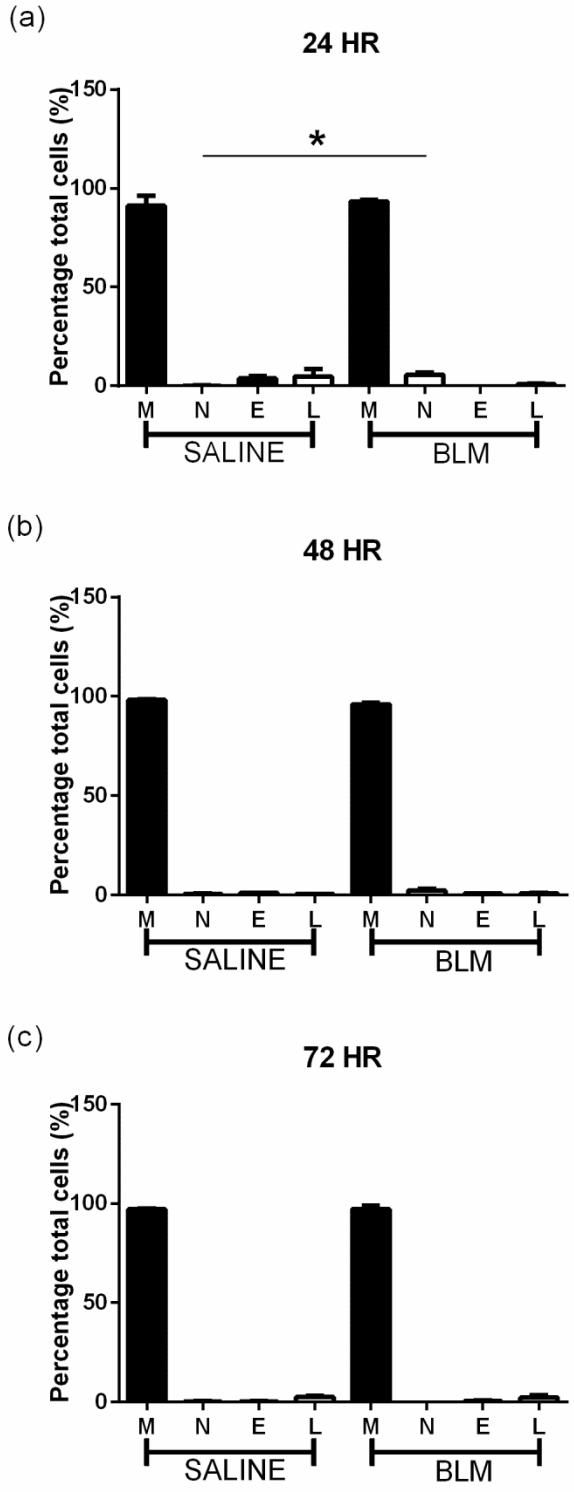

Figure 4.39: BAL cytospin differential cell counts at acute timepoints post-OA saline/bleomycin treatment. (a) 24 hours (n=3), (b) 48 hours (n=3) and (c) 72 hours (n=3) post injury/control treatment total macrophages (M), neutrophils (N), eosinophils (E) and lymphocytes (L) were counted. Percentage of total cells (approximately 300 cells and mean values for each group were calculated. For statistical significance unpaired t-tests were performed. ns $p>0.05$.

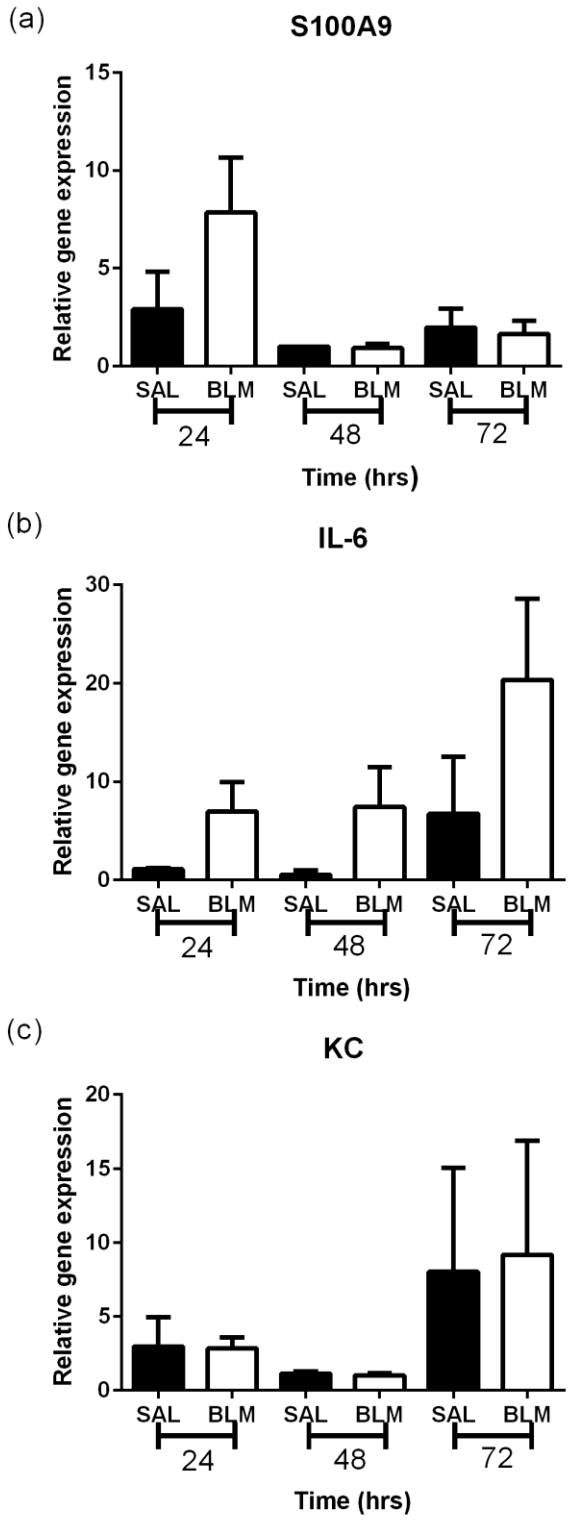

Figure 4.40: Gene expression of pro-inflammatory markers at 24, 48 and 72 hours post-OA saline/bleomycin treatment. mRNA levels of (a) S100A9, (b) IL-6 and (c) KC were determined by real-time PCR with GAPDH used as a housekeeping gene and expression normalised to control group (saline). n=3 per group at each time point. For statistical significance a one-way analysis of variance (ANOVA) was performed. ns, $p>0.05$.

4.2.10 Bone marrow chimera generation to determine cells responsible for FPR knockout protective effect

4.2.10.1 Hypothesis

Cells of non-phagocyte origin have an effect on the pathogenesis of bleomycin-mediated pulmonary fibrosis as well as neutrophils and other immune cells.

4.2.10.2 Aims

Utilisation of a bone marrow chimera model was employed to determine the role of architectural cells such as epithelium and fibroblasts as well as bone-marrow derived immune cells in the bleomycin-induced pulmonary fibrosis model. Another aim of this study was to find out whether the protective effect found at 21 days post-bleomycin treatment is conserved in bone marrow-reconstituted mice.

After donor harvesting irradiated recipient mice were IV injected with 1 x 10^7 cells per bone marrow suspension corresponding to the following groups:

Group 1 - WT recipient – WT donor bone marrow
Group 2 - WT recipient – KO donor bone marrow
Group 3 - KO recipient – WT donor marrow
Group 4 - KO recipient – KO donor marrow

4.2.10.3 Rationale

Irradiation of the bone-marrow derived component of the immune system was necessary to build upon previous studies which demonstrated a protective effect against lung fibrosis with ablation of *mfpr1* gene. FACs analysis of the inflammatory infiltrate showed little change in difference cell populations, apart from macrophage M1/M2 balance, potentially indicating a role for FPR1 expression on architectural cells in the bleomycin model.

As the principal location for stem cells production bone marrow is the hub for controlling the immune system. Haematopoiesis is the process by which immune cells are differentiated from haematopoietic stem cells to form distinct cell populations. Two distinct lineages are derived from these precursor cells: lymphoid and myeloid which subsequently differentiate into T-cell subsets: CD4, CD8, NK cells, B-lymphocytes and

myeloid populations such as neutrophils, macrophages, eosinophils, basophils, platelets and erythrocytes respectively.

Neutrophils are short-lived, hence their rapid circulation and clearance. Mature neutrophils are divided into two main subsets upon granulopoiesis from myeloid granulocyte precursors: circulating (1-2%) and marginated. This enables an efficient innate immune system response to damage and infection and due to neutrophil high turnover rate (up to 2^{11} cells per 24 hours in healthy adults) adaptive immunity is rapidly attained. The bone marrow is in essence the site of birth and death of the neutrophil with a majority of mobilisation occurring there as well clearance (Zhao *et al*., 2011; Casanova *et al*., 2013; Manz and Boettcher, 2014). The nature of neutrophils and their production has proved an integral part of the project's bleomycin investigations due to their role in both innate and adaptive immune responses which are intrinsically linked to this model.

4.2.10.4 Observations throughout chimera experiment including reconstitution and bleomycin administration

Over the course of the bone marrow depletion and reconstitution with donor cells from either wild type or knockout mice a number of observations were recorded over the 7 week period before bleomycin treatment. Donor leg bones yielded a high number of cells which was optimal for the experiment as this made successful reconstitution of the recipient's bone marrow significantly more probable. Irradiated mice typically display several signs of sickness as the procedure is severe affecting their bodies in a widespread, systemic fashion. During reconstitution the immune system is essentially immunocompromised/deficient so mice were supplied with antibiotic-treated water (Baytril) throughout to reduce/eliminate chances of opportunistic infection. The procedure is also typically associated with weight loss but some of the chimeric groups lost up to 20% (within project licence parameters), possibly due to complicating factors arising from the irradiation procedure.

Following bone marrow transplantation all mice lost weight with most recovering over time. However, over the course of the re-formatting of the immune system multiple mice were found dead or required culling due to internal bleeding and some instances of severe bleeding subcutaneously. Apparently, a number of mice developed clotting

defects after irradiation and donor cell injection. Characteristically of a chimera experiment several mice exhibited hair loss and greying of the remainder due to action of the radiation on hair follicles. Also noted was the appearance of dry skin around neck, head and shoulders not specifically in any group/genotype/gender. In particular cases this problem was associated with obvious skin inflammation typified by skin reddening and discharge. In cases of severe skin inflammation mice were treated with green clay (n=25) and claws were cut to reduce consequences of scratching.

Indeed in a small number of mice before onset of bleomycin administration skin inflammation were treated with subcutaneous dexamethasone steroid (2mg/kg; n=3) in conjunction with green clay to reduce the likelihood of a systemic inflammatory response which would have skewed the fibrotic endpoint. All groups were also switched to corn cob bedding and given soft nesting material to be less irritating on inflamed/sore skin.

In order to minimise the likelihood of excessive weight loss as a result of the irradiation procedure and the bleomycin treatment, mice were fed exclusively a diet gel (normal calorie). This was necessary in certain cases where mice exhibited broken and missing teeth. CBC and veterinary staff concluded that the radiation administered to the mice could had affected the way in which calcium is incorporated into the teeth as they grew affecting the overall strength.

From the point of bleomycin administration to the endpoint 21 days weights were taken for each mouse daily. The lack of weight loss observed in FPR1KO mice with previous bleomycin studies was not observed in this chimera experiment. No difference was apparent between any of the groups, some saline-treated animals lost as much or more weight than bleomycin-treated mice, probably due to irradiation background effects (Figure 4.41).

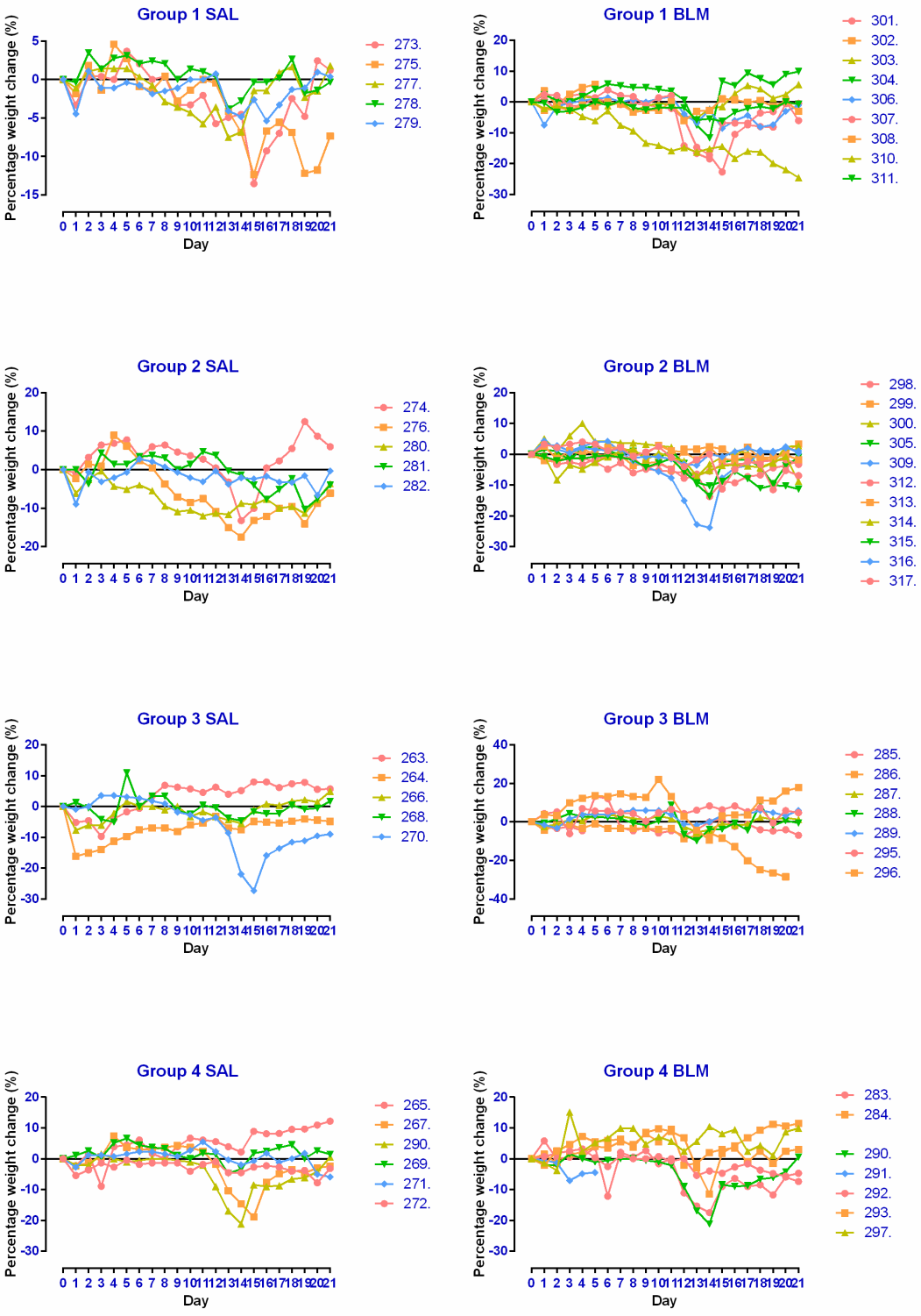

Figure 4.41: Weight percentage gain/loss post-bleomycin injury to different chimera groups. Treatment groups were as follows: 1-4 SAL (n=5 per group) and 1-4 BLM with different chimeric groups. Bleomycin-injured chimera groups were as follows: 1- WT-WT (n=8); 2- WT-KO (n=11); 3- KO-WT (n=6); 4- KO-KO (n=7). Percentage weight gain/loss calculated from original starting weight prior to bleomycin instillation.

4.2.10.5 Analysis of pulmonary fibrosis via PSR and alpha-SMA staining of bone marrow chimera FFPE tissue sections

Sirius red percentage area stained of paraffin-embedded lung tissue (Figure 4.42 (a)) demonstrated no significant increase between saline and bleomycin groups although there was a perceptible rise in collagen deposited between group 1 saline mean 6.84±1.199 % and group 1 BLM mean 8.65±1.206 % ($p>0.05$). Between respective bleomycin-treated chimeric groups there were demonstrable reductions in PSR staining. Groups 2 (WT recipient with KO donor) mean of 5.336±0.4731 % and Group 4 (KO recipient – KO donor) mean of 4.157±0.3301 % displayed significantly reduced levels compared to Group 1 (WT recipient WT donor; $p<0.05$ and $p<0.01$ respectively). Homogeneous chimeras showed the greatest difference in percentage area.

Alpha-SMA immunohistochemistry (Figure 4.42 (b)) stained displayed a similar pattern/trend with elevated percentage area in Group 1 bleomycin-treated chimeras over saline controls (non-significant). Alpha-SMA immunohistochemistry resulted in low levels of percentage area stained but a maximal response was only evident in bleomycin-treated Group 1 (WT recipient- WT donor; mean of 4.15±0.6641 %) compared to its respective saline control mean of 2.74±0.3295 % ($p>0.05$).

Hydroxyproline (total collagen content) assay (Figure 4.43) showed no clear differences between saline and bleomycin-treated mice in any of the chimeric groups regardless of genotype or recipient/donor mixture ($p>0.05$). This may be due to incomplete hydrolysis of samples but this seems unlikely. The problem is probably due to the nature of the model, potentially indicating the unsuitability of the bleomycin pulmonary fibrosis model in irradiated chimera mice.

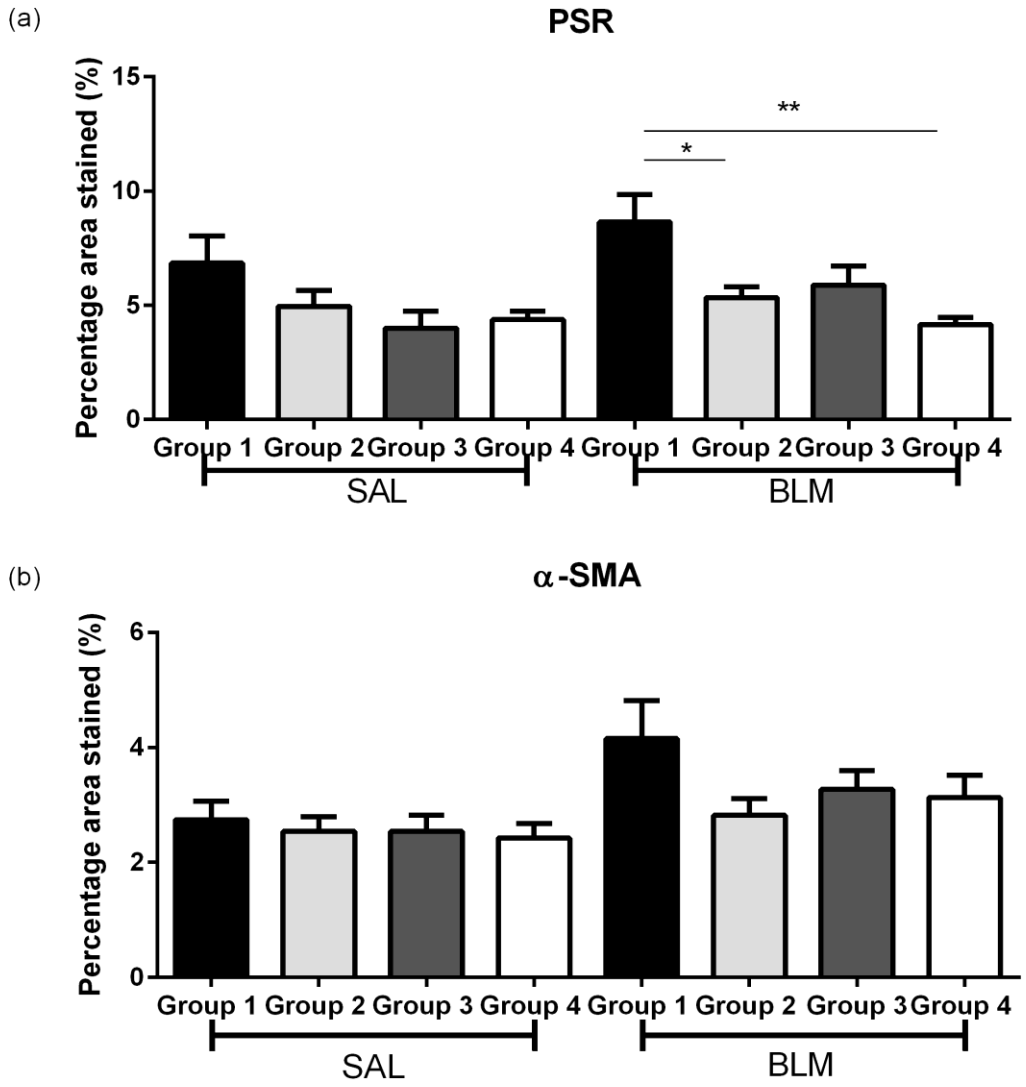

Figure 4.42: ECM production in chimera lung injured with bleomycin. Sections stained with PSR (a) for collagens I/III. (b) α-SMA production and results calculated as mean percentage area stained for different groups; 1-4 SAL (n=5 per group) and 1-4 BLM. Bleomycin-injured chimera groups were as follows: 1- WT-WT (n=8); 2- WT-KO (n=11); 3- KO-WT (n=6); 4- KO-KO (n=7). All p values calculated with Prism 5.0 software and analysed by a one-way ANOVA ns $p>0.05$.; * $p<0.05$. Relative photographs displayed in appendix B (i-ii).

4.2.10.6 Immune cell counts in chimera mice

Immunohistochemistry for markers of different immune cells was carried out to determine the tissue infiltrate in the chimeric mice (Figure 4.44 (a-b)). CD68+ (macrophage/monocyte marker) population showed relatively similar levels in FFPE tissue with a slight increase in the WT-WT chimera group, mean of 45.98±6.645 cells/field, over its saline control (mean cells 33.45±3.555/field) and the other groups' treatments ($p>0.05$).

NIMP (neutrophil marker) staining showed, to an extent, differing levels of neutrophil infiltration. Higher numbers than expected were observed at 21 days in this chimera experiment. Increased cells per high power field were demonstrated between saline and bleomycin-treated mice of groups 1 and 2 although not to significance ($p>0.05$). Levels in groups 3 and 4 remained at a consistent level with no change in neutrophil localisation in the tissue.

4.2.10.7 Total cell counts in bronchoalveolar lavage (BAL) fluid following bleomycin injury in chimera mice

BAL total cell counts performed for each group and their treatments showed the proportions of cell populations in the extracellular fluid within the pulmonary microenvironment (Figure 4.45). There was a clear increase in the BAL total cell count with bleomycin administration of Group 1 chimeric mice from a mean cells/ml 2.26±0.3381 increasing significantly to mean of 8.15±1.161 $x10^5$ cells/ml ($p<0.001$). In bleomycin-treated chimera groups there were significant reductions ($p<0.01$) when comparing group 1 (WT-WT) to the other donor-recipient groups possibly indicating that this group was the only chimeric combination that mounted a response to bleomycin.

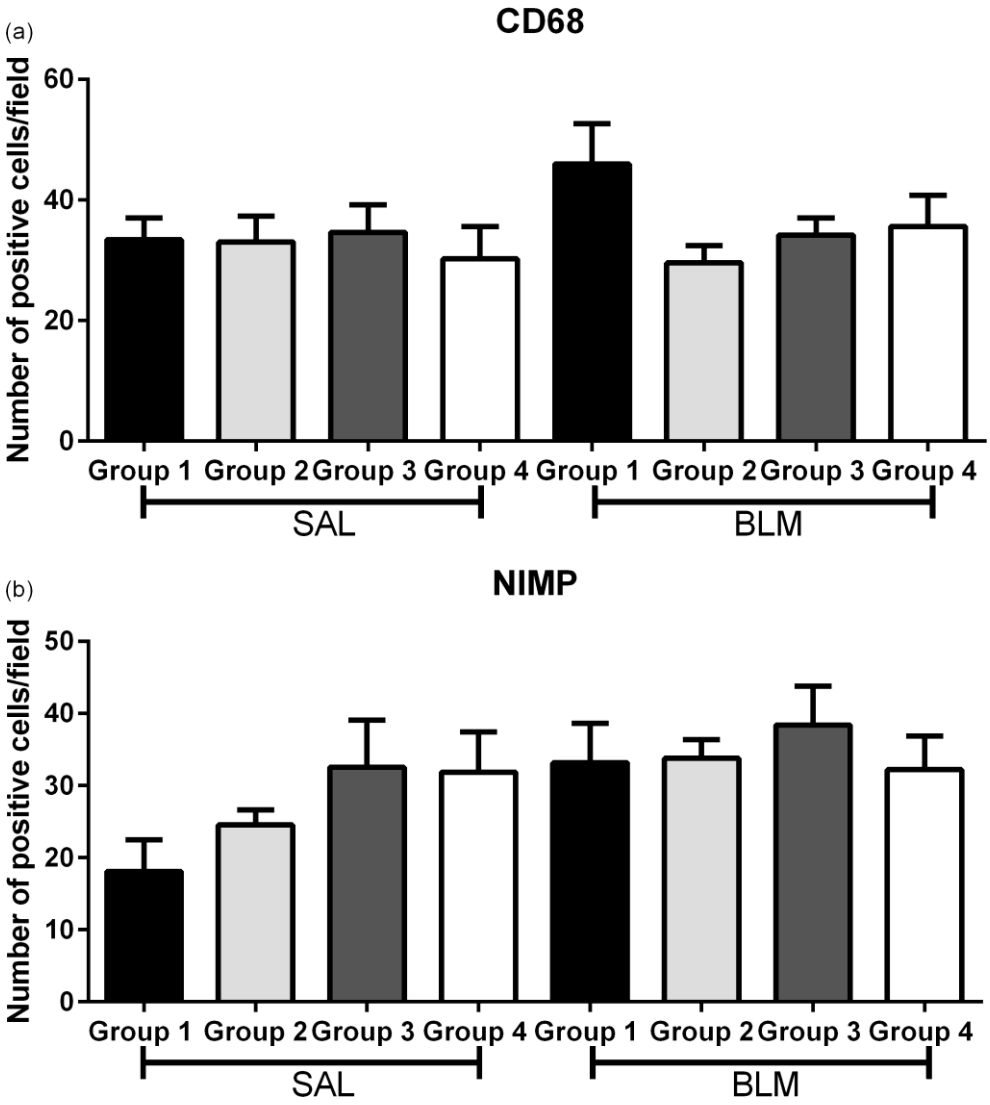

Figure 4.43: Immune cell counts of chimera lung injured with bleomycin. Sections stained with (a) CD68 for macrophages and (b) NIMP for neutrophils and results calculated as mean cells/high power field (hpf); 1-4 SAL (n=5 per group) and 1-4 BLM. Bleomycin-injured chimera groups were as follows: 1- WT-WT (n=8); 2- WT-KO (n=11); 3- KO-WT (n=6); 4- KO-KO (n=7). All p values calculated with Prism 5.0 software and analysed by one-way ANOVA * $p<0.05$. Relative photographs displayed in appendix B (iii-iv).

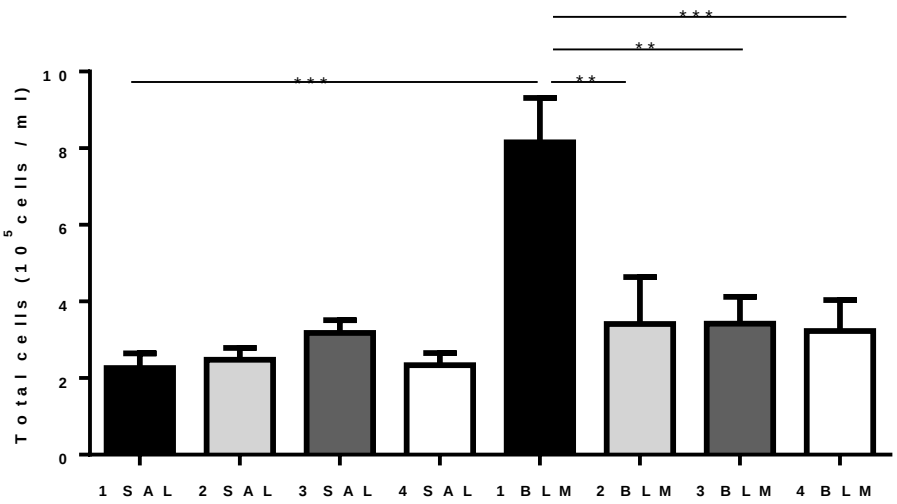

Figure 4.44: Total BAL cell counts from bone marrow chimera bleomycin-treated WT/KO mice. Total cell counts represented by cells/ml±SEM. Treatment groups were as follows: 1-4 SAL (n=5 per group) and 1-4 BLM with different chimeric groups. Bleomycin-injured chimera groups were as follows: 1- WT-WT (n=8); 2- WT-KO (n=11); 3- KO-WT (n=6); 4- KO-KO (n=7). All p values were calculated using a one-way analysis of variance (ANOVA). ns $p>0.05$, ** $p<0.01$, ***$p<0.001$.

4.2.11 Conclusion of findings

4.2.11.1 Bleomycin-injury induced pulmonary fibrosis and effect of FPR deletion

The *in vivo* model for investigating pulmonary fibrosis is limited due to the nature of its pathogenesis (acute and fibrotic). Features observed during studies involving bleomycin are facets/caveats of the model itself not necessarily the disease it is purposed to mimic. The distinct phases of the bleomycin model: acute and fibrotic are unlike the pathogenesis of IPF presented in the literature. Lung fibrosis is not an acute process but in a way this an advantage of the *in vivo* model as fibrosis is able to develop in a matter of weeks not months or years as is typically the case in human patients. Some individuals are genetically predisposed to ILD development or some have moderate lung function then an exacerbating effect like a virus or opportunistic infection comes along and the conditions worsens. Human fibrotic disease is far more complicated than the pathogenesis of different *in vivo* models but the nature of these short-term manifestations of disease makes them ideal for therapeutic agent development in a high-throughput fashion.

Due to its already characterised role on immune cells as a chemoattractant receptor (Zhang *et al*., 2010) the loss of the FPR gene would be expected to alter inflammation. The blunting of the inflammatory cytokine profile at day 5 fits with FPR's role in the migration of neutrophils and also macrophages to sites of damage. Without a normal inflammatory response being mounted through decreased secretion of IL-6, MCP-1, IL-1β and KC, the acute injury phase of the bleomycin is dampening affecting downstream events in the pathogenesis due to the intrinsic linking to the development of the fibrotic phase. The dysfunctional response equates to protection against the formation of fibrotic scar tissue as determined by histology and extracellular matrix (ECM) production after 21 days. Ablation of the FPR1 in mice has been revealed to be of importance in a cigarette-smoke extract (CS) based model lung emphysema showing a role for this receptor for inflammation in the lung mediated by neutrophils (Cardini *et al*., 2012).

Previously, FPR's role in pulmonary inflammation has been determined in terms of a cigarette-smoke (CS) extract-based emphysema model involving similar knockout mice. Cardini *et al.* (2012) showed reduced infiltration by neutrophils and macrophages with FPR deletion implicating it as a key player in inflammation and tracking of immune

cells to damage sites. Typically pulmonary fibrosis, in particular IPF, is not regarded as an inflammatory condition where repeated insults and damage propagate fibrogenesis and an aberrant wound-healing response. In this respect the bleomycin model differs significantly as it relies on an acute injury driving the entire process.

To determine the role of FPR on fibrosis more pulmonary fibrosis models would need to be utilised preferably with a pathogenesis that does not rely on directed inflammation in response to targeted injury by chemical agents (bleomycin or FITC). A TGF-β adenoviral overexpression method develops in a significantly different manner and would strengthen whether or not this receptor is a player in fibrosis disease mechanism. The use of this model could indeed be related to findings from the bleomycin studies. At day 5 during the acute phase of inflammation, fibrogenesis is beginning to occur and TGF-β1 cytokine is secreted. Of note was the fact that there was no difference in the BAL levels of this pro-fibrogenic cytokine. Although the signal waned by day 21 in knockout mice, the onset of the wound-healing response appears to be TGF-β1 independent which may be of interest with regards to the adenovirus model employed by multiple research groups (Sime *et al.*, 1997; Murray *et al*., 2011).

In order to fully understand the role of the *fpr1* gene in pulmonary fibrosis, a different model (preferably non-inflammation driven) should be used. Without replication of the effect in a different model the effects determined with the bleomycin injury may only be model-dependent.

4.2.11.1.1 Neutrophils in the pathogenesis of the bleomycin model

Ly6G-positive neutrophils were successfully depleted by mini-pump administration of soluble antibody over defined periods in an acute or fibrotic bleomycin model. The continuous delivery of the antibodies is preferable to repeated injections on a daily basis with a reduced chance of mis-dosing due to the mini-pump's osmotic action. Proof of concept short-term study which depleted neutrophils 2 days prior to bleomycin injury displayed reduced NIMP positivity in FFPE sections and PMNs in BAL cytospins. Effectively neutrophils are being drastically reduced in depleting antibody treatments compared to control IgG mini-pumps which ultimately triggered a downstream effect on ECM deposition specifically collagen as indicated by PSR immunohistochemistry. Alpha-SMA, a key marker of activated myofibroblasts showed a similar pattern but did

not reach significance. One major limitation of this study was the fact that when hydroxyproline assay was performed to determine total lung collagen content no difference was detected between any of the treatments groups. This may be due to incomplete hydrolysis of tissue prior to the colorimetric assay.

Other things to consider when interpreting the mild/moderate effect seen in the mini-pump study in terms of ECM production may be due to dosage of bleomycin and the age of mice used. Typically mice were 6-8 weeks old with a mix of males and females depending on stock of mice available. Some groups have reported that male mice develop worse fibrosis in response to bleomycin compared to females. If groups were mixed, treatments groups were given an even spread of males/females in case there were any differences. Due to the nature of the Ly6G experiment with the surgical implantation of a mini-pump 2 days prior to intratracheal dosing other things may have been at play. The procedure itself could have caused inflammatory events and the antibodies themselves may have triggered a systemic response resulting in higher numbers of neutrophils responding to bleomycin injury in IgG controls. This may account for the increased NIMP positivity determined in the acute bleomycin mini-pump study compared to the traditional 1 day bleomycin study. The nature of the ALZET mini-pump system minimises animal interference, infection and systemic toxicity (Perkins *et al.*, 2008). The implantation and the securing of the installed mini-pumps may have played a role, animals are prone to scratch uncomfortable areas in particular surgery sites. This will potentially break the skin causing inflammation and the recruitment of immune cells in a systemic response which may account for higher numbers determined at acute time point.

Long-term effects of mini-pump installation are hard to gauge but may have had an effect on the overall fibrotic response with cells in an inflammatory state rather than initiating wound-healing and progression to a fibrotic phenotype. 21 days post-saline/bleomycin in IgG/Ly6G mini-pump WT mice a fibrotic reaction is occurring with increased collagen deposition as well as α-SMA production. Levels of the pro-fibrogenic cytokine TGF-β1 were elevated in control IgG group, lower than at day 5 endpoint (~20pg/ml) indicating fibrogenesis and the development of fibrosis. With the mild effect observed with IHC and no difference in lung collagen content it appears that a different endpoint should be utilised to investigate fibrosis, perhaps 28 days as fibrosis may not be fully developed at 21 days.

4.2.11.2 Flow cytometry-based approach for analysis of inflammatory infiltrate induced by bleomycin injury

Markers evaluated in FACs phenotyping experiment would need refining for precise determination of inflammatory infiltrate. The antibody panels for differing 'activation states' of macrophages yielded preliminary indications of macrophage phenotype present at the time points of 5 day and 21 days.

Specific M2 markers for alternatively activated macrophages are complicated by the presence of the distinct population of resident alveolar macrophages in the lung microenvironment. CD206, mannose receptor is both of subsets making it difficult to interpret whether a decrease in M2 macrophages is shown or simply a reduction in alveolar macrophage population. Previous findings at 21 days post-bleomycin injury demonstrated a protective effect upon ablation of the *fpr1* gene which may correlate with this reduction in macrophages. The use of another M2 marker, Found in inflammatory zone (FIZZ) 1 for staining of the lung digests strengthens the hypothesis that a reduction in M2 macrophages is responsible for the dampened fibrotic response.

FIZZ-1 has previously been demonstrated to be important in Th2 immune response implicated in trophic/tissue remodelling functions (Jones, 2013). Increases in alternatively activated macrophages as part of a Th2-mediated response to PLC-/- Trypanosoma brucei brucei infection have been characterised by FIZZ-1 expression. Clarification of its M2 marker status is somewhat cemented by further studies *in vitro* where IL-4/IL-13 treatment of peritoneal macrophages isolated from different transgenic mice species (BALB/c C57Bl/6) induced its expression (Chung *et al*., 2007). Polarisation by Colony-stimulating factor-1 (CSF-1) *in vivo* exhibits a similar effect in neonatal mice to the aforementioned *in vitro* experiments (Jones, 2013).

A key point to note is that FIZZ-1 is recognised as being produced by the bleomycin model (Liu *et al*., 2004) with some studies showing localisation to lung epithelium not macrophages in rat bleomycin-injured lung. IL-4/IL-13 induce lung FIZZ-1 expression on a wider scale than previously considered which may be a thing to consider when evaluating the macrophage marker FACs data from the present bleomycin study. Part of the experimental design for this study eliminated this doubt due to gating for

CD45+ve cell populations which would have excluded epithelial cells from the FACs analysis.

FIZZ-1 is a RELM-α – resistin-like molecule originating from the FIZZ/RELM family with itself and other family members (FIZZ2/RELM-β, FIZZ3/resistin, and RELM-γ) associated historically with allergic exacerbations in the lung in the context of asthma. This 9.4 kilodalton protein is intracellularly localised with a conserved 10 cysteine amino-acid motif with expression documented in asthma-associated inflammation. FIZZ-1 is expressed in macrophages, bronchial epithelium and type II alveolar epithelial cells (AECs) (Chung *et al*., 2007).

With regards to the inflammatory infiltrate the populations lung digests were determined showing little difference in immune cells apart from macrophages expressing M2 (alternatively activated) markers. Neutrophils (total and activated) and eosinophils displayed consistent low levels with respect to the repertoire of CD45+ leukocytes. Evaluation of the infiltrate in the tissue at day 5 implies that peak neutrophil population may have migrated to injury site prior to this. The innate immune response occurs typically in a short period after damage triggering downstream processes (Fafyatis and Farina, 2012). Investigation was required for the peak immune response to be determined as low levels of infiltration were evident at day 5, even with accumulation of secreted inflammatory cytokines. Harvesting of animals 24 hours post-injury/saline instillation allowed further evaluation of acute phase of bleomycin model. Indeed more neutrophils and macrophages were infiltrating the lung tissue post-bleomycin and a reduced response was clear in knockout mice. A less developed pro-inflammatory cytokine response was evident at this earlier endpoint than at 5 days.

CD4+ lymphocytes showed increased infiltration to the lung 21 days post-bleomycin in wildtype mice with a reduced response in knockout group. Due to FPR's status as a major chemoattractant on primarily neutrophils it is logical to assume that the loss of FPR will affect neutrophil functionality. Neutrophils have demonstrated the ability to interact with T-cells displaying cross-talk properties (Thewissen *et al*., 2011). Impaired neutrophils with deficient FPR expression subsequently leads to impaired CD4+ T cell recruitment.

One of the key findings from the FACs analyses of the different cellular markers at day 5 and day 21 post-bleomycin was reduction in alternatively activated macrophages in

FPR knockout mice compared to WT controls. Total macrophages were elevated during fibrotic phase in C57Bl6 mice which according to literature represents the M2 macrophages which play a recognised role in wound-healing and tissue remodelling (Wynn, 2008; Brown *et al*., 2009). A point to consider is that CD206+ macrophage population are also high in CCR7 expression which implies a mixed M1/M2 phenotype. Cells may be subject to transdifferentiation with initiation and resolution of inflammation. There is a degree of controversy regarding the differentiation of macrophages into distinct subsets with recent research highlighting potential temporal and spatial regulation of macrophage phenotype (Porcheray *et al*., 2005; Murray *et al*., 2014). Other research highlights specificity of macrophage subset markers with M1 marker, inducible nitric oxide synthase (iNOS) differential suppression in alternatively activated macrophages on account of Arginase activity (Munder *et al*., 1998).These CD206+ macrophages exhibited high auto-fluorescence which is a common feature of alveolar macrophages resident in the pulmonary microenvironment. While CD206 has been associated with anti-inflammatory macrophage populations (Porcheray *et al*., 2005) it is also regarded as a marker of alveolar macrophages not specifically M2 macrophages (Kaku *et al*., 2014) drawing the FACs analyses of this panel into question. The inclusion of another macrophage antibody panel strengthened the data from the first set of markers especially with regards to FIZZ-1+ population.

Another thing to consider about FIZZ-1 as an M2 marker is expression is not solely restricted to alternatively activated macrophages. FIZZ-1 is also localised to lung epithelium in rat bleomycin models with IL-4/IL-13 able to induce lung FIZZ-1 expression on a wider scale than previously considered (Liu *et al*., 2004). With FIZZ-1+ expressing macrophages having low iNOS expression and fitting with the same pattern as that of CD206+ macrophages the evidence for a reduction in M2 macrophages with FPR deletion during bleomycin-induced pulmonary fibrosis is somewhat strengthened and a potential mechanism for the reduced fibrosis may be proposed. Reduction in M2 macrophages (recognised as players in the wound-healing response) in bleomycin-injured mice upon ablation of *fpr1* gene at 21 days is potentially responsible for protective effect.

MOMA-2, a glycoprotein macrophage marker was used due to its high degree of specificity for mononuclear phagocytes and also on account of its distinction from MOMA-1. MOMA-1, metallophilic macrophages are localised in spleen and peripheral

lymph nodes as part of the spleen marginal zone while MOMA-2 is used to determine total macrophages in lymphoid tissue and other organs such as the lung (Leenan *et al*., 1994). Determination of neutrophil activation status during acute and fibrotic phases seemed a reasonable angle to pursue due to little difference in neutrophil recruitment in the tissue. Upon activation PMNs migrate to sites of injury via innate homing mechanism increasing expression of different markers CD62L (L-selectin), ICAM-1, CD54, FCYRII (cd32), C5a receptor (CD88), CD66a and CD11b (Fortunati *et al*., 2008).

Sialic acid binding immunoglobulin-like lectin F (SigLecF) expression denoted the eosinophil population in the inflammatory infiltrate. This eosinophil-specific receptor has a conserved cytoplasmic immunoreceptor tyrosine-based inhibitory motif (ITIM), 4 immunoglobulin (Ig)-like domains as well as a transmembrane component. SigLecF shares a degree of homology with SigLec8, its human counterpart expressed on eosinophils due to a convergent evolution, both of which have glycan ligand recognition function acting as adhesion receptors (Tateno *et al.*, 2005). As yet no research has reported an effect of FPR1 upon eosinophil migration/function and the numbers are so minimal that there effect on the bleomycin is more than likely small.

4.2.11.3 Chimera mice injured with bleomycin

Although a set dose of 10 grays (6.8 Sv) was used to irradiate the mice prior to bone marrow transplantation if the machine was not calibrated properly the effects on the recipient mice could have catastrophic. This could potentially explain why the mice developed such severe problems and complications over the reconstitution period.

The irradiation procedure could also explain the mild effect observed in the chimera mice following bleomycin instillation. In radiation-induced models of pulmonary fibrosis as well as eradicating the host's immune system (bone marrow cell populations) epithelial cells are damaged. These resident populations may undergo epithelial-mesenchymal transdifferentiation (EMT) leading to myofibroblast and the development of a wound healing response. Also due to this EMT-driven process anti-inflammatory cytokines are secreted which if localised in the lung at the time of bleomycin/saline instillation could have hampered the acute inflammatory response by alternatively activated macrophages. Parallels can be drawn to radiation-induced lung fibrosis and the chimera bleomycin-injury model (Ding *et al*., 2013).

4.2.11.4 Fibrotic marker variability between different bleomycin studies

Variability in different fibrotic markers, for examples ECM production was evident between studies including the initial day 21 endpoint conducted at MedImmune, the Ly6G-mediated depletion study and the bone marrow chimera study. One thing to consider with this is that each study was analysed separately with different densitometry thresholds used each time for the PSR and α-SMA stains with the Nikon analysis software. Due to the difference in presentation in the histology perhaps some animals did not receive an optimal dose of bleomycin making groups (in particular injured mice) more variable thus creating inter-study differences. Another point to consider is the mice composing the groups in the different studies some of which were mixed gender.

4.3 Summary of bleomycin-injury *in vivo* studies

- FPR1KO mice are protected from bleomycin-induced pulmonary fibrosis compared to wildtype counterparts with dampened inflammation at 1 day and 5 days post-injury and fibrotic responses at 21 days post-injury.
- FPR1KO mice exhibited a switch in macrophage phenotype to M2 class in fibrotic phase.
- Ly6G-mediated depletion experiments demonstrated a neutrophil drop in bleomycin model along with a decrease in ECM production and CD68+ve macrophages/monocytes.
- Chimera experiments showed no clear effect of bone marrow reconstitution on the bleomycin model of pulmonary fibrosis.

5 Role of FPR1 in fibrosis in multiple organ *in vivo* models

5.1 Hypothesis

From the initial investigations of pulmonary fibrosis via the bleomycin-induced model using FPR1KO (*fpr643*) transgenic mutant mice the formyl-peptide receptor 1 (FPR1) has demonstrated a potential role in this microenvironment. In other organs, however, the cellular composition differs thus altering the pathogenesis of fibrosis in that particular environment. Indeed, most fibrogenesis mechanisms follow a similar process triggering a dysregulated wound-healing response. Investigation of *in vivo* fibrosis models in liver, kidney and skin were undertaken to elucidate effects on FPR1's role in fibrosis. Different microenvironments have altered neutrophil involvement in the pathogenesis of their fibrotic mechanisms therefore this chemoattractant receptor will have a differential role in multiple organs.

5.2 General fibrosis mechanism

Wound-healing is an essential process in the body preventing infection and degradation of tissue responsible for key functions. Programmed cell death (apoptosis) enables turnover of damaged cells (usually epithelium) and regeneration. This is a prevailing feature of the liver where injured tissue is replaced following inflammatory, remodelling and resolving events. In the normal response there is no long-term damage but in the case of repeated injury/damage functionality is lost even in regenerative organs such as the liver. The scheme postulated by Wynn (2004; 2007) displays the breakdown of the haemostatic mechanism resulting in the fibrotic phenotype. Quiescent fibroblast transformation to activated myofibroblast is a typical feature of the transition from fibrogenesis to fibrosis.

5.3 Liver fibrosis: an overview

5.3.1 Organ functionality

As a major part of the endocrine system the liver is responsible for a range of different homeostatic functions. Typically the liver is the largest gland in the human body which in adults may weigh up to 2.5% of total body weight (Si-Tayeb *et al*., 2010; Juza and Pauli, 2014). Within the adult liver multiple different cell types coordinate such as

hepatocytes, cholangiocytes, endothelial cells, sinusoidal endothelial cells, pit cells, kupffer macrophages and hepatic stellate cells (Si-Tayeb *et al*., 2010). Essentially the liver is composed of multiple lobes, each lobule separated by portal tracts. Each portal tract is made up of a portal vein, an arterial vessel and a bile duct, the close proximity of the blood supply enables transport of oxygenated blood to the lobule. Hepatocytes, cholangiocytes (biliary epithelial cells, BECs), endothelium, hepatic stellate cells (HSCs) and resident immune cells all work in concert to fulfil the liver's endocrine/exocrine functions (Si-Tayeb *et al*., 2010).

5.3.2 In vivo liver injury models

Different experimental models are available for investigating each of these factors but as with any *in vivo* study no single model will answer all the questions due to their limited nature. Studies involving mice and rats have greatly increased our knowledge of the liver disease both at injury level and in terms of fibrosis as a concept. The heterogeneity of the CLD has proved a problem for research often requiring multiple model strategies to elucidate pathways. Different approaches have been developed over the years to replicate the key features of different liver disease modalities. Commonly characterised are the Bile duct ligation (BDL) cholestatic injury model and toxin-mediated liver injury methods. BDL have been extensively used in rats and mice causing acute obstructive jaundice in under 2 weeks (Marques *et al*., 2012). Carbon tetrachloride (CCl_4) and thioacetamide (TAA) are damaging agents used to induce injury responses are routinely applied to rodents to allow investigation of liver fibrogenesis and fibrosis (Liedtke *et al*., 2013; Traber *et al*., 2013).

Research models employed depend on research questions as particular models are more applicable in certain situations. Of the *in vivo* tools available two main types exist: classical models which have some features of CLD but not all and those models which specifically mimic particular CLDs: immunodefects, viral infections, gene deletions for autoimmune/cholestatic liver diseases. Most models are not enough by themselves to present a conclusive therapeutic option but they are opportunities for the pathogenesis of CLDs to be elucidated (Liu *et al*., 2012).

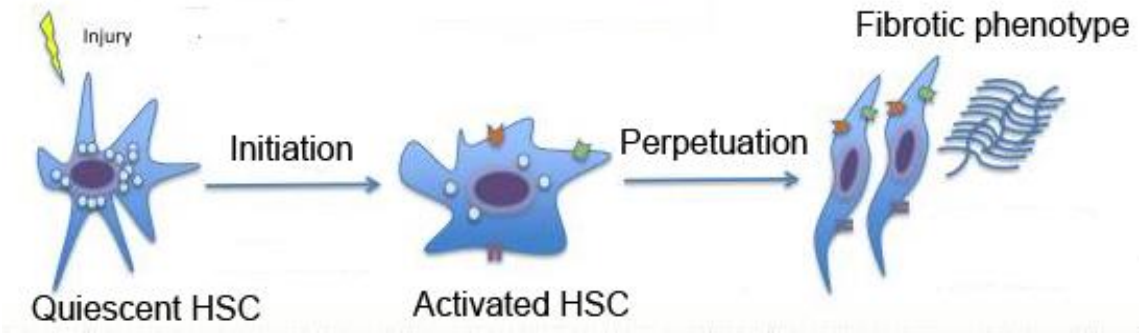

Figure 5.1: Schematic of hepatic fibrogenesis. Liver injury leads to initiation with quiescent hepatic stellate cells (HSCs) differentiating to activated HSCs. Fibrogenesis occurs and this is perpetuated to yield a reversible fibrotic phenotype with hyperproliferation and excessive ECM deposition. Adapted from Lee and Friedman (2011).

5.3.3 Liver fibrogenesis

5.3.3.1 *Acute CCL4*

For my purposes CCl_4 was the optimal model to use as its effects closely correlate with different stages and features of human liver fibrosis. These include inflammation, regeneration, myofibroblast proliferation and fibrotic phenotype if regimen is continued long enough. A single dose of CCl_4 results in what has been described as 'centrizonal necrosis and steatosis' triggers massive hepatocyte centrilobular death (Fujii *et al*., 2010). CCl_4 is metabolised by hepatocytes rapidly which generates $CCl_3°$ free radicals. This metabolite is degraded further to form reactive oxygen species (ROS) triggering lipid peroxidation and membrane impairment. Cytochrome CYP2E1 oxidase system is activated by CCl_4 metabolism causing the radical formation (Wu *et al*., 1996).

Due to the regenerative ability of the liver CCl_4 is used routinely for studying its acute and chronic effects. CCl_4 is only active for a short time with secretion occurring in 24 hours. This is the main reason behind its use with acute end-points of 1, 2 and 3 days. These end-points are equivalent to 'snapshots' for the early responses to injury: (1) Inflammation; (2) Fibrogenesis; (3) Resolution. All of these processes are overlapping in chronic CCl_4 model with repeated CCl_4 i.p. injections perpetuating the wound-healing response leading to a fibrotic nodular scar tissue pattern (Marques *et al*., 2012).

This invaluable tool is highly replicable essentially allowing insight into the CCl_4 metabolism effects on tissue in terms of damage level, inflammatory response, proliferation and fibrogenesis – the normal wound-healing response.

5.3.4 Liver fibrosis

5.3.4.1 *Chronic CCl_4*

Chronic toxic injury with carbon tetrachloride in rodent models is similar to human disease in that an aberrant dysregulated wound-healing response is initiated and sustained with repeated applications. With HSC activation from quiescent precursors 15% of cells in the liver suddenly have the ability to transform an organ. Development of a myofibroblast phenotype changes the balance of ECM in the liver with proliferation and excessive deposition by newly non-quiescent stellate cells. As more and more collagen, proteoglycans, fibronectin and hyaluronic acid are produced the regulation

mechanisms are impaired. The MMP and TIMP feedback loops are disrupted in this hepatotoxic environment eventually leading to scar tissue generation (Jang *et al*., 2008). After 4 weeks of biweekly CCl_4 intraperitoneal injections hepatic fibrosis is exhibited, 8 weeks cirrhosis develops and advanced micronodular fibrosis is demonstrated after 12 weeks. Repeated CCl_4 administration is causing chronic liver injury leading to chronic liver fibrosis (Liedtke *et al*., 2013; Constandiou *et al*., 2005).

Due to the similar pattern of disease progression in the CCl_4 model and human CLD, many of the same biomarkers are used for assessment. These include liver function tests (damage enzyme levels), fibrogenic stress and gene expression biomarkers. PicroSiriusRed (PSR) staining is an established tool for evaluation of tissue section fibrosis level and spread (Constandiou *et al*., 2005). Histology is graded (usually via Isaak Score) as with human biopsies accordingly for collagen deposition and portal inflammation (Jang *et al*., 2008).

5.4 Acute CCl_4 model

5.4.1 Hypothesis

Fpr-/- null transgenic mice will have a depleted immune response to toxic injury (24 hours) but I foresee no change in fibrogenesis (48 hours) and resolution (72 hours) mechanisms in the liver. Ultimately, the deletion of FPR1 will have no effect on the development of liver fibrosis via CCl_4 administration.

5.4.2 Aims

From acute administration CCl_4, 1:1 volume ratio with vehicle olive oil, and subsequent harvesting of blood and liver tissue at short-term endpoints of 24, 48 and 72 hours the effect of *fpr1* deletion on the early fibrogenesis processes would be elucidated. This initial 72 hours is comprised of the different stages of the wound-healing response with endpoint effectively acting as ‘snapshot’. By 24 hours the immune response has been initiated in response to the damage caused by degradation of CCl_4. After 48 hours fibrogenesis is occurring as myofibroblast activate and are subject to excessive proliferation. With 72 hours the injury is already resolving itself which is a testament to the liver’s regenerative capacity. By evaluation of KO mice compared to WT mice during these stages of the fibrogenesis the effect of FPR1 and its activity on the wound-healing response could be elucidated.

5.4.3 Liver weight (LW) to body weight (BW) ratio at acute endpoints

LW/BW ratios are used routinely to gauge liver damage and as an index of this organ's regeneration capacity (Figure 5.2). The LW/BW ratio was dramatically reduced with CCl_4 in KO mice at 24 hours (0.04447±0.008308) compared to vehicle control (0.002017±0.0003558; $p<0.0001$) and WT CCl_4 group, 0.04643±0.003675 ($p<0.01$). All groups at other endpoints exhibit no change in LW/BW ratio except for 72 hours where a significant increase in LW/BW ratio ($p<0.05$) was determined. The effect observed during the inflammatory, initiation phase of the toxic injury response may be due to altered proliferation with loss of FPR expression.

5.4.4 Serum damage enzyme markers

In response to human liver disease and *in vivo* injury by carbon tetrachloride Alanine aminotransferase (ALT) and Aspartate aminotransaminase (AST) are secreted by the liver into the blood. The liver produces more ALT than AST after liver injury acting as a more specific liver function test (Vroon and Israili, 1990; Marshall, 2012). In human liver disease AST and ALT can be potentially increased <8 and <5 times respectively compared to healthy serum biochemistry in alcoholic fatty liver disease and <4 times of normal patients in non-alcoholic fatty liver disease (Nyblom *et al*., 2004).

Following sacrifice blood was harvested from each animal and processed to obtain serum in which the above analytes were measured by catalytic activity (Figure 5.3; NHS Biochemistry department). Blood is composed of plasma (55%), erythrocytes (45%) and leukocytes (<1%). Centrifugation following animal sacrifice of blood samples separates cells from the plasma layer equating to serum (minus clotting factors). Plasma is principally made up of water (91%), blood proteins (7%) and nutrients (2%) which is then able to be analysed to determine levels of hepatocellular injury. Upon acute injury with CCl_4 liver function tests indicated secretion of ALT and AST with higher levels than olive oil (vehicle) controls. 24 hours post-injury WT and KO mice both exhibited increases in serum U/L but no difference between WT and KO-injured mice was detected ($p<0.01$ and $p>0.05$ respectively). After 48 hours both genotypes produced similar levels with CCl_4 injury, wildtype mice elicited a significant response with an increase to 6036±1077 U/L ($p<0.01$) while knockout mice elicited a

significant increase from 52±4 U/L, vehicle to 6943±829.4 U/L ($p<0.001$). With the acute model consisting of a single injection (vehicle/toxin) following the initial injury the inflammation is replaced by fibrogenic processes leading to resolution by 72 hours. By this time ALT levels have dropped compared to earlier endpoints with U/L similar to vehicle control levels.

With the other less specific serum damage enzyme, AST levels followed a similar trend as with ALT. 24 hours post-injury both WT and KO mice have increased serum concentrations with knockout exhibiting a significant increase over control group ($p<0.01$) elevating from mean U/L of 288±28 (OO) to 5136±1533 (CCl_4). WT mice exhibited a significant increase also ($p<0.0001$).

With a high degree of variability between samples in KO CCl4 group there is no difference detected when compared with WT CCl4 mice. By 48 hours (proliferation phase) AST levels show consistent raised levels in CCl4 groups with means of 6384±522.3 U/L (WT; $p<0.01$) and 7008±636.3 U/L (KO; $p<0.001$) and with resolution of injury (72 hours) serum concentrations are depleted to near baseline as with ALT.

Both ALT and AST liver responses to injury display no difference with loss of FPR expression potentially indicating a compensation mechanism during the inflammatory response for altered chemotactic function. Ultimately the response to liver damage during fibrogenesis in terms of these liver function tests was unchanged with *fpr1* gene ablation.

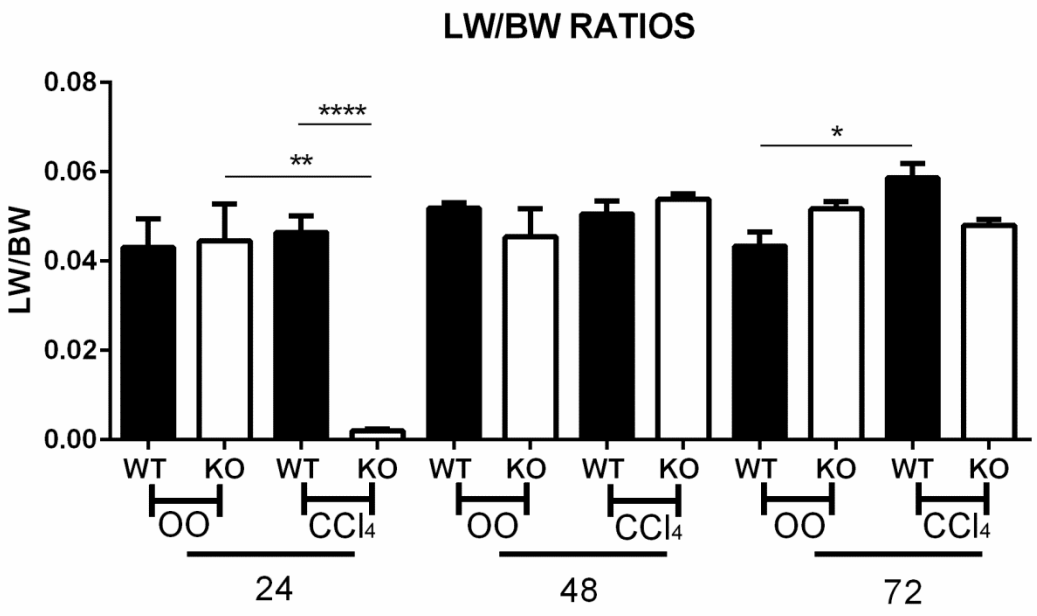

Figure 5.2: Liver weight (LW, g) to body weight (BW, g) ratios from acute CCl_4-injured mice. Harvested at 24, 48 and 72 hours after 1:1 Carbon tetrachloride (CCl_4): Olive oil (OO) intraperitoneal (i.p.) injection. All groups had a minimum of 4-5 mice analysed with values expressed as mean LW/BW and SEM displayed. All analysis performed by a one-way ANOVA * $p<0.05$; ** $p<0.01$; **** $p<0.0001$.

5.4.5 Fibrogenic gene expression at acute CCl_4 endpoints

At the different stages of fibrogenesis mRNA gene expression a variety of markers either pro-inflammatory or fibrogenic were analysed by quantitative real-time PCR. During the inflammatory initiation phase of acute liver injury (24 hours post-CCl_4 (Figure 5.4) collagen 1 (*col1*) expression relative to WT vehicle control remained at a consistent level with no increase/decrease upon injury ranging from 1.222 to 1.947 fold change ($p>0.05$). At this stage of acute liver injury the myeloid cell marker S100A9 expression was increased with CCl_4 injection. Relative gene expression increased from WT OO (2.097) to WT CCl_4 (26.57) and KO OO (1.345) to KO CCl_4 (24.99). The spread of these results was large with a sizable SEM of 18.29 and 10.72 in the toxin-treated groups respectively ($p>0.05$). Both cytokines IL-6 and KC were elevated in the liver of CCl_4 treated mice after 24 hours but this was no significant compared to vehicle controls or each other ($p>0.05$).

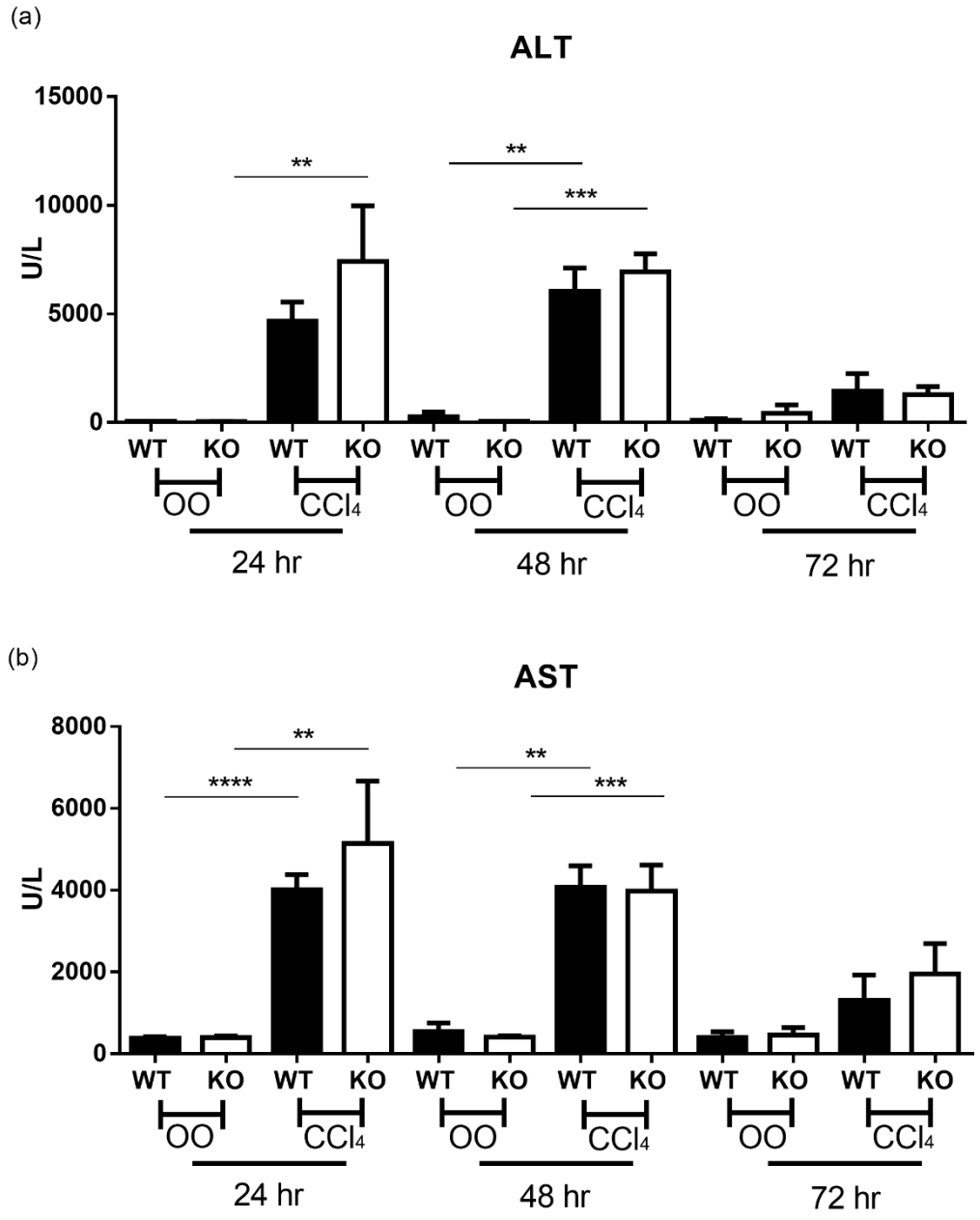

Figure 5.3: Serum damage enzyme concentrations after acute CCl_4 treatment. 24, 48 and 72 hours post-injection (a) ALT and (b) AST U/L were assayed by colorimetric analysis in vehicle olive oil (OO) and carbon tetrachloride (CCl_4) treated C57Bl6 (WT) and *fpr-/-* (KO) transgenic mice. All groups had a minimum of 4-5 serum samples analysed with values expressed as mean U/L and SEM displayed. All analysis performed by a one-way ANOVA; ** $p<0.01$, *** $p<0.001$ and **** $p<0.0001$.

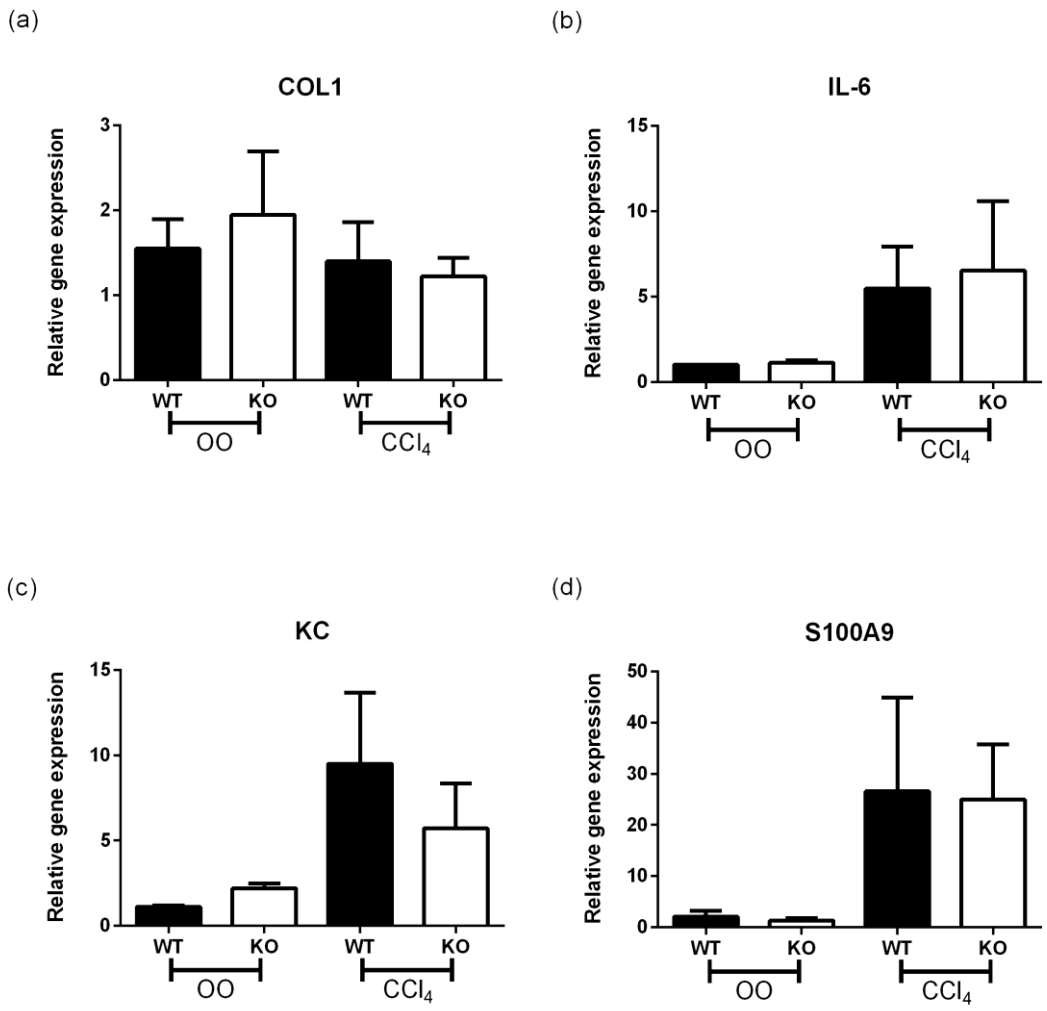

Figure 5.4: Gene expression 24 hours post-CCl_4 treatment. mRNA levels of (a) Col1, (b) IL-6, (c) KC and (d) S100A9 were assayed via real-time PCR. All groups, olive oil (OO) and carbon tetrachloride (CCl_4) treated had a minimum of 4-5 samples analysed with values expressed as mean fold change relative to WT vehicle controls (normalised to GAPDH housekeeping gene) and SEM displayed. All analysis performed by a one-way ANOVA; * $p<0.05$ and $p>0.05$.

48 hours post-CCl_4 injection fibrogenesis is beginning to occur with production of extracellular matrix (ECM) markers associated with activation of hepatic stellate cells (HSCs) and the wound-healing response (Figure 5.5). α-SMA gene expression was up-regulated non-significantly in WT and KO CCl_4 groups compared to vehicle controls; 11.43±5.827 fold and 35.02±14.3 fold change respectively. Collagen I expression was increased in a similar fashion at this 'snapshot' of fibrogenesis with levels of 7.632±1.383 (WT; $p>0.05$) and 16.48±5.367 (KO) fold change compared to vehicle controls ($p>0.05$). TIMP1, a regulator of ECM production also demonstrated an increase in expression with CCl_4 injury and levels increased to 46.26±10.61 (WT) and 78.39±18.41 (KO) fold change. Due to variability between liver cDNA samples no significance was attained by this response ($p>0.05$). Fibronectin, another ECM protein produced during fibrogenesis was increased in both WT ($p>0.05$) and KO ($p>0.05$) CCl_4 groups compared to vehicle counterparts. No apparent difference between injured groups in the expression pattern of this protein ($p>0.05$).

72 hours post-CCl4 injection the wound-healing response is underway with inflammatory events replaced by the resolution of the damaged areas by ECM production and HSC activation. mRNA levels (Figure 5.6) of α-SMA increased in CCl_4-treated groups (WT, $p<0.05$; KO, $p>0.05$) compared to that of vehicle controls irrespective of genotype. TIMP1 expression also rose in injured mice after 72 hours in WT and KO groups to 1.58±0.9781 fold change and 0.8836±0.3415 fold change respectively compared to vehicle controls ($p>0.05$). Monocyte chemoattractant peptide 1 (MCP-1) production by drug-treated livers demonstrated little or no change in gene expression with minimal fold change between vehicle control and CCl_4 groups ($p>0.05$). Myeloid cells, denoted by S100A9 expression, were increased from vehicle controls (mean of 0.4094±0.1569) to 3.536±2.151 fold change in C57Bl6 injured livers. Knockout expression of S100A9 elevated from 0.4828±0.2484 to 2.274±1.186 mean fold change in vehicle and CCl4 groups respectively ($p>0.05$). Although primarily a marker of neutrophils S100A9 is localised in monocytes and B-lymphocytes (Li *et al*., 2009) which is more likely responsible for the mRNA levels detected by real-time PCR.

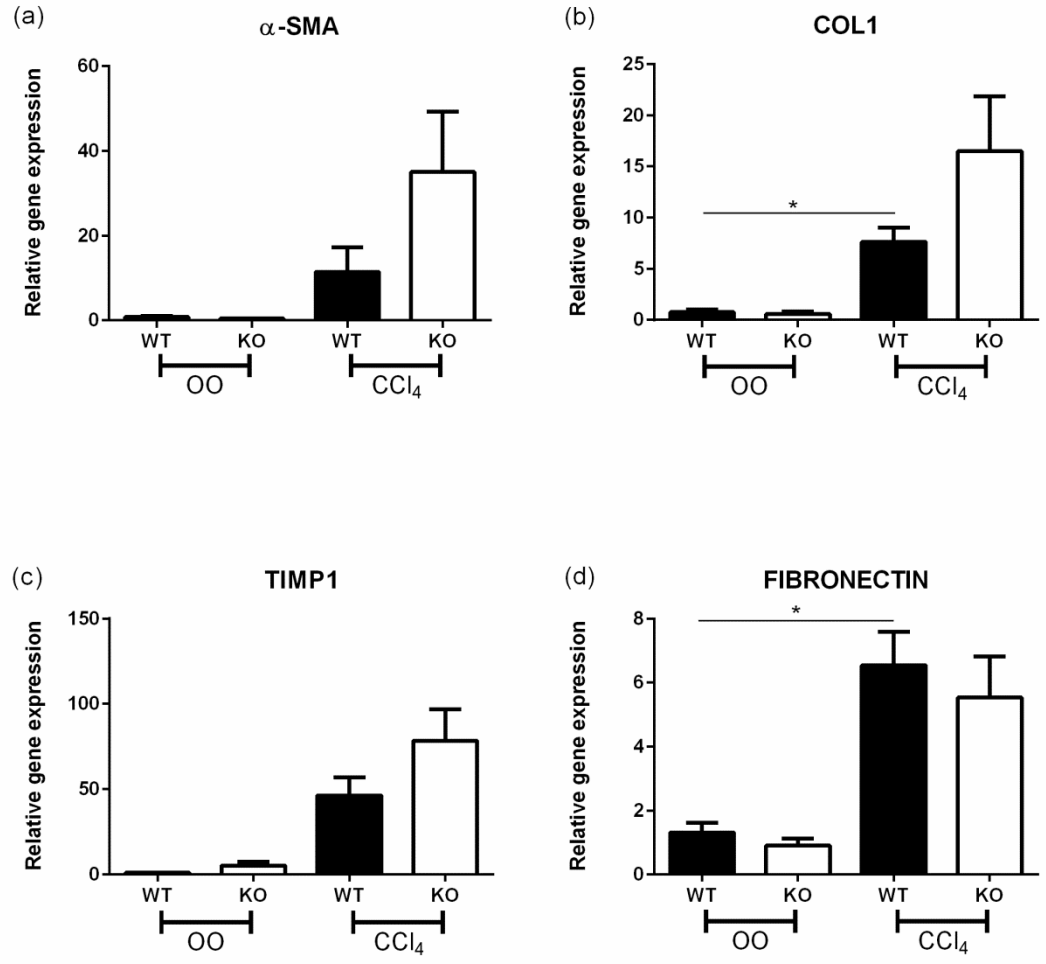

Figure 5.5: Gene expression 48 hours post-CCl_4 treatment. mRNA levels of (a) α-SMA, (b) Col1, (c) TIMP1 and (d) Fibronectin were assayed via real-time PCR. All groups, olive oil (OO) and carbon tetrachloride (CCl_4) treated had a minimum of 4-5 samples analysed with values expressed as mean fold change relative to WT vehicle controls (normalised to GAPDH housekeeping gene) and SEM displayed. All analysis performed by a one-way ANOVA * $p<0.05$.

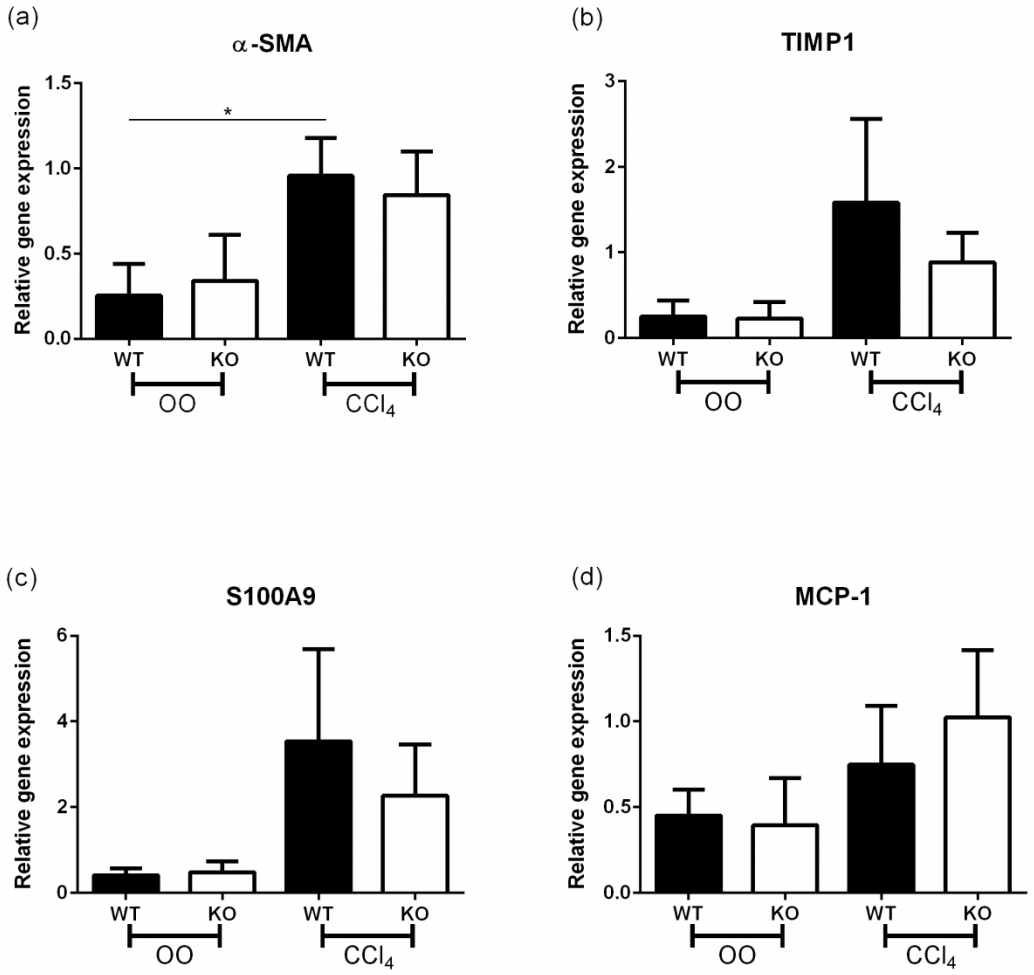

Figure 5.6: Gene expression 72 hours post-CCl_4 treatment. mRNA levels of (a) α-SMA, (b) TIMP1, (c) S100A9 and (d) MCP-1 were assayed via real-time PCR. All groups, olive oil (OO) and carbon tetrachloride (CCl_4) treated had a minimum of 4-5 samples analysed with values expressed as mean fold change relative to WT vehicle controls (normalised to GAPDH housekeeping gene) and SEM displayed. All analysis performed by a one-way ANOVA * $p<0.05$.

5.4.6 Immunohistochemistry of different cellular markers after acute CCl_4 application

5.4.6.1 *Alpha-SMA, a marker of activated HSCs, deposition*

Hepatic stellate cell (HSC) differentiation from quiescent to activated myofibroblast form is characterised by among other things alpha-smooth muscle actin. 24 hours post-CCl_4 injection following densitometry analysis the percentage area stained did not increase further than that of vehicle controls ranging from means of 0.34 to 0.55% ($p>0.05$). Corresponding with the fibrogenesis phase occurring 48 hours post-injury α-SMA production is elevated in both WT and KO mice. Upon transdifferentiation of quiescent stellate cells to their activated form the mean percentage area increased from 0.48±0.06% in olive oil vehicle WT controls to 2.001±0.2681% in CCl_4 group ($p<0.01$). In *fpr1*-deficient mice the area increased from a mean of 0.5±0.1183% to 1.877±0.3045% in vehicle and CCl_4 groups respectively ($p<0.01$). No clear difference is evident between genotypes at this endpoint. After 72 hours α-SMA deposition levels were clearly increased in WT CCl_4 (mean area of 1.98±0.2498%; $p<0.001$) over the corresponding control from baseline percentage area stained (mean of 0.44±0.075%). Knockout mice demonstrated a non-significant increase ($p>0.05$) with CCl_4 treatment to a mean area of 1.575±0.641% from vehicle control group. Both genotypes undergo fibrogenesis in the liver with CCl_4 application and resolution of the acute response by 72 hours followed a similar pattern.

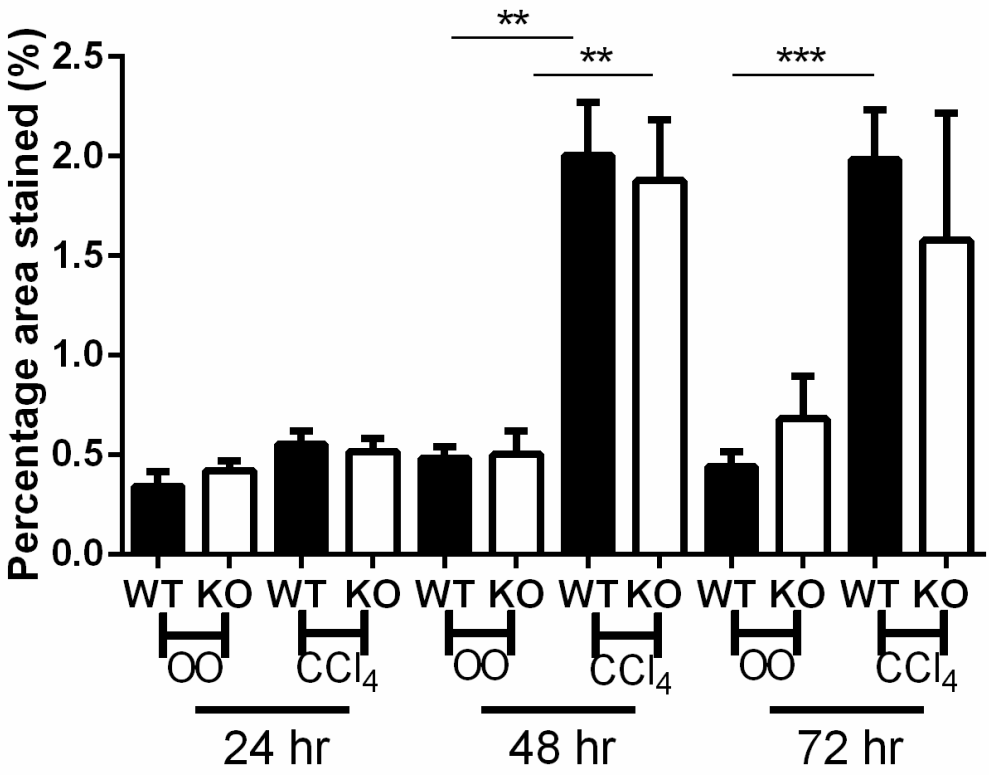

Figure 5.7: Alpha-Smooth Muscle Actin production in acute CCl_4-injured livers after 24, 48 and 72 hours. All groups, olive oil (OO) and carbon tetrachloride (CCl_4) treated had relative photomicrographs of FFPE wildtype (WT) and FPR knockout (KO) liver sections (see appendix C) stained indirectly via IHC of (x10 magnification) and had a minimum of 4-5 mice. Data was then analysed via densitometry using Nikon microscope software with results expressed as a mean percentage area stained ±SEM. All p values were calculated using a one-way analysis of variance (ANOVA); * $p<0.01$; *** $p<0.001$ and ns $p>0.05$.

5.4.6.2 *Proliferation in acute CCl_4 model*

With fibrogenesis hepatocytes enter a state of hyper-proliferation and IHC staining of proliferating cell nuclear antigen (PCNA) will indicate how the wound-healing response is progressing. PCNA positivity is exhibited by lymphocytes and hepatocytes, with hepatocytes positive cells per high per field (hpf) giving an indication of liver proliferation following injury. At 24 hours PCNA demonstrated no difference between controls and CCl_4 groups ($p>0.05$) with mean positive cells per field ranging from 2.712±0.4198 to 3.604±0.215. After this inflammatory, initiation phase the liver progresses to fibrogenesis at 48 hours post-CCl_4. Both WT and KO mice demonstrated an elevated PCNA positive count in WT injured groups in a significant manner with mean counts of 44.08±6.718 ($p<0.0001$) and 31.45±10.22 ($p<0.0001$) respectively. This fibrogenesis stage is associated with hyper-proliferation phenotype so this is of no surprise. No difference apparent between WT and KO in the CCl_4 groups ($p>0.05$). Loss of the FPR1 receptor does not affect hepatocyte proliferation which may be due to the fact that it has been primarily characterised in immune cells. Resolution of the CCl_4 response by 72 hours is evident by a decreased proliferation but still significant response in injured groups from mean cells/field 3.426±0.15 increasing to 17.49±4.704 in WT mice and means of 3.84±0.3712 rising to 18.5±4.558 cells/field in KO counterparts ($p<0.05$).

5.4.6.3 *Neutrophil recruitment in WT/KO mice post-acute CCl_4*

Neutrophil recruitment is a major feature of the response to liver injury and this is apparent by the NIMP positive cells elevated with CCl_4 after 24 hours. Both WT and KO mice showed demonstrable surges in PMN numbers but no apparent difference between genotypes. Mean cells/field increased from 2.25±0.5617 to 43.86±6,438 upon injury in C57Bl6 mice ($p<0.001$) while knockout mice exhibited a similar infiltration with 1.72±0.1868 cells/field rising to 35.25±6.537 cells/field in CCl_4-treated mice ($p<0.001$) By 48 hours post-CCl_4 neutrophil levels have dropped drastically to 20.96±3.34 and 20.71±4.71 cells/field in WT and KO CCl_4 groups, both showed significant responses over vehicle controls $p<0.01$ and $p<0.01$ respectively. No difference was detected between genotypes in terms of neutrophil recruitment at this endpoint, which is testament to the defined stages of the wound-healing response shown by analysis of livers injured with CCl_4 within 72 hours. Indeed the neutrophil response was fully

resolved by 72 hours post-CCl_4 treatment with no significant increase over vehicle controls.

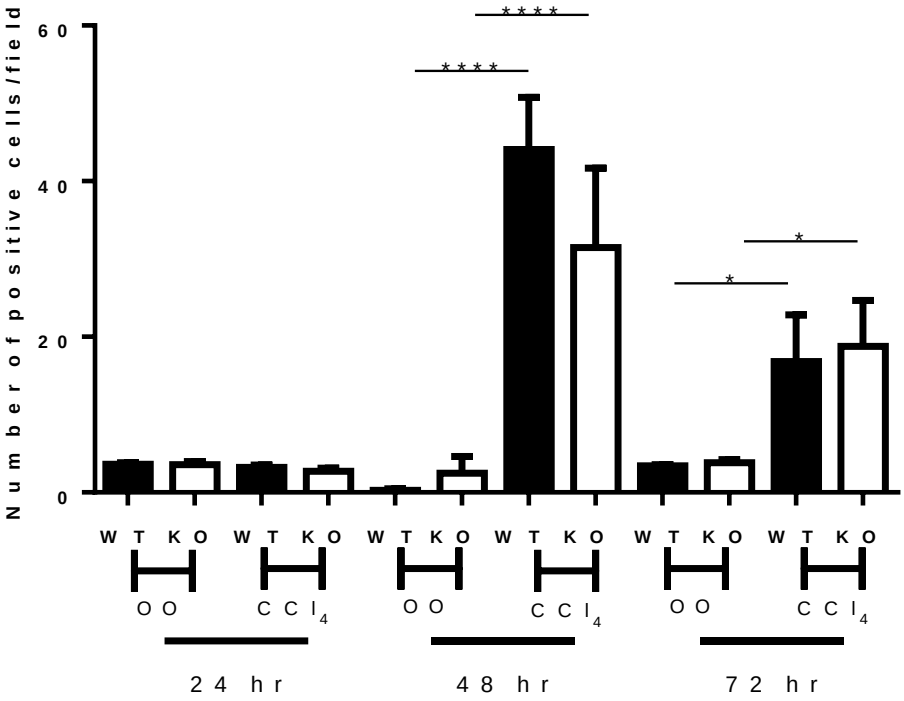

Figure 5.8: Proliferating cell nuclear antigen (PCNA)-positive hepatocytes in acute CCl_4-injured livers after 24, 48 and 72 hours. All groups, olive oil (OO) and carbon tetrachloride (CCl_4) treated had relative photomicrographs of FFPE wildtype (WT) and FPR knockout (KO) liver sections (see appendix C) stained indirectly via IHC of (x20 magnification) and had a minimum of 4-5 mice. Data was then analysed via counting software on the Nikon microscope with results expressed as mean positive cells per high power field (hpf) ±SEM. All p values were calculated using a one-way analysis of variance (ANOVA); **** $p<0.0001$, * $p<0.05$ and ns $p>0.05$.

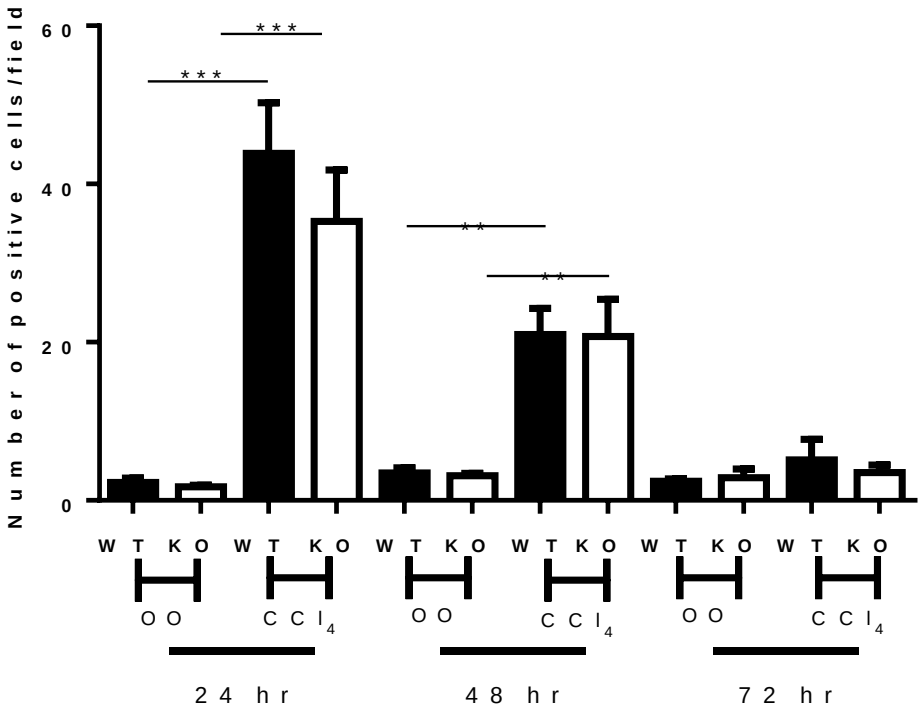

Figure 5.9: Neutrophil recruitment in acute CCl_4-injured livers after 24, 48 and 72 hours. All groups, olive oil (OO) and carbon tetrachloride (CCl_4) treated had relative photomicrographs of FFPE wildtype (WT) and FPR knockout (KO) liver sections (see appendix C) stained indirectly via IHC for NIMP (x20 magnification) and had a minimum of 4-5 mice. Data was then analysed via counting software on the Nikon microscope with results expressed as mean positive cells per high power field (hpf) ±SEM. All p values were calculated using a one-way analysis of variance (ANOVA); ** $p<0.01$; *** $p<0.001$ and ns $p>0.05$.

5.4.6.4 *CD68+ve macrophages in CCl_4-injured livers*

Resident kupffer macrophages are a main responder to hepatocellular injury by carbon tetrachloride drug (1:1 ratio with vehicle) driving fibrogenesis as a producer of TGF-β cytokine. After each time point: 24, 48 and 72 hours post-CCl_4 there was an increase in the number of CD68 positive cells per high power field (x 20 magnifications) from that of vehicle olive oil resident populations. 24 hours post-injury the majority of the inflammatory response is made up of neutrophils with a lesser response by macrophages. CD68+ve cells/field were increased in WT mice from a mean of 57.86±2.739 (vehicle) to 79.8±1.85 (CCl_4) in a significant response ($p<0.001$). KO groups exhibited a similar increase at this endpoint with a more dramatic increase to 82.96±4.58 mean positive cells per hpf ($p<0.001$). With loss of FPR1 there may be a compensatory mechanism at play here due to dampened neutrophil response in this phase. In the fibrogenesis phase at 48 hour endpoint CD68 macrophages increase their population correlating with increases in ECM production and fibrogenic markers. Both WT and KO livers demonstrated significant increases in macrophage infiltration (mean counts of 95.2±14.4 cells/field ($p<0.001$) and 109.2±7.823 cells/field ($p<0.001$)). Indeed it is at this endpoint during the wound-healing response that the peak level of macrophage recruitment is observed. This immune infiltration is dampened by 72 hours with resolution of the injury but significant elevations were determined compared to vehicle controls. WT levels rose from 42.91±4.382 to 79.36±3.154 mean cells/field ($p<0.0001$) and KO mice displayed an increase from 39.31±2.402 to 75.7±1.707 cells/field ($p<0.0001$) showing a dampened recruitment of this cell population by 72 hours indicating that this TGF-β reservoir is no longer required with resolution of injury.

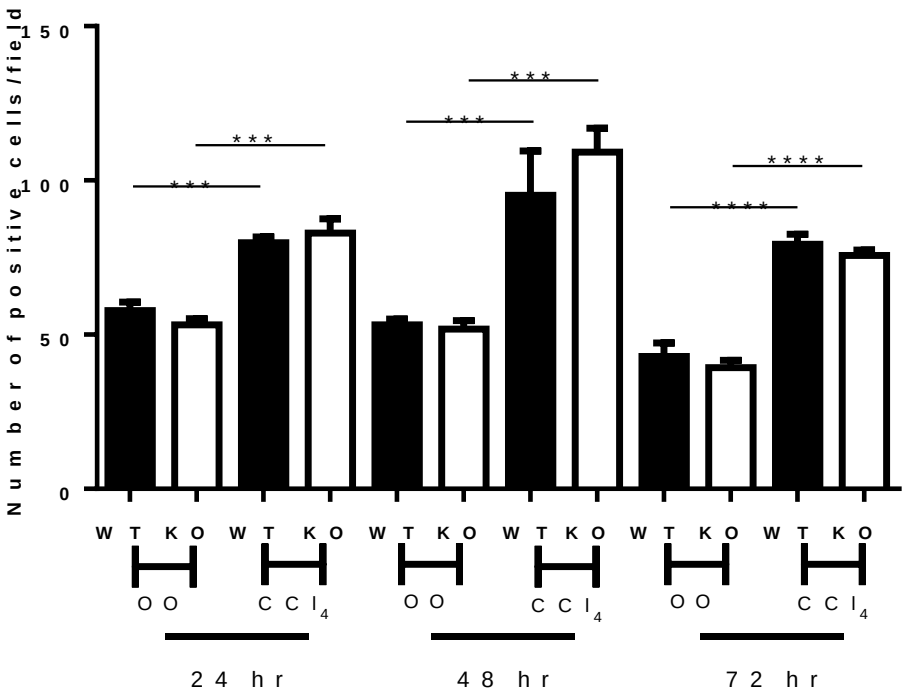

Figure 5.10: Macrophage recruitment in acute CCl_4-injured livers after 24, 48 and 72 hours. All groups, olive oil (OO) and carbon tetrachloride (CCl_4) treated had relative photomicrographs of FFPE wildtype (WT) and FPR knockout (KO) liver sections (see appendix C) stained indirectly via IHC for CD68 (x20 magnification) and had a minimum of 4-5 mice. Data was then analysed via counting software on the Nikon microscope with results expressed as mean positive cells per high power field (hpf) ±SEM. All p values were calculated using a one-way analysis of variance (ANOVA); *** $p<0.001$; **** $p<0.0001$ and ns $p>0.05$.

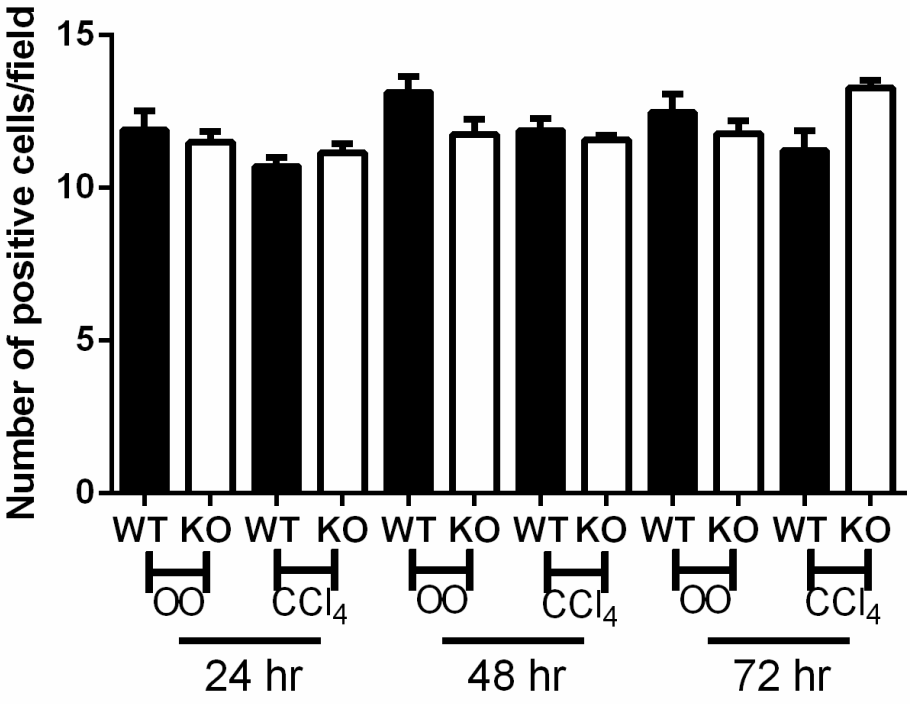

Figure 5.11: Lymphocyte recruitment in acute CCl_4-injured livers after 24, 48 and 72 hours. All groups, olive oil (OO) and carbon tetrachloride (CCl4) treated had relative photomicrographs of FFPE wildtype (WT) and FPR knockout (KO) liver sections (see appendix C) stained indirectly via IHC for CD3 (x20 magnification) and had a minimum of 4-5 mice. Data was then analysed via counting software on the Nikon microscope with results expressed as mean positive cells per high power field (hpf) ±SEM. All p values were calculated using a one-way analysis of variance (ANOVA) ns $p>0.05$.

5.4.6.5 *Lymphocyte populations upon acute CCl_4 liver injury*

CD3 positive lymphocytes displayed consistent counts at each endpoint regardless of phase, treatment (vehicle or CCl_4) or *fpr1* expression with no significant responses determined ($p>0.05$). With fibrogenesis in this acute model lymphocytes do not play a role during the inflammatory (24 hours post-CCl_4), fibrogenesis (48 hours post-CCl_4) and resolution phases (72 hours post-CCl_4).

5.4.7 Summary of FPR's role in fibrogenesis mediated by acute CCl_4 treatment

Co-ordination of multiple cell types such as hepatic stellate cells (HSCs), hepatocytes, kupffer macrophages and neutrophils is responsible for hepatic fibrogenesis. The resulting effect is production of extracellular matrix (ECM) protein and activation of myofibroblasts. With regards to the loss of the chemoattractant receptor, FPR1 there appears to be a minimal effect on the initial response to toxin-induced injury. A slight reduction in neutrophil infiltration during the inflammatory phase has little effect on hepatocyte proliferation and macrophage resident populations. Alpha-SMA deposition occurs mainly at fibrogenesis phase with no difference between CCl_4 injured livers of WT and KO livers.

5.5 Chronic CCL_4 model

5.5.1 Serum damage enzyme markers

As with the human disease serum ALT and AST levels were elevated with hepatic fibrosis induced by CCl_4 (Figure 5.12). No difference detectable between CCl_4 groups with either marker ($p>0.05$). ALT serum concentrations increased from mean values of 187.2±46.43 (WT OO) and 158.0±52.18 (KO OO) to 6934±805.3 (WT CCl_4) and 5147±776.3 (KO CCl_4) in a significant response ($p<0.0001$ and $p<0.001$ respectively, Figure 5.12 (a)). ALT is a more specific marker for liver damage than AST due to highly localised nature in that particular organ. AST is secreted in CCl_4-injured groups in a similar manner to ALT but due to its less specific secretion profile responses are notably less dramatic in WT and KO mice. WT mice exhibited an increase ($p>0.05$) with toxin treatment knockouts exhibited a significant response increasing from a mean concentration of 1115±481.8 U/L (vehicle) to 5104±1329 U/L (CCl_4; $p<0.05$) but this most likely due to variability in individual readings (as indicated by increased S.E.M.; Figure 5.12 (b)). Between chronically injured groups there is no difference in responses following the same patterns determined in fibrotic score and collagen deposition.

5.5.2 Fibrotic score and hydroxyproline content

Analysis of total collagen content was achieved by a hydroxyproline assay of acid-hydrolysed liver samples (Figure 5.13). Hydroxyproline content (µg) was derived from absorbance readings and normalised to weight of tissue pre-hydrolysis. Following 8 weeks of biweekly i.p. injections of vehicle/toxin both WT and KO mice exhibited significant increases in total collagen content ($p<0.05$). C57Bl6 increased from 0.2412±0.08704 µg/g to 1.034±0.1895 µg/g (olive oil to CCl_4 respectively) and KO mice displayed a similar response from 0.4204±0.08710 µg/g to 1.202±0.1945 µg/g (olive oil to CCl4 respectively).

Scoring of chronic CCl_4 model via PSR stained sections (Figure 5.14) showed no difference in the rank/level of fibrosis between WT and KO mice, both demonstrated more than 2 hepatic vessels bridging together by non-functional scar formation and multi-layered ECM deposition. Some mice from either genotype scored between ranks due to a lack of homogeneity between different lobes. WT and KO exhibited significant

increases in fibrotic score with CCl_4 regimen compared to vehicle controls ($p<0.0001$) with mean values of 2.944±0.1002 and 3.

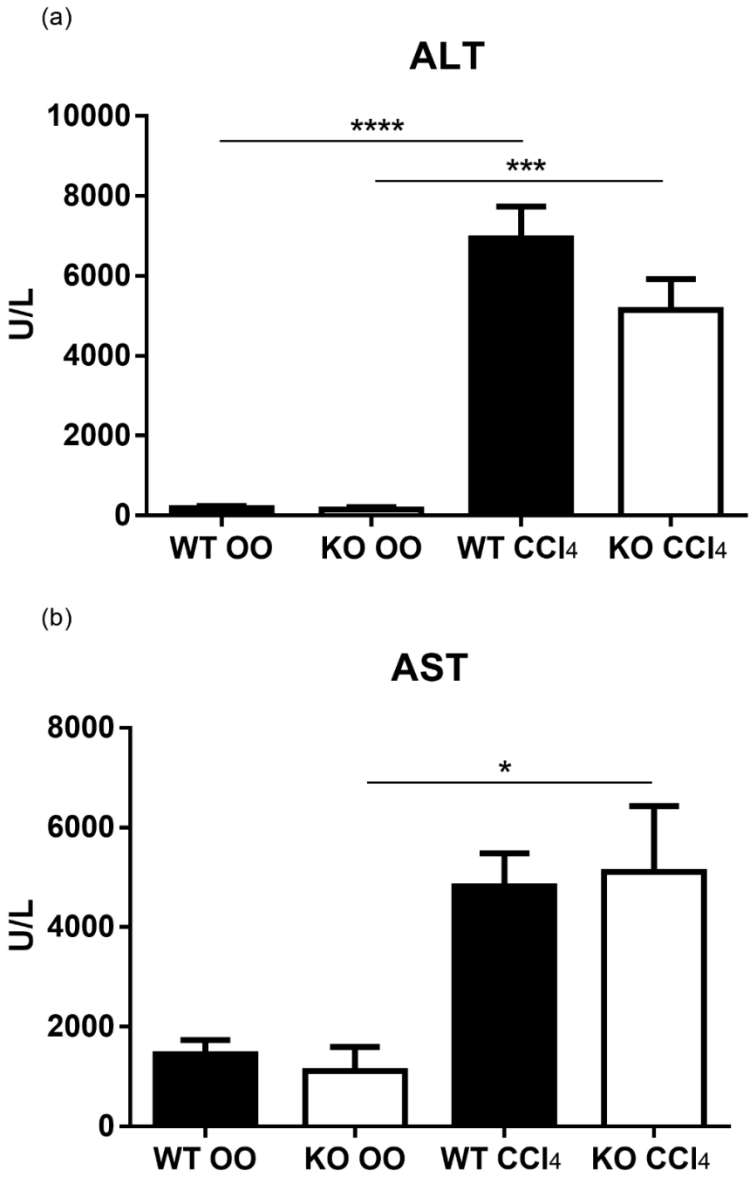

Figure 5.12: Serum liver damage enzymes released during chronic CCl_4 model. Liver function serum markers (a) ALT and (b) AST measured in U/L in WT vehicle (OO, n=5), KO vehicle (OO, n=6), WT CCl_4 (n=9), KO CCl_4 (n=9) groups after 8 weeks of biweekly carbon tetrachloride (CCl_4) or olive oil (OO) injections. Mean U/l of different groups expressed with SEM displayed. All p values were calculated using a one-way analysis of variance (ANOVA); * $p<0.05$, *** $p<0.001$, **** $p<0.0001$ and ns $p>0.05$.

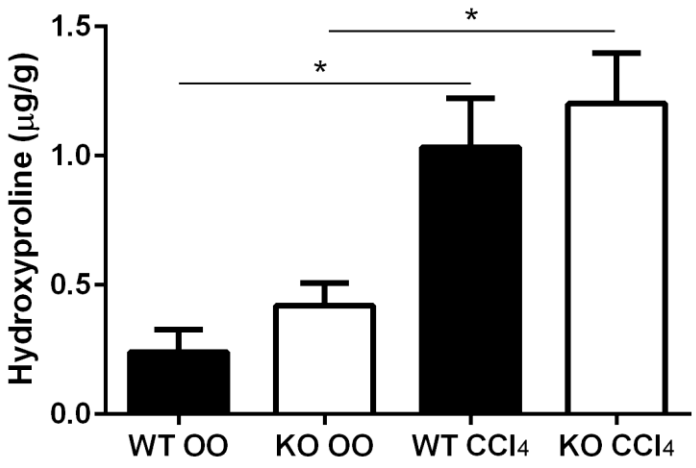

Figure 5.13: Hydroxyproline content of chronic CCl_4-treated WT/KO mice. Total collagen content per g of wet tissue was assayed in WT vehicle (OO, n=5), KO vehicle (OO, n=6), WT CCl_4 (n=9), KO CCl_4 (n=9) groups after 8 weeks of carbon tetrachloride (CCl_4) or olive oil (OO) biweekly injections. Mean hydroxyproline content (µg/g) of different groups expressed with SEM displayed. All p values were calculated using a one-way analysis of variance (ANOVA); * $p<0.05$.

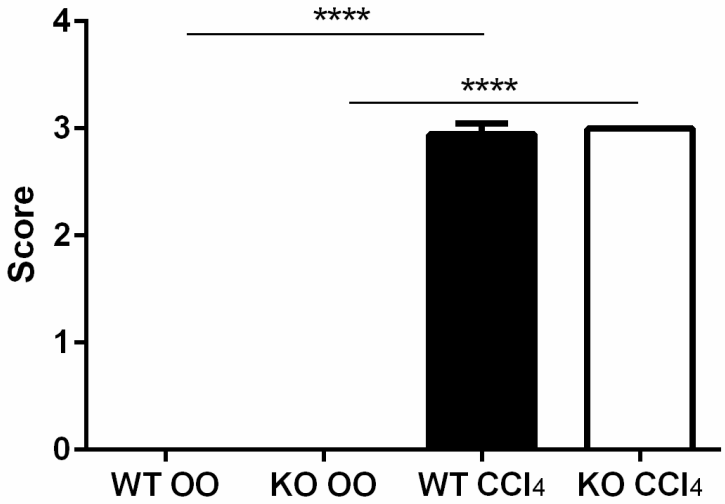

Figure 5.14: Fibrotic score of chronic CCl_4-treated WT/KO mice. Scoring ranked animals according to severity of bridging fibrosis and scar tissue formation in WT vehicle (OO, n=5), KO vehicle (OO, n=6), WT CCl_4 (n=9), KO CCl_4 (n=9) groups after 8 weeks of biweekly carbon tetrachloride (CCl_4) or olive oil (OO) injections. Means of different groups expressed with SEM displayed. All p values were calculated using a one-way analysis of variance (ANOVA); **** $p<0.0001$.

5.5.3 Fibrotic marker gene expression

Gene expression levels of different markers showed variable responses to chronic liver injury with repeated CCl_4 dosing (Figure 5.15). Pro-collagen 1 mRNA levels were used to measure collagen 1 gene expression in vehicle/toxin treated livers. Expression of collagen 1 increased (relative to WT vehicle control mean of 2.117±0.6844 fold) in WT CCl_4 group to 77.68±10.9 fold higher ($p<0.001$). With ablation of the *fpr* gene mice did not elicit a significant increase in gene expression but a notable elevation was evident in CCl_4 group (mean fold change: 40.2±9.683, $p>0.05$) hence between WT and KO injured groups a significant reduction in collagen 1 expression was determined ($p<0.05$). The regulator of ECM production, Tissue Inhibitor Of Metalloproteinases 1 (TIMP1) gene expression showed a similar pattern with a significant mean fold change increase relative to WT vehicle control, 4.019±1,435 (OO) to 71.56±12.93 in CCl_4 group ($p<0.01$). With TIMP1, as with collagen 1 expression there was a significant reduction ($p<0.05$) between WT and KO-injured groups (mean fold change decreasing from 71.56±12.93 to 36.37±7.39 respectively) probably caused by a less significant response in KO animals ($p>0.05$). Alpha-SMA, a major marker of activated myofibroblasts was expressed at high levels in CCl_4-injured groups with ~3-fold and ~2.5-fold increases compared to WT vehicle control in WT and KO mice respectively ($p>0.05$). MMP2 and MMP9 metallopeptidase, regulators of the extracellular matrix (ECM) expression exhibited a significant increase of 6-fold and 4-fold over wild-type vehicle controls with CCl_4 treatment respectively ($p>0.05$). Pro-inflammatory cytokines, KC and MCP-1 were notably increased in chronic injury groups; 9.915±2.336 fold increase of KC mRNA levels ($p>0.05$) and to a non-significant extent with MCP-1 ($p>0.05$) respectively over WT vehicle control group. Secretion of these cytokines in the chronic CCl_4 model indicates the overlapping processes of inflammation, fibrogenesis and the resolution occurring simultaneously in fibrotic liver tissue.

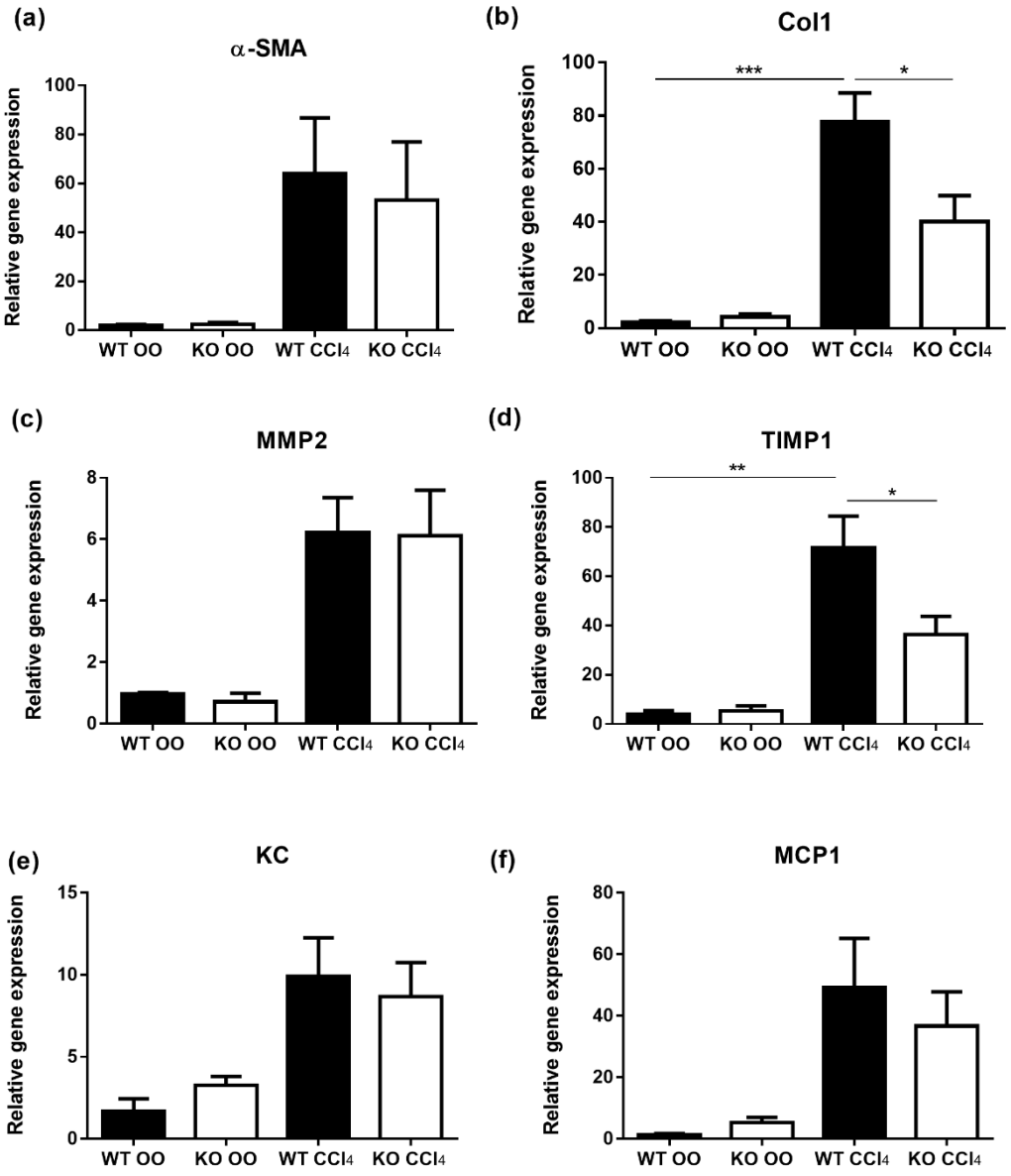

Figure 5.15: Fibrogenic and inflammatory marker gene expression in chronic CCl_4-treated WT/FPR1KO mice. Liver mRNA levels of (a) α-SMA, (b) collagen 1, (c) MMP2, (d) TIMP1, (e) KC and (f) MCP-1 were assayed by quantitative PCR in WT vehicle (OO, n=5), KO vehicle (OO, n=6), WT CCl_4 (n=9), KO CCl_4 (n=9) groups after 8 weeks of biweekly carbon tetrachloride (CCl_4) or olive oil (OO) injections. Fold change was calculated relative to WT vehicle (normalised to GAPDH housekeeping gene) to generate relative gene expression. Mean fold change of different groups are expressed with SEM displayed. All p values were calculated using a one-way analysis of variance (ANOVA); *** $p<0.001$, ** $p<0.01$ and *$p<0.05$.

5.5.4 Immunohistochemistry

5.5.4.1 *H&E*

Haemotoxylin and eosin (H&E) staining of chronic CCl_4 tissue sections demonstrated the characteristic scar formation with the biweekly treatment as indicated in Figure 5.16. Hepatocyte centrilobular death is evident with CCl_4 administration. From H&E sections inflammation and infiltration is similar between WT and KO CCl_4 overall. Some KO CCl_4 showed increased inflammation but with others it clearly down. KO mice showed variability in their immune response to the CCl_4 biweekly treatment possibly indicating compensation mechanisms to the loss of FPR expression resulting in altered inflammatory infiltrate profiles.

5.5.4.2 *Sirius Red*

PicroSiriusRed (PSR) staining of collagen I/III in FFPE liver sections (4µm) demonstrated similar levels of pixel intensity upon densitometry analysis in CCl_4-treated groups (Figure 5.17). Both WT and KO displayed significant increases in PSR percentage area ($p<0.0001$) from olive oil (mean % areas of 0.478±0.1128 and 0.5356±0.1025 respectively) to CCl_4 groups (mean % areas of 2.979±0.2451 and 3.731±0.2489 respectively). Collagen deposition showed no apparent increase/decrease between genotypes but both genotypes displayed clear bridging fibrosing patterns compared to vehicle controls.

5.5.4.3 *Alpha-SMA: an indicator of HSC activation during liver fibrosis*

Chronic CCl_4 biweekly injections induced alpha-smooth muscle actin fibre formation with clear elevations in percentage area from olive oil vehicle controls to CCl_4 in wild-type and knockout mice (Figure 5.18). WT mice mean positive area staining increased from 0.3367±0.02617 % to 3.618±0.3456 % in vehicle and drug-treated groups respectively ($p<0.0001$). KO mice also elicited a significant increase ($p<0.001$) in α-SMA mean positive area staining from 0.3761±0.07252 % to 2.549±0.3781 % in vehicle and drug-treated groups respectively. Although a slight reduction in positive staining was observed in KO mice compared to WT this difference was non-significant ($p>0.05$) with fibrosis developing in both genotypes to a similar severity. This was also indicated by IHC, histology, serum markers and hydroxyproline content.

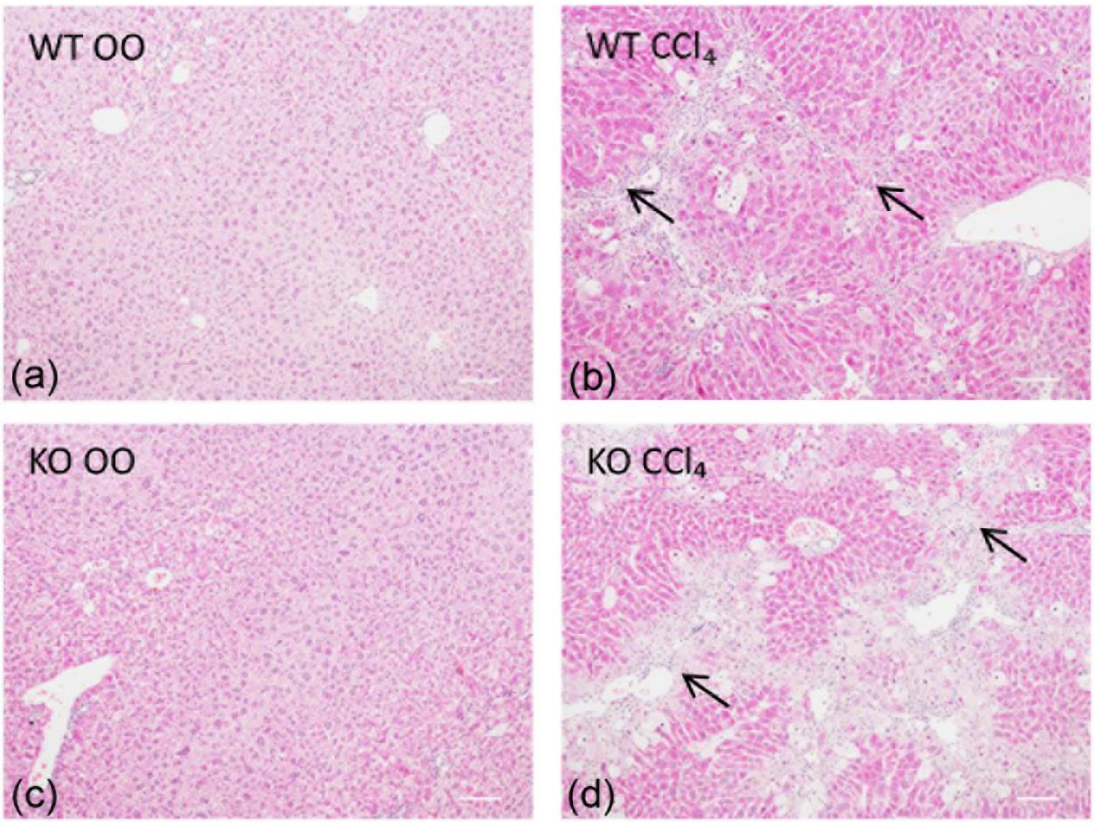

Figure 5.16: H&E highlighted histological features of chronic CCl_4. Relative photomicrographs of sections stained directly of WT and KO livers harvested after 8 weeks of biweekly carbon tetrachloride (CCl_4) or olive oil (OO) regimen (x20 magnification). (a) WT vehicle (OO, n=5), (b) WT CCl_4 (n=9), (c) KO vehicle (OO, n=6) and (d) KO CCl_4 (n=9) groups with arrows indicating areas of damage and scar formation.

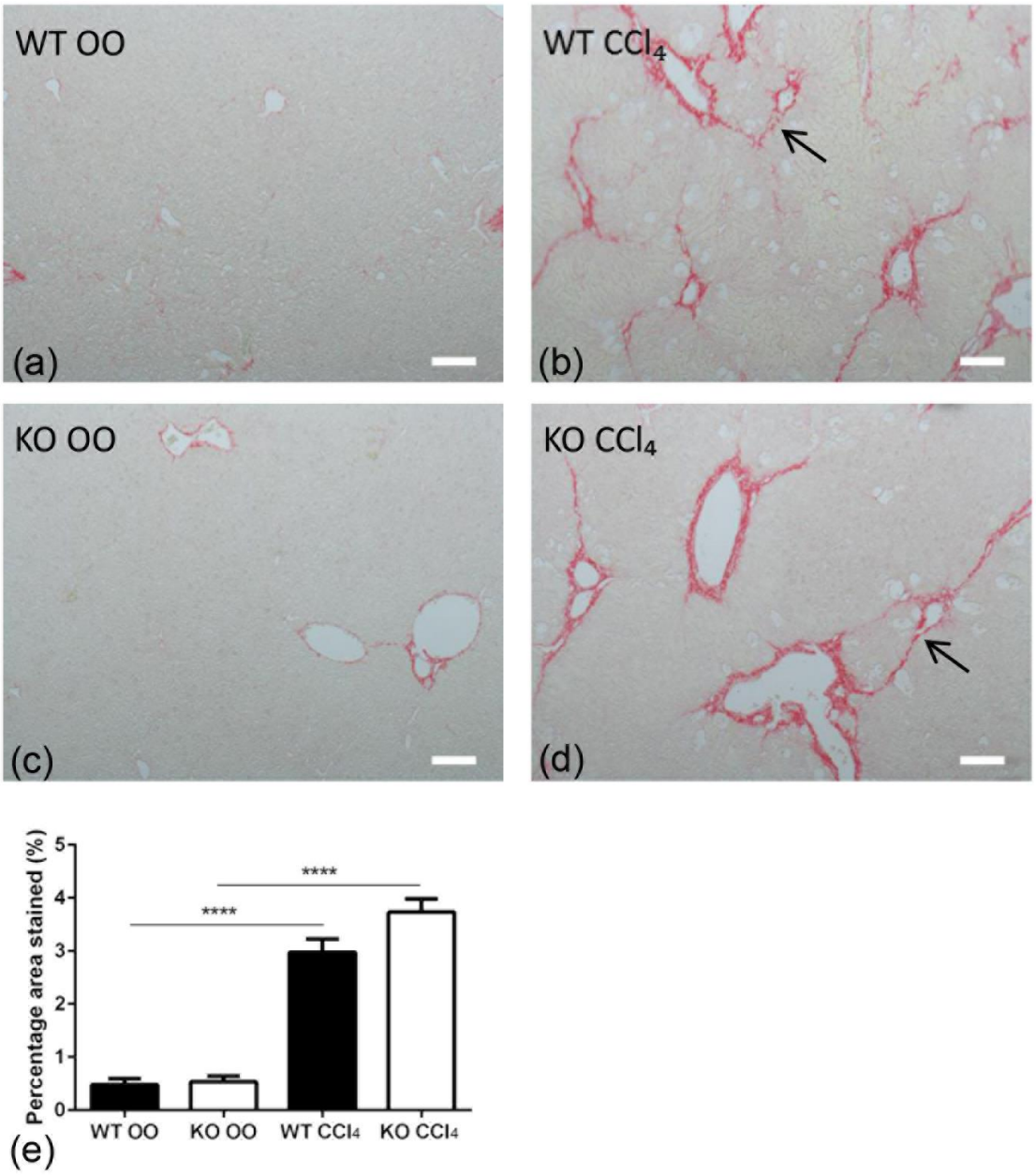

Figure 5.17: PSR collagen staining of chronic CCl_4 / vehicle-treated WT/KO livers. Relative photomicrographs of sections stained directly for collagen I/III in WT and KO livers (x10 magnification, scale bar represents 100µm) were analysed using densitometry. (a) WT vehicle (OO, n=5), (b) WT CCl_4 (n=9), (c) KO vehicle (OO, n=6), and (d) KO CCl_4 (n=9) groups were subject to 8 weeks of biweekly treatment. Arrows indicate areas of bridging fibrosis and collagen deposition. Results are expressed as mean percentage area ±SEM. All p values were calculated using a one-way analysis of variance (ANOVA); **** $p<0.0001$.

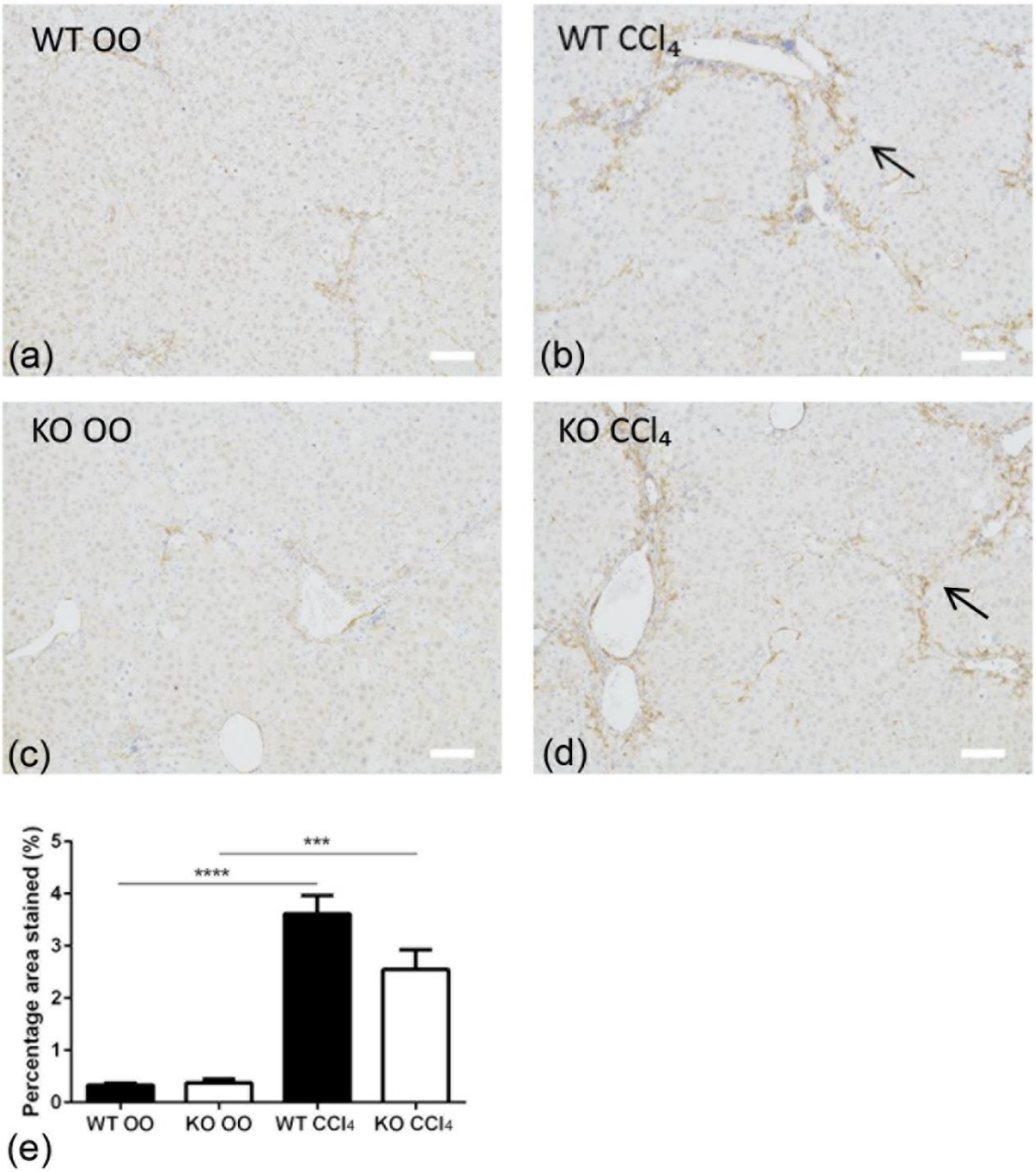

Figure 5.18: α-SMA production by activated stellate cells in chronic CCl_4 model. Relative photomicrographs of sections stained indirectly for α-SMA content in WT and KO livers (x10 magnification, scale bar represents 100μm) were analysed using densitometry. Arrows indicate area of ECM deposition and activated myofibroblasts. (a) WT vehicle (OO, n=5), (b) WT CCl_4 (n=9), (c) KO vehicle (OO, n=6), and (d) KO CCl_4 (n=9) groups were subject to 8 weeks of biweekly treatment. Results are expressed as mean percentage area ±SEM. All p values were calculated using a one-way analysis of variance (ANOVA); *** $p<0.001$ and **** $p<0.0001$.

5.5.4.4 *Proliferation of hepatocytes after chronic CCl_4*

In order to assess proliferation Proliferating cell nuclear antigen (PCNA) staining via IHC was performed on FFPE liver sections (Figure 5.19). PCNA has a well characterised role as a DNA sliding clamp with an essential role in DNA replication (Maga and Hübscher, 2003). Positive PCNA staining was exhibited by both proliferating liver hepatocytes and lymphocytes, the latter excluded from analysis. Numbers of positively stained hepatocytes were used as an index for proliferation following vehicle/drug treatment in WT and KO mice. Olive oil and CCl_4 groups for each genotype showed no difference in PCNA, therefore proliferation was not affected by FPR1 expression ($p>0.05$). PCNA expression in hepatocytes did increase significantly with drug treatment over vehicle control ($p<0.05$) with average counts of 16.42±2.987 cells/field and 16.11±2.903 cells/field in WT and KO CCl_4-treated groups respectively.

5.5.4.5 *NIMP, neutrophil marker*

During the course of chronic liver fibrosis induced by CCl_4 repeated application injury responses are renewed with every subsequent injection. Even highly fibrotic liver are undergoing inflammatory reactions with infiltrate increased in CCl_4-treated mice. Staining for neutrophil-specific NIMP expression through IHC methods was increased in WT hepatotoxin-treated compared to vehicle controls (Figure 5.20, reflected by mean positive cells elevation to 6.403±0.9007 from 1.647±0.142 per high power field ($p<0.01$). KO mice also exhibited significantly increased mean counts from 1.58±0.1495 (vehicle) to 8.807±1.177 (CCl_4) per field ($p<0.0001$). Despite this increased response no difference between WT and KO drug-treated groups was detected ($p>0.05$).

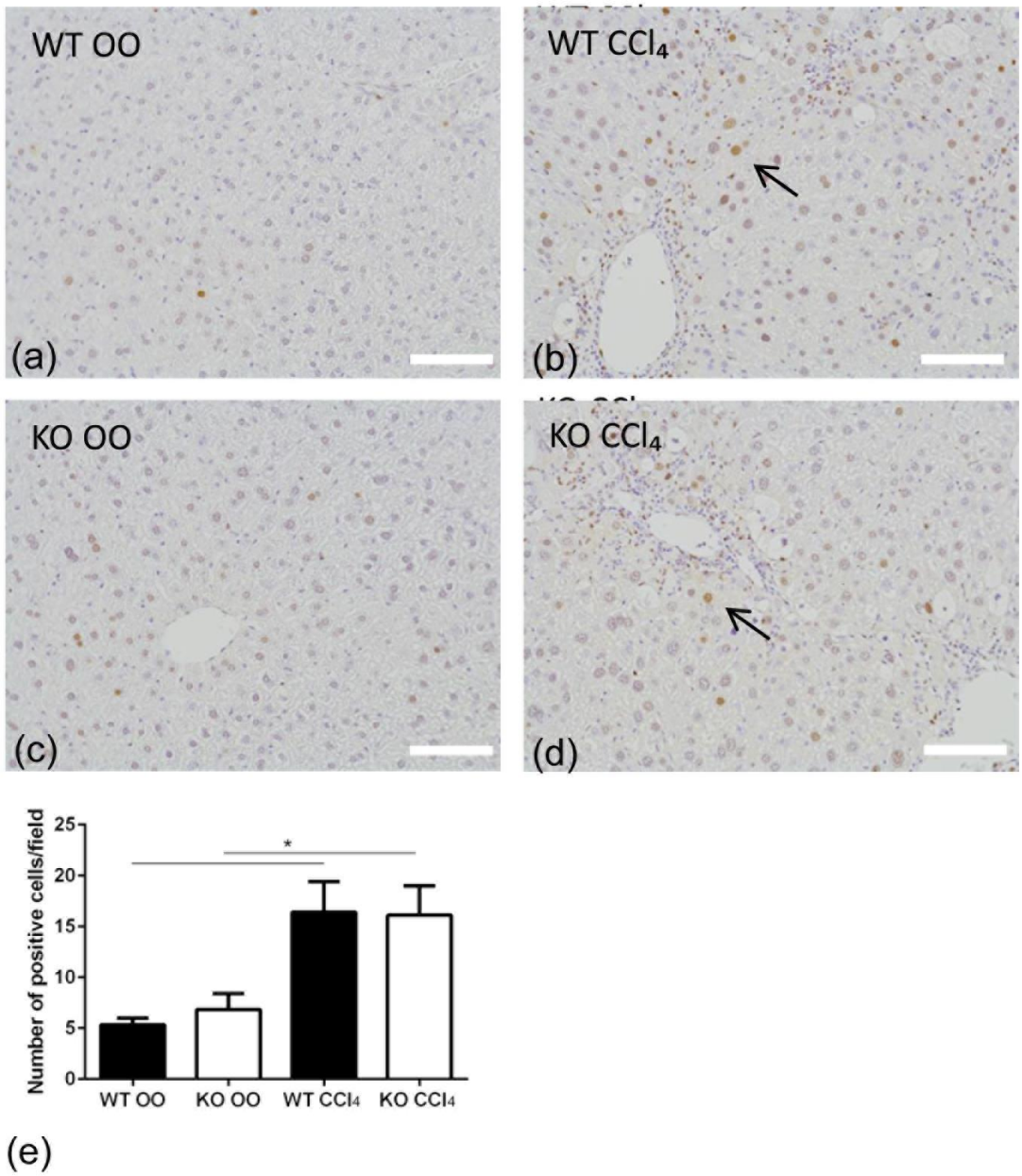

Figure 5.19: Proliferation in chronic CCl_4 model via PCNA positive hepatocytes. Relative photomicrographs of sections stained indirectly for PCNA via IHC of WT and KO livers (x20 magnification, scale bar represents 100µm) were analysed using counting software on Nikon microscope. Arrows indicate PCNA+ve hepatocytes. (a) WT vehicle (OO, n=5), (b) WT CCl_4 (n=9), (c) KO vehicle (OO, n=6), and (d) KO CCl_4 (n=9) groups were subject to 8 weeks of biweekly treatment. Results are expressed as mean positive cells per high power field ±SEM. All p values were calculated using a one-way analysis of variance (ANOVA) * $p<0.05$; ns $p>0.05$.

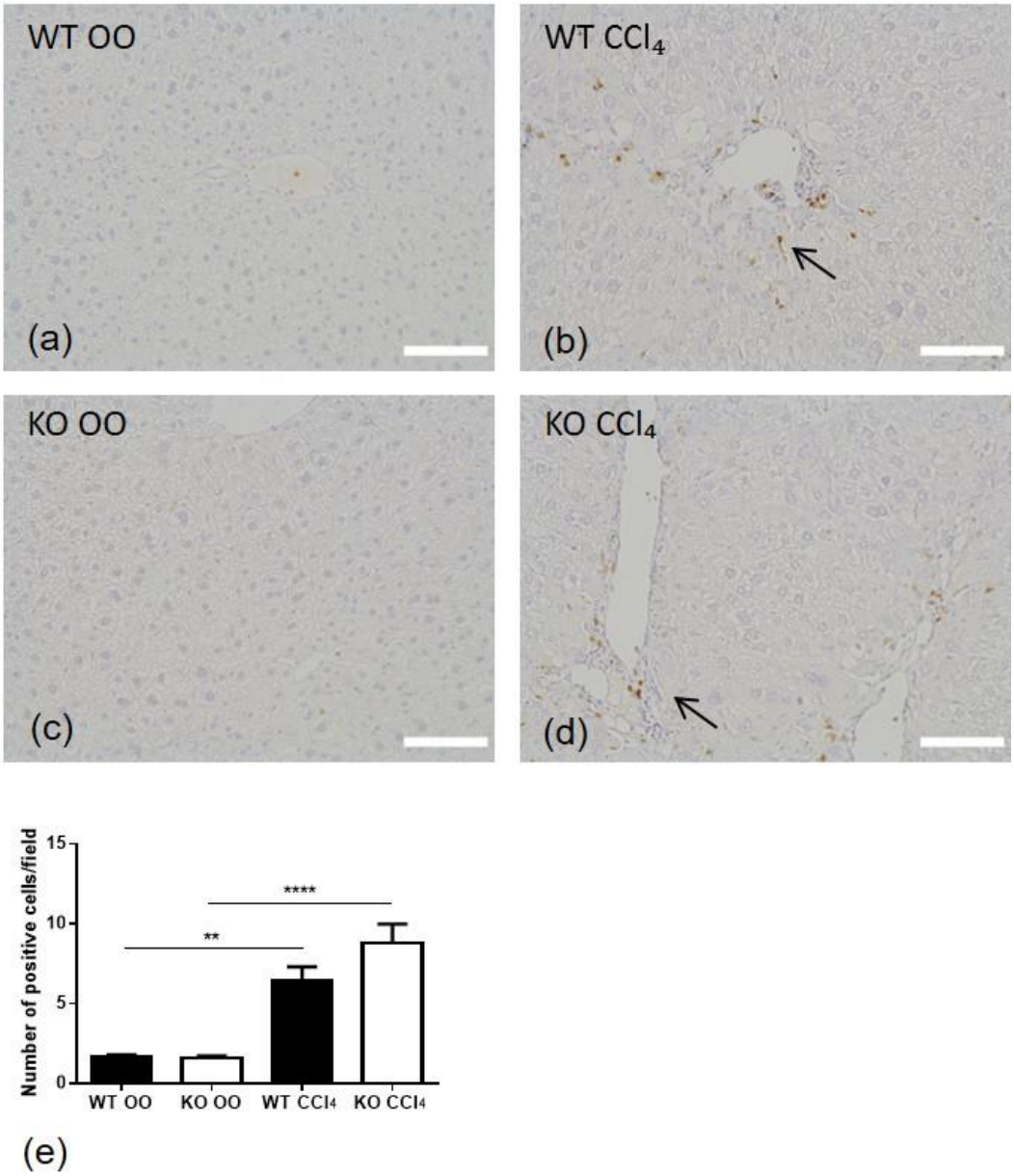

Figure 5.20: Neutrophil infiltration in chronic CCl_4 model. Relative photomicrographs of sections stained indirectly for NIMP via IHC of WT and KO livers (x20 magnification, scale bar represents 100µm) were analysed using counting software on Nikon microscope. Arrows indicate NIMP+ve neutrophils. (a) WT vehicle (OO, n=5), (b) WT CCl_4 (n=9), (c) KO vehicle (OO, n=6), and (d) KO CCl_4 (n=9) groups were subject to 8 weeks of biweekly treatment. Results are expressed as mean positive cells per high power field ±SEM. All p values were calculated using a one-way analysis of variance (ANOVA); ** $p<0.01$; **** $p<0.0001$ and ns $p>0.05$.

5.5.4.6 *CD68, macrophages/monocytes marker*

CCl_4-injured mice exhibited an elevated macrophage/monocyte (CD68+) count compared to vehicle-treated mice (Figure 5.21). Kupffer cells are liver-specific macrophages with known roles in different liver diseases such as hepatitis, steatohepatitis, alcoholic liver disease, allograft rejection and in particular liver fibrosis (Kolios *et al*., 2006). CD68+ cells increased significantly ($p<0.05$) in WT mice from OO group (61.60±2.187 cells/field) to CCl_4 group (107.9±12.46 cells/field). Knockouts also demonstrated an increase and the response displayed significance ($p<0.01$). CD68+ Kupffer cells were elevated from mean counts of 59.68±2.326 cells/field (vehicle) to 123.6±11.35 cells/field (CCl_4) but when compared with WT groups no difference was detected ($p>0.05$).

5.5.4.7 *CD3, total T-cell population marker*

CD3+ lymphocyte cells were evaluated via IHC in liver tissue sections following chronic application of vehicle/CCl_4 (Figure 5.20). No difference was determined between WT OO and WT CCl_4 groups ($p>0.05$). KO CCl_4 group (mean 13.8±0.6463 cells/field) displayed elevated CD3 positivity ($p<0.01$) from vehicle control group (8.532±1.367 cells/field). Chronic injured mice demonstrated a significant increase upon ablation of *fpr1* gene compared to WT counterpart ($p<0.05$).

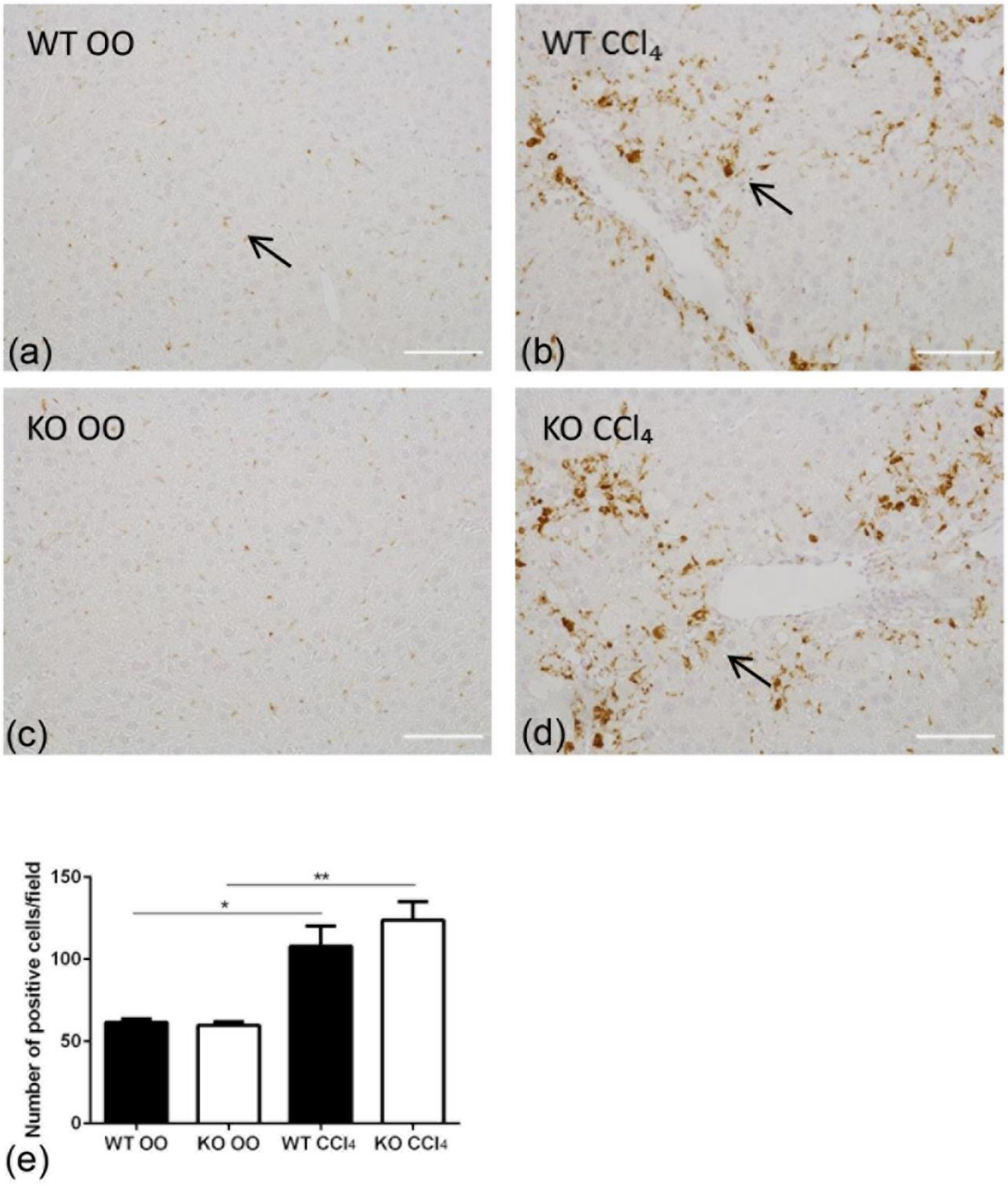

Figure 5.21: Macrophage accumulation after repeated CCl_4 injury and fibrosis development. Relative photomicrographs of sections stained indirectly for CD68 via IHC of WT and KO livers (x20 magnification, scale bar represents 100µm) were analysed using counting software on Nikon microscope. Arrows indicate CD68+ve macrophages. (a) WT vehicle (OO, n=5), (b) WT CCl_4 (n=9), (c) KO vehicle (OO, n=6), and (d) KO CCl_4 (n=9) groups were subject to 8 weeks of biweekly treatment. Results are expressed as mean positive cells per high power field ±SEM. All p values were calculated using a one-way analysis of variance (ANOVA); * $p<0.05$; ** $p<0.01$ and ns $p>0.05$.

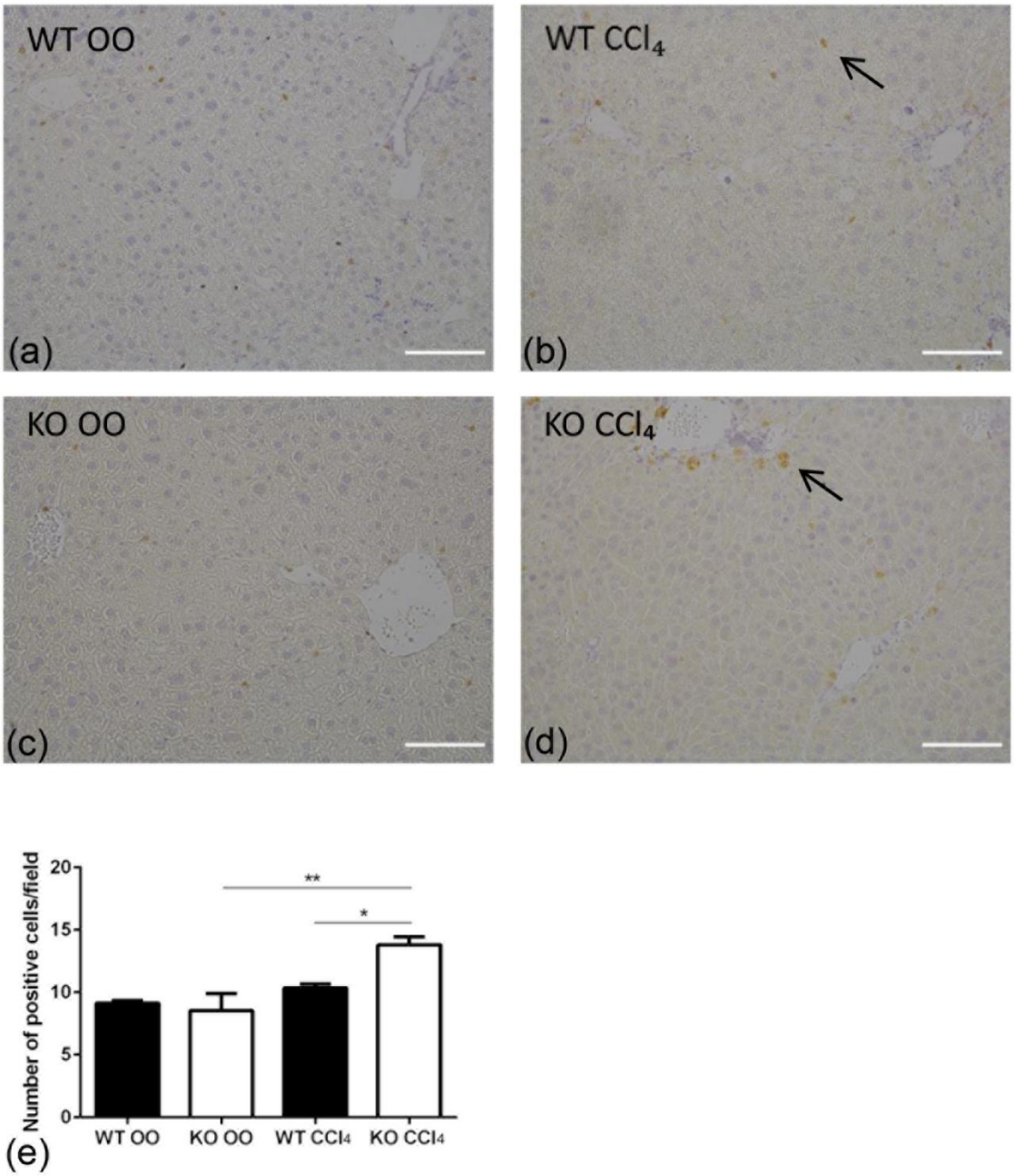

Figure 5.22: Lymphocyte localisation in fibrotic livers in chronic CCl_4 model. Relative photomicrographs of sections stained indirectly for CD3 via IHC of WT and KO livers (x20 magnification, scale bar represents 100µm) were analysed using counting software on Nikon microscope. Arrows indicate CD3+ve lymphocytes. (a) WT vehicle (OO, n=5), (b) WT CCl_4 (n=9), (c) KO vehicle (OO, n=6), and (d) KO CCl_4 (n=9) groups were subject to 8 weeks of biweekly treatment. Results are expressed as mean positive cells per high power field ±SEM. All p values were calculated using a one-way analysis of variance (ANOVA); ** $p<0.01$ * $p<0.05$ and ns $p>0.05$.

5.5.5 Conclusion of fpr1 deletion on the CCl_4 liver-injury model

Chronic liver fibrosis as induced by repeated CCl4 administration was not affected in terms of fibrosis. Fibrotic protein markers: collagen, α-SMA as well as hepatocyte proliferation (as indicated by PCNA marker) demonstrated no difference between WT and KO mice. The overlapping processes of inflammation, fibrogenesis and resolution coordinate in the chronic CCl4 model. With no protective effect demonstrated in this organ as opposed to the bleomycin-induced pulmonary fibrosis model it is apparent that the environment may have an effect on FPR1's role in fibrosis. With collagen, a key part of the ECM and the developing scar tissue in fibrosis, showing no significant difference between WT and KO there is apparent correlation with previous studies stating a redundancy for neutrophils in liver fibrosis. Defective PMN recruitment in S100A9 -/- null mice did not have an effect on liver fibrosis in the CCl4 model (Moles *et al*., 2013). FPR1 is expressed abundantly on neutrophils and was originally characterised as a chemoattractant receptor. In FPR1 deficient mice responses to chemotactic peptides will be compromised equating to an impaired neutrophil response. As neutrophils have been deemed unimportant in this chronic liver injury model it is unsurprising that WT and FPR1KO mice display no significant differences though is important to bear in mind that multiple factors are responsible for neutrophil infiltration such as S100A9, chemokine and cytokine receptors and secreted proteins and a myriad of different processes. Redundancy of these processes has been highlighted in neutrophil research therefore the lack of the effect of FPR1 may be linked to this highly conserved process.

An altered inflammatory profile was observed after the 8 week regimen which may indicate that the loss of functional *mfpr1* gene results in a compensatory response in the infiltrating immune cell populations. The altered chemotactic ability of neutrophils and macrophages may have reduced clearance of the organ following inflammation triggered by ROS generation. Loss of FPR1 will have affected expression of other receptors perhaps increasing levels of other members of the FPR family in particular mFPR2. Despite its low affinity the nature this receptor is promiscuous in nature, the absence of its high affinity counterpart could have well resulted in its up-regulation. The increased counts that were analysed by immunohistochemistry correlated with basic histology where a variable immune response was observed.

5.6 Unilateral ureter obstruction (UUO) kidney fibrosis model

5.6.1 Hypothesis

Since the UUO model is not characterised as a neutrophil-dependent mechanism fpr-/- null mice will exhibit no change in pathogenesis and resulting fibrotic phenotype.

5.6.2 Aims

Human Chronic Kidney Disease (CKD) is modelled by obstruction of the left kidney in the UUO murine setting. Since this is a mechanical model of renal fibrosis and not a toxin-mediated injury mechanism the pathogenesis is different from the other *in vivo* models investigated. For evaluation of the effect of the formyl-peptide receptor ligation and downstream signalling on renal fibrosis *in vivo* the UUO murine model was employed. Utilisation of the knockout FPR1 null mice allows the role of FPR1 activity to be elucidated in this organ setting. Examination of the left ureter's obstruction at day 5 and day 12 allowed two key parts of renal fibrosis in this model to be assessed via histological means.

5.6.3 CKD in vivo experimental models

Animal experimental models of CKD present a novel resource for the investigation of inflammation and fibrosis in the kidney to determine valid translational targets. There are a variety of different models available for the study of CKD *in vivo* which utilise different approaches including the 5/6 nephrectomy (primarily rat), adriamycin nephropathy, nephrotoxic serum (NTS) nephritis, diabetic nephropathy, chronic nephrotoxicity, ischaemia reperfusion and unilateral ureteral obstruction (UUO) tools (Eddy *et al*., 2012). Most of these models are well characterised in mechanistic investigations of CKD highlighting important contributions by such as the renin-angiotensin system (5/6 nephrectomy), mononuclear cells (adriamycin nephropathy), antibody-mediated glomerular injury (NTS), hyperglycemia (diabetic-associated CKD), folic acid and aristolochic acid (nephrotoxicity) and acute injury as precursor to CKD. All of these models are used to reduce RRT rates by enhancing renal outcome (Satoh *et al*., 2001; Eddy *et al*., 2012).

The UUO model is a valid, high throughput tool for studying renal disease on account of its pathogenesis' similarity with a variety of disorders encompassed by the term

CKD. Surgical ligation of the left ureter results in renal inflammation, progressive damage and fibrosis (Klahr & Purkerson, 1994) similar to obstructive nephropathy (ObN) in humans. Blocking of urine and waste product excretion triggers hydronephrosis and tubulointerstitial damage (Klahr, 2000). Obstruction is typified by vasoconstriction, leukocyte infiltration and fibrosis development by scar tissue formation (Guo *et al*., 2001). Structural changes are evident in the cortical region in this model by tubular dilatation and interstitial expansion. The mechanism is mediated by a mechanical injury rather than any specific injury agent. It is most commonly used in the screening of agonists and antagonists due to its ability to translate across to human disease (Zeisberg and Kalluri, 2013).

The UUO fibrosis model of progressive damage shares a degree of homology to the overall process of chronic kidney disease on account of the loss of nephron tissue. As with other fibrotic diseases fibrotic tissue is replaced by scar tissue with widespread destruction of parenchyma. As with other organ models of fibrosis *in vivo* the pathogenesis relies on an aberrant wound-healing response resulting from epithelial trans-differentiation and remodelling of the tissue. This leads to tubular dilatation and interstitial expansion with loss of parenchyma lining, atubular glomeruli generation and an interstitial-focussed deposition of extracellular matrix (ECM) fibrotic markers: collagen and fibronectin principally. Once in the fibrotic stage the UUO is virtually irreversible with permanent structural changes as the urinary pole of the capsule disconnects from the atrophic proximal tubular segment. Due to the interstitial focus and the preservation of distal tubular integrity of the model cortical region measurements are the standard method of assessing fibrosis via various staining techniques (Forbes *et al*., 2012).

5.6.4 Mechanism of UUO model

To assess the effect of the deletion of FPR1 on renal fibrosis the UUO model was utilised with surgeries performed by Christopher Fox (Research Assistant) and assisted by myself and Rachel Howarth (Technician). Following obstruction mice were harvested at 5 days and 12 days for evaluation of infiltration and fibrotic phases (shown in Fig 5.23). Contralateral controls were comprised of right uninjured kidneys providing basal levels for immunohistochemistry and histological scoring.

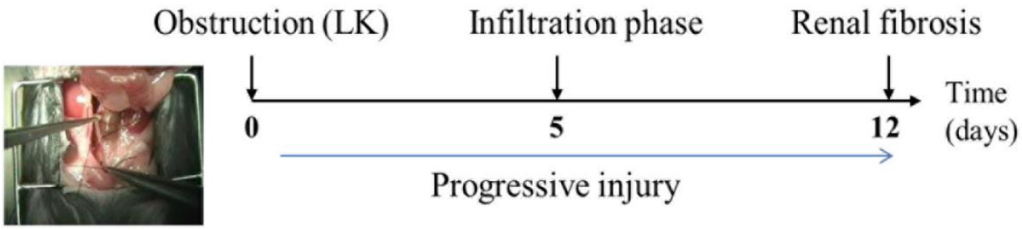

Figure 5.23: Mechanical injury of left kidneys with evaluation at early inflammatory stages (Day 5) and fibrotic phase (Day 12) following progressive damage. Obstruction of left kidneys (LK) as pictured while right kidney (RK) is left as a contralateral control for each animal.

5.6.5 Renal histology via PAS stain

Periodic acid Schiff's (PAS) staining of 4µm FFPE kidney tissue highlighted large carbohydrate structures in basement membranes and connective tissues which constitute components of renal tubules and interstitial areas respectively. Tubular dilatation and interstitial expansion are the two main histological measures of kidney damage mediated by the mechanical injury in this model. With injury tubules in cortical region dilate and interstitial area expands due to excessive extracellular matrix production. Essentially this histological scoring enables evaluation of the robustness of the UUO model by gauging the consistency of the mechanical injury through semi-quantification of cortical regions.

5 days (5D) post-ligation tubular dilatation (TD) and interstitial expansion (IE) were determined using PAS-stained tissue sections and a superimposed 10 x10 grid (Figure 5.24a). Interstitial expansion and tubular dilatation scores (%) were calculated by number of intersections located in tubular structures or interstitial areas divided by total grid intersections (maximum of 81). Any intersections present in glomeruli bodies were subsequently subtracted from the total number of intersections. WT 5D IE scores increased upon injury from mean of 9.113% (control group) to 18.76% in a significant manner ($p<0.0001$). KO mice exhibited a similar response to ureter ligation ($p<0.0001$) with the IE score rising from 9.05% (RK) to 18.31% (LK). TD scores for WT and KO UUO mice were elevated from 10.65% and 10.55% (contralateral) to 21.98% and 25.00% (ligated) respectively in similar responses ($p<0.0001$ both groups). After 5 days scoring indicates a consistent progressive injury from the initial mechanical procedure.

At 12 days post-UUO tubular dilatation (TD) or interstitial expansion (IE) scores were semi-quantified by number of grid intersections counted using a 10 x 10 grid (Figure 5.24b). IE scores displayed no difference between WT and KO mice each rising from 8.25% and 8.725% (contralateral) mean values respectively to 21.38% and 19.65% respectively in obstructed kidneys ($p<0.0001$ both groups). TD scores in WT and KO mice also increased from mean values of 10.16% and 10.55% (unobstructed) to mean values of 18.79% and 21.41% (obstructed) respectively ($p<0.0001$ both groups).

From the highly similar injury responses demonstrated in the cortical region scoring the robustness of the model is evident.

5.6.6 Day 5 UUO: Immune cell infiltrate

With histological staining displaying similar levels of injury with both WT and KO evaluation of the immune cell infiltrate in the tissue was carried out by IHC analysis using different cellular markers: CD68 for macrophages, CD3 for lymphocytes and NIMP for neutrophils (Figure 5.25 (a), (b) and (c))

The UUO is associated with leukocyte infiltration but neutrophils are regarded as having a minimal role (Figure 5.25a). At day 5 0.5571±0.1343 cells/field were counted on average for WT injured kidneys and KO had 0.7705±0.1283 cells/field ($p<0.05$) with no apparent difference between left kidneys groups ($p>0.05$). Although both genotypes displayed increased NIMP+ counts compared to contralateral control right kidneys the response is minimal.

CD68 macrophage infiltration observed in the cortices of obstructed kidneys (Figure 5.25b) exhibited little difference between WT and KO ($p>0.05$). Average IHC counts of 5.908±1.043 and 7.083±1.06 cells/field (WT and KO LK groups respectively) showed clear increases compared to contralateral WT ($p<0.01$) and KO ($p<0.001$) kidneys (1.078±0.1445 cells/field and 0.9424±0.1104 cells/field mean values respectively).

CD3 lymphocytes represent most subsets of T-cells excluding B-cells and Natural Killer (NK) cells. The determination of T-cell involvement is important to assess the immune cell infiltration (Figure 5.25c). CD3+ IHC counts increased in response to ureter ligation (WT: 45.33±3.291 cells/field; KO: 36.98±7.716 cells/field) with both genotypes exhibiting a shift in immune cell populations compared to non-injured controls ($p<0.0001$ and $p<0.001$ respectively). No difference between left-injured kidneys from WT and KO groups was elucidated ($p>0.05$).

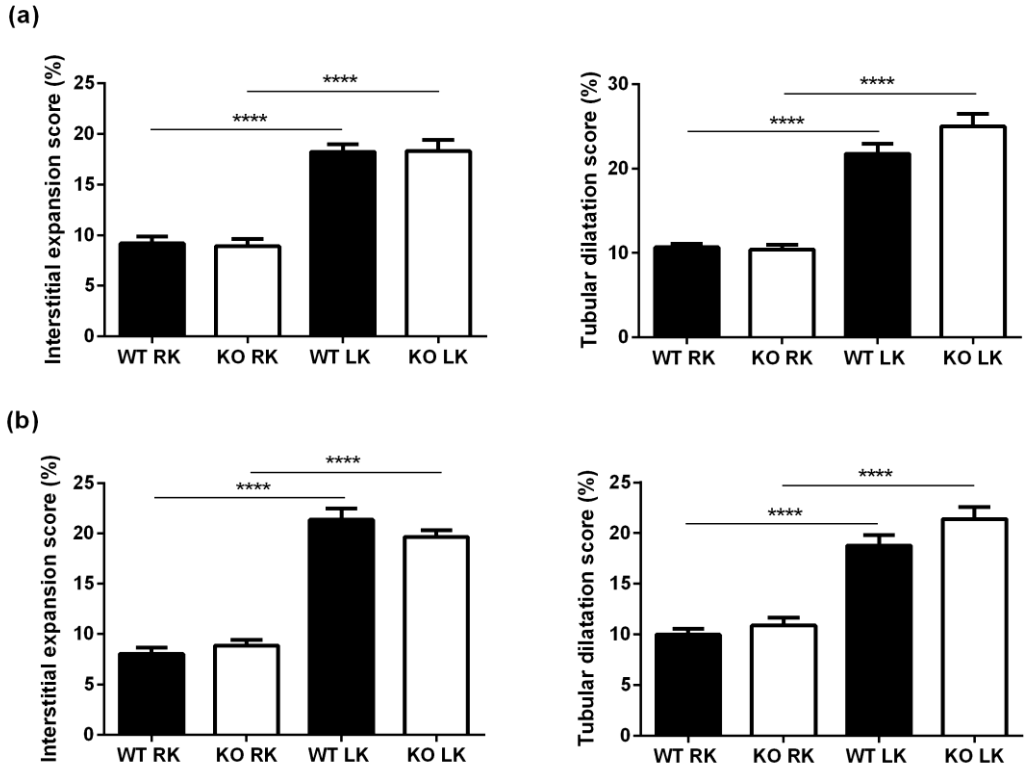

Figure 5.24: Histological scoring of UUO injured (LK) and control contralateral (RK) kidneys in WT/KO mice. Relative photomicrographs imaged at x20 magnification and analysed for interstitial expansion and tubular dilatation at (a) 5 days (n=7 WT and n=6 KO animals) and (b) 12 days (n=7 WT and n=7 KO animals) post-surgery. Results are expressed as mean grid intersections per high power field ±SEM. All p values were calculated using a one-way analysis of variance (ANOVA); **** $p<0.0001$.

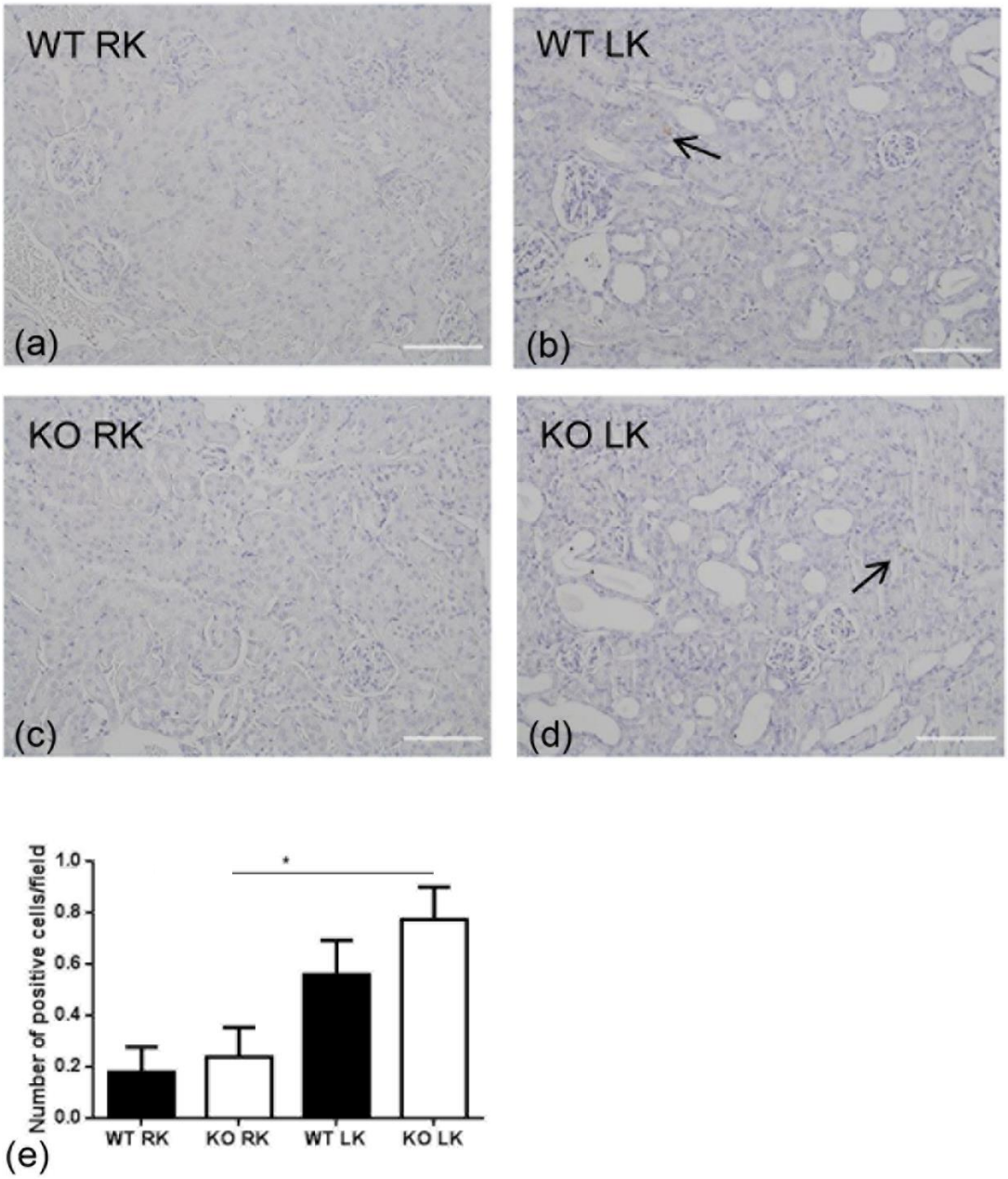

Figure 5.25 (a): Immune cell infiltration 5 days post-UUO in injured (LK) and control contralateral (RK) kidneys in WT/KO mice. Relative photomicrographs of sections indirectly stained for NIMP+ve neutrophils of (a) WT RK, (b) WT LK, (c) KO RK and (d) KO LK groups (imaged at x20 magnification, scale bar represents 100µm). Groups are as follows: n=6 WT and n=7 KO animals. Results are expressed as (e) mean positive cells per high power field ±SEM. All p values were calculated using a one-way analysis of variance (ANOVA); * $p<0.05$; ns $p>0.05$.

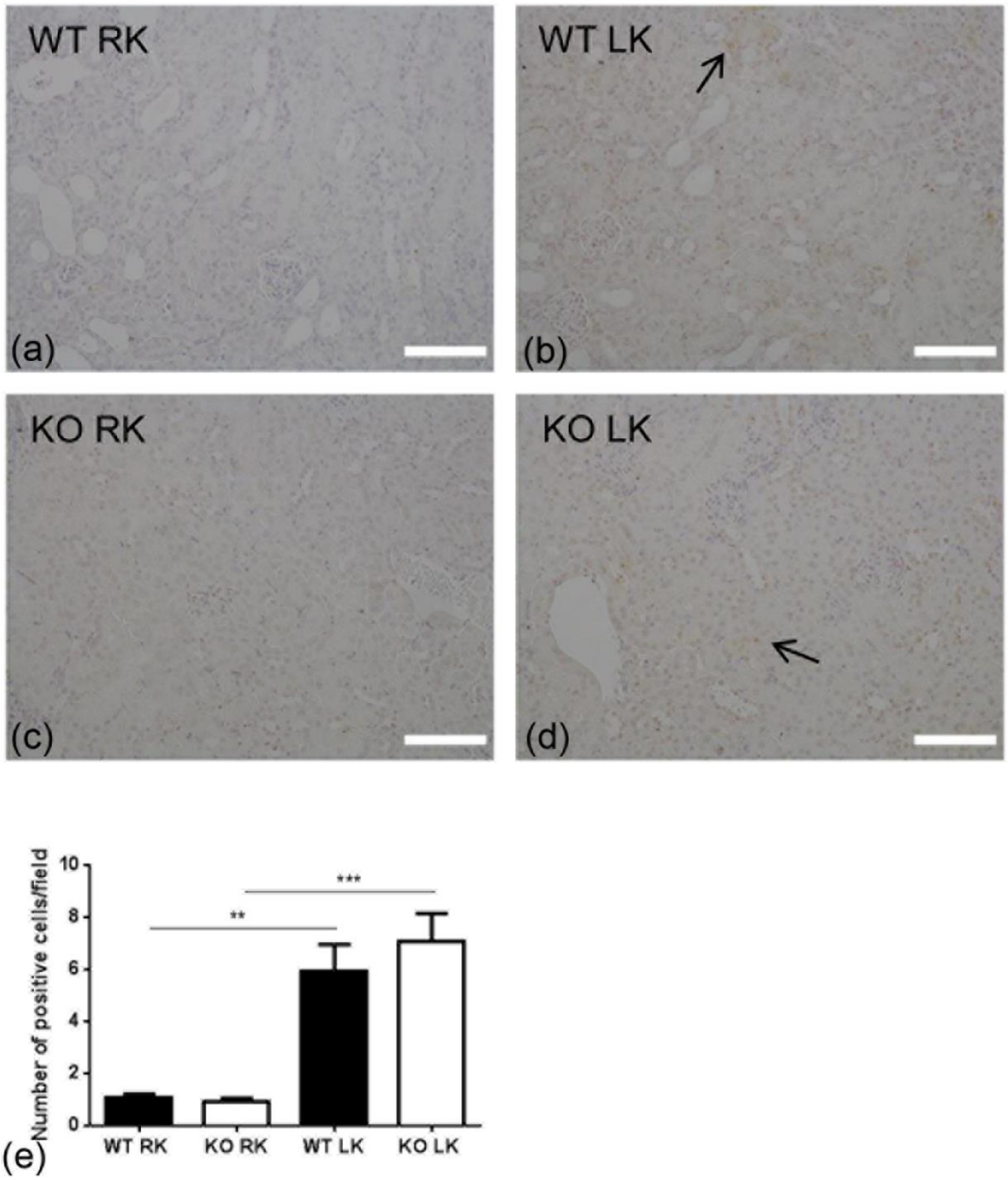

Figure 5.25 (b): Immune cell infiltration 5 days post-UUO in injured (LK) and control contralateral (RK) kidneys in WT/KO mice. Relative photomicrographs of sections indirectly stained for CD68+ve macrophages of (a) WT RK, (b) WT LK, (c) KO RK and (d) KO LK groups (imaged at x20 magnification, scale bar represents 100µm). Groups are as follows: n=6 WT and n=7 KO animals. Results are expressed as (e) mean positive cells per high power field ±SEM. All p values were calculated using a one-way analysis of variance (ANOVA); *** $p<0.001$; ** $p<0.01$.

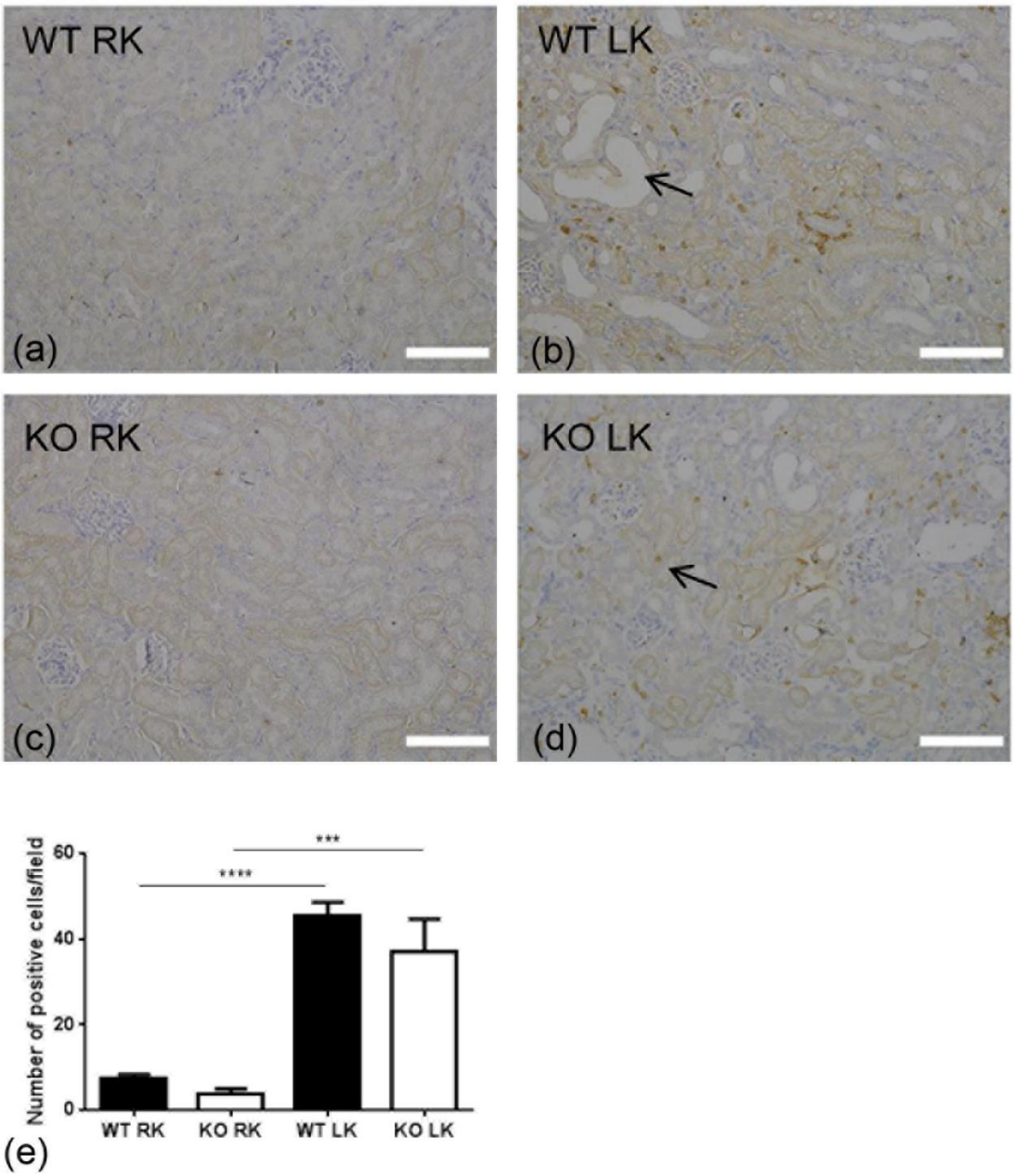

Figure 5.25 (c): Immune cell infiltration 5 days post-UUO in injured (LK) and control contralateral (RK) kidneys in WT/KO mice. Relative photomicrographs of sections indirectly stained for CD3+ve lymphocytes of (a) WT RK, (b) WT LK, (c) KO RK and (d) KO LK groups (imaged at x20 magnification, scale bar represents 100µm). Groups are as follows: n=6 WT and n=7 KO animals. Results are expressed as (e) mean positive cells per high power field ±SEM. All p values were calculated using a one-way analysis of variance (ANOVA); **** $p<0.0001$; *** $p<0.001$; ns $p>0.05$.

5.6.7 Fibrotic marker expression: PSR, ALPHA-SMA

At day 12 post-ligation fibrotic markers were evaluated via immunohistochemistry to determine if differences were exhibited between WT and KO injured mice (Figure 5.26). PicroSiriusRed (PSR) staining of collagen in the ECM displayed no difference between genotypes in response to obstruction. WT left-ligated kidneys displayed a significant response to progressive injury increasing from control RK mean value of 1.517±0.571 % area to 8.457±0.5707 % area ($p<0.0001$). A similar fibrotic response was shown by KO mice rising from contralateral mean of 0.7351±0.2031 % to 8.057±0.9559 % in injured left kidneys ($p<0.0001$). Most collagen deposition was observed by tubular wall regions and glomeruli fitting with this models pathogenesis.

Alpha-SMA IHC, a marker of activated myofibroblasts presumably abundant after this length of time after obstruction due to the progressive nature of the obstruction damage effects and fibrosis development. Typically, fibrosis begins to develop after 10 days post-ligation with wide scale obliteration by 14 days (Shao *et al*., 2010). Densitometry of anti-α-ASMA stained FFPE-sections (Figure 5.27) demonstrated an increase in obstructed compared to right kidneys but this change was relatively small. Both WT and KO showed elevated α-SMA % area in cortical regions of injured kidneys (LK) compared to controls (RK). WT mice demonstrated this with RK % area (0.7667±0.09215 mean value) escalating with injury to 2.826±0.3955 % (mean area, $p<0.0001$). Knockouts were subject to a similar fibrotic response evident by day 12 rising from 1.156±0.1243 % area to 2.837±0.3305 % area mean value in RK and LK groups respectively ($p<0.05$).

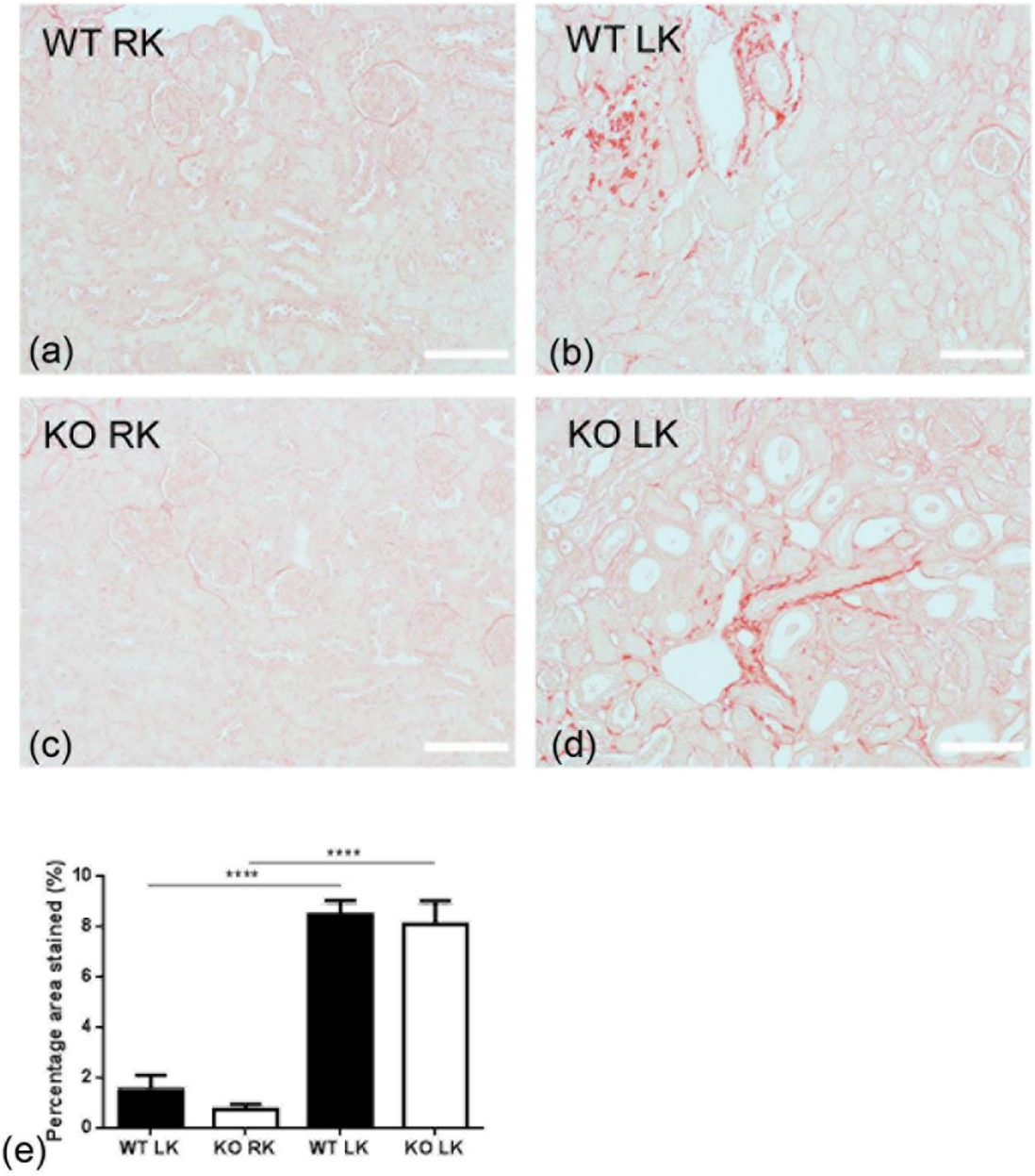

Figure 5.26: PSR staining of kidneys 12 days post-UUO in injured (LK) and control contralateral (RK) kidneys in WT/KO mice. Relative photomicrographs of sections directly stained for collagen I/III of (a) WT RK, (b) WT LK, (c) KO RK and (d) KO LK groups (imaged at x20 magnification, scale bar represents 100µm). Groups are as follows: n=7 WT and n=7 KO animals. Results are expressed as (e) mean percentage area per high power field (hpf) ±SEM. All p values were calculated using a one-way analysis of variance (ANOVA); **** $p<0.0001$.

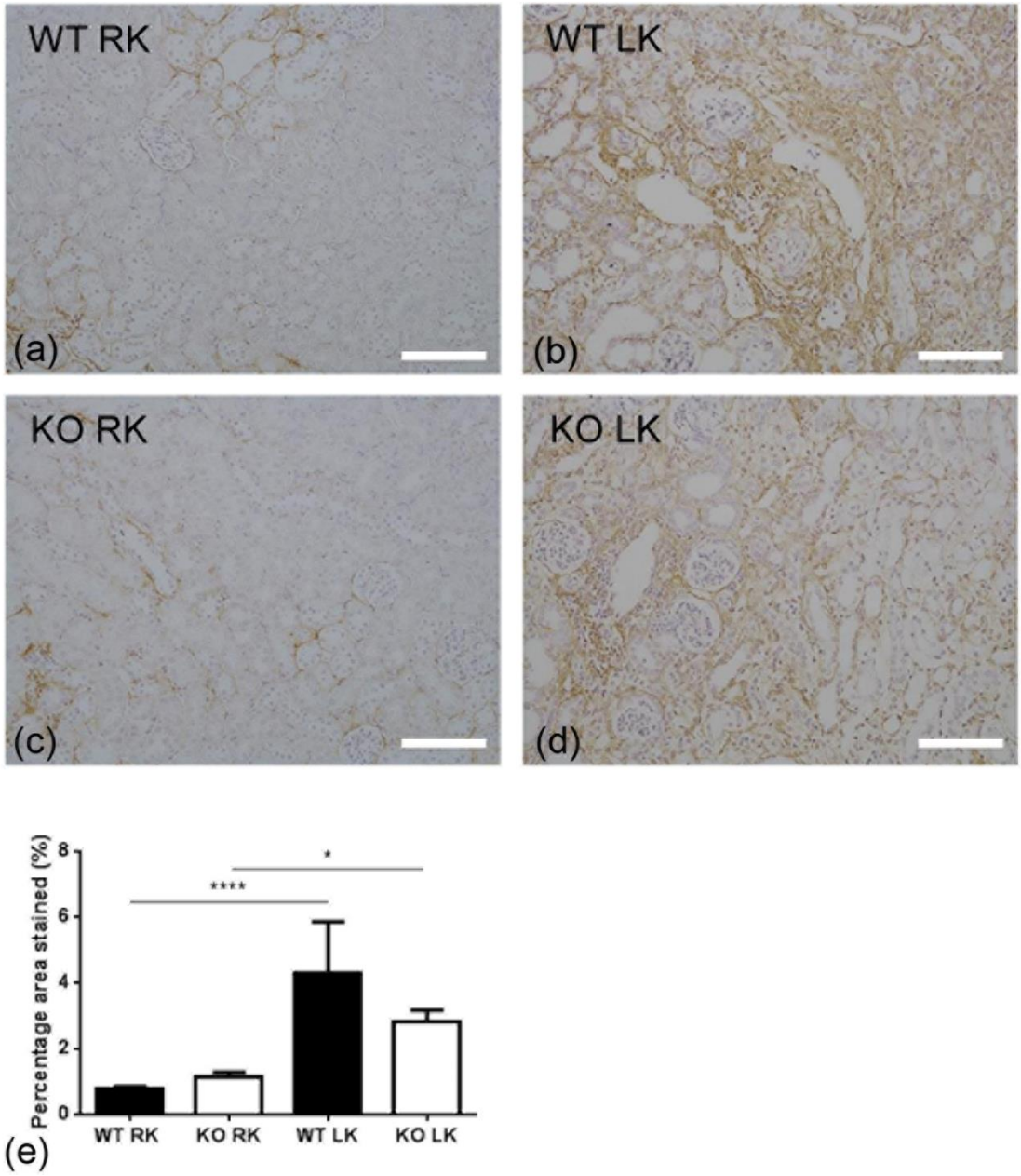

Figure 5.27: α-SMA production by kidneys 12 days post-UUO in injured (LK) and control contralateral (RK) kidneys in WT/KO mice. Relative photomicrographs of sections indirectly stained for α-SMA of (a) WT RK, (b) WT LK, (c) KO RK and (d) KO LK groups (imaged at x20 magnification, scale bar represents 100μm). Groups are as follows: n=7 WT and n=7 KO animals. Results are expressed as (e) mean percentage area per high power field ±SEM. All p values were calculated using a one-way analysis of variance (ANOVA); **** $p<0.0001$; * $p<0.05$; ns $p>0.05$.

5.6.8 Immune cell infiltration at day 12 post-UUO ligation

As for immune cells no difference in macrophage (CD68+ve) cells was exhibited at 12 days between genotypes (Figure 5.28). Even with the progressive injury the infiltrate remains the same when comparing the different genotypes. WT and KO control kidneys increased from 1.455±0.2473 cells/field and 1.364±0.2033 cells/field respectively to 6.66±0.8541 cells/field and 7.063±0.3254 cells/field respectively ($p<0.0001$). KO mice elicited a similar effect upon injury with an increase in mean counts of 1.364±0.2033 cells/field to 7.063±0.3254 cells/field ($p<0.0001$).

CD3+ lymphocyte staining via IHC of WT and KO kidney sections (Figure 5.29) revealed significant responses to progressive injury over contralateral controls ($p<0.0001$) albeit less T-cells were recruited than at 5 days post-ligation. WT mean counts increased from 1.455±0.2473 cells/field (RK control) to 13.09±1.27 cells/field (LK) while KO mean counts rose from 1.364±0.2033 cells/field (RK control) to 9.457±0.5241 cells/field (LK) in a significant manner ($p<0.0001$). With ablation of the gene WT LK and KO LK exhibited a significant difference ($p<0.01$). Apparently deficiency of this formyl-peptide receptor-1, a major chemoattractant receptor leads to downstream effects on T-cell infiltration in the fibrotic kidney.

5.6.9 Conclusion of fpr1-deletion effect on kidney fibrosis in UUO model

From histological scoring, immune cell IHC counts and ECM deposition at 5 days and 12 days post-surgery there was apparently no difference between injured kidneys of WT and KO mice. The nature of the injury process in this model was mechanical in origin resulting in a progressive development of fibrosis. The microenvironment of the kidney is different from that of the lung and liver which leads to an alternative fibrotic pathogenesis. Bleomycin and carbon tetrachloride induce acute injury processes triggering fibrogenesis and ultimately fibrosis if left unchecked. Ligation of kidneys in the UUO model instigates a very different pathogenesis and both WT and KO mice develop renal fibrosis in a similar manner. Perhaps this organ model is not the right method of analysing the role of *fpr1* due to the lack of a neutrophil response. Without a motivated granulocyte-driven infiltration phase formyl-peptide may not have a demonstrable effect in this setting. However, in an acute injury focussed methodology such as ischaemia reperfusion this chemoattractant receptor may have more a significant effect.

The effect of FPR1 deletion on the development of kidney fibrosis via mechanical injury was quite ambiguous. The process of the injury via ligation of the left ureter is distinct from the acute injury mediated by bleomycin in the lung or toxin-mediated liver fibrosis in the CCl_4 model. From the endpoints in this study there is no difference in the mechanical injury and the resulting fibrotic phenotypes as indicated by histological scoring and ECM deposition. As with the liver the fibrotic process in the renal setting is different from the pulmonary bleomycin model with regards to the microenvironment and the caveats of the UUO model itself. The pathogenesis of this model is not neutrophil-driven which may affect the role of FPR1 on the development of fibrosis.

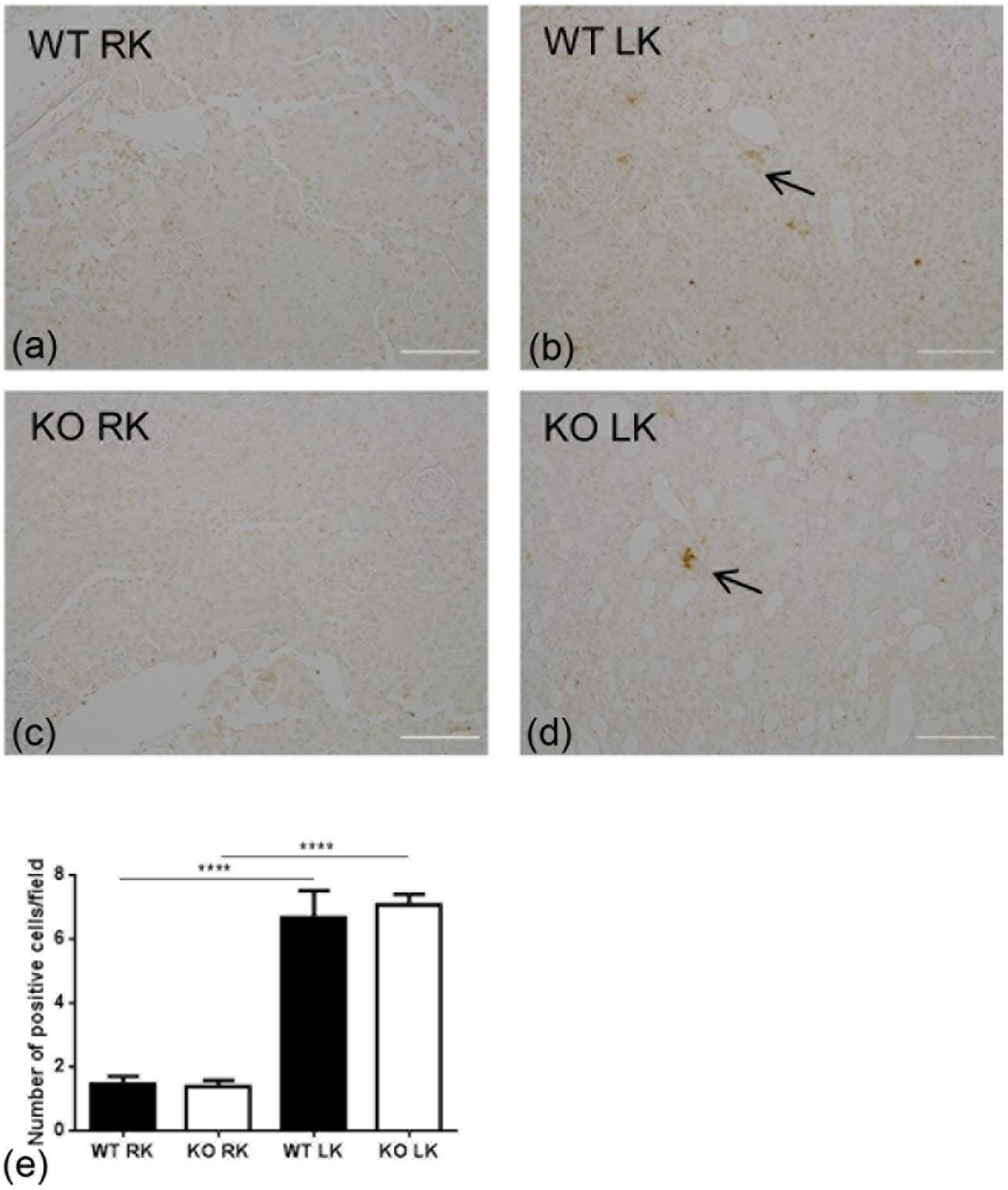

Figure 5.28: Macrophage infiltration 12 days post-UUO in injured (LK) and control contralateral (RK) kidneys in WT/KO mice. Relative photomicrographs of sections indirectly stained for CD68+ve macrophages of (a) WT RK, (b) WT LK, (c) KO RK and (d) KO LK groups (imaged at x20 magnification, scale bar represents 100µm). Groups are as follows: n=7 WT and n=7 KO animals. Results are expressed as (e) mean positive cells per high power field ±SEM. All p values were calculated using a one-way analysis of variance (ANOVA); **** $p<0.0001$.

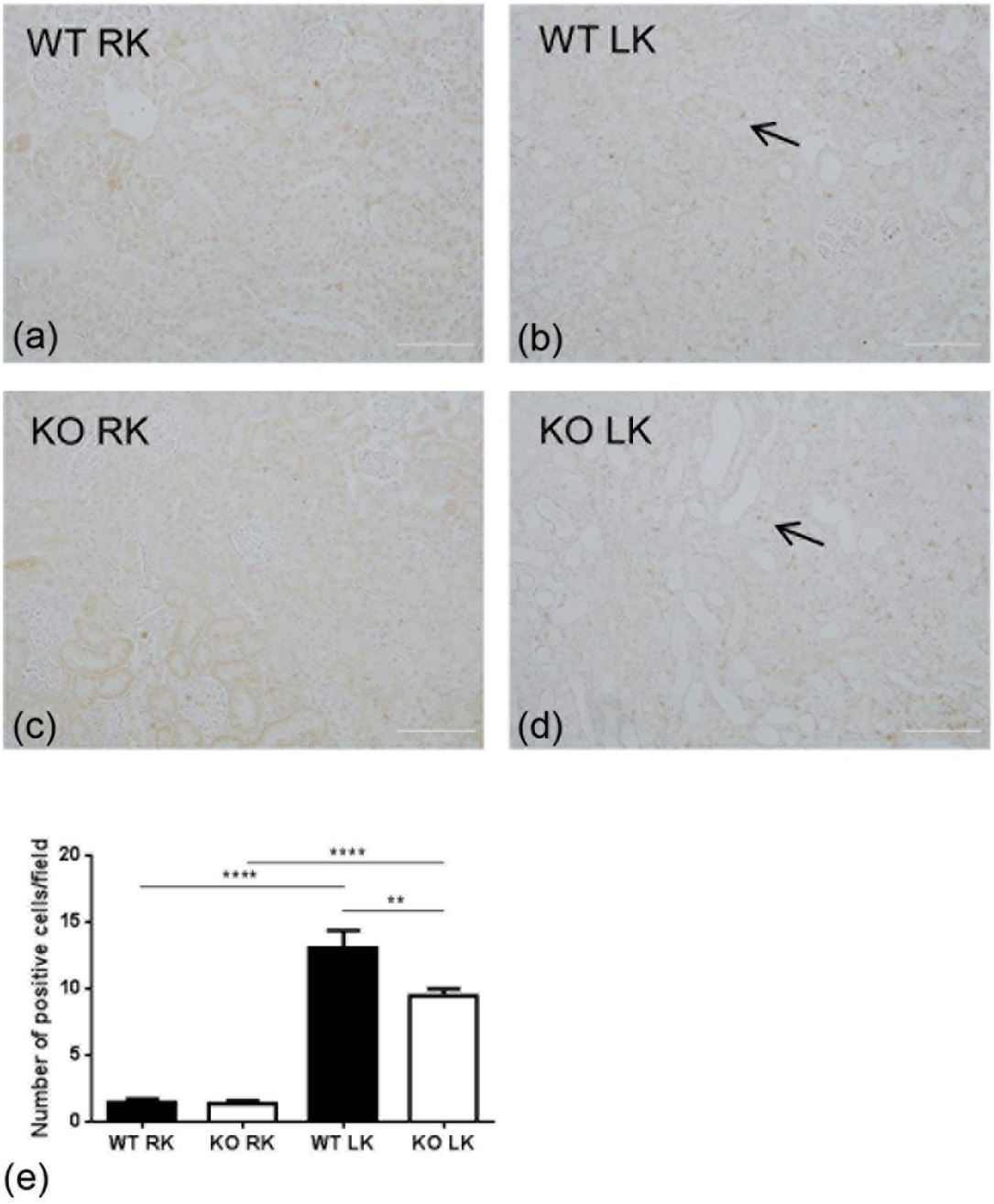

Figure 5.29: Lymphocyte infiltration 12 days post-UUO in injured (LK) and control contralateral (RK) kidneys in WT/KO mice. Relative photomicrographs of sections indirectly stained for CD3 of (a) WT RK, (b) WT LK, (c) KO RK and (d) KO LK groups (imaged at x20 magnification, scale bar represents 100µm). Groups are as follows: n=7 WT and n=7 KO animals. Results are expressed as (e) mean positive cells per high power field ±SEM. All p values were calculated using a one-way analysis of variance (ANOVA) **** $p<0.0001$; ** $p<0.01$; ns $p>0.05$.

5.7 Subcutaneous bleomycin skin fibrosis model

5.7.1 Hypothesis

As the SC bleomycin model does not follow the same pattern as the acute intratracheal instillation of bleomycin (with the latter's pathogenesis consisting of an inflammatory and fibrotic phases) the *fpr* transgenic mutants will not display the same protective effect as this dependent on an influx of neutrophils specifically in the pulmonary setting.

5.7.2 Aims

Determination of the effect of *fpr1*-deletion on skin and lung fibrosis by subcutaneous (s.c.) injection of bleomycin for 28 days. Systemic scleroderma has been previously determined to be caused by SC administration of bleomycin every other day (Fullard *et al*., 2012). This rare autoimmune disease in humans shows fibrotic patterns and lesion formation in skin in an aberrant wound-healing response and is successfully modelled by repeated bleomycin administration to focal areas (Ardett, 2014). With daily injections the systemic effect is greater and fibrosis develops in the lungs. This contrasts with the acute injury induced by intratracheal delivery of the same drug characterised previously with reduced mortality and severity of response (Yamamoto *et al*., 1999; Gupte *et al*., 2009).

5.7.3 Weight change over 28 day period for different treatment groups

Saline treated mice stayed consistently within 10% of original weight while WT bleomycin group displayed a stark decrease (10-20% loss) upon week 3 of injection regimen with recovery to basal weight after 4 weeks. KO saline and bleomycin groups remained at roughly similar levels throughout treatments displaying no significant weight loss at week 3 unlike WT mice (Figure 5.30).

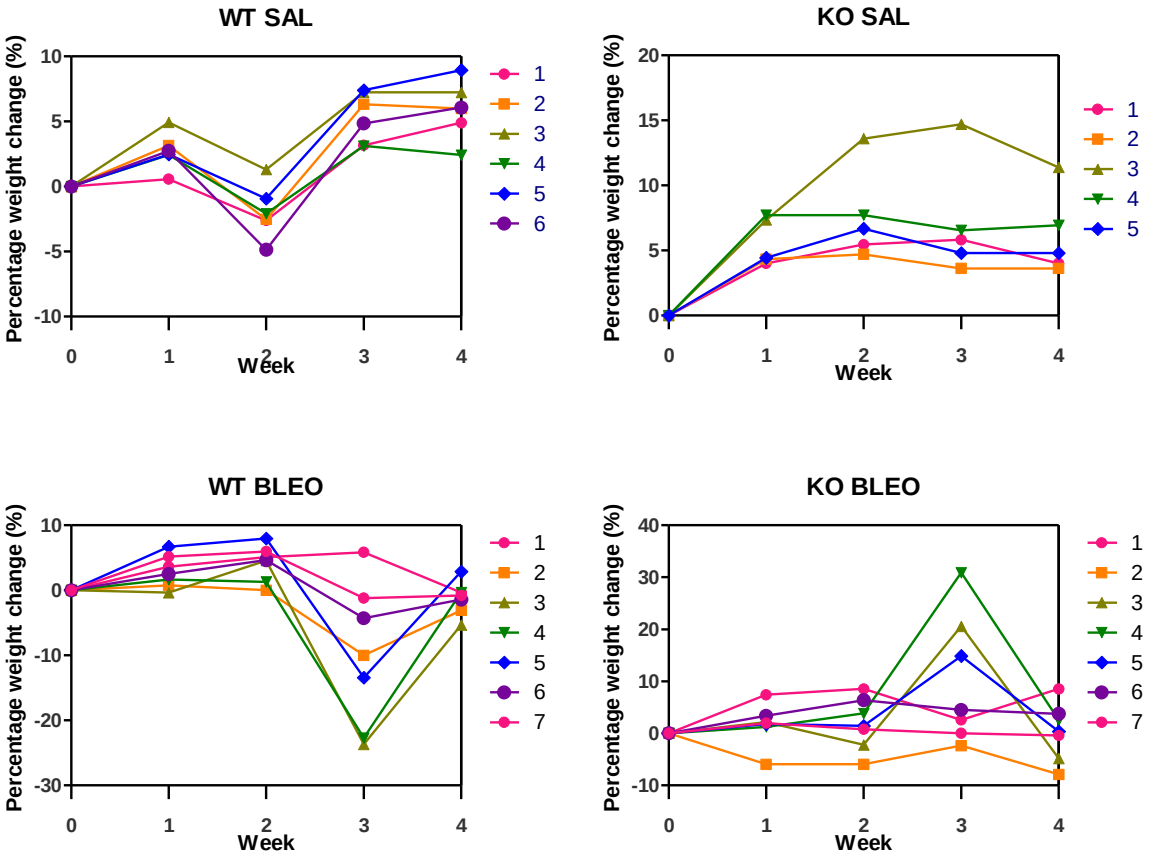

Figure 5.30: Weight change over course of 4 week regimen of daily bleomycin SC injection. Percentage weight change calculated accordingly from weight at day 0 and measured at weekly intervals in saline and bleomycin-treated WT and KO mice. Groups were as follows: (a) WT SAL (n=6), (b) WT BLM (n=7), (c) KO SAL (n=5) and (d) KO BLM (n=7).

5.7.4 Pulmonary fibrosis extracellular development following SC bleomycin

Skin fibrosis was not induced by the daily bleomycin injections but the systemic application of the drug did have an effect in the lung setting. PSR staining showed an increase in collagen deposition with bleomycin-treated mice regardless of genotype to 3.884% and 3.508% area stained from 1.292% and 1.780% (controls) in WT and KO mice respectively ($p>0.05$). Both wild type and knockout showed an increase when comparing saline and bleomycin groups but no significant difference observed between different genotype bleomycin groups (Figure 5.31).

5.7.4.1 *Hydroxyproline content of lung right lobe subjected to daily s.c. bleomycin injections*

Total collagen content as measured by this hydroxyproline assay demonstrated no significant difference between saline and bleomycin-treated or wild type and knockout groups (Figure 5.32). Mean values interpolated from an 8-point standard curve ranged from 1.028 to 1.224 with no significant response to repeated injury. Perhaps due to the systemic nature of the repeated injury response to bleomycin rather than a targeted bronchiolocentric mechanism pulmonary fibrosis does not develop to such a severity as observed previously.

5.7.5 Pulmonary fibrogenic marker: secreted TGFβ1 levels present in BAL fluid

Bronchoalveolar lavage (BAL) fluid from saline control and bleomycin-treated WT and KO mice was tested for levels of TGFβ1 cytokine via duoset ELISA (Figure 5.33). Upon repeated systemic injury with BLM the pro-fibrogenic cytokine is up-regulated compared to controls. WT and KO saline controls (mean values of 33.08±6.147pg/ml and 43.66±5.373pg/ml respectively) increased to 151.3±36.12pg/ml and 148.5±42.26pg/ml with SC bleomycin administration ($p<0.05$ both groups). After 28 days of bleomycin injections the responses by WT and KO mice is similar with no difference in response ($p>0.05$).

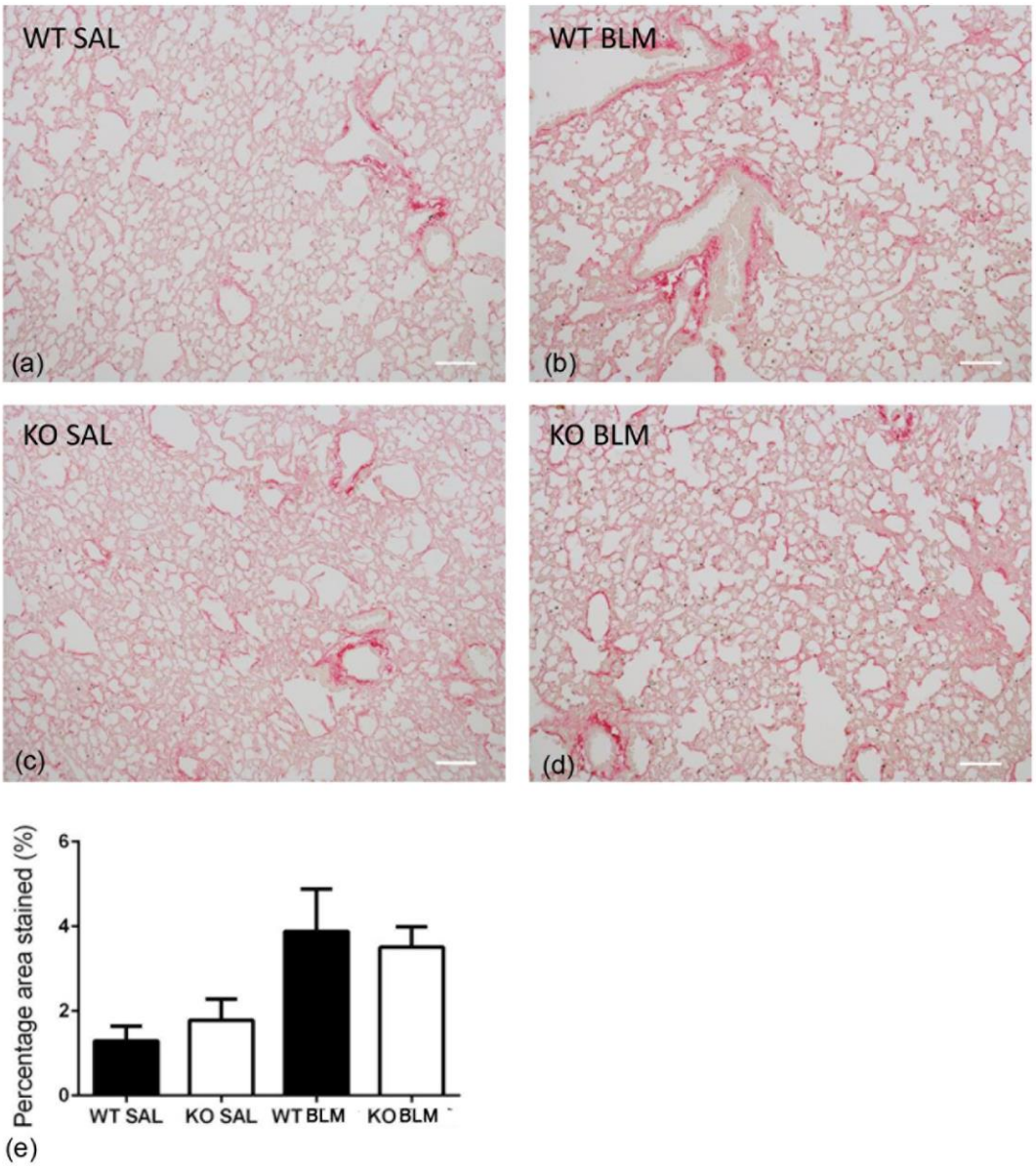

Figure 5.31: Collagen staining by PSR in lung sections from mice subcutaneously injected with bleomycin for 28 days. Sections from (a) WT SAL (n=6), (b) WT BLM (n=7), (c) KO SAL (n=5) and (d) KO BLM (n=7) groups were analysed via densitometry to yield (e) mean percentage (%) area (scale bars = 100μm). All p values calculated using one-way analysis of variance (ANOVA); ns $p>0.05$.

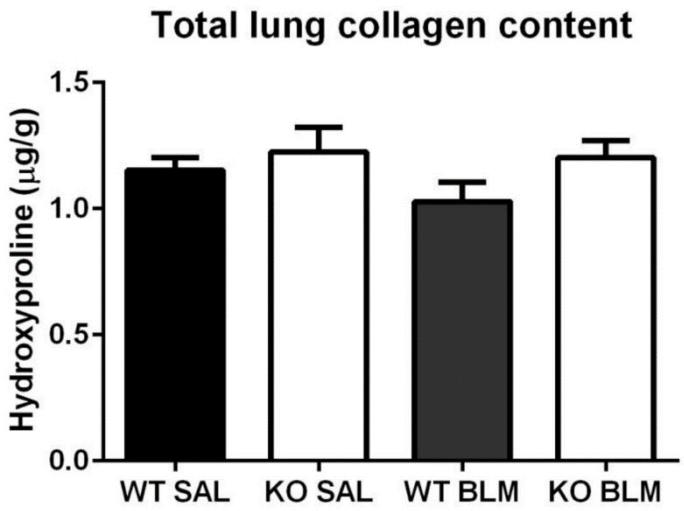

Figure 5.32: Hydroxyproline content of lung right lobes of 28 day s.c. bleomycin model. Lung homogenate of WT SAL (n=6), WT BLM (n=7), KO SAL (n=5) and KO BLM (n=7) groups were assayed for hydroxyproline content which was calculated by interpolation on Graphpad Prism from an 8-point set of hydroxyproline standards. Absorption readings normalised to the weight of each lobe measured at harvest prior to acid hydrolysis with results represented as mean of duplicate wells in µg/g±SEM. Statistical significance determined by using a one-way analysis of variance (ANOVA); ns, $p>0.05$

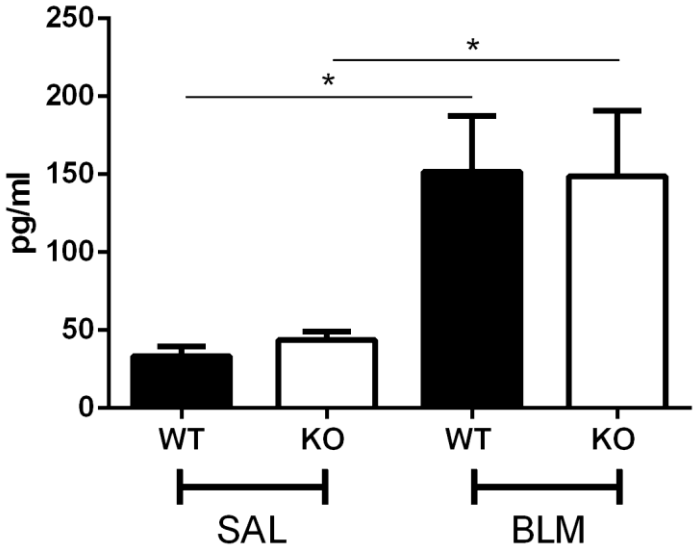

Figure 5.33: TGF-β1 cytokine secretion in WT/KO BAL fluid with SC bleomycin administration. BAL perfused from WT SAL (n=6), WT BLM (n=7), KO SAL (n=5) and KO BLM (n=7) groups assayed by duoset ELISA. Results expressed as a mean of duplicate wells in pg/ml±SEM. All p values calculated using one-way analysis of variance (ANOVA); * $p<0.05$, ns $p>0.05$.

5.7.6 Mediator levels in lung homogenate in WT and FPR KO mice ascertained via MSD multiplex ELISA

Multiple pro-inflammatory cytokines were analysed via an MSD platform designed for IL-1β, MCP-1, IL-6 and KC analytes (Figure 5.34 a-d respectively). All showed increased levels following bleomycin treatment in both WT and KO mice. Basal level analyte measurement observed with saline groups was consistent with different markers. IL-1β was significantly elevated upon injury with BLM in WT mice, mean value of 7.07±1.519 pg/ml vs. 1.753±0.268 pg/ml in saline control ($p<0.01$). It is worth noting that the 7 mice within this group exhibit a high degree of variability with an outlier of 14.1pg/ml. KO mice elicited a similar response with bleomycin treatment ($p>0.05$) with a lot less variability in cytokine level.

MCP-1 cytokine levels demonstrated clear increases from control to BLM groups in lung homogenate. WT saline-treated mice produced 34.71±3.431pg/ml which was subsequently increased to 68.43±9.778pg/ml in a significant response ($p<0.05$). KO mice also demonstrated an increase in MCP-1 from 29.42±3.883pg/ml to 72.87±5.87pg/ml in control and bleomycin groups respectively ($p<0.01$). The difference in the responses with regards to this cytokine may in fact be due to variable levels in the WT BLM group ranging from 28.19 to 112.2pg/ml.

KC, the mouse equivalent of human IL-8, was another analyte measured in lung homogenate which in fact displayed a significant response to SC bleomycin. WT mice secreted a mean value of 7.616±0.9812pg/ml in control group and increased to 19.3±3.887pg/ml with BLM ($p<0.05$). KO mice elicited a similar response rising from 7.358±1.663pg/ml to 18.52±1.34pg/ml in saline and bleomycin groups respectively ($p<0.05$).

IL-6 cytokine was significantly increased in WT with bleomycin repeated treatment with injury rising to 82.6±34.35 pg/ml ($p<0.05$) but did not increase significantly in KO groups ($p>0.05$). No apparent difference was observed between knockout and wild type bleomycin groups with any of the analytes.

Bleomycin daily treatment does appear to be having an effect on cytokines in the lung environment even after 28 days possibly due to repeated dosing but the effect is distinct from acute lung injury response induced by a more targeted dosing.

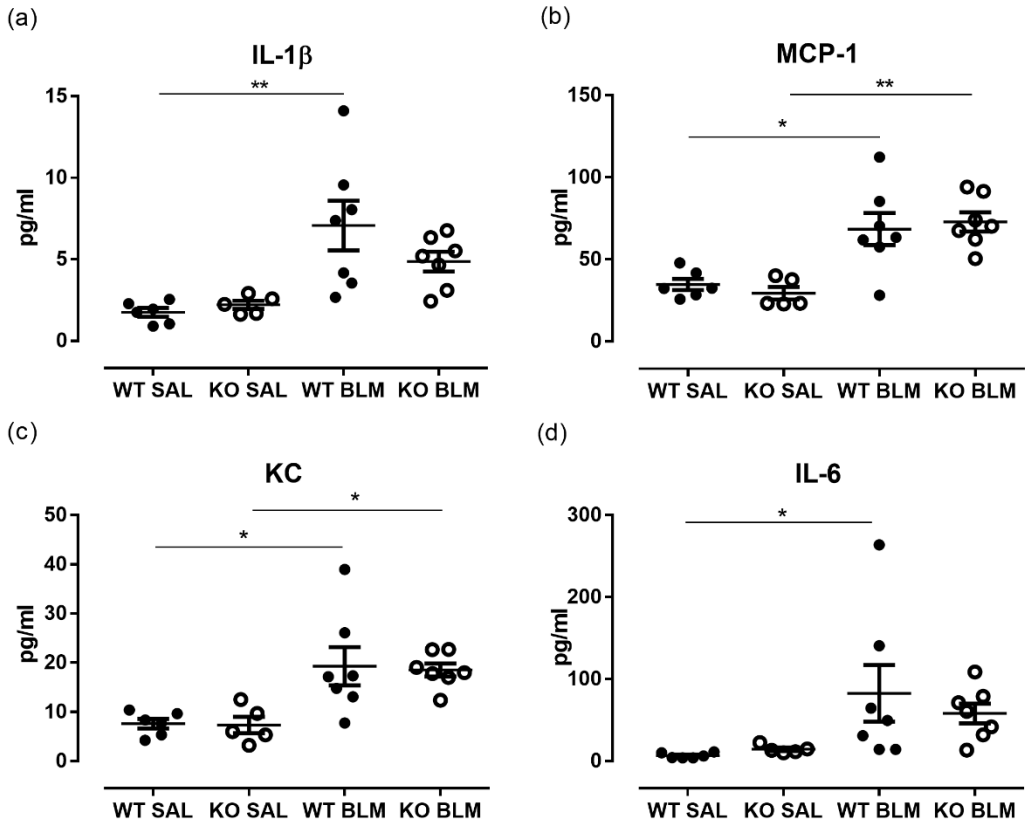

Figure 5.34: Inflammatory cytokine mediators in SC bleomycin model. Lung homogenate from WT SAL (n=6), WT BLM (n=7), KO SAL (n=5) and KO BLM (n=7) groups assayed for pro-inflammatory cytokine levels pf (a) IL-1β, (b) MCP-1. (c) KC and (d) IL-6 was measured by MSD as a mean of duplicate wells in pg/ml ±SEM. All p values calculated using one-way analysis of variance (ANOVA); * $p<0.05$, ** $p<0.01$ and ns $p>0.05$.

5.7.7 Conclusion of fpr1 deletion in subcutaneous bleomycin model

Although this model was originally employed to investigate another method of bleomycin administration which would hypothetically induce fibrosis in two separate organs the data generated indicates that it at least partially failed. Skin fibrosis did not develop after 28 days of daily injections with no dermal thickening in bleomycin-treated mice irrespective of genotype. Indeed variable responses were observed in control groups potentially indicating an inflammatory reaction despite no stimulus, perhaps repeated injections triggered a wound-healing response of its own or injection sites were compromised by infection triggering an immune response. Due to these results the effect of FPR1 on skin fibrosis *in vivo* could not evaluated.

From the systemic effects of bleomycin administration over the 28 days the lungs of WT and KO mice were subject to subtle changes in ECM proteins and fibrogenic triggers such a TGF-β. Despite not being an acute response-driven pathogenesis there is a definite effect after 28 days but with little difference between genotypes potentially indicating that FPR1 acts primarily on the wound-healing process via neutrophil-mediated mechanisms.

5.8 Summary of *fpr1* deletion in non-pulmonary fibrosis *in vivo* models

- Carbon tetrachloride-induced liver injury and fibrosis model
    - Slightly reduced inflammatory response with ablation of fpr1 expression but fibrogenic mechanisms unaffected in acute CCl4 snapshot post-injury time points.
    - FPR1KO mice exhibit no effect on chronic CCl4 –mediated liver fibrosis with regards to ECM production.

- Unilateral ureteral obstruction (UUO) renal fibrosis model
    - Infiltration (day 5 post-surgery) and fibrotic (day 12 post-surgery) phases exhibited no differences in histological features or IHC profile, *fpr1* deletion has no effect on the pathogenesis of this model.

- Subcutaneous bleomycin systemic injury model
    - Daily treatment of bleomycin elicited a moderate response in the lungs of mice. FPR1KO animals did not respond differently to repeated injury with bleomycin.
    - Intratracheal bleomycin administration results in a pulmonary-specific injury and localised disease development unlike this model.

6 FPR expression profile in human/murine cells

6.1 Hypothesis

Regardless of whether cells are immune or architectural such as fibroblasts and epithelial cells the expression of the FPR family will be elevated with inflammatory stimuli.

6.2 Aims

Characterisation of the expression in multiple cell types is an important step in determining the role of the formyl peptide receptor in fibrogenic/fibrotic mechanisms. Through the use of multiple modalities FPR expression will be determined in cell lines and primary cells/tissue. *In vivo* effects of FPR1 have been observed in this present project and in other investigations, so it was logical to investigate FPRs expression profile.

6.3 Human FPR1/2 expression in a variety of different cell types

6.3.1 HEK transfectants overexpressing FPR1 and FPR2

To evaluate human FPR1 and FPR2 gene expression human embryonic kidney (HEK) cells were stably transfected with control plasmids. Positive control cell lines HEK HFPR Ga16 Cl.1 and HEK Ga16 pGENIRES neo FPRL-1 Cl.5 overexpressed FPR1 and FPR2 receptors respectively. Depending on the cell line different selection components supplemented the respective growth media. Human FPR1 expression in FPR1-HEK cells was elevated compared to FPR2-HEK cells (Figure 6.1(a)) with a mean fold change of 2.867±1.9 ($p>0.05$). In turn FPR2-HEK cells demonstrated high expression compared to basal, negligible levels in FPR1-HEK negative controls (Figure 6.1(b)) with a 4557.34 fold increase ($p<0.0001$).

6.3.2 Immune cell FPR cell expression

Due to the high amount of FPR1/FPR2 expression in these control cell lines they were ideal positive controls for gene and potentially protein expression. Neutrophils are typically well known for their abundancy of these membrane-bound chemoattractant receptors and may also be good controls for human FPR expression. In Figure 6.2

expression of the FPRs is clearly elevated in neutrophils over the other immune cells and the control cells lines (both positive and negative).

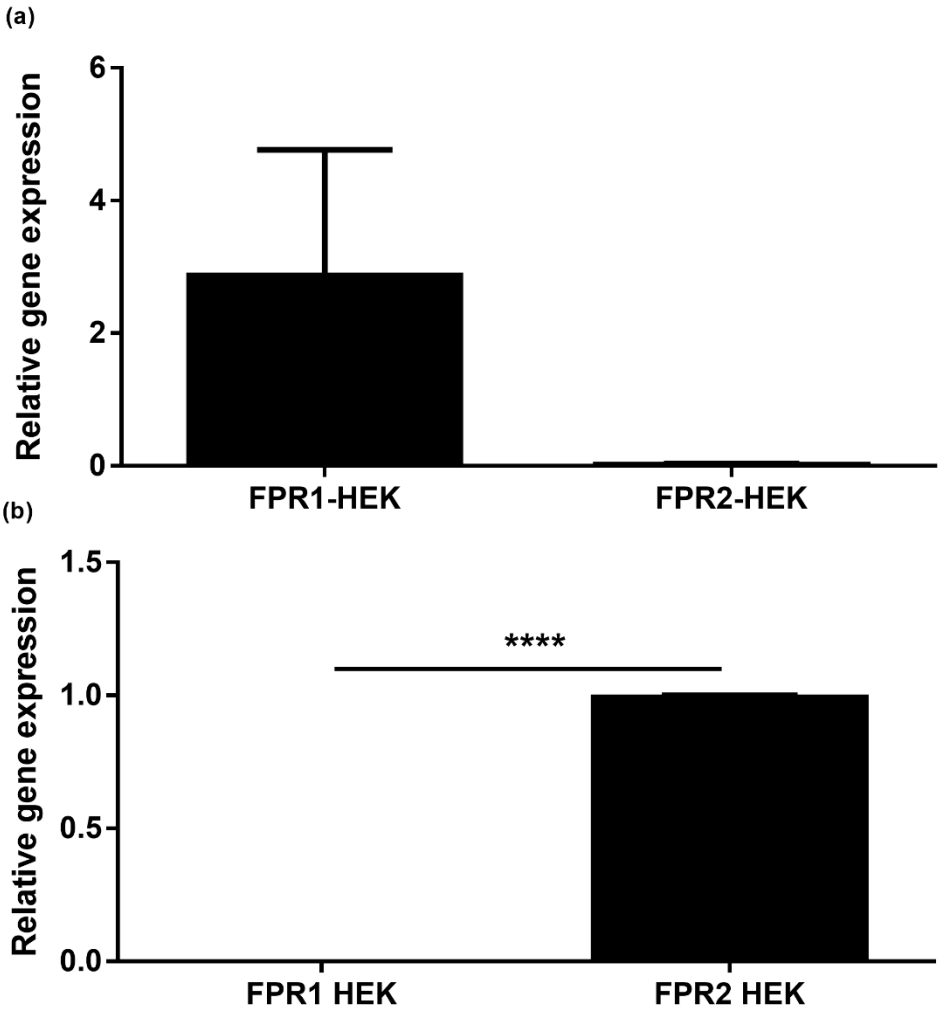

Figure 6.1: Validation of human FPR1 and FPR2 in control cell lines via real-time PCR. Quantitative PCR determined mRNA levels of (a) FPR1 and (b) FPR2 in FPR1-/FPR2-HEK transfected cells. Results calculated as mean relative fold change compared to respective control (normalised to GAPDH housekeeping gene). Data is representative of 3 independent experiments. All p values determined by an unpaired *t*-test, **** $p<0.0001$.

Both FPR2-HEK and T-cells had minimal FPR1 mRNA levels compared to that of FPR1-HEK (mean of 2.867±1.9), primary neutrophils (mean of 126.5±111.9) and macrophages (mean of 6.574±3.187).

While changes in HFPR1 expression between different cell types were not significant, HFPR2 mRNA levels were significantly increased between positive and negative controls (FPR2-HEK and FPR1-HEK respectively, $p<0.001$). PMNs exhibited a high level of expression compared to FPR1-HEK negative control ($p<0.0001$), FPR2-HEK ($p<0.001$), primary macrophages ($p<0.0001$) and T-cells ($p<0.0001$).

6.3.3 THP-1, monocytic cell line

THP-1, a non-adherent monocyte cell line was activated with PMA (5ng/ml) to trigger expression of its adhesion molecules thereby differentiating the cells to an activated, adherent form. This cell line has been extensively utilised to investigate macrophage differentiation enabling FPR expression to be determined in pro-inflammatory and anti-inflammatory phenotypes. Plated cells were treated accordingly to induce differentiation to an M1 (classically activated) or M2 (alternatively activated) phenotype via IFN-γ and IL-4/IL-13 treatments respectively. In PMA-activated THP-1 cells expression was significantly upregulated from 1.051±0.029 to 4.129±0.011 mean fold change with LPS (100ng/ml) treatment ($p<0.0001$). M1-activated THP-1 cells exhibited no such increase with stimulus but actually a significant decrease ($p<0.05$). M2-activated THP-1 cells also had increased FPR1 expression from untreated controls to LPS-treated groups with a mean fold change from 1.151±0.017 to 3.824±0.047 respectively ($p<0.0001$). M2 macrophages have been typically characterised as having a role in the wound-healing response (Wynn, 2004).

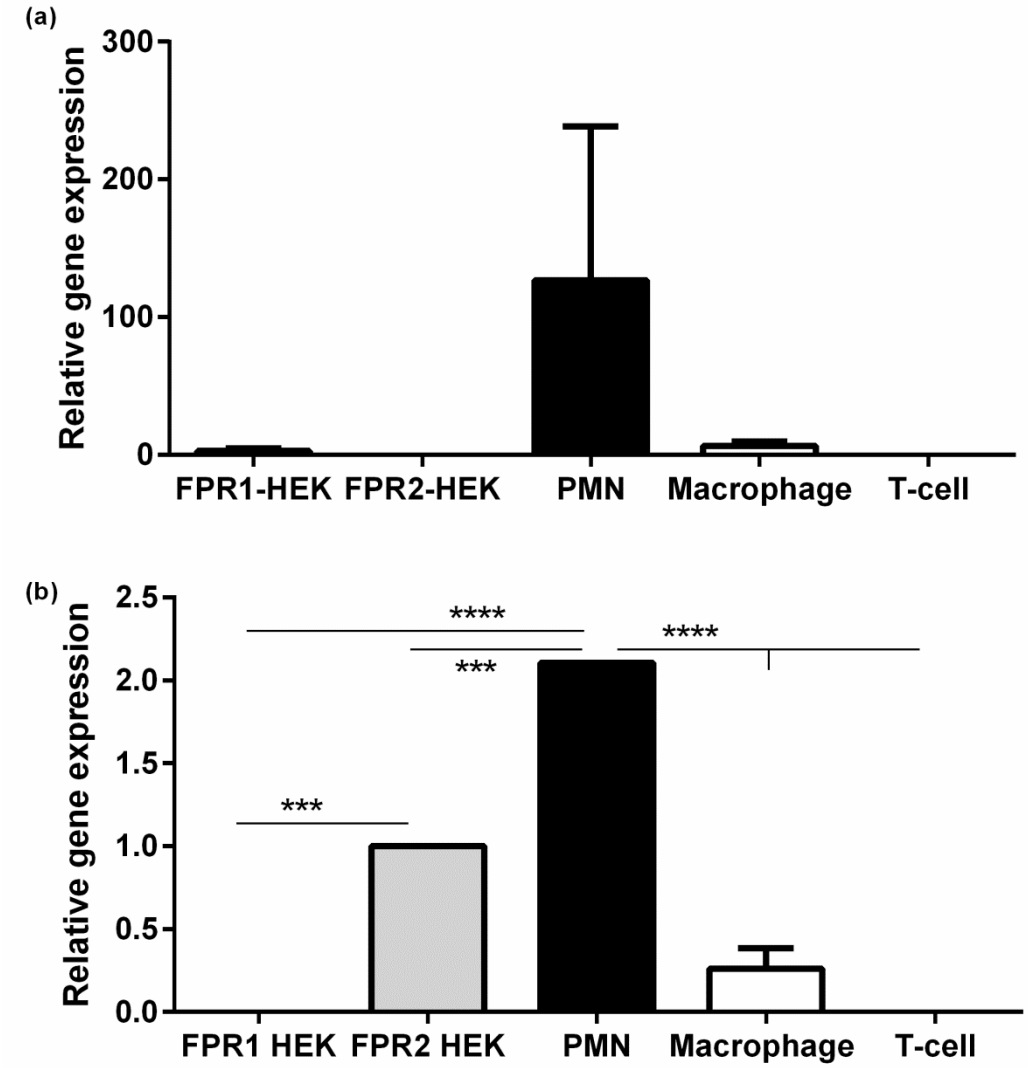

Figure.6.2: Human FPR1 and FPR2 mRNA levels in different immune cells. Quantitative PCR determined mRNA levels of (a) FPR1 and (b) FPR2 in FPR1-/FPR2-HEK cells, PMNs, macrophages and T-cells. Results were calculated as mean relative fold change compared to respective control (normalised to GAPDH housekeeping gene). Data is representative of 3 independent experiments. All p values determined by using a one-way analysis of variance (ANOVA); **** $p<0.00001$; *** $p<0.001$.

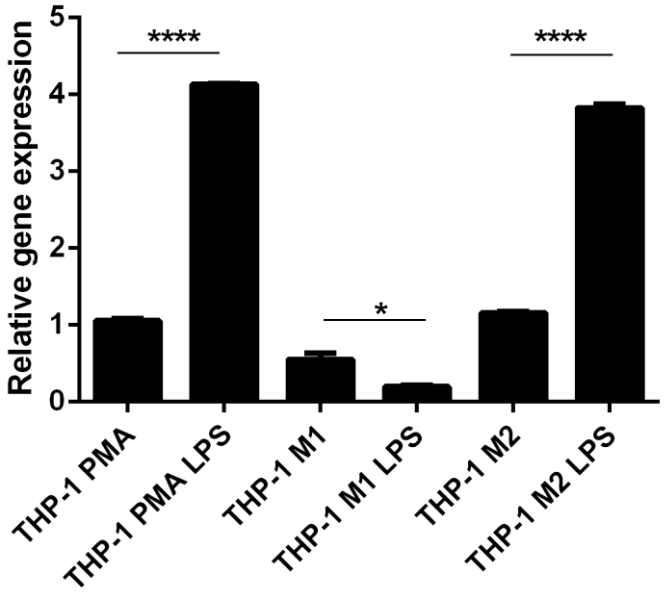

Figure 6.3: Differentiated THP-1 cells and FPR expression. Quantitative PCR determined mRNA levels of respective FPR1 in THP-1 cells treated with polarising cytokines and LPS (100ng/ml). Results were calculated as mean relative fold change compared to respective control (normalised to GAPDH housekeeping gene). Data is representative of 3 independent experiments. All p values determined by using a one-way analysis of variance (ANOVA); * $p<0.05$ and **** $p<0.0001$.

6.3.4 FPR expression in non-phagocyte pulmonary architectural cells

While expression of the FPR1 and FPR2 is widely characterised in granulocytes such as neutrophils little is known of its expression in architectural cells such as fibroblasts and epithelial cells. Van Compernolle *et al*. (2003) determined that FPR expression in lung epithelium plays a role in wound-healing homeostatic mechanisms. Utilising positive and negative controls described previously FPR1 expression was investigated using RT-PCR (non-quantitative) to assess levels in different cultured cell types (Figure 6.4).

Evidently, there are high levels in FPR1-HEK as well as in PMN. FPR2-HEK have no detectable expression which is mirrored in primary lung fibroblasts, MRC5 cell line and primary bronchial epithelial cell (PBEC). The basal, untreated expression of HFPR1 is non-existent compared to levels in transfected controls and neutrophils.

The next step was to determine if FPR1/2 expression changed in response to inflammatory stimuli such as LPS treatment (Figure 6.5) 100ng/ml for 24 hours. Human FPR1 expression remained low even after treatment in PBEC, HBEs (an immortalised PBEC cell line) and primary lung fibroblasts with no significant change ($p>0.05$). FPR2 expression, however, was greatly increased in PBEC and to a smaller extent in HBE cells. Primary lung fibroblast expression remained low as with FPR1. Compared to FPR1, FPR2 is a more promiscuous receptor with the ability to bind a greater repertoire of ligands that the high-affinity receptor. One consideration of these results is that environment of cultured cells is entirely artificial with supplemented media and adherence to a plastic flask exerting unknown effects on the cells used to a specific microenvironment in the human body with multiple, coordinating cell types.

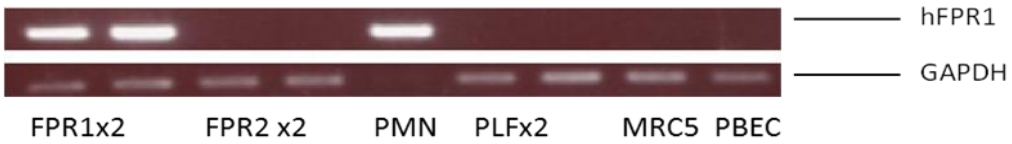

Figure 6.4: RT-PCR of human FPR1 expression in different cell types. FPR1 (FPR1-HEK), FPR2 (FPR2-HEK), PMN (Neutrophil), PLF (Primary Lung Fibroblast), MRC5 (fibroblast cell-line) and PBEC (Primary Bronchial Epithelial Cells). GAPDH used a loading control; PMN does not express GAPDH to the same level of other cells. Photograph taken of PCR samples obtained after 40 cycles and gel electrophoresis using a 2% agarose gel.

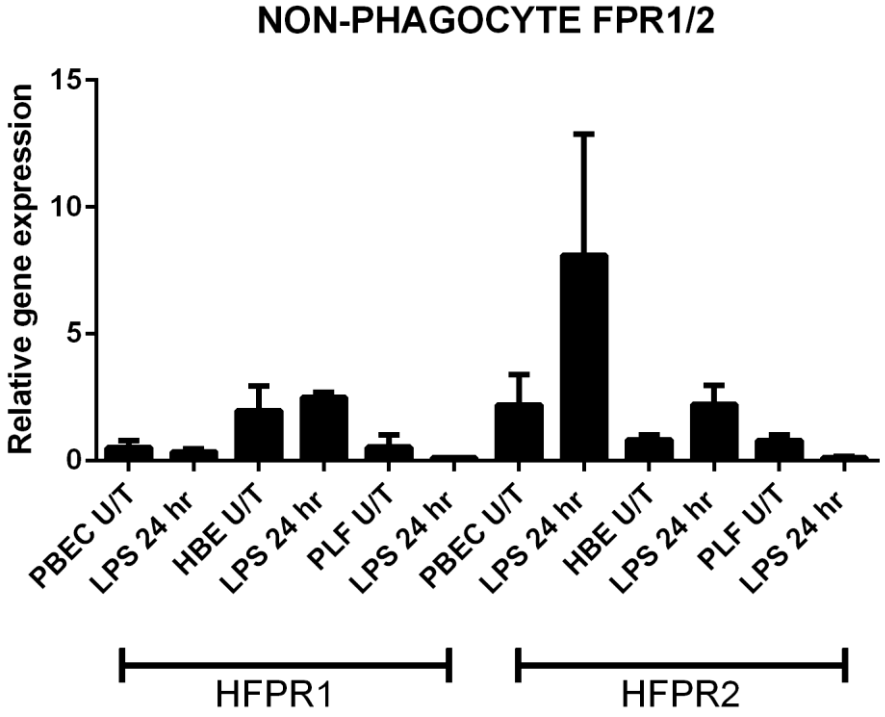

Figure 6.5: Non-phagocyte expression of FPR1 and FPR2. PBEC (Primary Bronchial Epithelial Cells), HBE (Human Bronchial Epithelium) and PLF (Primary Lung Fibroblasts) were treated for 24 hours with LPS (100ng/ml). Results were calculated as mean relative fold change compared to respective control (normalised to GAPDH housekeeping gene). Data is representative of 3 independent experiments. All p values determined by using a one-way analysis of variance (ANOVA); $p>0.05$ and * $p<0.05$.

6.3.5 TLR expression levels in control transfectants overexpressing FPR1/FPR2

Co-ordination of FPR signalling with other pathways has been demonstrated with regards to chemokines in particular CCR3 in human eosinophils (Svensson *et al*., 2009). The role of TLRs was investigated as inflammatory stimulus LPS has been shown to increase expression of FPR1 in neutrophils and macrophages. Also another key mitochondrial DAMP that has been characterised is mtDNA. This CpG-island rich motif is bound by TLR9 (Zhang *et al*., 2010) and has been shown to activate p38 MAPK. A disadvantage of these stable-transfected cells is that they were derived from clones. Different clones could have a different gene expression profiles due to the strength of the transfection. Perhaps by expanding with different constructs TLR expression data could be validated further. Figure 6.6 demonstrates an increase in TLR9 ($p<0.0001$) and TLR10 in FPR2-transfected HEK cells over THP-1, FPR1-transfectants and HEK-293 cells. TLR10 is also upregulated in FPR1-HEK cells in comparison to un-transfected HEK 293 cells as well as THP-1 (PMA-activated) control template ($p<0.01$).

6.4 Formyl peptide receptor mRNA levels in different murine organs

Expression in a variety of different organs: spleen, kidney, brain, lung, liver and gut was analysed by real-time quantitative PCR of the three members of the FPR family (Figure 6.7). RNA isolated from primary neutrophils derived from bone marrow were utilised to synthesize cDNA which was used as positive control for chemoattractant receptor expression. In comparison with the different organs neutrophils have higher levels of mFPR1, mFPR2 and S100A9 mRNA. The high affinity receptor, mFPR1 expression was undetectable in several of the different organs: kidney, lung, liver and gut with low levels determined in the spleen and brain ($p>0.05$). mFPR2 expression was clearly more abundant in the PMN controls compared to total organ DNA templates. Minimal levels were detected in spleen, kidney, brain, lung, liver and gut. S100A9 is a well characterised marker of myeloid cells such as neutrophils with expression elevated in this subset rather than in different organs.

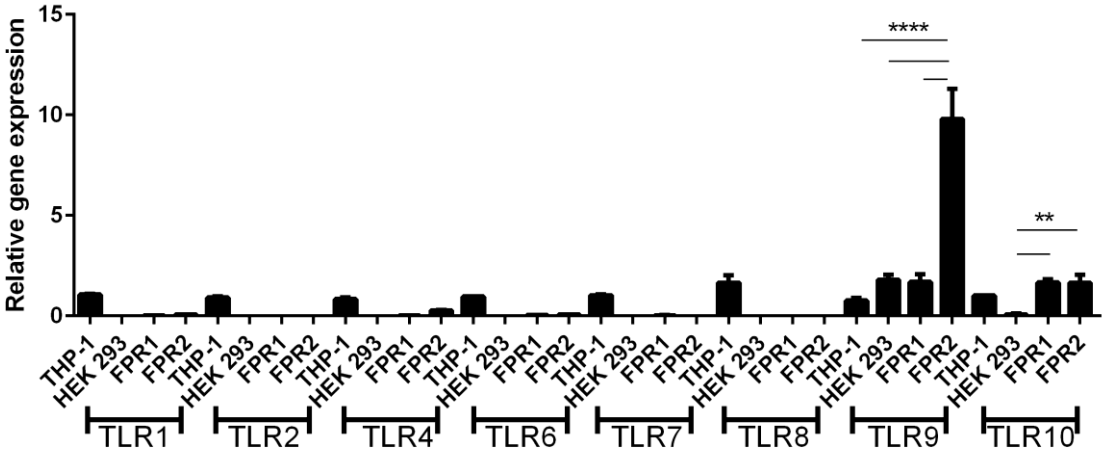

Figure 6.6: Toll-like receptor (TLR) expression in THP-1, HEK-293, FPR1-HEK and FPR2-HEK cells. TLR1, 2, 4, 6, 7, 8, 9 and 10 were assayed. Results were calculated as mean relative fold change compared to respective control (normalised to GAPDH housekeeping gene). Data is representative of 3 independent experiments. All p values determined by using a one-way analysis of variance (ANOVA); ** $p<0.01$ and **** $p<0.0001$.

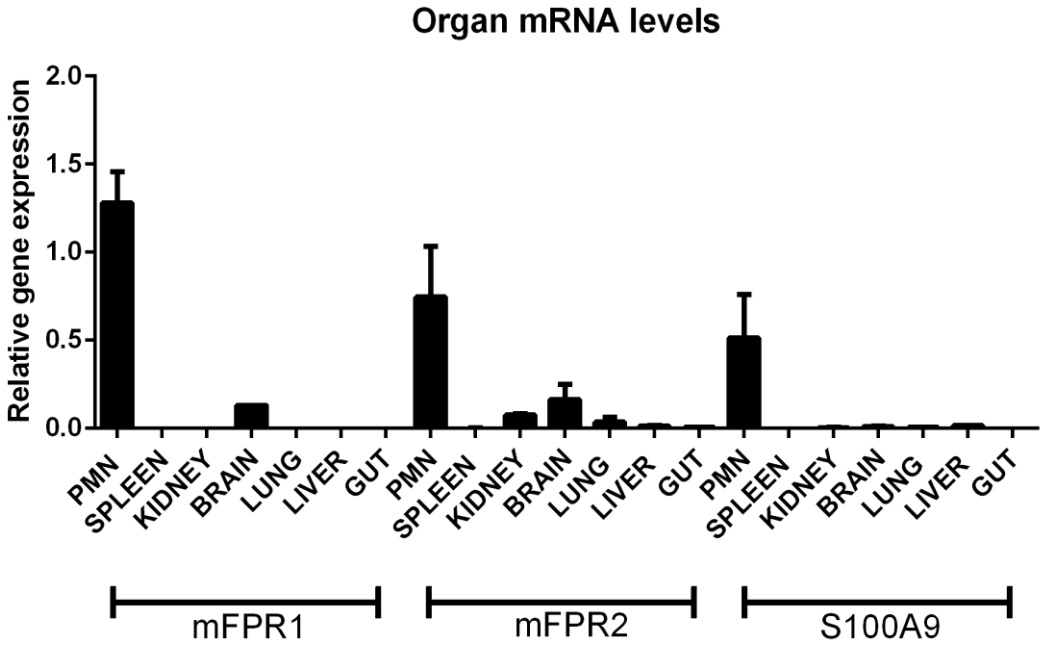

Figure 6.7: Murine FPR1, FPR2 and S100A9 gene expression in different organs. Results were calculated as mean relative fold change compared to respective control (normalised to GAPDH housekeeping gene). Data is representative of 3 independent experiments. All p values determined by using a one-way analysis of variance (ANOVA); $p>0.05$.

6.5 Priming of GPCR expression with inflammatory stimulus

FPR expression is somewhat lower in non-immune cells according to data arising from recent studies. As with other receptors there is a potential rationale for up-regulation with inflammatory stimuli. Non-sterile injury and sepsis-related effects are related to bacterial release of N-formyl peptides. In bacterial infections other products are exuded in the form of PAMPs which bind pattern recognition receptors (PRRs). One such receptor is TLR4 which binds LPS as well the endogenous alarmin HMGB1.

A hypothesis for stimulating cultured cells with inflammatory stimuli was that evidence has determined cross-talk between signalling pathways resulting in co-ordination of events. Recent research has highlighted co-ordination between uPA, EGFR and CXCR2 downstream signalling is not as simple in the cell as ligation of the receptor by formyl peptide molecules.

6.5.1 Priming of expression in immune cells

6.5.1.1 *mFPR1 expression in neutrophils*

Expression of FPR1 is most abundant in PMNs (mouse and human) with a much higher baseline than in non-phagocyte cells. Even with high basal protein and mRNA levels, upon stimulation with LPS (TLR4 ligand) there was a non-significant increase after 3 hours in mFPR1 expression (Figure 6.8) from 2.611±1.133 fold to 84.73±10.58 ($p>0.05$) respectively. After 24 hours of LPS treatment there was a significant fold change of 141.7±57.66 relative untreated (U/T) controls ($p<0.05$). Essentially the inflammatory stimulus is inducing expression of receptor via a ‘priming’ mechanism.

6.5.1.2 *mFPR1 expression in macrophages*

Macrophages are susceptible to the formyl peptide chemoattractant properties with expression of the GPCR in question characterised. Compared to neutrophils, macrophages have significantly less expression. A time course of LPS treatments on primary macrophages isolated from murine bone marrow (Figure 6.9). In wild type mice bone marrow-derived macrophages elicited a significant increase in mFPR1 mRNA from a mean fold change to 0.7861±0.1059 to 1414±536.7 ($p<0.01$) in untreated and 16 hours LPS respectively. After 24 hours mFPR1 expression was increased in a

significant manner ($p<0.0001$) with a mean fold change 3085±244.1 compared to untreated controls. Neutrophils are evidently more reactive to LPS stimulus than macrophages which fit with more abundant expression in this cell type.

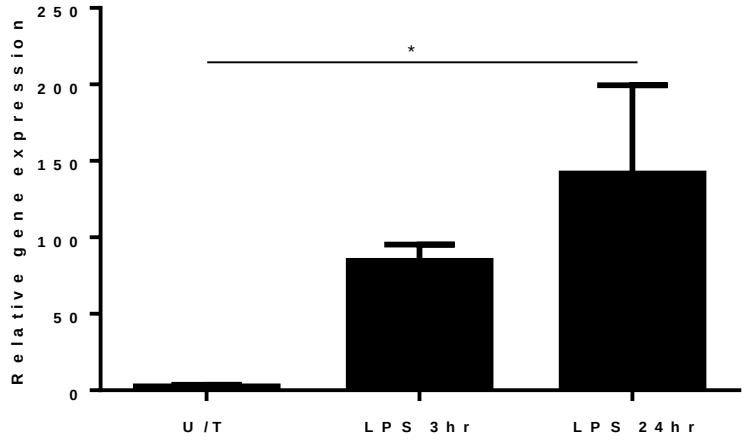

Figure 6.8: Neutrophil stimulation of FPR1 expression by LPS. Cells were treated at respective time points with LPS (100ng/ml). Results were calculated as mean relative fold change compared to respective control (normalised to GAPDH housekeeping gene). Data is representative of 3 independent experiments. All p values were determined by using a one-way analysis of variance (ANOVA) * $p<0.05$.

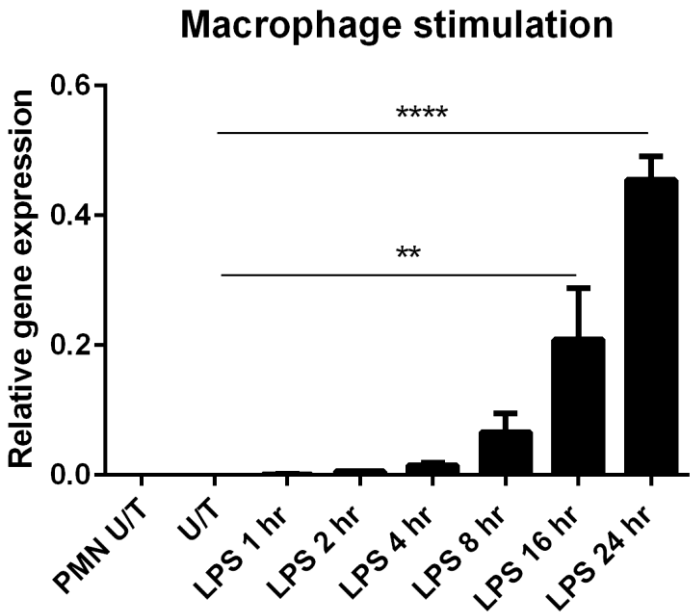

Figure 6.9: Macrophage stimulation of FPR1 expression by LPS. Cells were treated at respective time points with LPS (100ng/ml). Results were calculated as mean relative fold change compared to respective control (normalised to GAPDH housekeeping gene). Data is representative of 3 independent experiments. All p values were determined by using a one-way analysis of variance (ANOVA); ** $p<0.01$, **** $p<0.0001$.

6.5.1.3 *Induction in non-phagocyte cells*

As with PMNs and macrophages non-phagocyte cells are capable of expressing mFPR1. Previously shown is the LPS induction of this GPCR in bone marrow-derived cells but murine hepatic stellate cells (mHSCs) and murine lung fibroblasts (MLFs) also increased their expression with inflammatory stimulus. MLFs (Figure 6.10) isolated by collagenase digestion of murine lung tissue significantly increased their expression from U/T control (mean fold change 1.334±0.2699) when treated with LPS for 24 hours (mean fold change 31.94±11.82; $p<0.05$).

In a similar manner expression was elevated in HSCs (Figure 6.11) cultured and treated with different inflammatory stimuli. LPS treated cells had increased FPR1 expression compared untreated controls exhibiting a significant mean fold change of 10.44±0.6493 after 24 hour treatment ($p<0.0001$). Poly I:C treated cells also had a marked increase in FPR1 expression from a mean fold change of 0.6353±0.099 to 3.646±0.5949 in U/T and treated groups respectively ($p<0.001$).

In both immune cells and fibroblasts (liver and lung) FPR1 expression is increased by cells subjected to inflammatory stimuli suggesting a priming mechanism. This may indeed relate to models of acute injury where damaged epithelium initiate the development of a fibrotic phenotype. Damage response is potentially mimicked by inflammatory stimuli *in vitro* with increased FPR1 expression enabling increased ligand ligation of the receptors.

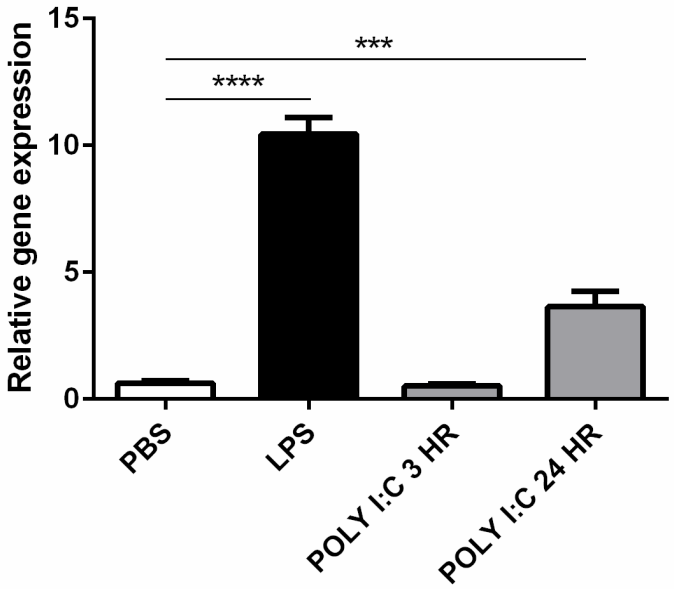

Figure 6.10: Murine lung fibroblast (MLF) expression of FPR1. Isolated cells were treated with LPS (100ng/ml) and poly I: C (HMW, 4µl/ml). Results were calculated as mean relative fold change compared to respective control (normalised to GAPDH housekeeping gene). Data is representative of 3 independent experiments. All p values determined by using a one-way analysis of variance (ANOVA); **** $p<0.0001$ and *** $p<0.001$.

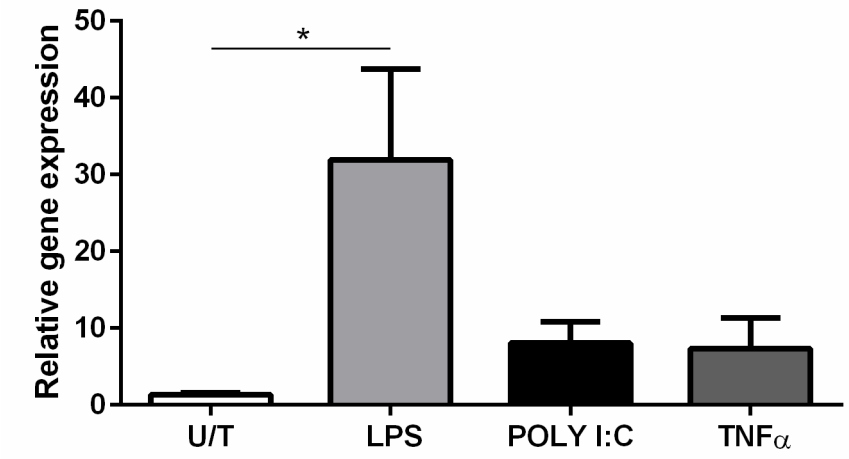

Figure 6.11: Murine hepatic stellate cell (mHSC) expression of FPR1. Isolated cells were treated with LPS (100ng/ml), poly I:C (4µl/ml) and TNFα (50ng/ml) for 24 hours. Results were calculated as mean relative fold change compared to respective control (normalised to GAPDH housekeeping gene). Data is representative of 3 independent experiments. All p values determined by using a one-way analysis of variance (ANOVA); * $p<0.05$.

6.5.2 Protein expression of FPR1 in human tissue

In order to validate expression of human FPR1 and FPR2 western blot analysis was performed. Protein expression was not forthcoming due to problems with commercial antibodies (Abcam and R&D systems respectively). Cross-reactivity with FPR2 was not tested by suppliers. Both antibodies display a lack of specificity to individual receptors: FPR1 and FPR2. Determination of a suitable negative control has as yet proved elusive. With regards to the FPRL1-antibody shows FPR2-expression in FPR2-transfected HEK cells specifically but this result was not reproducible.

Due to the lack of commercial antibodies that specifically detect members of the FPR family the evaluation of receptor expression proved difficult. From the industrial collaboration with MedImmune (Cambridge, UK) an in-house human FPR1 antibody became available for determining expression *in vitro*. This antibody was validated in-house for specificity and enzyme kinetics (data not available; Douthwaite *et al*., 2014).

6.5.2.1 *Immunohistochemistry of human tissue sections for human FPR1 expression*

The phage-display selected monoclonal antibody was directly linked to a horseradish-peroxidase (HRP) conjugate (InnovaBiosciences) to enable selective staining of cells expressing FPR1. IHC staining of IPF human tissue sections showed areas of what appeared to be specific positive FPR1 expression in macrophage/monocyte cells. With this high expression in macrophage immune cells the antibody appeared to be suitable for determining protein expression (Figure 6.12).

This immunostaining method yielded positive (brown) staining in different areas of diseased IPF lung tissue sections. In initial IHC tests of this antibody there was staining observed in macrophages, airway epithelium and serous mucosa glands (Figure 6.12 (a)). The extent to which this staining is valid was hampered by extensive background staining. One problem encountered was the antigen retrieval method and blocking of the sections to eliminate non-specific binding as background was an issue. Following several protocol refinements using different blocking steps including pig and goat serum to eliminate non-specific binding, a Bovine serum albumin (BSA) block was chosen. The method demonstrated positivity in monocytes/macrophages and also epithelial serous mucosa (Figure 6.12 (b)). This may indeed be due to the monoclonal

antibody staining but the level of background is a concern so the validity of its specificity is in question.

The BSA block method resulted in the least amount of background staining but due to widespread staining after the DAB step it appears that IHC may not be optimal method for this antibody. Direct linkage to an HRP-conjugate did not produce an expression profile that was believable; perhaps a dual-IHC method with multiple colours would have been ideal as cell types showing positivity could have been classified according to another cell surface marker's expression. Human FPR1 expression in IPF cases (Figure 6.12 (c)) despite several optimisation protocols which demonstrated what appears to be specific expression in macrophage/monocyte cells, other cell types demonstrated non-specific staining.

6.5.2.2 *Immunocytochemistry of FFPE lung tissue*

Determining a method for visual confirmation of FPR1 expression was important to validate the same antibody used in a FACs based strategy (Douthwaite *et al*., 2014). Direct linkage to a fluorescent conjugate, allophycocyanin (APC, InnovaBiosciences) in a similar manner to the IHC method enabled intracellular staining of cells expressing human FPR1. The APC fluorophore is a phycobiliprotein isolated from red algae with excitation at 594-633nm and emission at 660nm. APC, a chemically cross-linked molecule, is ideally suited for highly sensitive fluorescence detection methods while distinct from the FITC excitation and emission wavelengths, 495nm and 519nm respectively. Due to the fact that APC is excited at a different wavelength to FITC and/or TRITC secondary antibodies there is no crossover between channels. This enabled the use of the labelled antibody in a triple staining method to determine co-localisation (if any) of FPR1 with different cellular markers: immune or architectural (Figure 6.13).

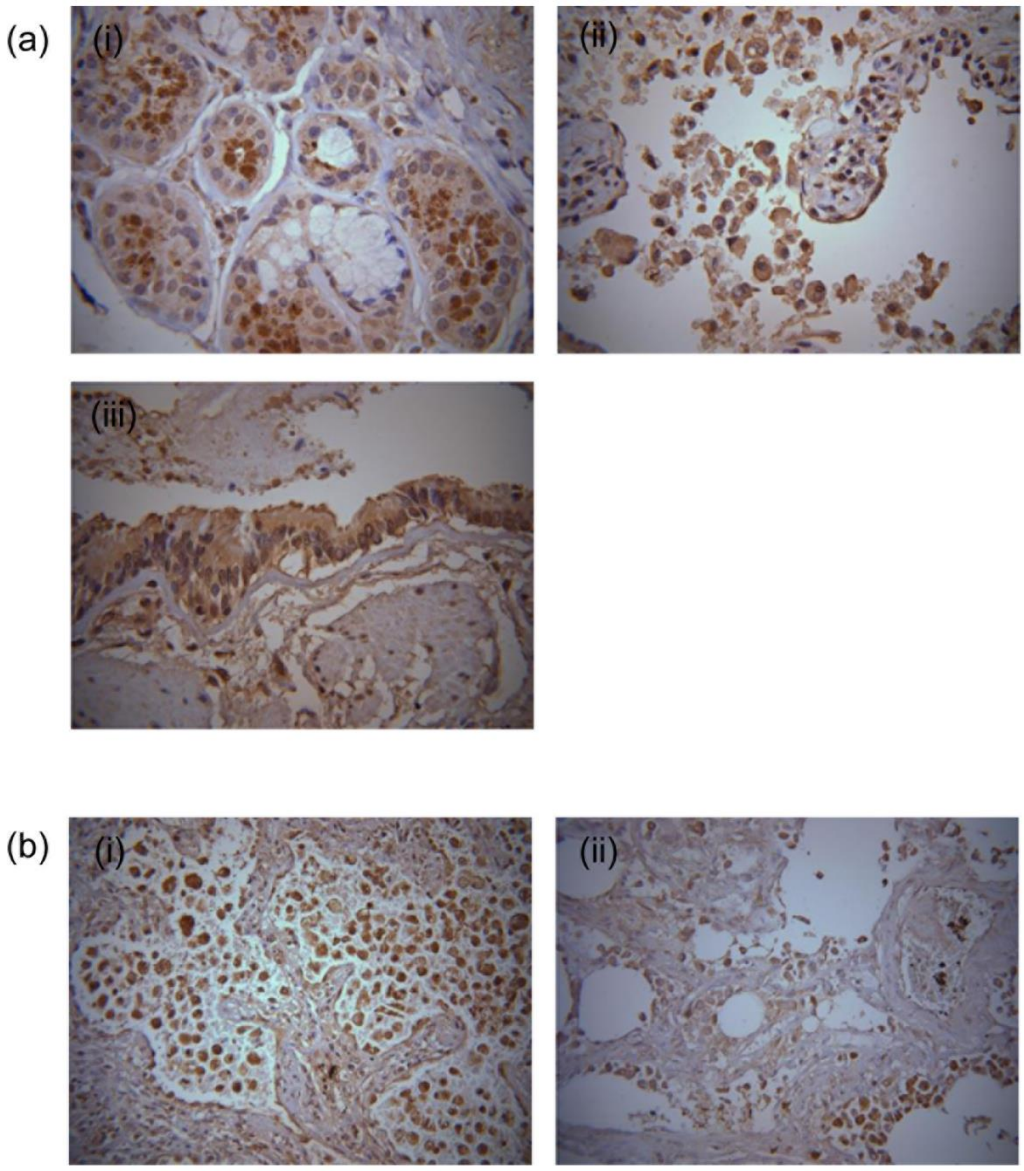

Figure 6.12: Immunostaining of primary human IPF lung tissue sections. Human FPR1 antibody was directly labelled to an HRP-conjugate and was used to stain FFPE tissue. Different optimisation runs shown in (a) and (b) utilising varying blocking methods and incubation periods.

(c)

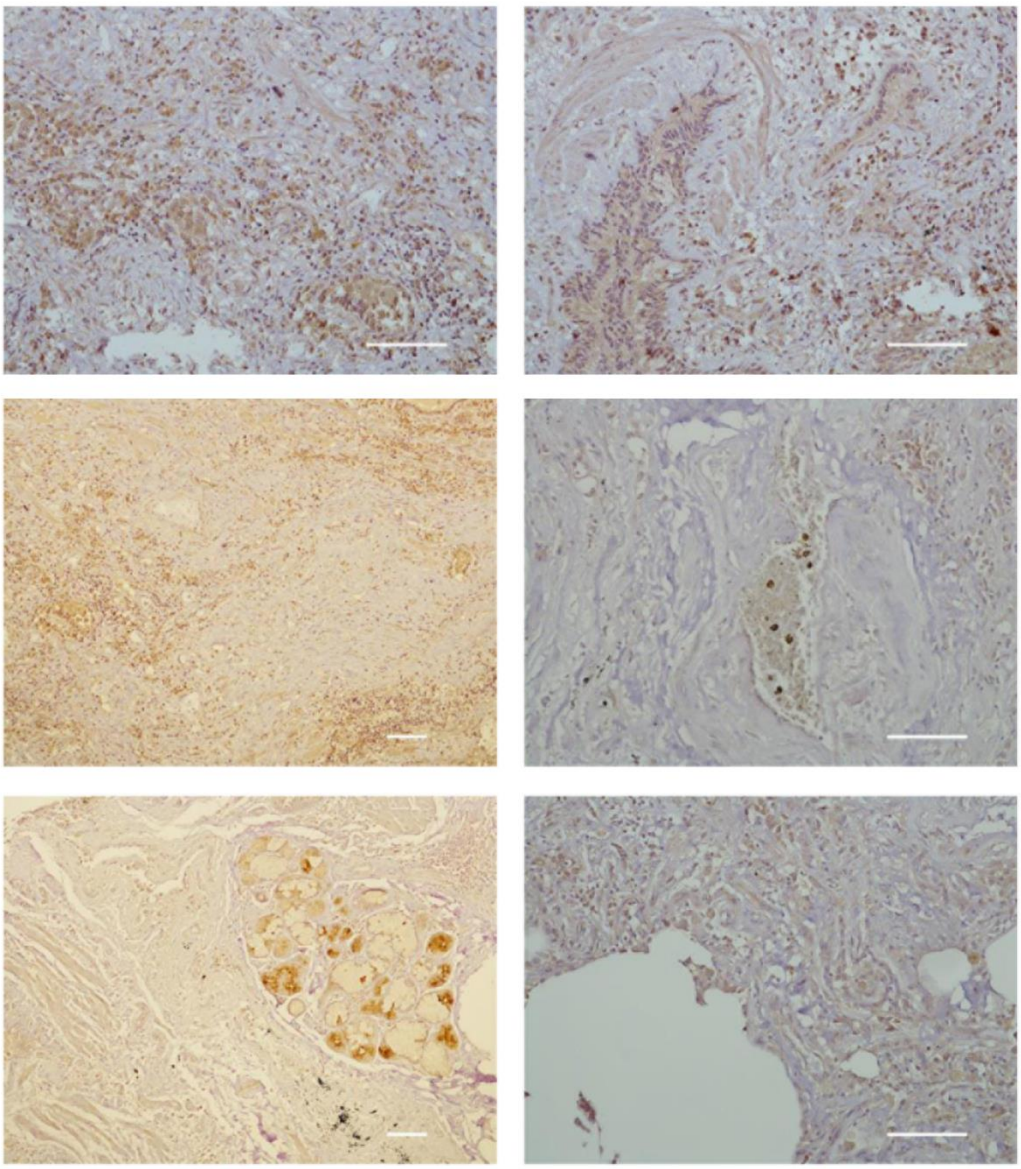

Figure 6.12: Immunostaining of primary human IPF lung tissue sections. Human FPR1 antibody was directly labelled to an HRP-conjugate and was used to stain FFPE tissue. Different optimisation runs shown in (c) demonstrate persistent background staining of fixed human tissue even with refined protocol.

6.5.2.3 *Validation of hFPR1-APC antibody for immunofluorescence*

PMT gain and control settings were set on negative control slides, stained only with secondary antibodies. These included FITC, TRITC and IgG-APC isotype antibodies. These values determined by LSCM were applied to all subsequent immune-fluorescently labelled tissue sections for the elimination of background auto-fluorescence and non-specific binding. Normalising to these control slides ensures that any staining for the different cellular markers: CD45, CD68, E-CAD, VIM and FPR1 is true rather than artefact (Figure 6.14).

As well as validation by flow cytometry-based methods the human FPR1 APC conjugated antibody was used for immunofluorescence. Transfected human embryonic kidney (HEK) cells were used as positive controls for FPR1 expression (Figure 6.15). These cells overexpress the two main receptors of this family of G-protein coupled receptors. Staining of fixed cultured cells from both of these cell lines demonstrated high FPR1 localisation in the membrane/cytoplasmic compartments with intense expression. FPR1 expression was lower in HEK-FPR2 overexpressing cells as in these cells the GPCR is only present at basal level. In FPR2 HEK cells FPR1 is still localised to the membrane and also the cytoplasm. Localisation in methanol-fixed cells fits with the expression pattern of the receptor and internalisation via endocytosis. DAPI (4',6-diamidino-2-phenylindole) was used to counterstain nuclei by binding to A-T rich DNA regions. DAPI staining determined that FPR1 staining was true and localised correctly. If more time had been available more cell types would have been tested for FPR1 expression in this manner particularly the THP-1 cell line which did show a minimal increase in gene expression with inflammatory stimuli and phenotype change.

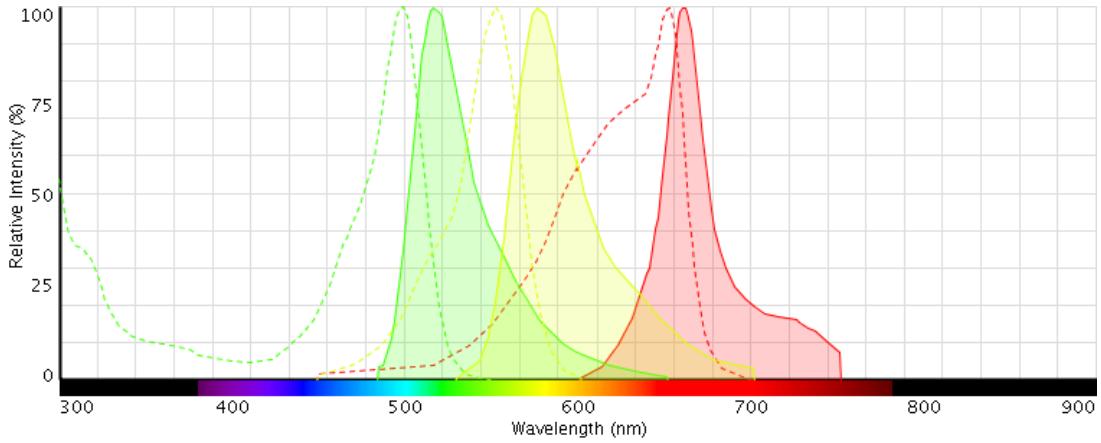

Figure 6.13: Spectral overview of FITC, TRITC and APC excitation (dotted line) and emission (solid line) wavelengths. FITC (green), TRITC (yellow) and APC (red) peaks.

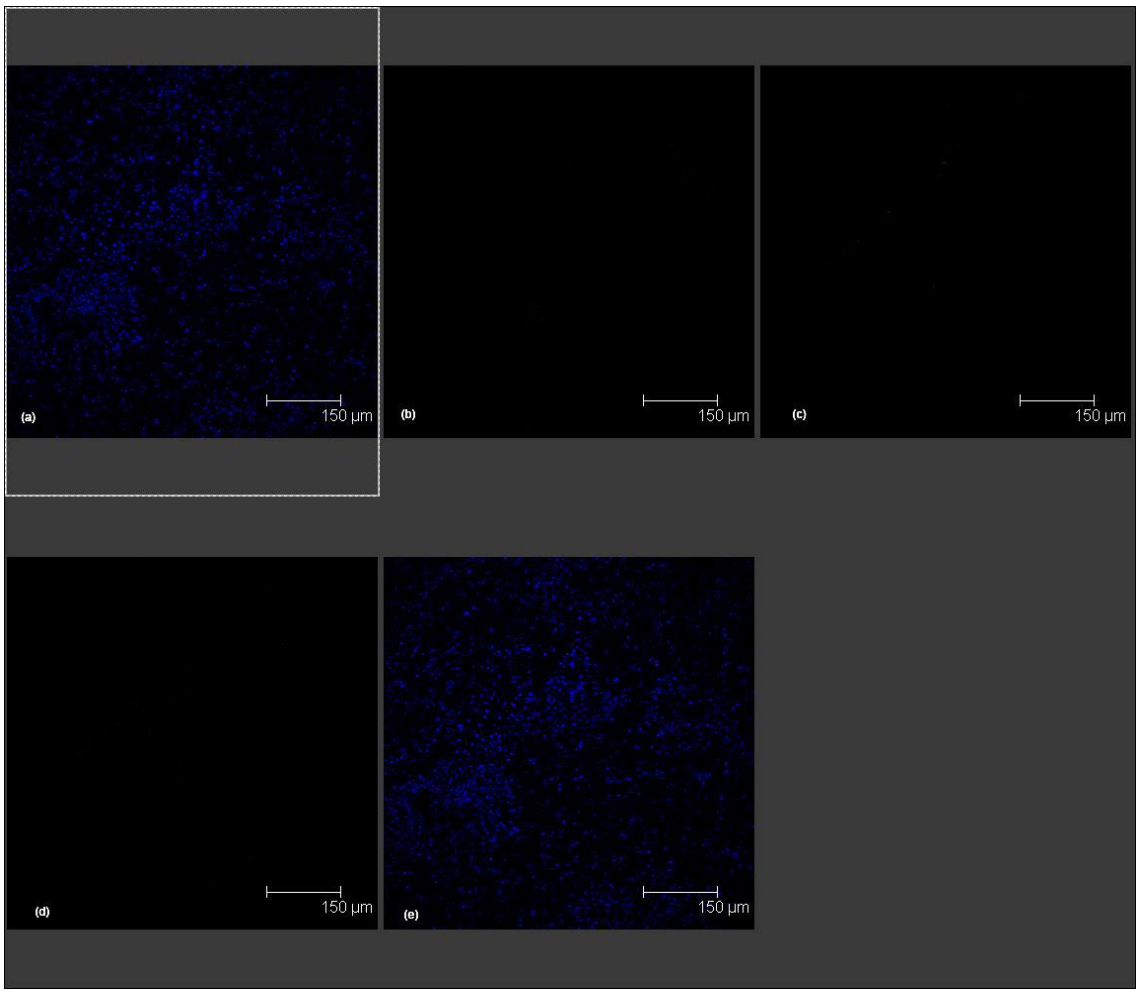

Figure 6.14: Control antibody staining of FFPE sections. (a) DAPI, (b) isotype (IgG-APC), (c) FITC and (d) TRITC controls on FFPE sections. (e) Overlay composite of different fluorescent conjugates. Images are representative of 3 independent experiments.

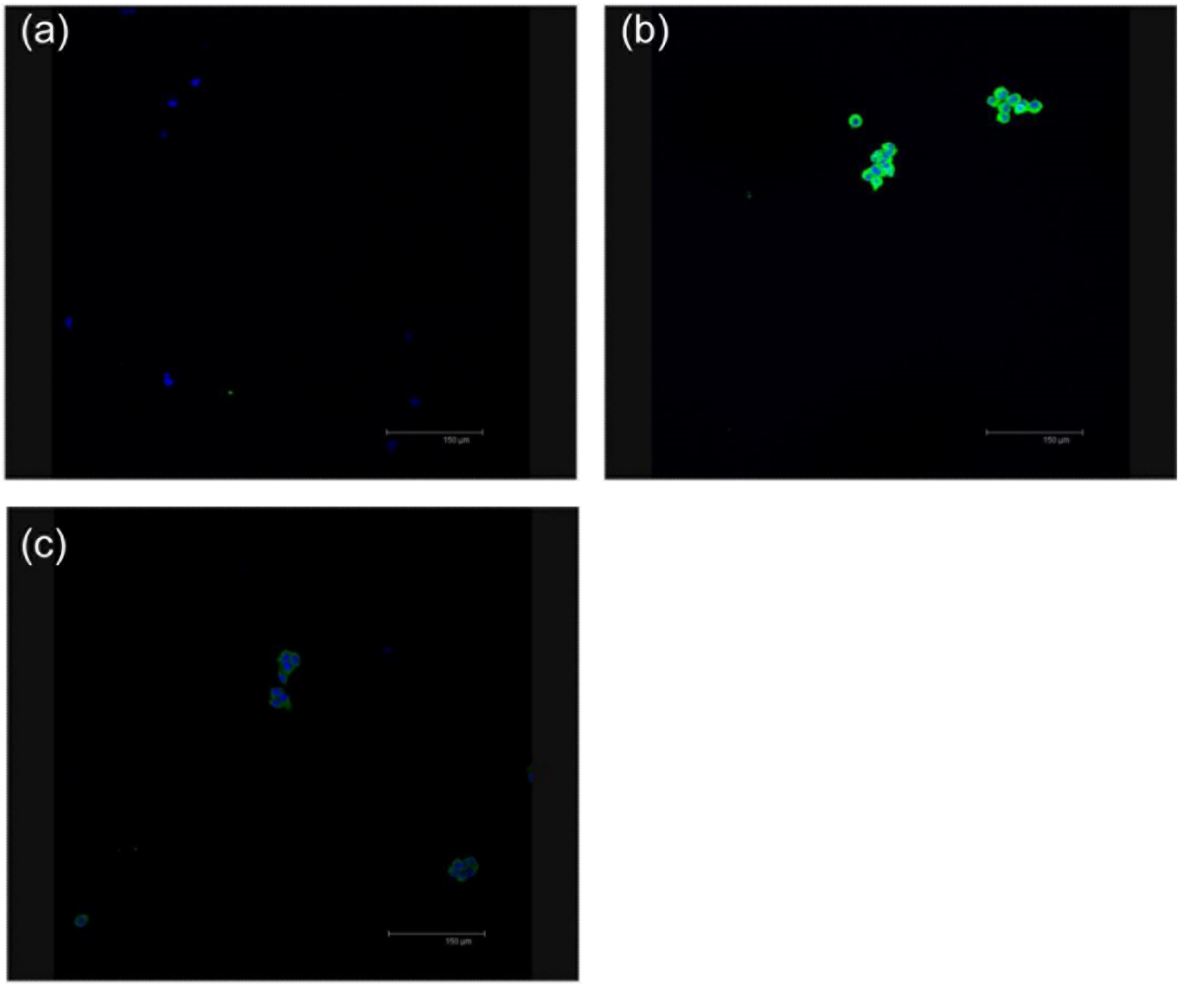

Figure 6.15: Immunocytochemistry for FPR1 in cultured cells. (a) Unstained controls with DAPI nuclear stain, (b) FPR1-HEK transfectants and (c) FPR2-HEK transfectants. Images are representative of n=3 independent experiments.

6.5.2.4 *Immunocytochemistry of FFPE diseased lung tissue*

6.5.2.4.1 Architectural cells: Fibroblasts and Epithelium

Essentially the two panels of antibodies used on the primary human tissue allowed evaluation of architectural and immune cells localisation with respect to FPR1 expression. E-Cadherin positive cells represented lung epithelium, vessel and lung airway walls with Vimentin positive expression in fibroblasts. Any co-localisation of the TRITC paired antibodies (Vimentin or CD45) with FPR1 resulted in a distinct magenta colourisation.

As all cellular markers are present on the surface membrane EDTA antigen retrieval was employed to enable staining of epitopes. Different antibodies were evaluated in the architectural panel to determine which pair of epithelial and fibroblast markers worked in an optimal fashion. E-Cadherin showed highly specific localisation to epithelium through the diseased lung tissue with intense staining of airway walls and mucosa areas. Alpha-smooth muscle actin (α-SMA), fibronectin and vimentin were used as potential markers for the fibroblast population in human lung tissue as research has cited them all as key markers of fibroblasts and also cells were have undergone EMT. α-SMA and E-Cadherin used with TRITC (Red) and FITC (Green) secondary antibodies did not represent a usable pair for the architectural panel. Cells stained well for the epithelial marker but in terms of the fibroblast marker extensive auto-fluorescence and non-specific binding were clearly evident with high background levels in the TRITC channel. Both fibronectin and vimentin stained distinct populations in the tissue sections with localisation in the cellular cytoplasmic compartment as ECM components. Although specific staining was shown by fibronectin (Figure 6.16), vimentin was chosen due to its stronger profile in the same subset of cells in the tissue sections.

Of antibodies tested to stain the fibroblast population in the fixed tissue vimentin exhibited the strongest specificity and signal. Alpha-SMA antibody (Abcam) revealed no strong pattern of expression coupled with TRITC secondary. Fibronectin, another extracellular matrix protein whose deposition is typically increased in fibrosis, did reveal specific staining in the cytoplasm of fibroblast populations. With vimentin a larger proportion of cells revealed positive expression which may be due to the fact

that this marker is increased in cells undergoing EMT as well as having stable expression in fibroblasts.

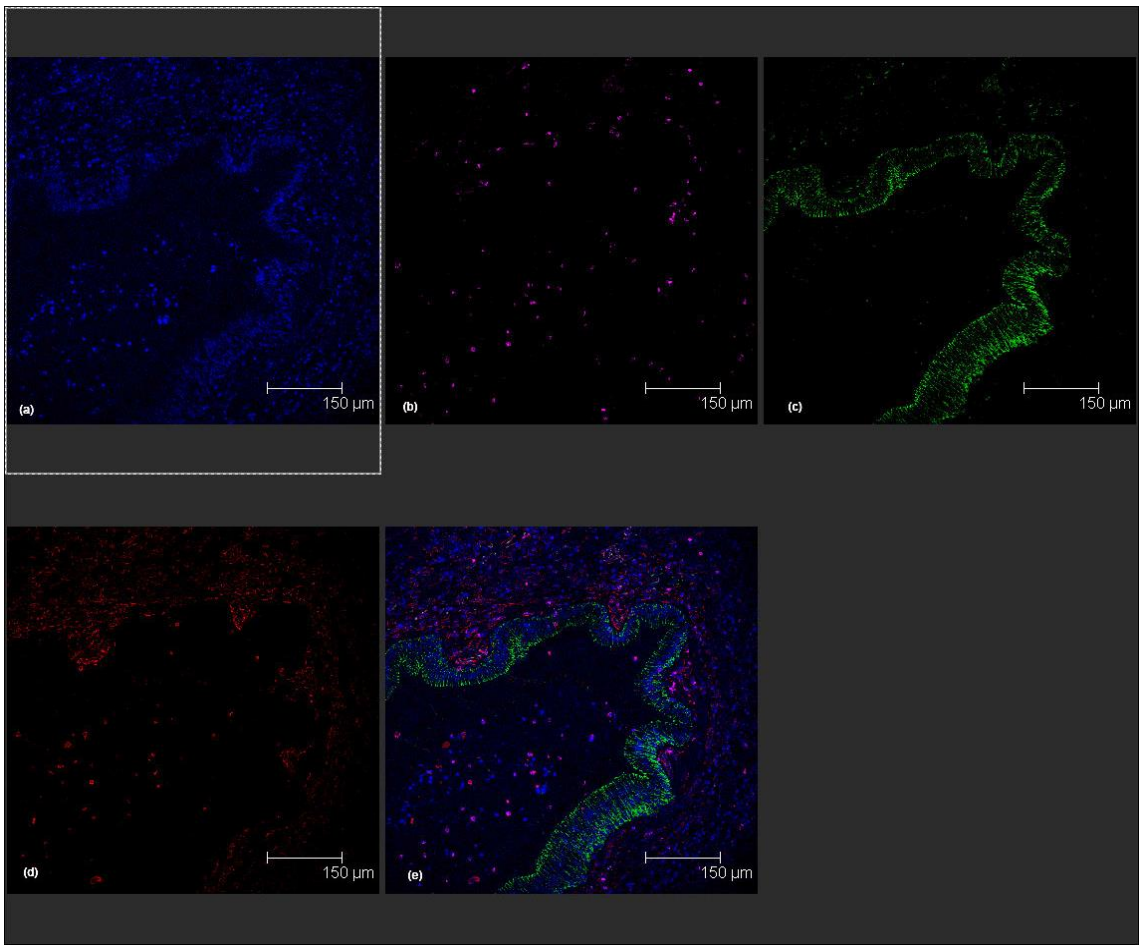

Figure 6.16: Architectural staining of FFPE lung sections with fibronectin as fibroblast marker. (a) DAPI (nuclear stain), (b) FPR1-APC, (c) E-Cadherin (FITC), (d) Fibronectin (TRITC) and (e) overlay composite. Magnification at x20 (Images representative of n=3 IPF cases).

Vimentin was selected as marker to selectively stain fibroblasts in the interstitium of IPF lung paraffin-embedded sections. Encoded by the VIM gene, this type III intermediate filament protein is an integral part of the cytoskeleton, the framework of the cell. For many years it has been characterised as a fibroblast marker along with other markers such as alpha-smooth muscle actin and fibronectin. In particular Vimentin is noted to be present in a majority of alveolar fibroblasts in ILDs (Fireman *et al*., 2001).

Although it has been extensively used more markers should be used as vimentin is also a marker of cells undergoing epithelial-to-mesenchymal transdifferentiation (EMT). The passage to a mesenchymal phenotype results in a loss of epithelium marker expression such as cytokeratin 19/7 and an increase in vimentin expression (Strutz *et al*., 1995). The specificity of this marker was a concern as primary alveolar epithelial cells (AECs) demonstrate EMT-driven changes in gene expression and protein translation. The complexity of the cells making the architecture of lung tissue is a factor to be considered as fibroblasts provisionally identified through vimentin staining may be resident alveolar fibroblasts or mesenchymal EMT-derived cells displaying fibroblasts properties (Kim *et al*., 2006).

6.5.2.5 *IPF FFPE tissue sections*

In terms of the staining pattern observed in IPF tissue sections (Figure 6.17) there were different patterns exhibited. Epithelial cells with strong expression of E-Cadherin showed defined structures such as vessel and airway walls displayed no co-localisation with human FPR1. Fibroblasts positive for vimentin expression were clearly distinct from epithelium populations but co-localisation did occur with E-Cadherin and Vimentin potentially indicating the process of EMT. Of particular note was that isolated fibroblasts (Vimentin positive) demonstrated clear expression of FPR1 resulting in a magenta stain from mixing of red (vimentin) and FPR1 (blue). This is fitting with recent literature where FPR1 expression was reported in lung fibroblasts (Van Compernolle *et al*., 2003). Higher magnification of immunostained sections shows localisation of FPR1 receptor in the cytoplasmic-membrane region of isolated cells which are vimentin positive fibroblasts (Figure 6.18).

6.5.2.6 *Normal, COPD and bronchiectasis FFPE tissue sections*

Other chronic pulmonary disease conditions were subjected to immunocytochemistry using the same panel of antibodies on IPF tissue sections: DAPI, E-Cadherin, Vimentin and FPR1-APC. Normal lung tissue fixed in formalin was obtained from archived tissue sampled during ex vivo lung perfusions. A COPD case of fixed tissue exhibited a similar staining pattern to normal lung tissue with E-Cadherin and Vimentin localisation in the epithelium and fibroblasts respectively. Human FPR1 detected in tissue via the DAPI Cy7.7 channel distinct from FITC and TRITC emissions spectra (Figure 6.13) was not shown in normal or COPD cases stained (n=1 for each; COPD case shown in Figure 6.19). Ideally if more time had been available more cases from each group would have been tested for each cellular marker. Bronchiectasis-sourced tissue stained as with the others cases expressed in a similar fashion E-Cadherin, Vimentin and FPR1. Patients exhibited co-localisation of human FPR1 and vimentin resulting in a magenta colourisation. As with IPF FFPE sections co-localisation occurred in isolated fibroblasts also expressing vimentin (Figure 6.20). Increased magnification (x1.77 zoom) of stained sections enabled zoomed-in imaging of co-localisation in fibroblast cells (Figure 6.21).

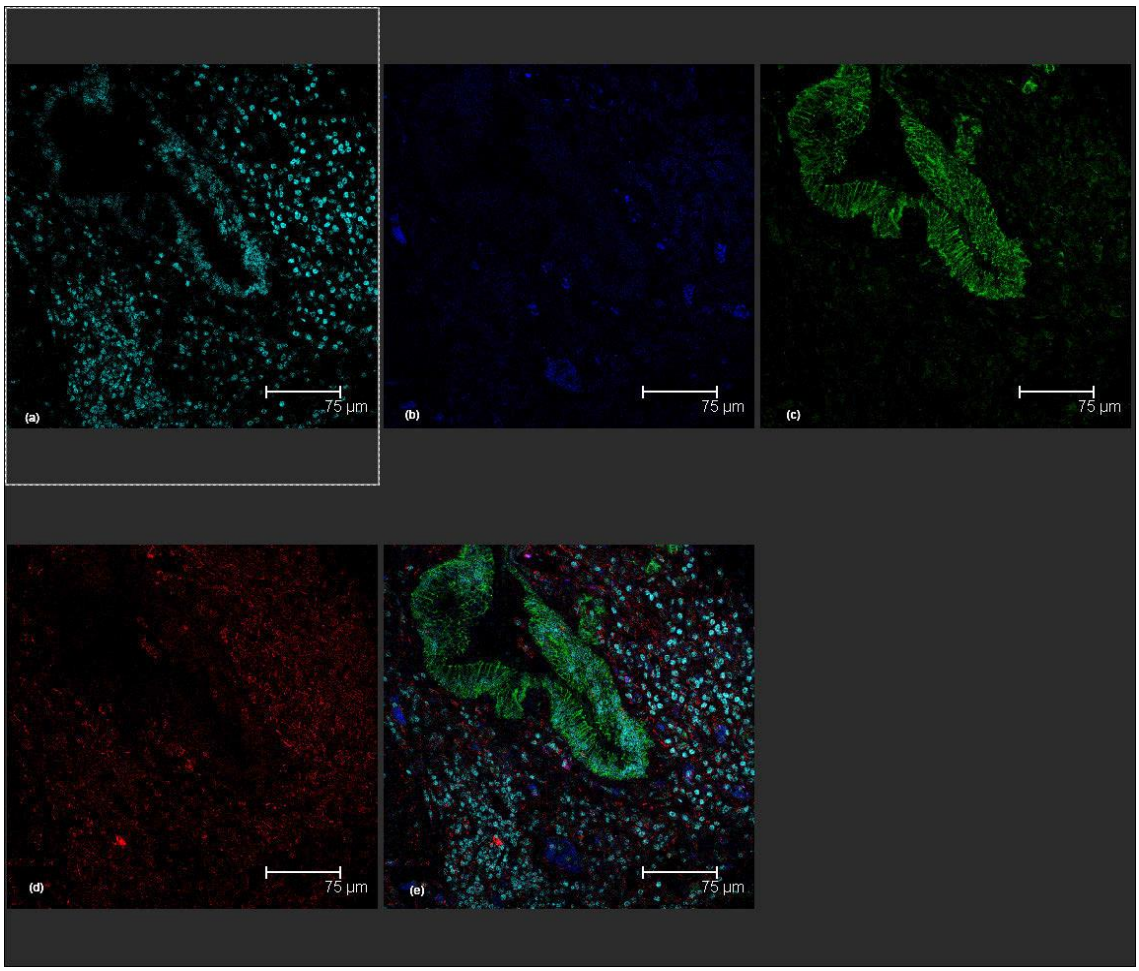

Figure 6.17: Architectural cell immunocytochemistry of IPF tissue sections using vimentin as fibroblast marker. FFPE sections were stained for (a) DAPI (cyan), (b) FPR1-APC (blue), (c) E-Cadherin (green), (d) Vimentin (red) and (e) overlap composite image with LCSM performed at x40 magnification. Image panel representative of n=3 IPF cases.

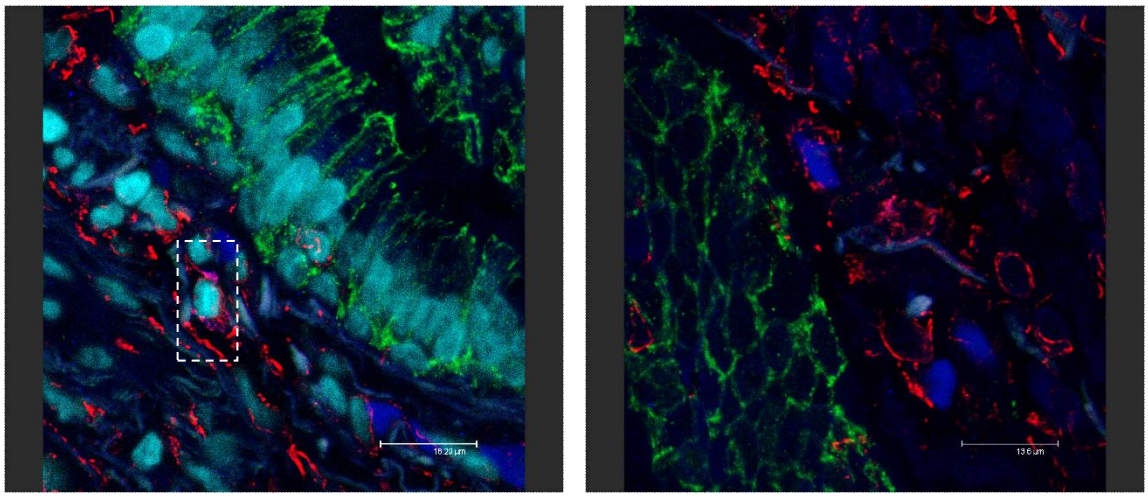

Figure 6.18: Co-localisation of FPR1-APC and vimentin in IPF FFPE sections. FFPE sections were stained for DAPI (cyan), FPR1-APC (blue), E-Cadherin (green) and Vimentin (red). Overlap composite image in left panel with LCSM performed at x63 magnification. Images representative of n=3 IPF cases.

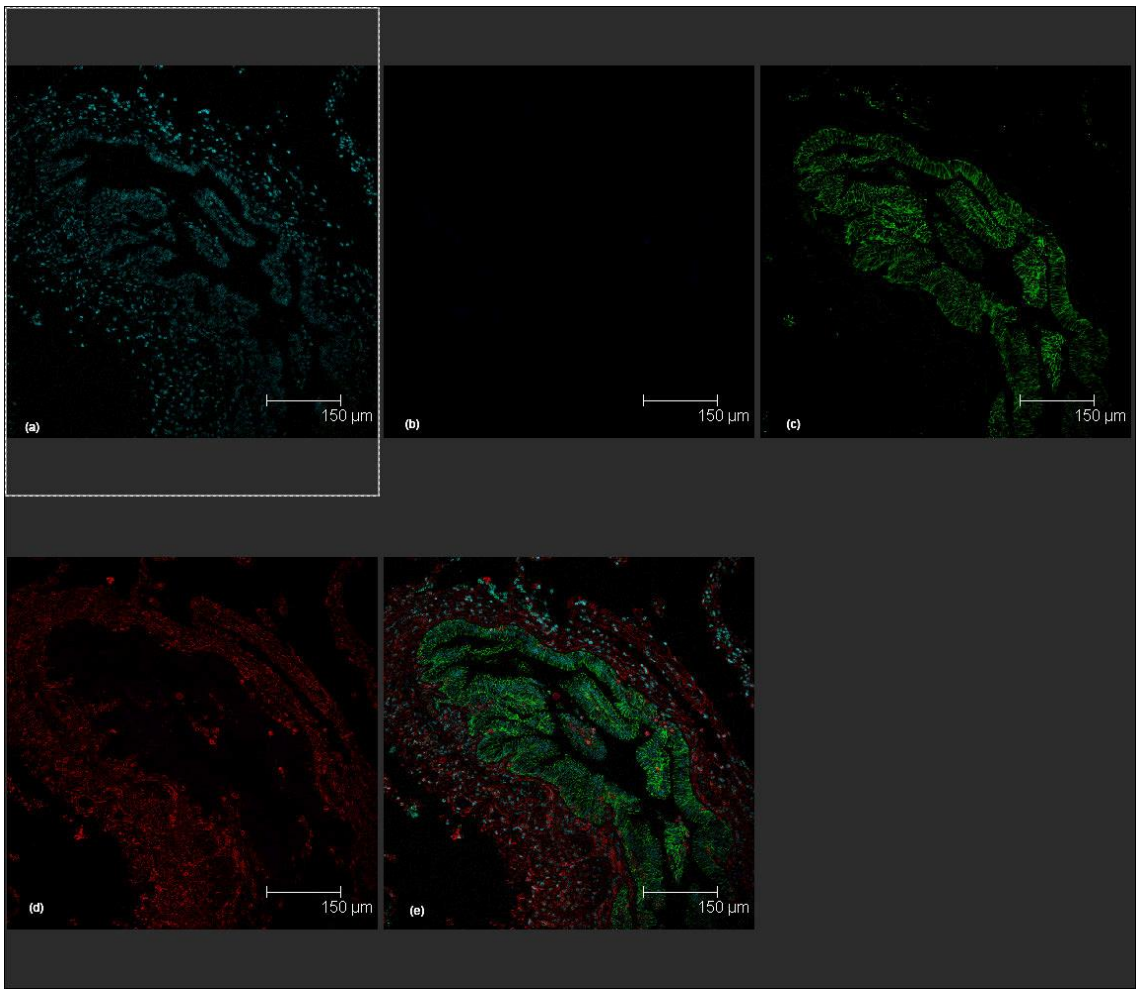

Figure 6.19: COPD FFPE section staining pattern of architectural cellular markers. FFPE sections were stained for (a) DAPI (cyan), (b) FPR1-APC (blue), (c) E-Cadherin (green), (d) Vimentin (red) and (e) overlap composite image with LCSM performed at x20 magnification. Images representative of n=2 COPD cases.

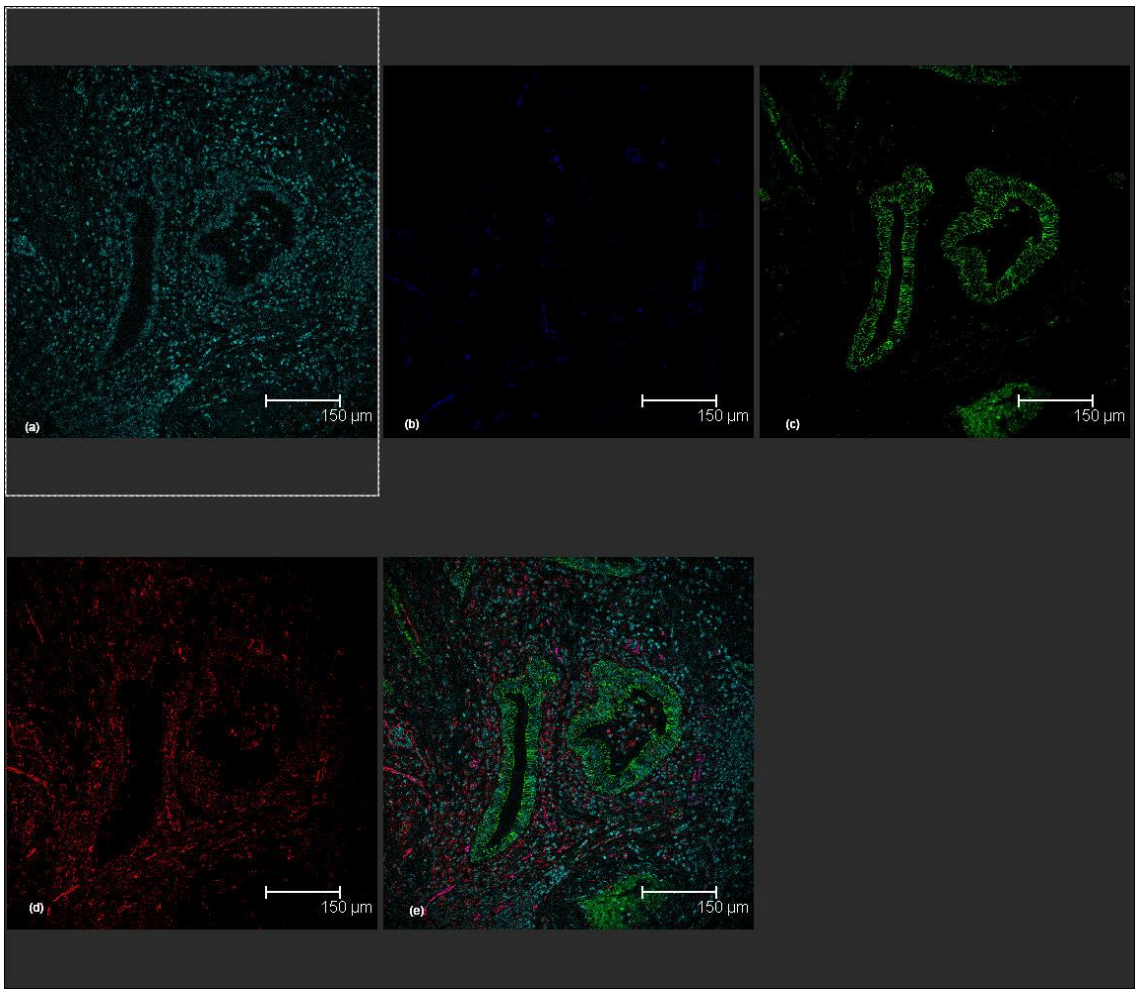

Figure 6.20: Bronchiectasis lung FFPE section staining pattern of architectural cellular markers. FFPE sections were stained for (a) DAPI (cyan), (b) FPR1-APC (blue), (c) E-Cadherin (green), (d) Vimentin (red). Co-localisation of FPR1 with vimentin resulted in magenta colourisation. (e) Overlap composite image in last panel with LCSM performed at x20 magnification. Images representative of n=3 cases.

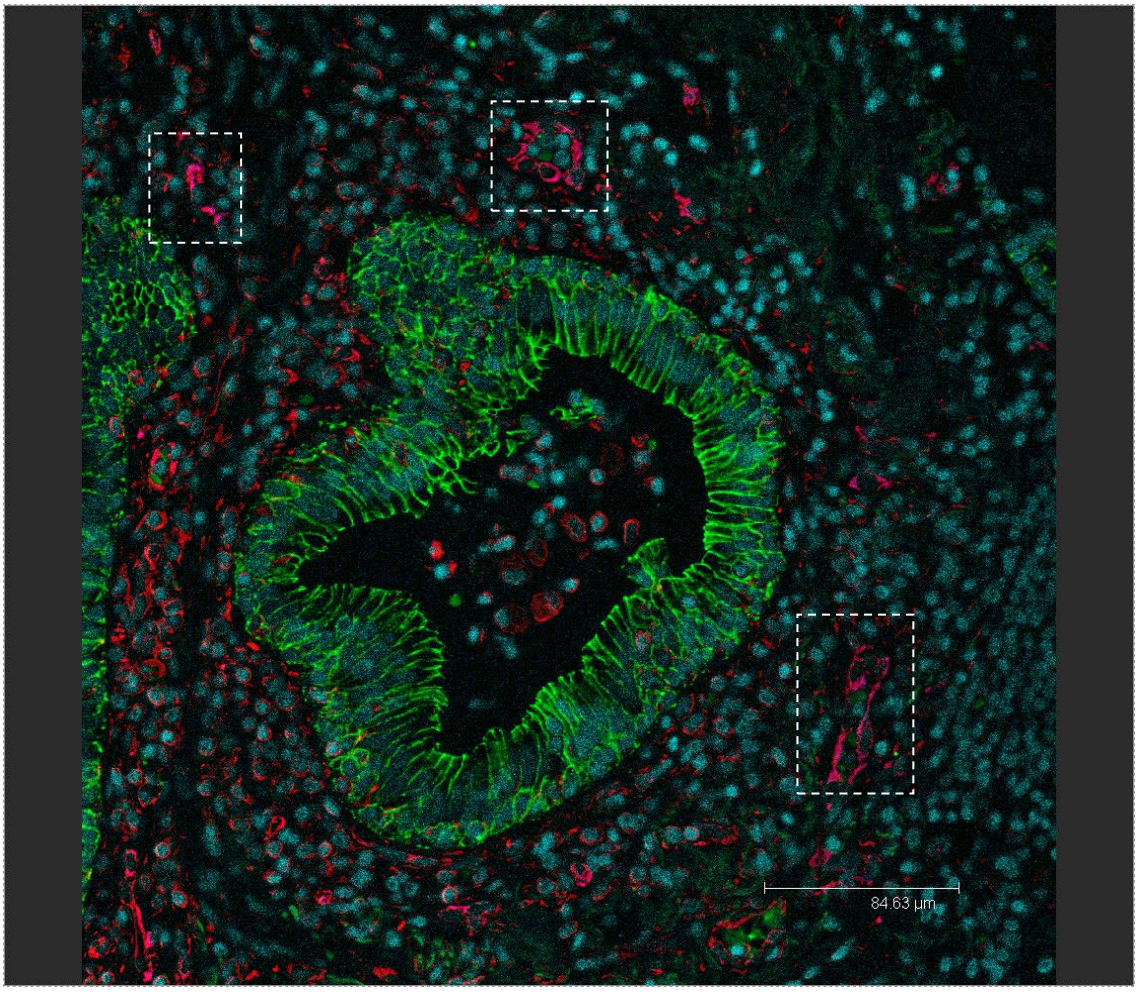

Figure 6.21: Bronchiectasis lung FFPE section staining pattern of architectural cellular markers. FFPE sections were stained for DAPI (cyan), FPR1-APC (blue), E-Cadherin (green) and Vimentin (red). Co-localisation of vimentin and FPR1 resulted in magenta colourisation (highlighted by white dashed boxes). Overlap composite image generated with LCSM performed at x60 magnification (n=3 cases).

6.5.2.7 *Immune cell staining in lung tissue sections*

Monocyte/macrophages localised in the tissue of the fixed lung sections were determined by Cluster of Differentiation 68 (CD68) glycoprotein immune-fluorescent staining. This 110 kilodalton (kD) transmembrane protein has long been characterised in this population (Wang *et al*., 2006). As a key immune cell in the lungs as either resident or infiltrating populations' co-localisation with FPR1 is an important factor to be elucidated as well as co-localisation with other markers such as CD45, E-Cadherin and Vimentin.

Leukocytes (white blood cells) are all CD45+ and CD68+ macrophages/monocytes are represented by FITC staining. As part of the immune cell markers used to stain lung sections CD45 was utilised to determine distribution of leukocytes. This includes lymphocytes, neutrophils and macrophages and as FPR1 is most abundant in neutrophils not all CD45 cells are expected to FPR1 positive. Firstly, a directly labelled CD45 (FITC) antibody was tested for its specificity for leukocytes. Unfortunately this antibody would not bind CD45+ cells and exhibited only non-specific staining in fixed lung tissue of artefact. This is clearly demonstrated by the absence of positivity in Figure 6.22 which is changed dramatically when the PMT gain is elevated past control settings showing a clear indiscriminate pattern.

Obviously another antibody was sought to enable accurate visualisation of CD45+ leukocytes, a rabbit polyclonal (Abcam, UK) was chosen. Testing on human fixed tissue revealed specific staining of distinct cell populations in the lung. Indirect staining of tissue with the anti-CD45 primary and subsequently a TRITC secondary antibody demonstrated clear localisation of CD45 on the membrane/cytoplasm compartments.

With the panels consisting of representative, functional markers FFPE-sections from normal, COPD, IPF and Bronchiectasis patients were subjected to immunocytochemistry to reveal co-localisation (if any) with human FPR1. As expected, a proportion of CD45+ cells (leukocytes) expressed FPR1 with this subpopulation most likely consisting of neutrophils. Correlating with previous data detailing lower expression in macrophages compared to PMNs, CD68+ cells did not co-localise with FPR1.

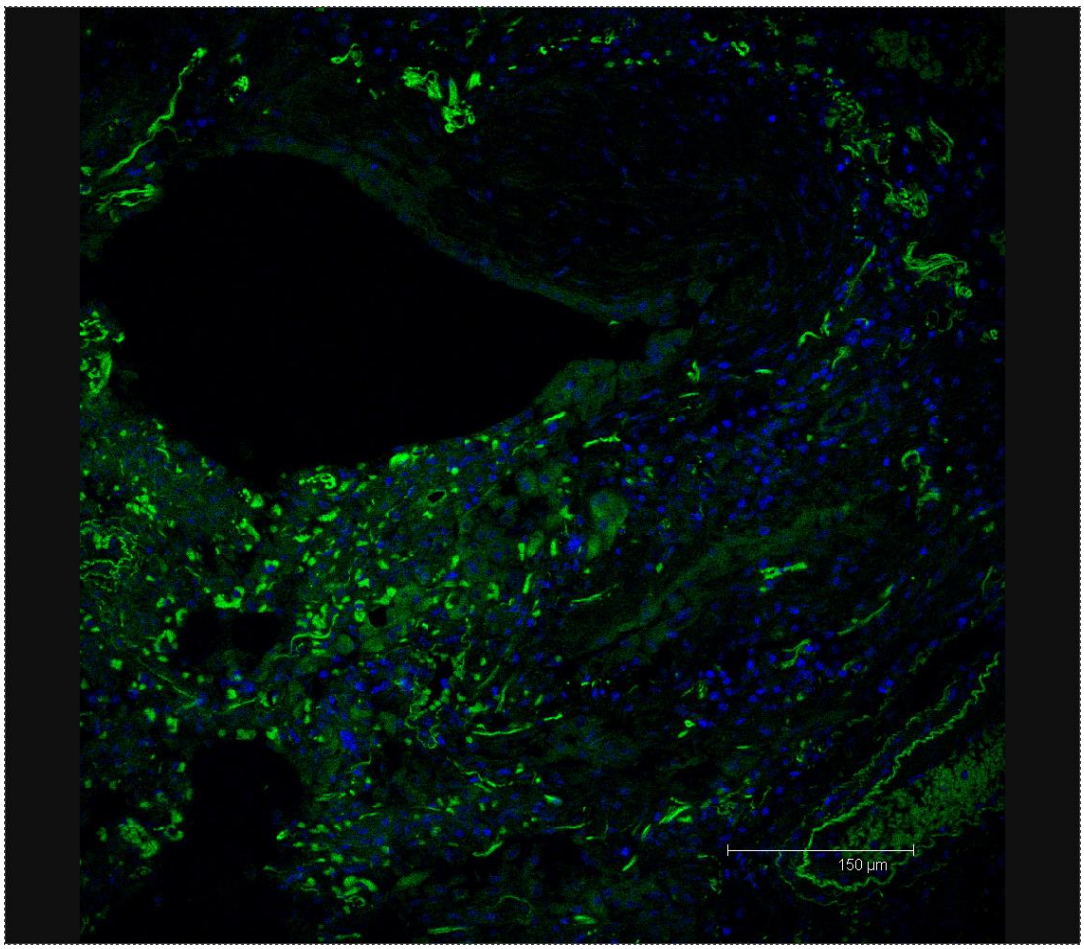

Figure 6.22: Immunocytochemistry with directly labelled CD45 antibody on FFPE sections. Sections counterstained with DAPI nuclear dye as well as CD45-FITC (x20 magnification). With no specific staining the exposure was increased until signal was visible (above).

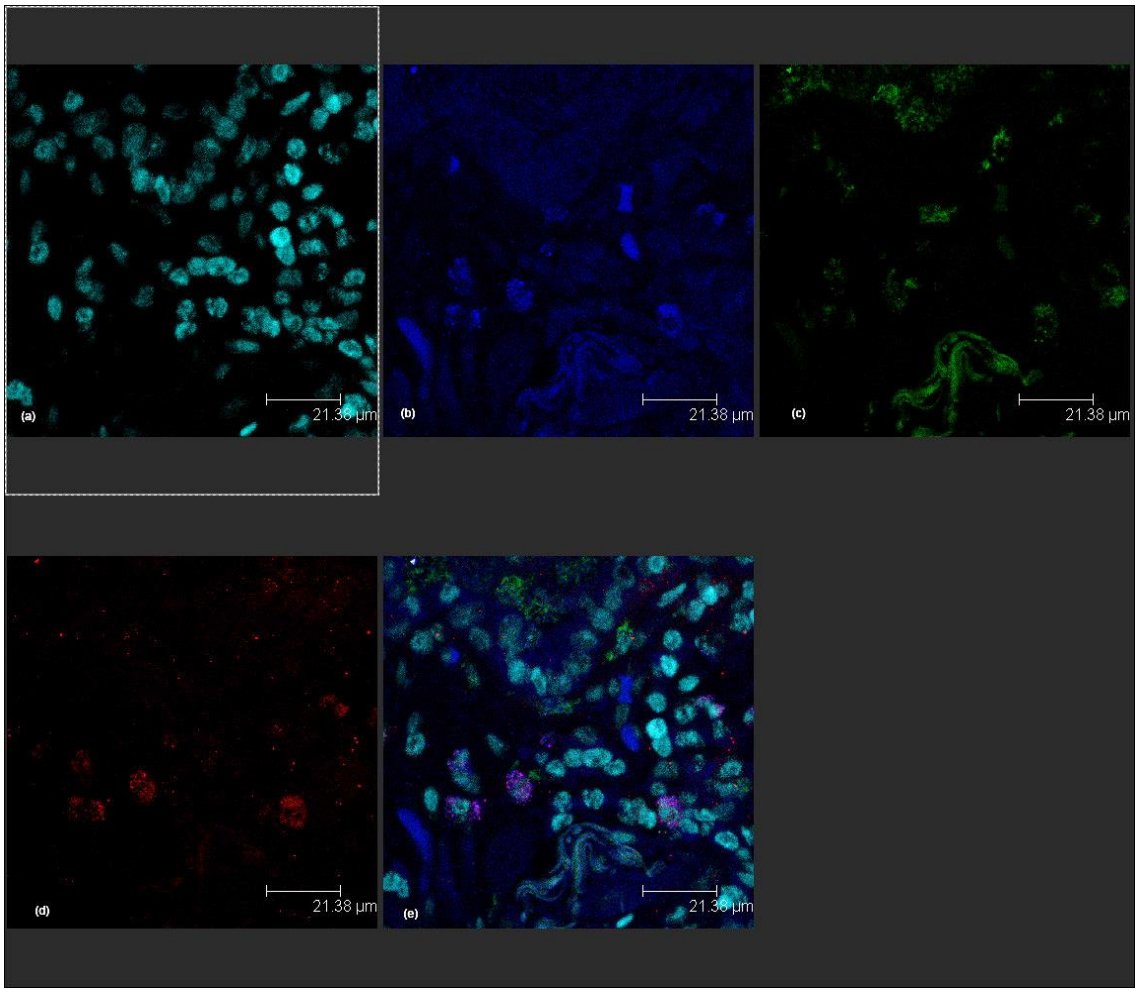

Figure 6.23: Immune cell staining of IPF FFPE tissue sections. FFPE sections were stained for (a) DAPI (cyan), (b) FPR1-APC (blue), (c) CD68 (green), (d) CD45 (red) and (e) overlap composite image generated with LCSM performed at x63 magnification. Images representative of n=3 IPF cases.

Ideally increased numbers of patients from the different disease groups: IPF, COPD and normal would have been used but limited numbers of tissue blocks were available at the time. In the future more tissue sections from different patients should be stained for these markers to increase the power and validity of the expression profile that is demonstrated in the limited number of cases.

6.6 Flow cytometry of cultured cells for human FPR1 protein expression

Due to the lack of specific and good quality antibodies for western blotting an alternative strategy for evaluating protein expression of the formyl-peptide receptor was sought. A FACs-based method was investigated as MedImmune had recently generated an in-house antibody for human FPR1 along with a corresponding isotype control. Douthwaite *et al*. (2014) demonstrated abundant expression in neutrophils isolated from healthy volunteers.

The direct linkage of the human FPR1 antibody (generated in-house by MedImmune, Cambridge) to an allophycocyanin (APC) fluorophore, according to lightning-linker protocol (InnovaBiosciences), enabled evaluation of FPR1 protein expression in a variety of different cell types. With the inclusion of an appropriate isotype control (IgG), unstained cells and viability dyes the median fluorescent intensity (MFI) is able to be calculated.

Flow cytometry is a process by which dyes and fluorochromes absorb light and emit a higher wavelength. Dichroic mirrors are responsible for the reflection of light at specific wavelengths. These emissions are detected and converted to an electrical current with a proportional voltage relative to the amount of light resulting in a digital signal in form of median fluorescence intensity (MFI).

Side and forward scatter equate to the two main measurements of the physicality of the cells being analysed. Forward scatter is the diffracted light from the laser is proportional to size. Side scatter is the refracted (plus reflected) light from the different lasers allowing intracellular complexity to be gauged.

In the event of multi-parameter analysis when multiple antibodies are used to stain the same sample a variety of different channels are required. In the case of multiple fluorophore utilisation spectral overlap is a concern as conjugates with emission

ranges that are close together may result in false positive signals. Electronic compensation is required to correct signal 'bleeding' between different channels. Ideally fluorophores should be chosen with separate emission ranges such FITC and PerCp.

Each experiment will have several different controls such as unstained cells, compensation controls and isotype controls. The latter control will define the non-specific background. A threshold can be generated by defining a cut-off for negative and positive staining when using a multi-parameter panel.

Following dissociation of cultured cells and staining in a 96-well format samples were run through the flow cytometry machine and analysed accordingly. Populations were gated to exclude cellular debris and doublets for live, single cells proportion. After live/dead exclusion following viability dye incubation cells were gated according to the signal for APC. For cultured cells appropriate controls were used including unstained, isotype APC antibody as well FPR1-APC antibody staining. The gating strategy employed for cultured cells was consistent with all cell types evaluated.

6.6.1 HFPR1-APC antibody validation

Firstly, the HFPR1-APC antibody was validated using the control transfectants overexpressing FPR1 and FPR2 respectively. As with gene expression ascertained by real-time PCR method FPR1 is abundant in FPR1-HEK cells while expression is dramatically reduced in FPR2-HEK cells. In FPR2-HEK cells expression drops to near basal levels showing little increase over unstained (U/S) and IgG isotype controls in terms of MFI (Figure 6.24).

Validation of this antibody using control HEK HFPR Ga16 Cl.1 (MedImmune, UK) transfectants revealed strong expression in cells overexpressing FPR1. Cells had a mean MFI of 53.83±23.08 in unstained controls and 97.83±21.38 in the isotype APC control. FPR1-HEK cells showed high levels of FPR1 expression as indicated by a mean MFI of 452.5±24.62. There is a clear shift in signal between the negative controls and FPR1-APC stained cultured cells ($p<0.0001$).

A different cell line, HEK Ga16 pGENIRES neo FPRL-1 Cl.5 (MedImmune) capable of overexpressing FPR2 (FPRL-1) exhibited a basal level of FPR1 expression.

Transfected to synthesise this FPR family member has normal expression of FPR1 compared to FPR1-HEK cells with a clear reduction ($p<0.01$).

Another way of validating the antibody was undertaken by testing neutrophils isolated from healthy human volunteers (carried out by John Simpson's group). HFPR1 expression is elevated in this cell type with significant signal shift compared to U/S and IgG controls (Figure 6.25). Cells had a mean MFI of 92.4±11.55 in unstained controls and 145.7±6.173 in the isotype APC control ($p<0.05$). PMNs showed high levels of FPR1 expression as indicated by a mean MFI of 340.3±9.433 rising significantly ($p<0.0001$) from unstained and isotype controls. This correlates with methodology in Douthwaite *et al*. (2014)'s paper where abundant expression of HFPR1 was reported as demonstrated by the quantitation of FPR receptors on the surface membrane.

6.6.2 HFPR1 expression in primary human fibroblasts

6.6.2.1 *Normal lung fibroblasts*

Isolated from *ex vivo* perfused lungs these 'normal' phenotype lung fibroblasts were analysed for expression of FPR1 by flow cytometry. Cultured cells grown in 6-well plates were harvested for flow cytometry to evaluate FPR1 expression. Normal cells were treated with different inflammatory stimuli: lipopolysaccharide (LPS, a TLR4 ligand); transforming growth factor-Beta (TGF-β1) and poly I:C (TLR3 ligand). TLR4 expression is reported to be markedly low in lung fibroblasts compared to TLR3 expression. Untreated normal fibroblasts exhibited no change in MFI between IgG and hFPR1-stained cells. Compared to unstained cells there was a significant increase in signal from both IgG and FPR1-stained cells ($p<0.0001$). With no difference between isotype and antibody stained cells in any of the treatments and certainly no increase in FPR1 MFI, the expression of human FPR1 is undetectable (Figure 6.26).

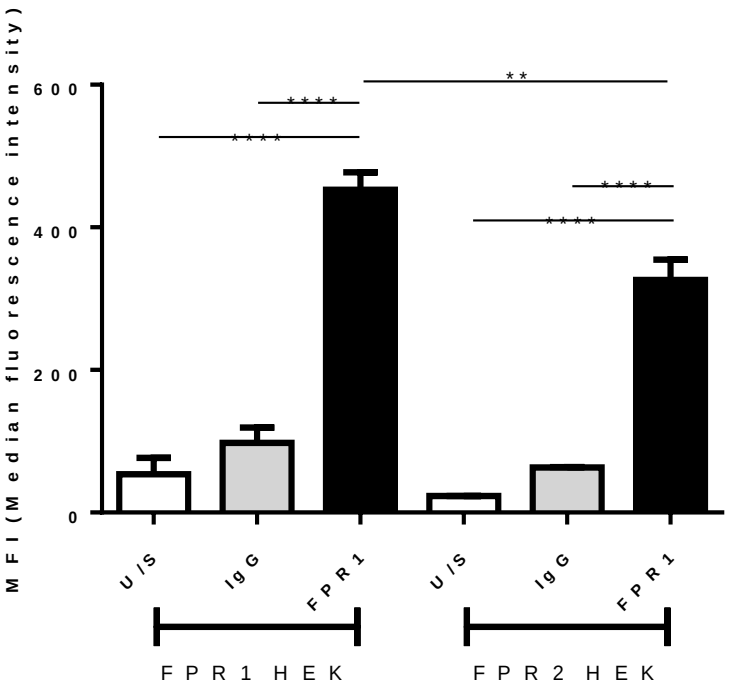

Figure 6.24: Validation of human FPR1-APC labelled antibody using control cell lines transfected with FPR1 and FPR2. U/S (unstained), IgG (isotype control) and FPR1 (APC conjugate) antibody stained cells yielded a digital signal, median fluorescence intensity (MFI). Data is representative of 3 independent experiments. Results were calculated as mean MFI. All p values determined by using a one-way analysis of variance (ANOVA); **p<0.01, **** p<0.0001.

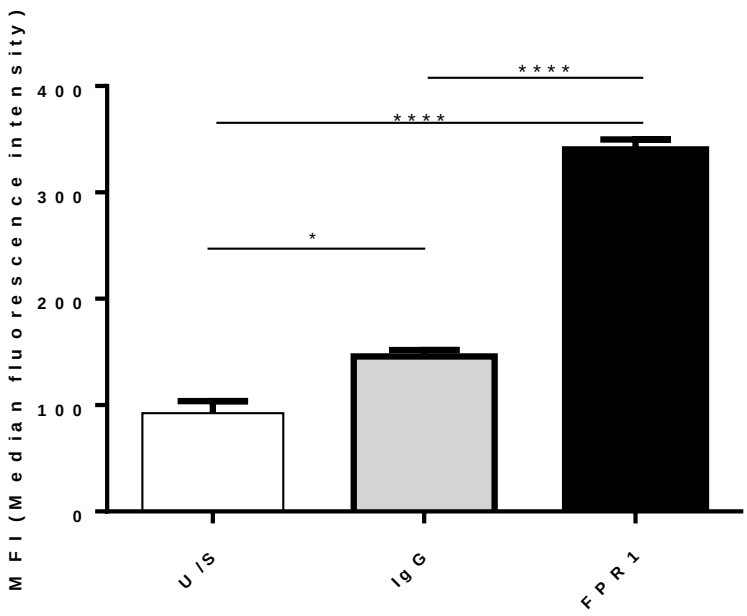

Figure 6.25: Human FPR1 levels in primary neutrophils. U/S (unstained), IgG (isotype control) and FPR1 (APC conjugate) antibody stained cells yielded a digital signal, median fluorescence intensity (MFI). Results were calculated as mean MFI. Data is representative of 3 independent experiments. All p values determined by using a one-way analysis of variance (ANOVA) * $p<0.05$, **** $p<0.001$.

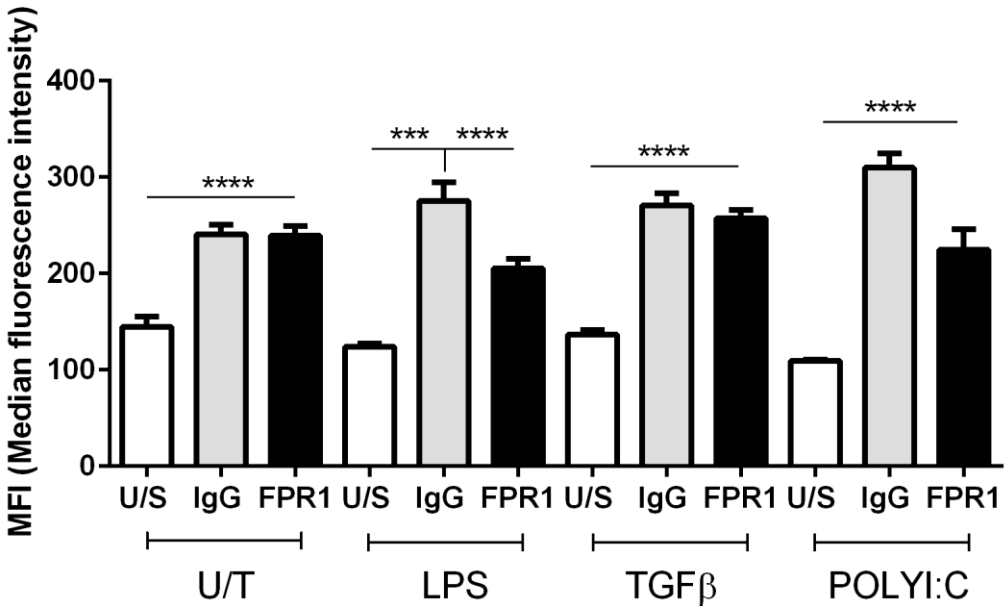

Figure 6.26: Normal human lung fibroblasts and their FPR1 levels following inflammatory stimuli. Isolated cells were treated with LPS (100ng/ml), poly I:C (4µl/ml) and TGFβ (10ng/ml). U/S (unstained), IgG (isotype control) and FPR1 (APC conjugate) antibody stained cells yielded a digital signal, median fluorescence intensity (MFI). Data is representative of 3 independent experiments. Results were calculated as mean MFI. All p values determined by using a one-way analysis of variance (ANOVA); *** $p<0.001$, **** $p<0.0001$.

6.6.2.2 *Diseased lung fibroblasts*

Fibroblasts derived from the lungs of diseased patients either IPF or COPD were analysed for hFPR1 expression at a basal, untreated state. Expression was compared between untreated controls and the two chronic diseases. As shown before NHL fibroblast there was no significant shift in MFI which indicated a barely detectable level of expression. In cells isolated from IPF lungs (n=3 patients) the MFI signal increased significantly from U/S negative controls (mean MFI of 136.8±28.73) to 284.7±33.05 (IgG control; $p<0.05$) and 454±76.32 (hFPR1; $p<0.0001$). Human FPR1 expression was increased in IPF fibroblast significantly ($p<0.05$) comparing IgG and FPR1-stained cells. Compared to normal lung fibroblasts there is clear expression in cells isolated from fibrotic explant tissue (Figure 6.27).

Fibroblasts derived from COPD patient fibroblasts (n=3) were also assayed for FPR1 expression (Figure 6.28). From IgG-isotype stained controls and FPR1-stained cells increasing from mean MFIs of 250.4±25.59 to 335±16.52 respectively ($p<0.05$). In untreated cells human FPR1 expression was evident in fibroblasts sourced from diseased explant lungs potentially indicating a role for chronic lung conditions where repeated inflammation/damage is a common theme.

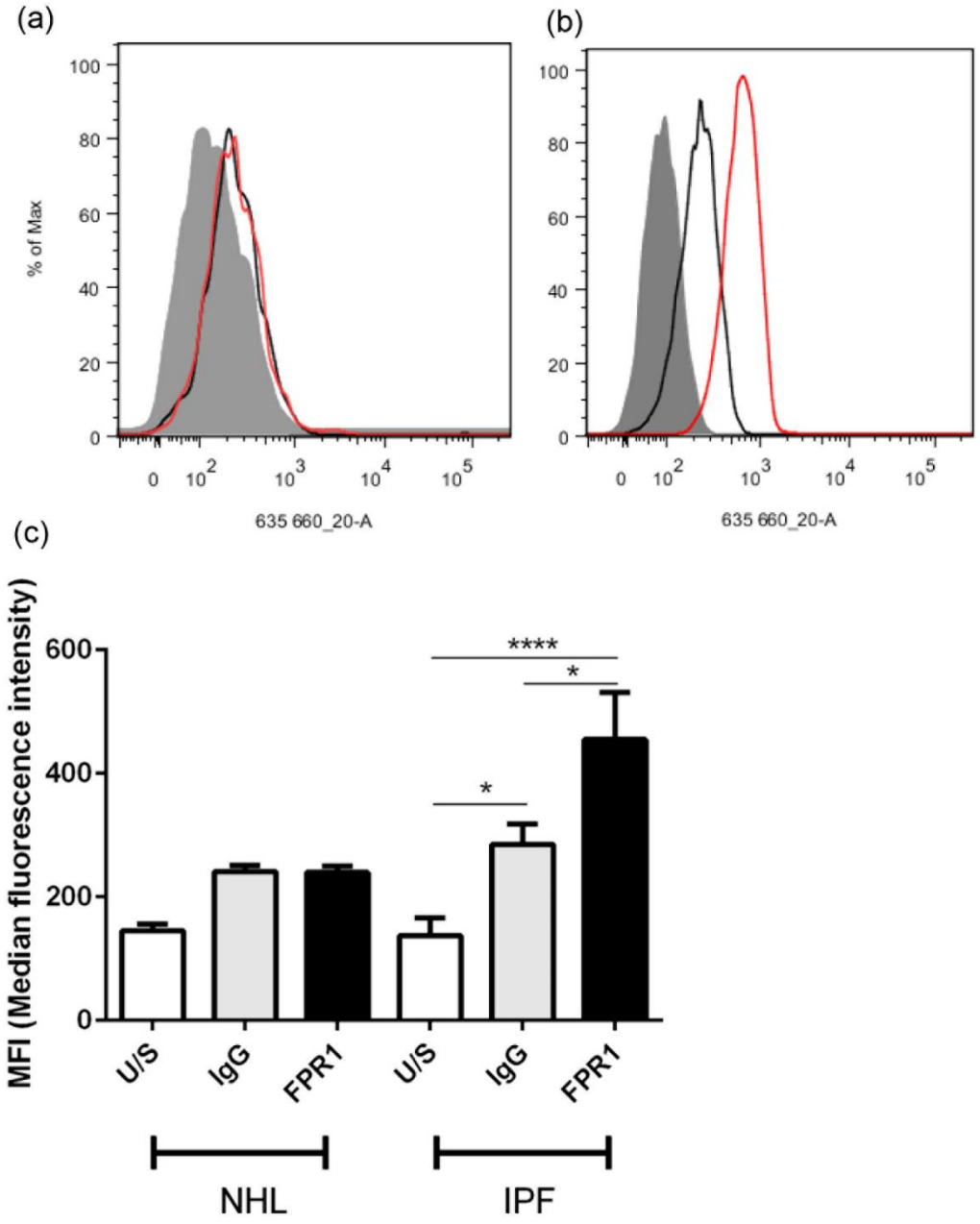

Figure 6.27: IPF and NHL fibroblast hFPR1 levels at a basal level. (a) Fluorescence histogram for NHL fibroblasts; (b) Fluorescence histogram for IPF fibroblasts. U/S (unstained, grey peak), IgG (isotype control, black peak) and FPR1 (APC conjugate, red peak) antibody stained cells yielded a digital signal; (c) median fluorescence intensity (MFI). Data is representative of 3 independent experiments. Results were calculated as mean MFI. All p values determined by using a one-way analysis of variance (ANOVA) * $p<0.05$, **** $p<0.0001$

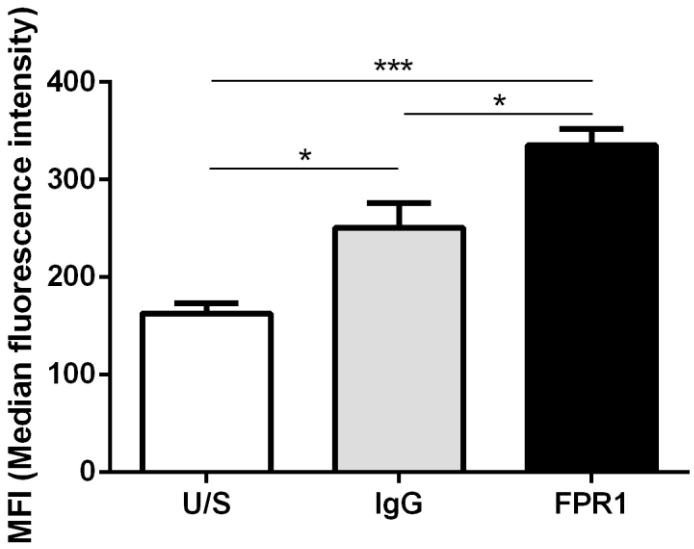

Figure 6.28: COPD fibroblast hFPR1 levels at a basal level. U/S (unstained), IgG (isotype control) and FPR1 (APC conjugate) antibody stained cells yielded a digital signal, median fluorescence intensity (MFI). Data is representative of 3 independent experiments. Results were calculated as mean MFI. All p values determined by using a one-way analysis of variance (ANOVA) * $p<0.05$, *** $p<0.001$.

6.6.3 Conclusion of in vitro FPR profile

Expression of the FPR family in different cell types was demonstrated in typical immune cells and non-phagocyte cells. Priming by inflammatory stimuli may indicate co-ordination of different signalling pathways perhaps involving the pattern recognition receptors, the TLRs. Analysis of protein expression proved difficult due to a lack of validated, commercial antibodies but from access to an in-house antibody (MedImmune, UK) as part of my industrial collaboration enabled preliminary experiments to be performed to determine protein expression in different cell types. Positive human FPR1 expression by flow cytometry was exhibited in IPF and COPD fibroblasts isolated from diseased tissue as well as in positive controls such as transfected cell line FPR1-HEK and neutrophils. By itself this is not definitive proof of expression in diseased fibroblasts hence determination of a FPR1 expression profile in FFPE lung tissue sections. Immunocytochemistry with the same antibody used in a FACs-based strategy showed that isolated fibroblasts in IPF sections and not in COPD sections were positive for FPR1 expression. Perhaps in culture the microenvironment of the cells changes to a non-physiologically relevant variant which is different in the FFPE sections.

6.7 Summary of FPR expression profile

- Inflammatory stimulus such as LPS ‘primed’ FPR expression at gene level in non-phagocytes and immune cells.

- Expression was demonstrated in IPF lung sections and primary lung fibroblasts contrasting with normal human tissue.

7 Discussion

7.1 Bleomycin-mediated fibrosis and FPR1

The *in vivo* model for investigating pulmonary fibrosis is limited due to the nature of its pathogenesis (acute and fibrotic). Features observed during studies involving bleomycin are facets/caveats of the model itself not necessarily the disease it is purposed to mimic. The distinct phases of the bleomycin model: acute and fibrotic are unlike the pathogenesis of IPF presented in the literature. Lung fibrosis is not an acute process but in a way this an advantage of the *in vivo* model as fibrosis is able to develop in a matter of weeks not months or years as is typically the case in human patients. Some individuals are genetic predisposed to ILD development or some have moderate lung function then an exacerbating effect like a virus or opportunistic infection comes along and the conditions worsens. Human fibrotic disease is far more complicated than the pathogenesis of different *in vivo* models but the nature of these short-term manifestations of disease makes them ideal for therapeutic agent development in a high-throughput fashion.

The bleomycin acute injury model is analogous to acute lung injury (ALI) in humans. Grommes and Soehnlein (2011) describe how an oedema forms with neutrophils as part of the innate immune response, migrating to injury site first to interstitial area in lung tissue as well as bronchoalveolar fluid. BAL is typically used to evaluate the inflammatory cellular infiltrate in the clinical setting and *in vivo* pulmonary fibrosis models. ILDs have an altered cytokine/chemokine level in BAL fluid (Vasakova *et al*., 2008).

Essentially the bleomycin *in vivo* is a combination of ALI and IPF due to the acute injury component which is not typical in the latter condition. The bithiazole ring side chain binds DNA resulting in thickening of the alveolar walls and epithelial/endothelial damage (Hay *et al*., 1990). FPR1 deletion provided protection against pulmonary fibrosis induced by bleomycin. TGFβ shown by Khalil *et al* (1989) to be elevated in BLM-induced fibrosis with a majority of cytokine production by alveolar macrophages which subsequently drives fibroblast proliferation. Transforming growth factor Beta-1 was apparently not affected by ablation of FPR1 in my project's bleomycin model. FPR1's role in fibrosis is independent of this pro-fibrogenic mechanism inherently linked to the development of a fibrotic phenotype. As this cytokine is not affected by

the ablation of the *fpr1* gene the adenoviral TGF-β1-overexpression model is an ideal candidate to evaluate the role of FPR1 in another pulmonary fibrosis mechanism/pathogenesis. Further investigation of FPR1 expression and its effect on TGFβ1 activity could potentially elucidate how this cytokine's downstream signalling is affected in the non-functional mutants.

7.1.1 Microenvironment of organ and FPR1's role in fibrosis

The role of neutrophils in chronic lung disease such as IPF is unclear, differential BAL counts and neutrophil elastase IHC increased counts in primary human tissue suggest a potential role for polymorphonuclear leukocyte (PMN) in this rare condition (Obayashi *et al*., 1997). Neutrophil properties include the production of cytokines, chemokines, proteases, reactive oxidants, prostaglandins, leukotrienes and presentation of Class II MHC on their cell surface membrane. These different products interact enabling multi-functionality to be exhibited in terms of T-cell activation, adhesion molecules expression, chemoattraction and migration towards injury site. While it is apparent that neutrophils are certainly present in chronic disease in the lung, liver, kidney and other organs its function in the development of fibrosis is not as well defined.

PMNs are a major part of the adaptive and innate immune response as clearly indicated at acute endpoints in the lung and the liver of mice dosed with bleomycin and carbon tetrachloride respectively where distinctive elevations of NIMP+ve cells were shown by IHC. Hepatic infiltration of the liver following CCl_4 injury consists of migration into the parenchyma (Hasegawa, 2006). At 24 hours there were more PMNs present in the tissue than at 5 days post-bleomycin instillation which is in keeping with their short life span of approximately 12 hours in a non-activated state (Hu, 2012). With activation may live in the human body/culture for up to 48 hours so a peak neutrophilic response will be observed in this period.

7.1.2 Liver fibrosis and the neutrophil

The role of neutrophils in the liver is controversial with regards to fibrosis but in acute liver injury they are key players. Induction of PMNs and other immune cells with acute injury via CCl_4 injections in the present project indicates a strong response to hepatotoxic injury. Acetaminophen (APAP), CCl_4 and ischaemic reperfusion are all capable of triggering hepatocyte cell death in a sterile fashion which in turn leads to

the release of endogenous alarmins such as N-formylated peptides. Of particular note, recent research has highlighted that DAMPs released from damaged/dying hepatocytes may direct neutrophil homing to injury sites (Marques *et al*., 2013). Sterile inflammation may have more of an impact in the liver per say than the lung due to the nature of the organ microenvironment. Direct inhibition of neutrophil migration/activation with chemokine and FPR1 antagonists did indeed decrease PMN chemotaxis and ultimately liver injury. Blockage *in vitro* of neutrophils' CXCR2 and FPR1 by antagonist correlated with *in vivo* work clearly demonstrating the well, characterised role for FPR1 in the chemotactic behaviour of neutrophils in the liver setting.

Sterile inflammation in the liver as well as other organs is a relatively new concept with a multitude of different DAMPs released as a result cellular damage being present in the liver (Kubes and Mehal, 2012). In the liver DAMPs bind a variety of pattern recognition receptors including TLR2, TLR4, TLR9, RAGE, CD14, CD91, CD2 and formyl-peptide receptors, FPR1 and FPRL1. Certainly the range of diverse endogenous alarmins present due to injury, trauma and oxidative stress means that even without bacterial infection an inflammatory signal is able to be generated as a result of inflammasome activity (Moles *et al.,* 2014)

Sterile and non-sterile immune responses are important processes in the body as tissue injury is not necessarily associated with infection. Neutrophils, a key effector in the innate immune response are vital in any inflammatory events in the body especially since they respond to both endogenous and exogenous stimuli. tlr2-/- and s100a9-/- mice exhibited defective neutrophil recruitment to sites of injury induced by CCl_4, a hepatotoxin. While neutrophils may not be as important in this model they are commonplace in liver disease such as acute alcoholic hepatitis (AAH), acetaminophen induced liver failure (APAP ALF), primary biliary cirrhosis (PBC), primary sclerosing cholangitis (PSC), alcoholic liver disease (ALD) and non-alcoholic steatohepatitis (NASH). The extent of neutrophil involvement in chronic fibrotic conditions such as cirrhosis is yet to be fully elucidated. Neutrophil recruitment with acute injury such as CCl_4 toxin is triggered by the release of mediators from injured hepatocytes as well as Kupffer macrophage cell produced chemokines. These factors direct the neutrophils to the site of injury along a gradient enabling a rapid response in acute models/diseases (Moles *et al*., 2014).

N-formyl peptides are potent chemoattractant dictating the migration of immune cells towards sites of injury, damage and infection. NFPs and bacterial formyl-peptides elicit similar effects in neutrophils. Endogenous mechanisms play an inherent part in wound-healing and fibrosis development (Ariel and Timor, 2013). Typically with neutrophils and macrophages this occurs along a gradient which cells follow. The role of neutrophils in the development of liver fibrosis or lack thereof is further supported by Saito *et al*. (2002) where they reported that depletion of PMNs demonstrated no effect on hepatic fibrogenesis in a bile duct ligation (BDL) cholestatic liver disease model. This model has different pathogenesis to the toxin-mediated models with ligation of the biliary structures leading to ductular inflammation, proliferation of bile ducts and development of portal fibrosis. Due to the high amount of infiltration in the BDL model of neutrophils to fibrotic areas and the fact that treatment with anti-neutrophil antiserum did not ECM deposition significantly, further cements the theory that neutrophils have little regulatory effect on liver fibrosis regardless of the model's pathogenesis. The recent research of neutrophils in the liver with regards to acute injury, wound-healing, fibrosis development and hepatocellular carcinoma (HCC) highlights that neutrophils have a variety of pleiotropic functions depending on disease-specific mechanisms or 'redundancies' in the case of liver fibrosis. If more time had been available another liver fibrosis model would have been utilised to confirm that FPR1+ve neutrophils do not have a major role.

7.1.3 DAMPs in the liver

7.1.3.1 *FPR2, a better therapeutic target?*

Ablation of FPR1 and FPR2 expression in mice elicited downstream effects on the liver's response to LPS, a bacterial membrane component. Without FPR1/2 the immune response is dysregulated leading uncontrolled inflammation and unchecked damage as indicated by serum transaminase levels, AST and ALT (Giebeler *et al*., 2014). Key studies include: a murine model of hepatic (liver) necrosis induced by a targeted thermal injury. This model highlighted the importance of FPR1-mediated neutrophil accumulation at lesions (McDonald *et al.*, 2010). With injury to the liver neutrophils are critical to the damage response. This clearly evident in my own project with neutrophil infiltration of the liver upon acute injury with carbon tetrachloride. The

controversy with liver fibrosis is whether neutrophils are key players in its development or redundant as recent studies suggest.

Looking another member of the formyl-peptide receptor family, FPR2/FPRL1 appears to have a myriad of different roles in disease probably due to its large repertoire of ligands often with differing downstream signalling effects. Indeed the ALX/FPR2 has emerged recently as a potential therapeutic target in the treatment of chronic inflammation in COPD (Bozinovski *et al*., 2013). Opportunistic and persistent microbial insults provide a source of Serum Amyloid A (SAA) which induces downstream pro-inflammatory effects. Interestingly, endogenous molecules and metabolites such as LXA_4 have the opposite effect triggering pro-resolution events. FPR2 knockout mice were protected from OVA/alum-induced allergy model in lung with a reduced inflammatory response. This asthma *in vivo* model demonstrated a reduced CD11c+ dendritic cell infiltration in airways and lymphatic system along with lower levels of IL-13, IL-4 and IL-5 Type II cytokines and allergy-mediator IgE (Chen *et al* 2010). The importance of FPR2 in airway inflammation was furthered by wild type BAL eliciting agonistic behaviour on bronchial embryonic epithelial cells. FPR2 is again associated with inflammation in the neurological setting with contributions to Alzheimer's disease (AD) and other neurodegenerative disorders proven. Agonistic activity by $A\beta_{42}$ plaque units, the causative agent behind the progressive neuronal loss, implicates FPR1 and FPR2 (Yazawa *et al*., 2001). One thing to consider in the FPR1 knockout mice is what is the deletion and loss of functionality doing to the activity of FPR2 in the different models of fibrosis. Are there compensatory mechanisms at play here that would perhaps explain why no effect is seen in the CCl_4 and UUO models or is this purely due to the microenvironment/model-specific caveats?

As for other immune cells heavily implicated in liver fibrosis, Kupffer macrophages, FPR1 appeared to have no effect on infiltration into CCl_4-chronically injured livers. These resident liver macrophages act as TGFβ1 cytokine reservoirs thus are responsible for stellate cell activation and from human and mouse *in vivo* equivalents of liver fibrosis are key effectors of fibrogenesis (Kolios *et al*., 2006). Previously, data from the bleomycin-mediated pulmonary fibrosis model suggested a TGFβ1-independent mechanism which may be consistent in the liver microenvironment. Since

a similar level of CD68 positive cells is observed in WT and KO injured livers there should be no change in TGFβ1 level between genotype. Hepatic Kupffer macrophages are also implicated in resolution of fibrosis as well as being a driving force behind fibrogenesis and stellate cell activation. Studies have shown that Kupffer cells have an indirect effect on re-balancing the ECM matrix equilibrium through neutrophil infiltration (Harty *et al*., 2008). Reparation of BDL-induced damage by biliary decompression of obstructed bile ducts is an ideal liver repair model. –evaluation of FPR1 deletion in this acute mechanical injury model would have been optimal.

7.1.4 Renal fibrosis and FPR1

To expand the work already completed with the UUO model in terms of histology and immunohistochemistry more aspects of this intriguing model should be considered before writing off the role of FPR in renal fibrosis. Gene expression levels of different renal injury and healing markers would be vital in fully determining the effect of FPR deletion in this novel microenvironment. One such specific biomarker is Kidney Injury Molecule-1 (KIM-1) a proximal tubular damage biomarker. This type 1 TM protein is well characterised in chronic kidney disease (human and *in vivo*) with defined diagnostic tests for urinary and serum outputs. Recent papers have highlighted this biomarker in the wider context of wound-healing rather than just an injury marker of proximal tubular epithelial cells (PTECs). Its expression on tubules and interstitial areas is an interesting avenue to consider due to the lack of knowledge in non-acute renal injury models such as the UUO model (Lim *et al*., 2013). Han *et al*.(2002) also highlight the importance of KIM-1 in proximal tubule injury processes and acute tubular necrosis (ATN) patients.

Different endpoints are easily utilised in the UUO model to represent the infiltration and renal fibrotic phases. Tubular damage was assessed in a MMP-12 -/- based model with KIM-1 by Abraham *et al*. (2012). The ability to assess injury at a molecular level will strengthen histological scoring of the PAS-stained tissue sections which determines the extent of tubular dilatation and interstitial expansion, two key measures of the progressive injury in this renal setting. The UUO model involves a different type of injury compared to bleomycin acute model and CCl_4-chronic model. Ischaemia-reperfusion (I/R) injury models of kidney chronic disease may be more suitable for

investigation of formyl peptide receptor in this setting. One of the features of this model in the kidney and other organs is major leukocyte migration (Gavins, 2010).

7.1.5 Induction of FPR expression

A common theme determined in cells cultured *in vitro*, whether they be immune or non-phagocyte, is that FPR expression is 'primed' or up-regulated by inflammatory stimulus lipopolysaccharide (LPS) treatment. This suggests a co-ordination of signalling pathways such a TLR2/4 which LPS binds. LPS significantly heightens expression of FPR in macrophages, neutrophils and fibroblasts which would theoretically increase FMLF activity in those cells due to increased ligand-receptor interaction. Synergy of LPS and FMLF functionality in cultured has been shown to demonstrate coordinated cytokine inflammatory responses (Chen *et al*., 2009). In non-sterile microenvironments in the body endogenous N-formylated peptides are released from necrotic/dead cells which in conjunction with underlying conditions such as opportunistic infections (bacterial/viral) exacerbate inflammation and potentially the subsequent wound-healing response. Contrary to this coordinated affair, earlier research by Vulcano *et al*. (1998) elucidated a tolerising effect of FMLF pre-treatment on human neutrophil resulting in a dampened pro-inflammatory TNFα response. It is worth considering that different ligands interacting with the different FPRs have a plethora of effects and co-ordination with a myriad of signalling pathways including CXCR2, uPA and EGFR. FPR2 does not bind high affinity ligands such as FMLF but a more promiscuous role in the body not restricted to inflammation and immune cell migration.

TLR4 has reportedly very low expression in human fibroblasts unlike mouse equivalents hence responsiveness may be affected between species.

7.2 Future work

7.2.1 FMLF activity

Due to the effect determined in the lungs of bleomycin-injured mice depleted of FPR1 expression further work is required to elucidate the mechanism behind N-formyl peptide involvement in pulmonary fibrosis. A key experiment that would have added to existing data regarding the acute injury model would be to ascertain if formyl peptides

are located in diseased human lung of IPF patients. Although no antibodies are commercially available, some immunoglobulins have been generated that select for N-formyl peptides. Antibody FTD6G5 and other selective N-formyl peptide antibodies may indeed be further developed for therapeutic interventions for use in a myriad of different diseases (Tanaka *et al*., 2007). Another potential strategy for detection of these peptides in diseased lung whether from injured mice or chronic human cases could be the utilisation of mass spectroscopy. Breitung *et al*. (2008) describe a method for generating labelled N-formylated peptide: N-formyl-Met-Leu-Phe-OH (1) in a mild synthetic manner consisting of solid phase amino acid polymerisation, N-formylation and purification via high-performance liquid chromatography (HPLC). For validation of the produced peptide f-MLF-OH was radiolabelled and analysed for its mass spectrum yielded a value of 460.3. The detection of this labelled tri-amino acid chain via solid state NMR may indicate a novel method for determining formyl peptide release in the injured lung microenvironment (Breitung *et al*., 2008).

In order to build upon the nature of formyl peptide involvement in lung fibrosis a mechanistic, more ligand-driven approach is required. The use of knockout mice with ablated FPR1 expression was a useful tool to investigate how ligation of this receptor affected fibrosis in the lung and other organs but the effect of formyl peptides to the pulmonary environment needs to be elucidated. Since a significant reduction in the bleomycin-injury model was determined via a drop in a variety of different fibrotic markers in knockout mice, the activation of this receptor by formyl peptides may potentially have an effect on the development of pulmonary fibrosis. One point to consider is on the main caveats of bleomycin's pathogenesis: the dependence of the latter fibrosis stage on the acute inflammatory phase. This complicates any findings from the bleomycin model as it any protective effects in FPR1 null mice may be due to inflammation-dependent fibrosis. A key point worth investigating is whether FMLF administration before/after bleomycin-injury would augment the fibrosis development in the latter phase. The groups of such an experiment would be as follows: 1) WT - Bleomycin IT - Twice weekly saline IN; 2) WT - Bleomycin IT - Twice weekly FMLF IN; 3) fpr-/- - Bleomycin IT - Twice weekly saline IN; 4) fpr-/- - Bleomycin IT - Twice weekly FMLF IN; 5) WT - Saline IT; 6) fpr-/- - Saline IT with harvesting after 21 days.

Regardless, FMLF ligand downstream effects in the lung need to be addressed apart from the bleomycin model. As well allowing determination of high formyl peptide involvement in lung fibrosis this will enhance the data obtained by the preliminary investigation into the role of FPR+ve neutrophils in pulmonary fibrosis. If time and resource constraints had not been a problem dosing of wild type and knockout mice repeatedly with formyl peptide intranasally would have been undertaken. This would've answered the question of whether FMLF drives persistent neutrophil and other immune cell recruitment in the lung. The repeated dosing of the ligand is equivalent to successive damage to cells which has demonstrated to release endogenous sources of this DAMP. As with other inflammatory events in the bleomycin model: cell infiltration and pro-inflammatory cytokine release the response would be more than likely reduced in fpr1-/- mice. Ideally this experiment will consist of 4 groups: 1- WT saline; 2- WT FMLF; 3- fpr-/- saline; 4- fpr-/- FMLF with saline as the control treatment for each genotype. The lung showed how fast it reacts to acute stimuli in the bleomycin model when mice were sacrificed a day after dosing, neutrophils are rapidly localised to sites of injury as indicated by increased NIMP counts. IHC of tissue harvested 24 hours post-FMLF administration will enable measurement of neutrophil recruitment when the level of chemoattractant is artificially elevated. The expected outcome of this experiment will be vastly increased migration of neutrophils in lungs of FMLF-dosed mice in acute model.

This approach is a tantalising route to assess the role of formyl peptide activity in the lung microenvironment but several things must be considered. FMLF treatments *in vivo* should be undertaken with the knowledge that FMLF has a transient stability in the mouse lung due to rapid metabolism. Potential adverse effects also present a problem as FMLF causes direct bronchoconstriction with high doses triggering pulmonary toxicity. Corteling *et al*. (2002) present a novel method of lung neutrophil activation in different strains of mice and hamsters but the practicalities of such the intranasal method are a major consideration. BAL differential cell counts for neutrophils, lymphocytes and eosinophils all showed significant increases in different strains of mice (BALB/c and C57BL/6) with inflammatory stimulus, lipopolysaccharide (LPS). Of particular note for the work undertaken previously in my project is that C57BL/6 mice display neutrophil infiltration with LPS and FMLF treatment. Essentially, a priming mechanism is in effect due to FMLF alone having no effect on neutrophilic response.

Myeloperoxidase (MPO) and elastase activity was drastically increased in dual-treated mice compared to that of vehicle and single-treatments also suggesting a priming mechanism based on co-ordination of different pathways.

Reproducibility of the FMLF response coupled with the similar effects of LPS on neutrophils in the lung are key factors to take into account for this method. Utilisation of a high-grade purity source of FMLF with no LPS contamination would eliminate any doubt over responses elicited following treatment which is a concern due to reported synergy of the LPS-driven pathways and FMLF activity (Chen *et al*., 2009). In-house experiments conducted at MedImmune (Cambridge, UK) determined that combined treatments of LPS and FMLF triggered variable responses with little reproducibility.

The activity of FMLF in the lung is a key area with many unknowns and due to optimisation issues in terms of its stability and adverse effects this may prove a difficult task to elucidate. Determining whether FMLF exacerbates lung injury is not a simple experiment due to the fact that FMLF causes direct bronchoconstriction. This may be related to its contractile effects on smooth muscle directly induced by FMLF-driven calcium ion influx (Arreto *et al*., 1993; Kawata *et al*., 2005). Airway smooth muscle studies in guinea pig *T. coli* tissue have demonstrated clear increases in insuflation pressure (cmH_2O) which presents a problem for acute lung injury bleomycin mice models. A double insult with FMLF and bleomycin may be too severe for the animals for treatments to be performed. The bronchoconstriction function of the high affinity FPR ligand is not restricted to mice, hamsters or guinea pigs, preliminary investigations in non-asthmatic human patients indicated contraction of primary airway cells *in vitro* and a response to nebulised FMLF on airway function (Berend *et al*., 1987).

As previously stated other models of inducing fibrosis and airway remodelling are required to determine if FPR ligation is playing a key role in this disease. One of many well-characterised *in vivo* methods is the chronic house-dust mite (HDM) model, a type II allergy-driven response. The inclusion of a FMLF ligands/saline regimen into the model will enable the role the ligand in airway remodelling to be elucidated. The groups for this experiment if performed in the future would be as follows: 1) WT - biweekly saline IN for 8 weeks; 2) WT - biweekly FMLF IN for 8 weeks; 3) fpr-/- - biweekly saline IN for 8 weeks; 4) fpr-/- - biweekly FMLF IN for 8 weeks. As with assessment of fibrosis

3 weeks post-bleomycin i.t. data from the 8 week endpoint would include hydroxyproline content, PSR and α-SMA IHC and ECM marker gene expression.

7.2.2 Formyl-peptide levels in the lung

The issue of assessing levels of formyl peptides in diseased tissue is a complicated one. In terms of human disease (Idiopathic pulmonary fibrosis) a potential method of assessing FP activity could be to digest explant tissue (probably via collagenase) to release peptides. The mixture would then be applied to human neutrophils (isolated from blood) for use in chemotaxis assay. Negative controls would consist of blank media and anti-FPR1 blocked neutrophils. The latter control is important as this will block any ligation of the high affinity receptor. This experiment plan is actually similar to a study conducted by Hauser *et al*. (2010) where mitochondrial-derived N-formyl peptides and DNA triggered rapid Ca^{2+} production, MAPK activation, IL-8 and MMP-9 secretion in neutrophils. Such responses were blocked by antagonist action of CsH or anti-formyl peptide receptor-1. Another potential way of determining formyl peptide activity in diseased human/mouse tissue may to utilise the bronchoalveolar lavage (BAL) fluid. Application of the supernatant to human/mouse neutrophils *in vitro* could then be assessed for chemotactic effects, cytokine secretion and MAPK activation. From these tests the functionality of the BAL with regards to formyl peptide activity through ligation of FPR1/2 would be determined.

Mass spectrometry of the BAL samples would be needed to confirm the presence of formyl peptides in the extracellular fluid, to be performed in a similar manner to Breitung *et al*. (2008). Mass spectrometry is an ideal method to the lack of available antibodies for formyl-peptides and the separation by mass (Daltons, Da) and electrical charge (MacGregor *et al*., 2008). Other studies have applied surface enhanced laser desorption ionisation time of flight (SELDI-TOF) mass spectrometry to BAL fluid for assessing cystic fibrosis biomarkers. An advantage of this protocol is the avoidance of biased protein identification by fingerprinting of trypsin digests as well as the low volumes required for analysis (MacGregor *et al*., 2008).

7.3 Conclusions

This project has yielded interesting data regarding the role of the formyl-peptide receptor in the development of pulmonary fibrosis. The abundance of this chemoattractant receptor on neutrophils and to a lesser extent macrophages is perhaps highlighted in the animal models utilised to investigate its role in fibrosis in different organs. The pathogenesis of the fibrotic mechanism and the degree of neutrophil involvement varies between the lung, liver and kidney due to their specific microenvironments and cellular interactions. These observations may be purely bleomycin-model caveats but the aetiology of IPF is complicated which in turn could indicate a potential therapeutic target perhaps in the form of monoclonal antibody therapy. Immunofluorescent staining revealed expression of human FPR1 in CD45+ve neutrophils as well as in isolated vimentin positive fibroblasts. The same fluorescent antibody conjugate validated this localisation in cultured IPF fibroblasts indicated a possible role for FPR1 architecture. Bacterial and endogenous N-formylated peptides could in effect bind both immune cells and these FPR1+ve fibroblasts in the event of opportunistic infection, sepsis or trauma/tissue damage leading to release of cellular contents.

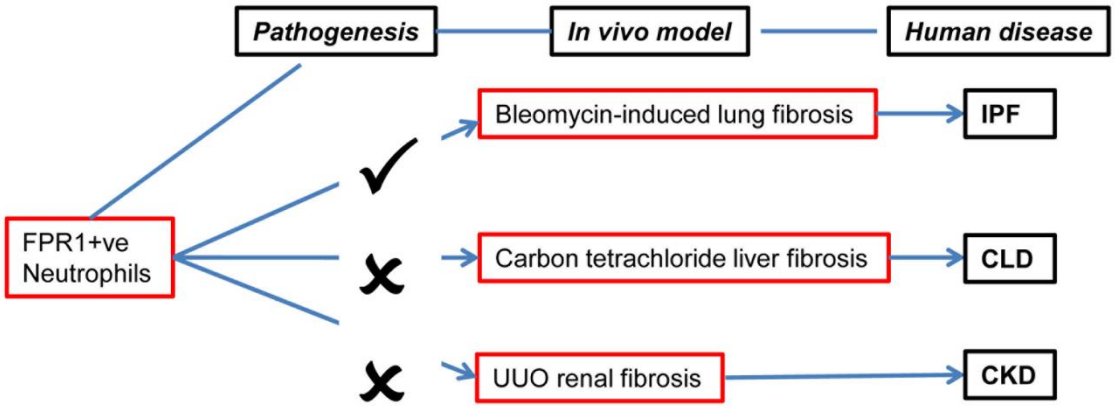

8 Presentations

Nottingham (UK) July 2013 British Association Lung Research (BALR): Poster presentation

Estoril (Portugal) March 2014 European Respiratory Society (ERS): Poster presentation

Institute of Cellular Medicine (ICM) Research Day – June 2015 Oral presentation

Cambridge (UK) September 2014 British Pharmacological Society (BPS): Poster presentation

9 Bibliography

Abraham, A.P. *et al*., 2012. Macrophage infiltration and renal damage are independent of matrix metalloproteinase 12 in the obstructed kidney. *Nephrology*, 17(4), pp.322–329.

Amatruda, T.T. *et al*., 1995. Signal transduction by the formyl peptide receptor: Studies using chimeric receptors and site-directed mutagenesis define a novel domain for interaction with G-proteins. *Journal of Biological Chemistry*, 270(47), pp.28010–28013.

Amulic, B *et al*., 2012. Neutrophil function: from mechanisms to disease. *Annual Review of immunology*, 30, pp. 459-89.

Araya, J. & Nishimura, S.L., 2010. Fibrogenic reactions in lung disease. *Annual review of pathology*, 5, pp.77–98.

Ariel, A. & Timor, O., 2013. Hanging in the balance: Endogenous anti-inflammatory mechanisms in tissue repair and fibrosis. *Journal of Pathology*, p.229 (2): 250–263.

Arnoult, D. *et al*., 2011. Mitochondria in innate immunity. *EMBO reports*, 12(9), pp.901–910.

Arreto, C.D. *et al*., 1993. Pharmacological differentiation by pertussis toxin of the *in vivo* acute responses to fMLF and PAF in guinea-pig lungs. *British journal of pharmacology*, 108(2), pp.412–417.

Arterburn, J.B. *et al*., 2009. Discovery of selective probes and antagonists for G protein-coupled receptors FPR/FPRL1 and GPR30. *Current Topics in Medicinal Chemistry*, 9(13), pp. 1227-1236.

Artlett, C.M., 2014. Animal models of systemic sclerosis: Their utility and limitations. *Open Access Rheumatology: Research and Reviews*, p.6: 65–81.

Becker, E.L. *et al*., 1998. Broad immunocytochemical localization of the formylpeptide receptor in human organs, tissues, and cells. *Cell Tissue Research,* 292(1): pp129-135.

Berend, N. *et al*., 1988. Effect of inhaled formyl-methionyl-leucyl-phenylalanine on airway function. *Thorax*, 43(1), pp.36–40.

Boulay, F. *et al*., 1990. The human N-formylpeptide receptor. Characterization of two cDNA isolates and evidence for a new subfamily of G-protein-coupled receptors. *Biochemistry*, 29(50), pp.11123–33.

Bozinovski, S. *et al*., 2013. Treating neutrophilic inflammation in COPD by targeting ALX/FPR2 resolution pathways. *Pharmacology and Therapeutics*, 140(3), pp.280–289.

Branton, M.H. & Kopp, J.B., 1999. TGF-beta and fibrosis. *Microbes and Infection*, 1(15), pp.1349–1365.

Breitung, S.T. *et al*., 2008. A practical synthesis of the 16C/15N-labelled tripeptide N-formyl-Met-Leu-Phe, useful as a reference in solid-state NMR spectroscopy. *Beilstein journal of organic chemistry*, 4(35), Epub October.

Brown, B.N. *et al*., 2009. Macrophage phenotype and remodeling outcomes in response to biologic scaffolds with and without a cellular component. *Biomaterials*, 30(8), pp.1482–1491.

Cardini, S. *et al*., 2012. Genetic ablation of the Fpr1 gene confers protection from smoking-induced lung emphysema in mice. *American Journal of Respiratory Cell and Molecular Biology*, 47(3), pp.332–339.

Carp, B.H., 1982. As for neutrophils. *Power*, 155(January), pp.264–275.

Casanova-Acebes, M. *et al*., 2013. Rhythmic modulation of the hematopoietic niche through neutrophil clearance. *Cell*, 153(5), pp.1025–1035.

Caskey, F.J. *et al*., 2011. Global variation in renal replacement therapy for end-stage renal disease. *Nephrology Dialysis Transplantation*, 26(8), pp.2604–2610.

Caunt, C.J. *et al*., 2006. Seven-transmembrane receptor signalling and ERK compartmentalization. *Trends in Endocrinology and Metabolism*, 17(7), pp.276–283.

Chakraborty, S. *et al*., 2014. Expert Opinion on Investigational Drugs Emerging therapeutic interventions for idiopathic pulmonary fibrosis. *Expert Opinion on Investigational Drugs*, 237, pp.893–910.

Chandler, D.B., Hyde, D.M. and Giri, S.N., 1983. Morphometric estimates of infiltrative cellular changes during the development of bleomycin-induced pulmonary fibrosis in hamsters. *American Journal of Pathology*, 112(2), pp. 170-177.

Chen, L.-Y. *et al*., 2009. Synergistic induction of inflammation by bacterial products lipopolysaccharide and fMLF: an important microbial pathogenic mechanism. *Journal of immunology*, 182(4), pp. 2518-24.

Chen, G.Y. & Nuñez, G., 2010. Sterile inflammation: sensing and reacting to damage. *Nature reviews. Immunology*, 10(12), pp. 826-37

Chen, K. *et al*., 2010. A critical role for the G protein-coupled receptor mFPR2 in airway inflammation and immune responses. *Journal of immunology*, 184(7), pp. 3331–3335.

Chua, F., Gauldie, J. and Laurent, G.J., 2005. Pulmonary fibrosis: Searching for model answers. *American Journal of Respiratory Cell and Molecular Biology*, 33(1), pp. 9–13.

Chung, M.J. *et al*., 2007. Anti-apoptotic effect of found in inflammatory zone (FIZZ)1 on mouse lung fibroblasts. *Journal of Pathology,* **212**(2), pp. 180-187.

Cirillo, M., 2010. Evaluation of glomerular filtration rate and of albuminuria/proteinuria. *Journal of Nephrology*, 23(2), pp. 125-132.

Constandinou, C., Henderson, N. and Iredale, J.P., 2005. Modeling liver fibrosis in rodents. *Methods in Molecular Medicine*, 117, pp. 237-250.

Corteling, R., Wyss, D. & Trifilieff, A., 2002. In vivo models of lung neutrophil activation. Comparison of mice and hamsters. *BMC pharmacology*, 2, p.1.

Crouser, E.D. *et al*., 2009. Monocyte activation by necrotic cells is promoted by mitochondrial proteins and formyl peptide receptors. *Critical care medicine*, 37(6), pp. 2000–9.

Crystal, R.G. *et al*., 2008. Airway epithelial cells: current concepts and challenges. *Proceedings of the American Thoracic Society*, 5(7), pp. 772-7.

Daley, J.M. *et al*., 2008. Use of Ly6G-specific monoclonal antibody to deplete neutrophils in mice. *Journal of leukocyte biology*, 83(1), pp.64–70.

Devaraj, A., 2014. Imaging: How to recognise idiopathic pulmonary fibrosis. *European Respiratory Review*, 23(132), pp.215–219.

Ding, N.-H., Li, J.J. & Sun, L.-Q., 2013. Molecular Mechanisms and Treatment of Radiation-Induced Lung Fibrosis. *Current Drug Targets*, 14, pp.1347–1356.

Douthwaite, J.A. *et al*., 2015. Affinity maturation of a novel antagonistic human monoclonal antibody with a long V H CDR3 targeting the Class A GPCR formyl-peptide receptor 1. *mAbs*, 7(1), pp.152–166.

Dransfield, I. *et al*., 1994. Neutrophil apoptosis is associated with a reduction in CD16 (Fc gamma RIII) expression. *Journal of Immunology*, 153, pp. 1254-1263.

Elsharkawy, A., Austin, A. and Ryder, S., 2002. Clinical impact of transjugular liver biopsies in a non-transplant center. *Hepatology*, 36, pp. 728A.

Ellson, C.D. *et al*., 2014. Danger-associated molecular patterns and danger signals in idiopathic pulmonary fibrosis. *American Journal of Respiratory Cell and Molecular Biology*, 51(2), pp. 163-8.

Farahi, N. *et al*., 2012. Uses of 111-Indium-labeled autologous eosinophils to establish the *in vivo* kinetics of human eosinophils in healthy subjects. *Blood*, 120(19), pp. 4068-4071.

Fireman, E. *et al*., 2001. Morphological and biochemical properties of alveolar fibroblasts in interstitial lung diseases. *Lung*, 179(2), pp. 105-17.

Fisher, C.E. *et al*., 2005. FITC-induced murine pulmonary inflammation: CC10 up-regulation and concurrent Shh expression. *Cell Biology International*, 29(10), pp.868–876.

Forbes, M.S. *et al*., 2012. Fight-or-flight: murine unilateral ureteral obstruction causes extensive proximal tubular degeneration, collecting duct dilatation, and minimal fibrosis. *AJP: Renal Physiology*, 303(1), pp.F120–F129.

Fortunati, E. *et al*., 2009. Human neutrophils switch to an activated phenotype after homing to the lung irrespective of inflammatory disease. *Clinical and Experimental Immunology*, 155(3), pp. 559-66.

Freer, R.J., *et al*., 1980. Further studies on the structural requirements for synthetic peptide chemoattractants. *Biochemistry*, 19(11), pp. 2404-2410.

Friedman, S.L., 2003. Liver fibrosis - From bench to bedside. *Journal of Hepatology*, Supplement, 38(1), pp. S38-S53.

Friedman, S.L., 2008. Mechanisms of Hepatic Fibrogenesis. *Gastroenterology*, 134(6), pp. 1655-69.

Fujii, T. *et al*., 2010. Mouse model of carbon tetrachloride induced liver fibrosis: Histopathological changes and expression of CD133 and epidermal growth factor. *BMC Gastroenterology*, 10, p.79.

Fullard, N., *et al*., 2012. Roles of c-Rel signalling in inflammation and disease. *International Journal of Biochemistry and Cell Biology*, 44(6), pp.851–860.

Gao, J.L., Lee, E.J. & Murphy, P.M., 1999. Impaired antibacterial host defense in mice lacking the N-formylpeptide receptor. *The Journal of experimental medicine*, 189(4), pp. 657-62.

Gavins, F.N.E., 2010. Are formyl peptide receptors novel targets for therapeutic intervention in ischaemia-reperfusion injury? *Trends in pharmacological sciences*, 31(6), pp. 266-76.

Gerack, C. & McElwee-White, L., 2014. Formylation of Amines. *Molecules*, 19, pp. 7689-7713.

Gibbons, M.A. *et al*., 2011. Ly6Chi monocytes direct alternatively activated profibrotic macrophage regulation of lung fibrosis. *American Journal of Respiratory and Critical Care Medicine*, 184(5), pp. 569-81.

Giebeler, A. *et al*., 2014. Deficiency of Formyl Peptide Receptor 1 and 2 Is Associated with Increased Inflammation and Enhanced Liver Injury after LPS-Stimulation. *PLOS ONE*, 9(6), e100522

Grande, N.R. *et al*., 1998. Lung fibrosis induced by bleomycin: structural changes and overview of recent advances. *Scanning Microscopy*, 12(3), pp.487–494.

Greenberger, J.S., Newburger, P.E. and Sakakeeny, M., 1980. Phorbol myristate acetate stimulates macrophage differentiation and replication and alters granulopoiesis and leukomogenesis in long-term bone marrow cultures. *Blood*, 56(3), pp. 368-379.

Grommes, J. & Soehnlein, O., Contribution of neutrophils to acute lung injury. *Molecular medicine (Cambridge, Mass.)*, 17(3-4), pp. 293-307.

Guo, G. *et al*., 2001. Contributions of angiotensin II and tumor necrosis factor-α to the development of renal fibrosis. *American Journal of Physiology - Renal Physiology,* 280(5), pp. F777-F785.

Guck, J. *et al*., 2001. The optical stretcher: a novel laser tool to micromanipulate cells. *Biophysical Journal*, 81(2), pp.767–784.

Guo, S. & Dipietro, L.A., 2010. Factors affecting wound healing. *Journal of Dental Research*, 89(3), pp. 219-229.

Gupte, V. V. *et al*., 2009. Overexpression of fibroblast growth factor-10 during both inflammatory and fibrotic phases attenuates bleomycin-induced pulmonary fibrosis in mice. *American Journal of Respiratory and Critical Care Medicine*, 180(5), pp.424–436.

Han, W.K. *et al*., 2002. Kidney Injury Molecule-1 (KIM-1): A novel biomarker for human renal proximal tubule injury. *Kidney International*, 62(1), pp. 237-44.

Harris, K.P.G., 2006. The implications of the renal NSF for diabetologists. *Diabetic Medicine*, 23(SUPPL. 3), pp. 13-15.

Hartt, J.K. *et al*., 1999. N-formylpeptides induce two distinct concentration optima for mouse neutrophil chemotaxis by differential interaction with two N-formylpeptide receptor (FPR) subtypes. Molecular characterization of FPR2, a second mouse neutrophil FPR. *The Journal of Experimental Medicine*, 190(5), pp. 741-7.

Harty, M.W. *et al*., 2008. Hepatic macrophages promote the neutrophil-dependent resolution of fibrosis in repairing cholestatic rat livers. *Surgery*, 143(5), pp. 667-78.

Hasegawa, T. *et al*., 2006. Histological classification of liver fibrosis and its impact on the postoperative clinical course of patients with congenital dilatation of the bile duct. *Surgery today*, 36(2), pp. 151-154.

Hauser, C.J., *et al*., 2010. Mitochondrial damage associated molecular patterns from femoral reamings activate neutrophils through formyl peptide receptors and P44/42 MAP kinase. *Journal of orthopaedic trauma*, 24(9), pp. 534-538.

Hay, J., Shahzeidi, S. & Laurent, G., 1991a. Mechanisms of bleomycin-induced lung damage. *Archives of toxicology*, 65(2), pp.81–94.

He, H.-Q. *et al*., 2013. Functional Characterization of Three Mouse Formyl Peptide Receptors. *Molecular Pharmacology*, 83, pp.389–398.

He, R., Browning, D.D. and Ye, R.D., 2001. Differential roles of the NPXXY motif in formyl peptide receptor signalling. *Journal of immunology*, 166(6), pp. 4099-105.

Heyworth, P., Cross, A. and Curnutte, J., 2003. Chronic granulomatous disease. *Current Opinion in Immunology*, 15(5), pp. 578-84.

Hold, G.L. *et al*., 2009. Role of host genetics in fibrosis. *Fibrogenesis Tissue Repair*, 2(1), pp. 6

Huang, J. *et al*., 2010. The G-protein-coupled formylpeptide receptor FPR confers a more invasive phenotype on human glioblastoma cells. *British Journal of Cancer*, 102(6), 1052-60.

Hwang, P.F. *et al*., 2011. Trauma is danger. *Journal of Translational Medicine*, 9, pp. 92.

Hu, Y., 2012. Isolation of human and mouse Neutrophils Ex vivo and *in vitro*. *Methods in Molecular Biology,* 844, pp.101-113.

Jang, Y.Y. & Sharkis, S.J., 2007. A low level of reactive oxygen species selects for primitive hematopoietic stem cells that may reside in the low-oxygenic niche. *Blood*, 110(8), pp. 3056-3063.

Jones, C. V & Ricardo, S.D., 2013. Macrophages and CSF-1. *Organogenesis*, 9(4), pp.249–260.

Juza, R.M. and Pauli, E.M., 2014. Clinical and surgical anatomy of the liver: A review for clinicians. *Clinical Anatomy,* 27(5), pp. 764-769.

Kaku, Y. *et al*., 2014. Overexpression of CD163, CD204 and CD206 on alveolar macrophages in the lungs of patients with severe chronic obstructive pulmonary disease. *PLOS ONE*, 9(1), pp.1–8.

Kao, W. *et al*., (2014), A formyl peptide receptor agonist suppresses inflammation and bone damage in arthritis. *British Journal of Pharmacology*, 171: 4087–4096.

Kawata, H. *et al*., 2005. The mechanism underlying the contractile effect of a chemotactic peptide, formyl-Met-Leu-Phe on the guinea-pig Taenia coli. *British Journal of Pharmacology*, 145(3), pp. 353-63.

Khalil, N. *et al*., 1989. Macrophage production of transforming growth factor β and fibroblast collagen synthesis in chronic pulmonary inflammation. *The Journal of Experimental Medicine*, 170(September), pp. 727–737.

Khlebnikov, A.I., Schepetkin, I. and Quinn, M.T., 2010. Computational structure-activity relationship analysis of small-molecule agonists for human formyl peptide receptors. *European Journal of Medicinal Chemistry*, 45(11), pp.5406–19.

Kim, K.K. *et al*., 2006. Alveolar epithelial cell mesenchymal transition develops *in vivo* during pulmonary fibrosis and is regulated by the extracellular matrix. *Proceedings of*

the National Academy of Sciences of the United States of America, 103(35), pp. 13180-5.

Kirpotina, L.N. *et al*., 2010. Identification of novel small-molecule agonists for human formyl peptide receptors and pharmacophore models of their recognition. *Molecular Pharmacology*, 77(2), pp. 159-70.

Klahr, S., 2000. Obstructive nephropathy. *Internal medicine*, 39(5), pp.355–361.

Klahr, S. & Purkerson, M.L., 1994. The pathophysiology of obstructive nephropathy: the role of vasoactive compounds in the hemodynamic and structural abnormalities of the obstructed kidney. *Pediatric Nephrology*, 8(6), pp. 771.

Kobayashi, Y., 2015. Neutrophil biology: an update. *EXCLI Journal*, 14, pp. 220-227.

Kolb, M. & Collard, H.R., 2014. Staging of idiopathic pulmonary fibrosis: past, present and future. *European Respiratory Reviews*, 23(132), pp. 220-4.

Kolios, G., Valatas, V. and Kouroumalis, E., 2006. Role of Kupffer cells in the pathogenesis of liver disease. *World Journal of Gastroenterology*, 12(46), pp. 7413-20.

Kono, H., Onda, A. and Yanagida, T., 2014. Molecular determinants of sterile inflammation. *Current Opinion in Immunology*, 26(1), pp.147–156.

Kubes, P. & Mehal, W.Z., 2012. Sterile Inflammation in the Liver. *Gastroenterology*, 143(5), pp.1158–1172.

Krysko, D. V *et al*., 2011. Emerging role of damage-associated molecular patterns derived from mitochondria in inflammation. *Trends in Immunology*, 32(4), pp.157–64.

Lafyatis, R. & Farina, A., 2012. New insights into the mechanisms of innate immune receptor signalling in fibrosis. *Open Rheumatology Journal,* 6(1), pp. 72-79.

Lakatos, H.F. *et al*., 2006. Oropharyngeal aspiration of a silica suspension produces a superior model of silicosis in the mouse when compared to intratracheal instillation. *Experimental Lung Research*, 32(5), pp. 181-99.

Lala, a, Gwinn, M. & De Nardin, E., 1999. Human formyl peptide receptor function role of conserved and non-conserved charged residues. *European journal of biochemistry / FEBS*, 264(2), pp.495–9.

Le, Y., Murphy, P.M. & Wang, J.M., 2002. Formyl-peptide receptors revisited. *Trends in immunology*, 23(11), pp.541–8.

Le, Y. *et al*., 2000. Expression of functional formyl peptide receptors by human astrocytoma cell lines. *Journal of Neuroimmunology*, 111(1-2), pp. 102-8.

Leask, A. & Abraham, D.J., 2004. TGF-beta signalling and the fibrotic response. *The FASEB Journal*, 18(7), pp. 816-27.

Lee, U.E. & Friedman, S.L., 2011. Mechanisms of hepatic fibrogenesis. *Best Practice and Research: Clinical Gastroenterology*, 25(2), pp.195–206.

Leenen, P.J.M. *et al*., 1994. Markers of mouse macrophage development detected by monoclonal antibodies. *Journal of immunological methods*, 174(1-2), pp. 5-19.

Levey, A.S. *et al*., 2010. Chronic kidney disease, diabetes, and hypertension: what's in a name? *Kidney international*, 78(1), pp. 19-22.

Liedtke, C. *et al*., 2013. Experimental liver fibrosis research: update on animal models, legal issues and translational aspects. *Fibrogenesis & Tissue Repair*, 6, p.1.

Lim, A.I. *et al*., 2013. Kidney injury molecule-1: More than just an injury marker of tubular epithelial cells? *Journal of Cellular Physiology*, 228(5), pp. 917-24.

Liu, T. *et al*., 2004. Regulation of found in inflammatory zone 1 expression in bleomycin-induced lung fibrosis: role of IL-4/IL-13 and mediation via STAT-6. *Journal of immunology*, 173(5), pp.3425–3431.

Liu, M. *et al*., 2014. Formylpeptide receptors mediate rapid neutrophil mobilization to accelerate wound healing. *PLOS ONE*, 9(6), p.e90613.

Loor, F. *et al*., 2002. Cyclosporins: Structure-activity relationships for the inhibition of the human FPR1 formylpeptide receptor. *Journal of Medicinal Chemistry*, 45(21), pp. 4613-4628.

Maaty, W.S. *et al*., 2013. Identification of C-terminal phosphorylation sites of N-formyl peptide receptor-1 (FPR1) in human blood neutrophils. *Journal of Biological Chemistry*, 288(38), pp. 27042-58.

MacGregor, G. *et al*., 2008. Biomarkers for cystic fibrosis lung disease: Application of SELDI-TOF mass spectrometry to BAL fluid. *Journal of Cystic Fibrosis*, 7(5), pp. 352-8.

Mader, D. *et al*., 2013. Role of N-terminal protein formylation in central metabolic processes in *Staphylococcus aureus*. *BMC Microbiology*, 13(7), pp. 1-9.

Mantovani, A *et al*., 2011. Neutrophils in the activation and regulation of innate and adaptive immunity. Nature Reviews Immunology, 11, pp. 519-531.

Manz, M.G. & Boettcher, S., 2014. Emergency granulopoiesis. *Nature reviews. Immunology*, 14(5), pp.302–14.

Marques, P.E. *et al*., 2012. Chemokines and mitochondrial products activate neutrophils to amplify organ injury during mouse acute liver failure. *Hepatology*, 56(5), pp. 1971-82.

Matzinger, P. & Kamala, T., 2011. Tissue-based class control: the other side of tolerance. *Nature reviews. Immunology*, 11(3), pp.221–30.

McDonald, B. *et al*., 2010. Intravascular danger signals guide neutrophils to sites of sterile inflammation. *Science*, 330(6002), pp. 362-6.

Miettinen, H.M., 2011. Regulation of human formyl peptide receptor 1 synthesis: Role of single nucleotide polymorphisms, transcription factors, and inflammatory mediators. *PLOS ONE*, 6(12), e28712.

Migeotte, I., Communi, D. and Parmentier, M., 2006. Formyl peptide receptors: A promiscuous subfamily of G protein-coupled receptors controlling immune responses. *Cytokine and Growth Factor Reviews*, 17(6), pp.501-19.

Mócsai, A., 2013. Diverse novel functions of neutrophils in immunity, inflammation and beyond. *The Journal of Experimental Medicine*, 210(7), pp. 1283-1299.

Moeller, A. *et al*., 2008. The bleomycin animal model: a useful tool to investigate treatment options for idiopathic pulmonary fibrosis? *The International Journal of Biochemistry & Cell Biology*, 40(3), pp. 362-382.

Moeller, A. *et al*., 2006. Models of pulmonary fibrosis. *Drug Discovery Today: Disease Models*, 3(3), pp. 243-249.

Moles, A. *et al*., 2014. A TLR2/S100A9/CXCL-2 signalling network is necessary for neutrophil recruitment in acute and chronic liver injury in the mouse. *Journal of Hepatology*, 60(4), pp.782–791.

Moore BB, H.C., 2008. Murine models of pulmonary fibrosis. *American Journal of Physiology. Lung Cellular and Molecular Physiology*, 294(2), pp.L152–160.

Mura, M. *et al*., 2005. Inflammatory activity is still present in the advanced stages of idiopathic pulmonary fibrosis. *Respirology*, 10(5), pp. 609-614.

Murphy, P.M. *et al*., 1992. A structural homologue of the N-formyl peptide receptor: Characterization and chromosome mapping of a peptide chemoattractant receptor family. *Journal of Biological Chemistry*, 267(11), pp. 7637-43.

Murphy, P.M. *et al*., 1993. Sequence and organization of the human N-formyl peptide receptor-encoding gene. *Gene*, 133(2), pp. 285-90.

Murray, L.A. *et al*., 2011. TGF-beta driven lung fibrosis is macrophage dependent and blocked by Serum amyloid P. *International Journal of Biochemistry and Cell Biology*, 43(1), pp. 154-162.

Murray, L.A., 2012. Commonalities between the pro-fibrotic mechanisms in COPD and IPF. *Pulmonary Pharmacology and Therapeutics*, 25(4), pp. 276-80.

Murray, P.J. *et al*., 2014. Macrophage Activation and Polarization: Nomenclature and Experimental Guidelines. *Immunity*, 41(1), pp.14–20.

Mutsaers, S.E. *et al*., 2004. Evaluation of experimental models of idiopathic pulmonary fibrosis. *Drug Discovery Today: Disease Models*, 1(3), pp.329–336.

Nakazoto, H. *et al*., 2002. A novel anti-fibrotic agent pirfenidone suppresses tumor necrosis factor-α at the translational level. *European Journal of Pharmacology*, 446(1-3), pp. 177-185.

Nguyen, K.T. *et al*., 2003. Characterization of a human peptide deformylase: implications for antibacterial drug design. *Biochemistry*, 42(33), pp.9952–8.

Nguyen, H.T.Q. & Murray, V., 2012. The DNA sequence specificity of bleomycin cleavage in telomeric sequences in human cells. *Journal of Biological Inorganic Chemistry*, 17(8), pp. 1209-1215.

Nyblom, H. *et al*., 2004. High AST/ALT ratio may indicate advanced alcoholic liver disease rather than heavy drinking. *Alcohol and Alcoholism*, 39(4), pp. 336-339.

Obayashi, Y. *et al*., 1997. The role of neutrophils in the pathogenesis of idiopathic pulmonary fibrosis. *Chest*, 112(5), 1338-43.

Oku, H. *et al*., 2008. Antifibrotic action of pirfenidone and prednisolone: Different effects on pulmonary cytokines and growth factors in bleomycin-induced murine pulmonary fibrosis. *European Journal of Pharmacology*, 590(1-3), pp. 400-8.

Pallen, M.J., 2011. Time to recognise that mitochondria are bacteria? *Trends in Microbiology*, 19(2), pp.58–64.

Panaro, M.A. *et al*., 2007. Formyl peptide receptors on immune and nonimmune cells: analysis of sequence conservation in FPR genes. *Immunopharmacology and Immunotoxicology*, 29(2), pp. 243-69.

Panaro, M.A. *et al*., 2008. Mutation, selection, and functional repair in formyl peptide receptor genes: a view on the selection processes occurring in this gene subfamily. *Immunopharmacology and Immunotoxicology*, 30(2), pp. 383-97.

Park, E.K. *et al*., 2007. Optimized THP-1 differentiation is required for the detection of responses to weak stimuli. *Inflammation Research*, 56(1), pp. 45-50.

Pechkovsky, D. V *et al*., 2010. Alternatively activated alveolar macrophages in pulmonary fibrosis-mediator production and intracellular signal transduction. *Clinical immunology*, 137(1), pp.89–101.

Perkins, L., Peer, C. and Murphey-Hackley, P., 2000. The Use of Mini-Osmotic Pumps in Continuous Infusion Studies. *Handbook of Pre-Clinical Continuous Intravenous Infusion*, 21, pp.330.

Piccini, a M. & Midwood, K.S., 2010. DAMPening inflammation by modulating TLR signalling. *Mediators of inflammation*, 672395.

Pohlers, D. *et al*., 2009. TGF-β and fibrosis in different organs - molecular pathway imprints. *Biochimica et Biophysica Acta*, 1792(8), pp.746-56.

Porcheray, F. *et al*., 2005. Macrophage activation switching: An asset for the resolution of inflammation. *Clinical and Experimental Immunology*, 142(3), pp.481–489.

Pouwels, S. *et al*., 2014. A specific DAMP profile identifies susceptibility to smoke-induced airway inflammation. *European Respiratory Journal*, 43(4), pp1183-1186.

Prevete, N. *et al*., 2014. The formyl peptide receptor 1 exerts a tumor suppressor function in human gastric cancer by inhibiting angiogenesis. *Oncogene*, 34(29), pp. 3826-38.

Prossnitz, E.R. & Ye, R.D., 1997. The N-formyl peptide receptor: a model for the study of chemoattractant receptor structure and function. *Pharmacology & therapeutics*, 74(1), pp. 73-102.

Rabiet, M.-J., Huet, E. and Boulay, F., 2005. Human mitochondria-derived N-formylated peptides are novel agonists equally active on FPR and FPRL1, while Listeria monocytogenes-derived peptides preferentially activate FPR. *European journal of immunology*, 35(8), pp.2486–95.

Rabiet, M.-J., Huet, E. and Boulay, F., 2007. The N-formyl peptide receptors and the anaphylatoxin C5a receptors: an overview. *Biochimie*, 89(9), pp.1089–106.

Raoof, M. *et al*., C.J., 2010. Mitochondrial peptides are potent immune activators that activate human neutrophils via FPR-1. Journal of Trauma - Injury, *Infection and Critical Care*, 68(6), pp. 1328-1332.

Reinert, T. *et al*., 2013. Bleomycin-Induced Lung Injury. *Journal of Cancer Research*, 480608.

Rescher, U. *et al*., 2002. Functional activation of the formyl peptide receptor by a new endogenous ligand in human lung A549 cells. *Journal of immunology,* 169(3), pp.1500–4.

Riffo-Vasquez, Y., Man, F. and Page, C.P., 2014. Doxofylline, a novofylline inhibits lung inflammation induced by lipopolysacharide in the mouse. *Pulmonary Pharmacology and Therapeutics*, 27(2), pp. 170-8.

Roberts, S.N. *et al*., 1995. A novel model for human interstitial lung disease: hapten-driven lung fibrosis in rodents. *Journal of Pathology,* 176(3): pp309-18.

Rock, J.R., Randell, S.H. and Hogan, B.L.M., 2010. Airway basal stem cells: A perspective on their roles in epithelial homeostasis and remodeling. *DMM Disease Models and Mechanisms*, 3(9-10), pp. 545-556.

Rock, J.R. & Hogan, B.L.M., 2011. Epithelial progenitor cells in lung development, maintenance, repair, and disease. *Annual Review of cell and developmental biology*, 27, pp. 493-512.

Roux, B.T. & Cottrell, G.S., 2014. G protein-coupled receptors: What a difference a “partner” makes. *International Journal of Molecular Sciences*, 15(1), pp. 1112-42.

Sahagun-Ruiz, A. *et al*., 2001. Contrasting evolution of the human leukocyte N-formylpeptide receptor subtypes FPR and FPRL1R. *Genes and immunity*, 2(6), pp. 335-42.

Saito, J.M. *et al*., 2003. Infiltrating neutrophils in bile duct-ligated livers do not promote hepatic fibrosis. *Hepatology Research*, 25(2), pp. 180-191.

Satoh, M. *et al*., 2001. Renal interstitial fibrosis is reduced in angiotensin II type 1a receptor-deficient mice. *Journal of the American Society of Nephrology,* 12(2), pp. 317-325.

Schwartz, W.B., Levey, A.S. and Coresh, J., 2012. Chronic kidney disease. *The Lancet*, 379, pp.165–180.

Scotton, C.J. & Chambers, R.C., 2007. Molecular targets in pulmonary fibrosis: The myofibroblast in focus. *Chest*, 132(4), pp.1311–1321.

Selman, M., King T.E., J. and Pardo, A., 2001. Idiopathic pulmonary fibrosis: Prevailing and evolving hypotheses about its pathogenesis and implications for therapy. Annals of Internal Medicine, 134(2), pp. 136-151.

Selvatici, R. *et al*., 2006. Signal transduction pathways triggered by selective formylpeptide analogues in human neutrophils. *European Journal of Pharmacology*, 534(1-3), pp. 1-11.

Shay, J.W. & Wright, W.E., 2000. Hayflick, his limit, and cellular ageing. *Nature Reviews Molecular Cell Biology*, 1(1), pp. 72-76.

Shao, G. *et al*., 2011. Formyl peptide receptor ligands promote wound closure in lung epithelial cells. *American Journal of Respiratory Cell and Molecular Biology*, 44(3), pp. 264-9.

Shi, Y., Evans, J.E. and Rock, K.L., 2003. Molecular identification of a danger signal that alerts the immune system to dying cells. *Nature*, 425(6957), pp. 516-21.

Shin, M.K. *et al*., 2011. N-formyl-methionyl-leucyl-phenylalanine (fMLF) promotes osteoblast differentiation via the N-formyl peptide receptor 1-mediated signalling pathway in human mesenchymal stem cells from bone marrow. *The Journal of biological chemistry*, 286(19), pp.17133–43.

Sime, P.J. *et al*., 1997. Adenovector-mediated gene transfer of active transforming growth factor-1 induces prolonged severe fibrosis in rat lung. *Journal of Clinical Investigation*, 100(4), pp.768–776.

Si-Tayeb, K., Lemaigre, F.P. and Duncan, S. a., 2010. Organogenesis and Development of the Liver. *Developmental Cell*, 18(2), pp.175–189.

Snapkov, I. *et al*., 2014. Expression of formyl peptide receptor 1 (FPR1) in neuroblastoma: Implications in tumorigenesis. *AACR Annual Meeting,* Abstract 3976.

Stenfeldt, A.L. *et al*., 2007. Cyclosporin H, Boc-MLF and Boc-FLFLF are antagonists that preferentially inhibit activity triggered through the formyl peptide receptor. *Inflammation,* 30(6): pp224-9.

Stevens, P.E. *et al*., 2007. Chronic kidney disease management in the United Kingdom: NEOERICA project results. *Kidney international*, 72(1), pp. 92-9.

Strutz, F. *et al*., 1995. Identification and characterization of a fibroblast marker: FSP1. *Journal of Cell Biology*, 130(2), pp. 393-405.

Svensson, L. *et al*., 2009. Interplay between signalling via the formyl peptide receptor (FPR) and chemokine receptor 3 (CCR3) in human eosinophils. *Journal of Leukocyte Biology*, 86(2), pp. 327-36.

Tanaka, F. *et al*., 2007. Anti-formyl peptide antibodies. *Bioorganic and Medicinal Chemistry Letters*, 17(7), pp. 1943-5.

Tateno, H., Crocker, P.R. and Paulson, J.C., 2005. Mouse Siglec-F and human Siglec-8 are functionally convergent paralogs that are selectively expressed on eosinophils and recognize 6′-sulfo-sialyl Lewis X as a preferred glycan ligand. *Glycobiology*, 15(11), pp.1125–1135.

Thewissen, M. *et al*., 2011. Neutrophils and T cells: Bidirectional effects and functional interferences. *Molecular Immunology*, 48(15-16), pp.2094–2101.

Tiffany, H.L. *et al*., 2011. Characterization of Fpr-rs8, an atypical member of the mouse formyl peptide receptor gene family. *Journal of Innate Immunity*, 3(5), pp. 519-29.

Tolle, L.B. & Standiford, T.J., 2013. Danger-associated molecular patterns (DAMPs) in acute lung injury. *Journal of Pathology*, 229(2), pp. 145-56.

Traber, P.G. *et al*., 2013. Regression of Fibrosis and Reversal of Cirrhosis in Rats by Galectin Inhibitors in Thioacetamide-Induced Liver Disease. *PLOS ONE*, 8(10).

Uchida, M. *et al*., 2012. Periostin, a matricellular protein, plays a role in the induction of chemokines in pulmonary fibrosis. *American Journal of Respiratory Cell and Molecular Biology*, 46(5), pp. 677-86.

Unitt, J. *et al*., 2011. Discovery of small molecule human FPR1 receptor antagonists. *Bioorganic & medicinal chemistry letters*, 21(10), pp.2991–7.

Umezawa, H. *et al*., 1966. New antibiotics, bleomycin A and B. *Journal of Antibiotics*, 19(5), pp. 200-209.

VanCompernolle, S.E. *et al*., 2003. Expression and function of formyl peptide receptors on human fibroblast cells. *Journal of immunology*, 171(4), pp.2050–6.

Vane, J. & Botting, R., 1998. Mechanism of action of nonsteroidal anti-inflammatory drugs. *The American Journal of Medicine*, 104(3A), pp. 2S-8S.

Vargas-Parada, L. (2010) Mitochondria and the Immune Response. *Nature Education*, 3(9), pp. 15

Vasakova, M. *et al*., 2009. Bronchoalveolar lavage fluid cellular characteristics, functional parameters and cytokine and chemokine levels in interstitial lung diseases. *Scandinavian Journal of Immunology*, 69(3), pp. 268-74.

Viswanathan, A. *et al*., 2007. Functional expression of N-formyl peptide receptors in human bone marrow-derived mesenchymal stem cells. *Stem cells (Dayton, Ohio)*, 25(5), pp.1263–9.

Vroon, Z & Israili, D.H.V. Aminotransferases. *Clinical Methods*, Chapter 99.

Vulcano, M. *et al*., 1998. N-formyl-methionyl-leucyl-phenylalanine (fMLF) inhibits tumour necrosis factor-alpha (TNF-α) production on lipopolysaccharide (LPS)-

stimulated human neutrophils. *Clinical and Experimental Immunology*, 113(1), pp. 39-47.

Wang, X. *et al*., 2006. Monocyte/macrophage and T-cell infiltrates in peritoneum of patients with ovarian cancer or benign pelvic disease. *Journal of translational medicine*, 4, pp. 30.

Weichhart, T. *et al*., 2010. The anti-inflammatory potency of dexamethasone is determined by the route of application *in vivo*. *Immunology Letters*, 129(1), pp. 50-52.

Wenceslau, C.F. *et al*., 2013. Mitochondrial-derived N-formyl peptides: Novel links between trauma, vascular collapse and sepsis. *Medical Hypotheses*, 81(4), pp. 532-5.

Wilson, M.S. *et al*., 2010. Bleomycin and IL-1beta-mediated pulmonary fibrosis is IL-17A dependent. *The Journal of Experimental Medicine*, 207(3), pp.535–552.

Wilson, C.L. *et al*., 2015. NFkB1 is a suppressor of neutrophil-driven hepatocellular carcinoma. *Nature Communications*, 16(6), 6818.

Wilson, M. & Wynn, T., 2010. Pulmonary fibrosis: pathogenesis, etiology and regulation. *Mucosal Immunology*, 2(2), 103-21.

Witko-Sarsat, V *et al*., 2000. Neutrophils: Molecules, functions and pathophysiological aspects. *Laboratory Investigation*, 80(5), pp. 617-653.

Wolters, P.J., Collard, H.R. and Jones, K.D., 2014. Pathogenesis of idiopathic pulmonary fibrosis. *Annual Review of Pathology*, 9, pp. 157-79.

Wright, M.C. *et al*., 2001. Gliotoxin Stimulates the Apoptosis of Human and Rat Hepatic Stellate Cells and Enhances the Resolution of Liver Fibrosis in Rats. *Gastroenterology*, 121(3), pp. 685-98.

Wu, M.-Z. *et al*., 2011. Interplay between HDAC3 and WDR5 Is Essential for Hypoxia-Induced Epithelial-Mesenchymal Transition. *Molecular cell*, 43(5), pp. 811–22.

Wynn, T.A., 2004. Fibrotic disease and the T(H)1/T(H)2 paradigm. Nature reviews. *Nature Reviews Immunology*, 4, pp. 583-594.

Wynn, T.A., 2008. Cellular and molecular mechanisms of fibrosis. *Journal of Pathology*, 214(2), pp.199–210.

Wynn, T.A., 2010. Fibrosis under arrest. *Nature medicine*, 16(5), pp. 523-5.

Yamamoto, T. *et al*., 1999. Animal model of sclerotic skin. I: Local injections of bleomycin induce sclerotic skin mimicking scleroderma. *Journal of Investigative Dermatology*, 112(4), pp.456–462.

Yan, P. *et al*., 2006. The immunosuppressant cyclosporin A antagonizes human formyl peptide receptor through inhibition of cognate ligand binding. *Journal of Immunology*, 177(10), pp.7050–8.

Yang, K.H. *et al*., 2008. The main functions and structural modifications of tripeptide N-formyl-methionyl-leucyl-phenylalanine (fMLF) as a chemotactic factor. *Pharmazie*, 63(11), pp. 779-83.

Yao, H. *et al*., 2008. Disruption of p21 attenuates lung inflammation induced by cigarette smoke, LPS, and fMLF in mice. *American Journal of Respiratory Cell and Molecular Biology*, 39(1), pp. 7-18.

Yarnold, J. & Brotons, M.C., 2010. Pathogenetic mechanisms in radiation fibrosis. *Radiotherapy and Oncology*, 97(1), pp. 149-61.

Yazawa, H. *et al*., 2001. Beta amyloid peptide (Abeta42) is internalized via the G-protein-coupled receptor FPRL1 and forms fibrillar aggregates in macrophages. *The FASEB journal: official publication of the Federation of American Societies for Experimental Biology*, 15(13), pp. 2454–2462.

Ye, R.D. *et al*., 2009. International Union of Basic and Clinical Pharmacology. LXXIII. Nomenclature for the formyl peptide receptor (FPR) family. *Pharmacological reviews*, 61(2), pp. 119-61.

El Zein, N., D'Hondt, S. and Sariban, E., 2010. Crosstalks between the receptors tyrosine kinase EGFR and TrkA and the GPCR, FPR, in human monocytes are

essential for receptors-mediated cell activation. *Cellular signalling*, 22(10), pp.1437–47.

Zeisberg, M. & Kalluri, R., 2013. Cellular Mechanisms of Tissue Fibrosis. 1. Common and organ-specific mechanisms associated with tissue fibrosis. *American Journal of Physiology. Cellular Physiology*, 304(3), pp. 216-25.

Zhang, Q., Raoof, M., *et al*., 2010. Circulating mitochondrial DAMPs cause inflammatory responses to injury. *Nature*, 464(7285), pp.104–7.

Zhang, Q., Itagaki, K. and Hauser, C.J., 2010. Mitochondrial DNA is released by shock and activates neutrophils via p38 map kinase. *Shock*, 34(1), pp. 55–9.

Zhao, X., Huang. X., Wang, H., Lu, M. and Tian, K., 2011. Effect of acupuncture-moxibustion on bone marrow suppression and leukocytes after chemotherapy. *Journal of Acupuncture and Tuina Science*, 9(6), pp. 331-335.

Zhou, Y. *et al*., 2005. Formylpeptide receptor FPR and the rapid growth of malignant human gliomas. *Journal of the National Cancer Institute*, 97(11), pp. 823-35.

Zoccali, C., Kramer, A. and Jager, K.J., 2010. Chronic kidney disease and end stage renal disease-A review produced to contribute to the report ‘the status of health in the European union: Towards a healthier Europe’. *Nephrology Dialysis Transplantation*, 3, pp. 213-224.

10 Appendix

A (i) Gating strategy for FACs panel 1 for neutrophil activation markers: CD11b and CD66a following bleomycin injury.

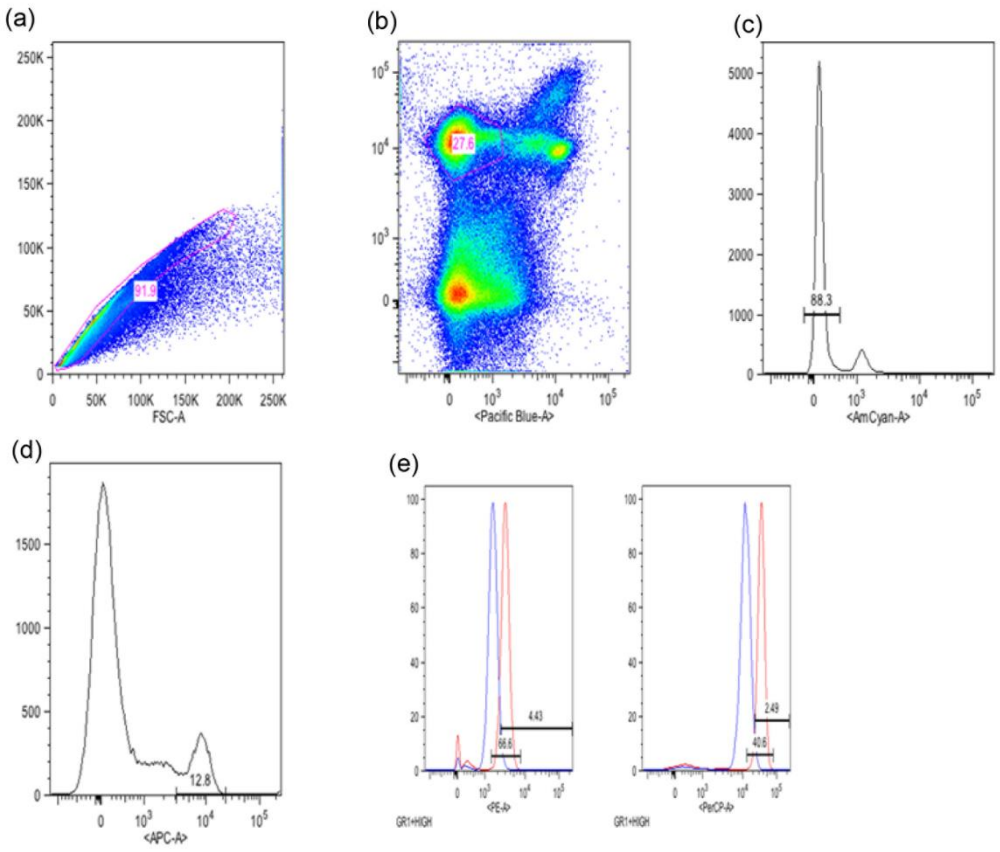

A (ii) Gating strategy for FACs panel 2 for neutrophils (Ly6G) versus eosinophils (SigLecF) populations following bleomycin injury.

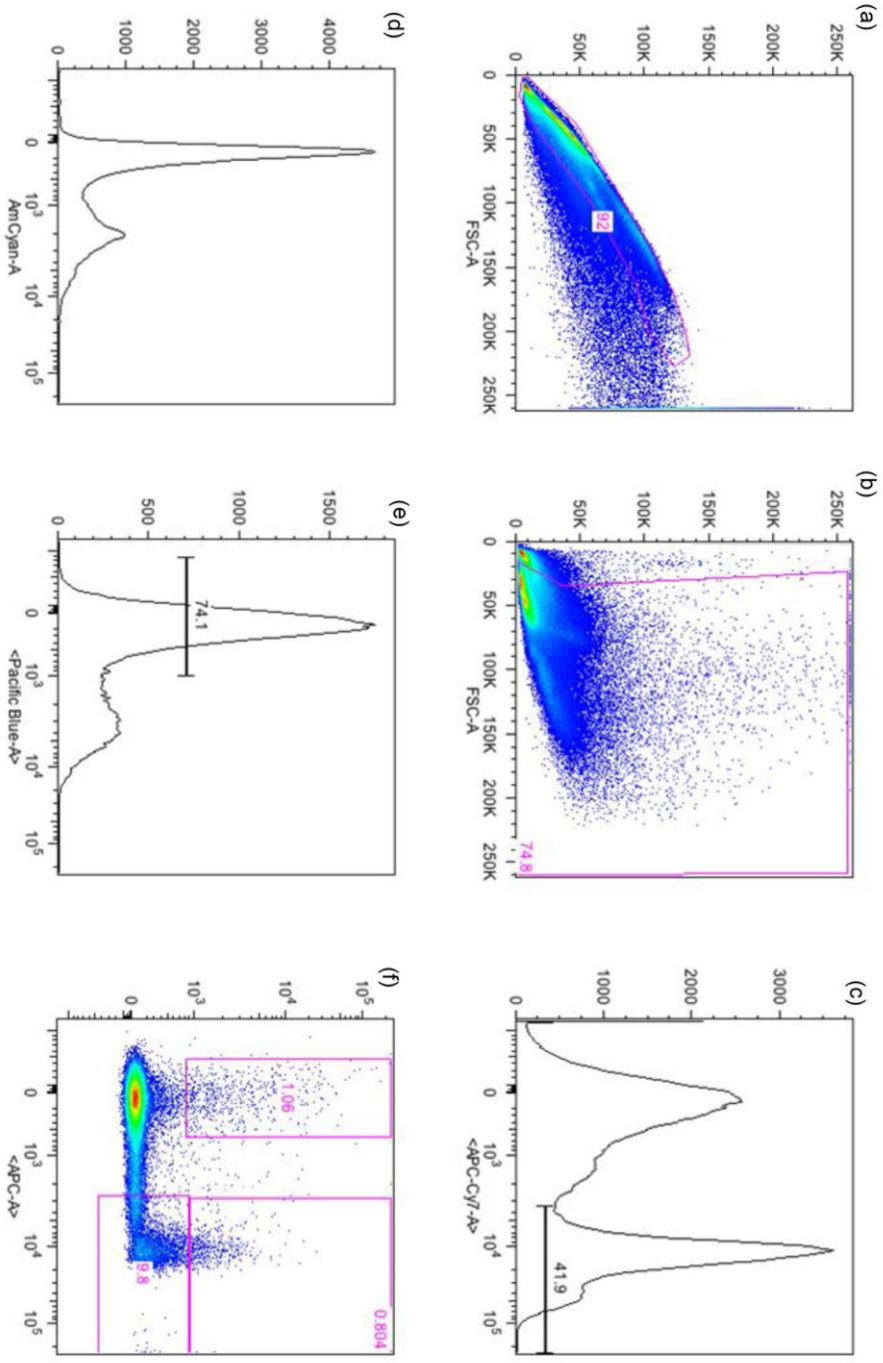

A (iii) Gating strategy for FACs panel 3 for lymphocytes: CD3+CD4+/CD8+, B220+ B-cells and NK1.1 CD49b natural killer cells following bleomycin injury.

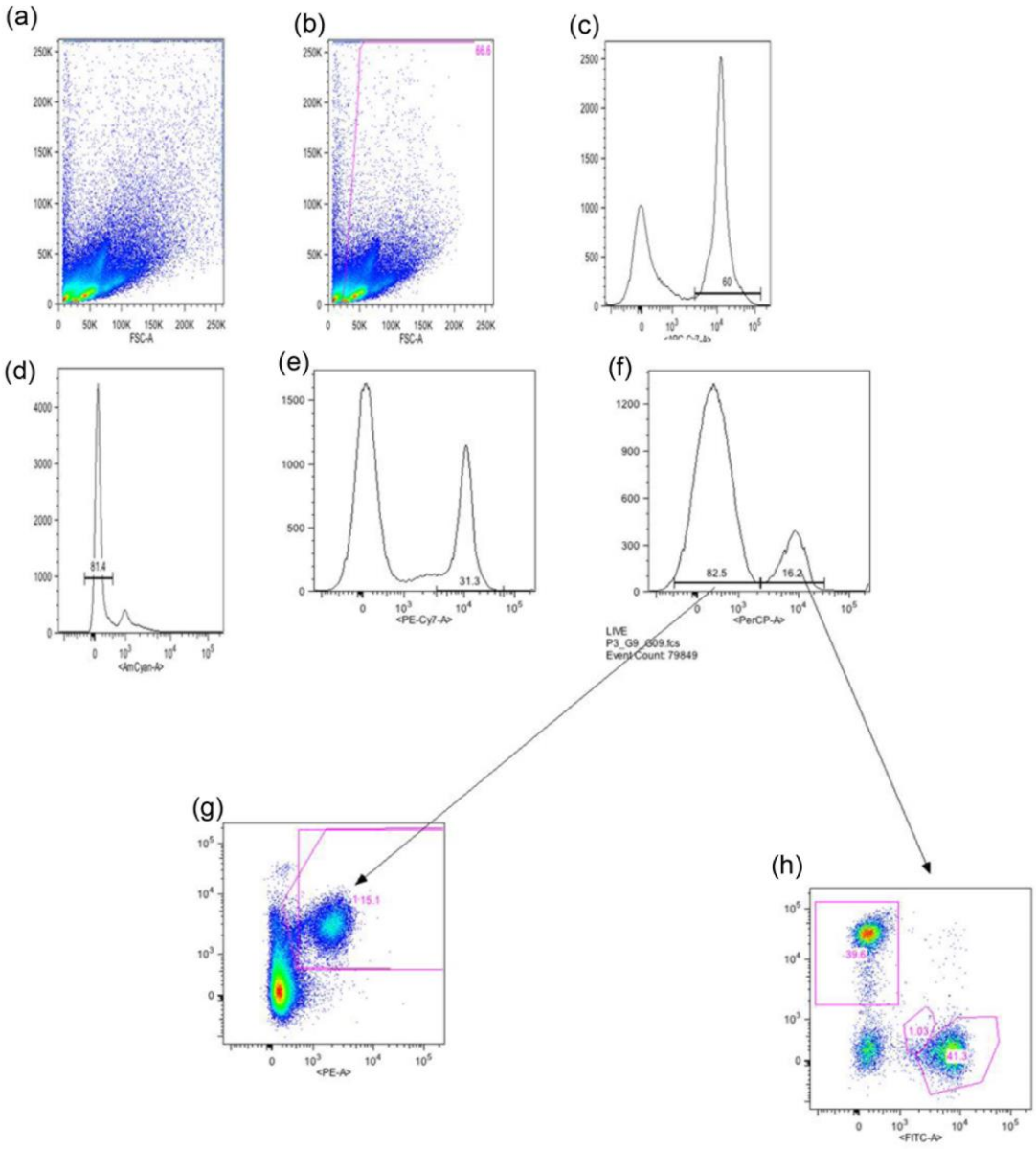

A (iv) Gating strategy for FACs panel 4 for macrophage phenotype following bleomycin injury. CCR7 (M1) and CD206 (M2) expression gated accordingly.

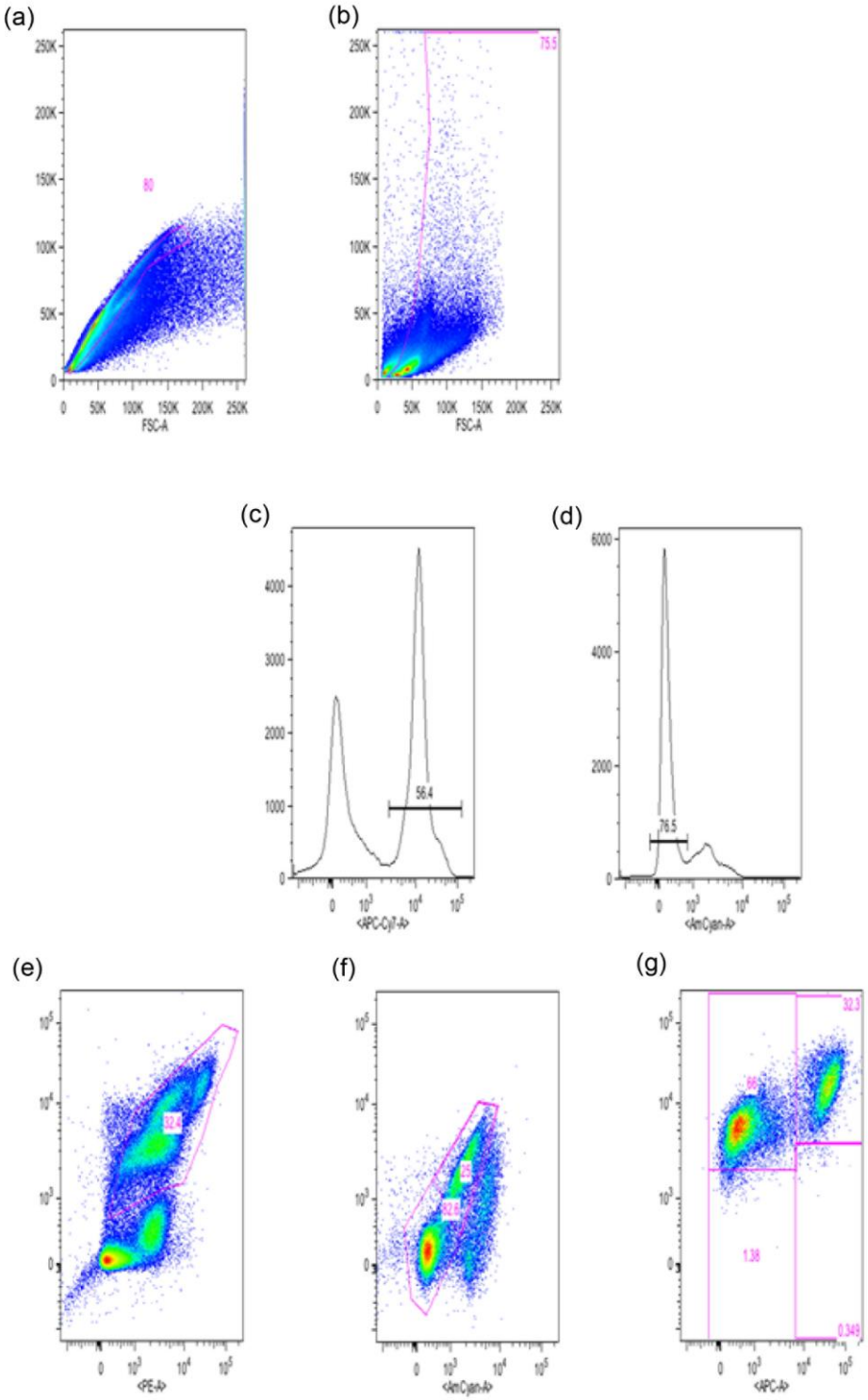

A (v) Gating strategy for FACs panel 5 for macrophage phenotype M1/M2 populations following bleomycin injury. iNOS (M1) and FIZZ-1 (M2) markers gated accordingly.

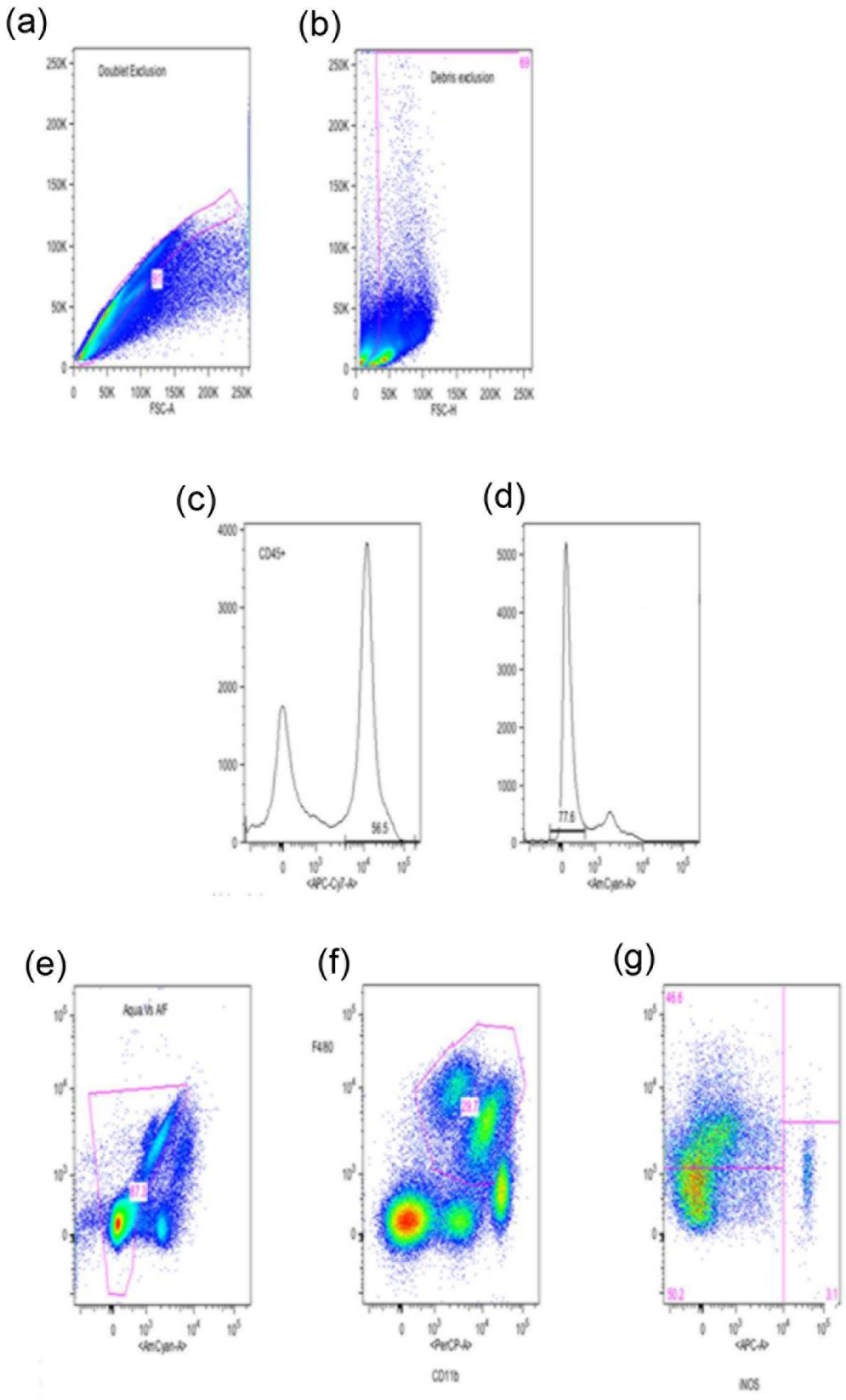

B (i) Immunohistochemistry relative photographs of bone marrow chimera lungs stained for PicroSiriusRed (PSR). Group 1 – WT-WT, Group 2 – WT-KO, Group 3 – KO-WT and Group 4 – KO-KO (Recipient-Donor bone marrow groups), x10 magnification with scale bars representing 100µm.

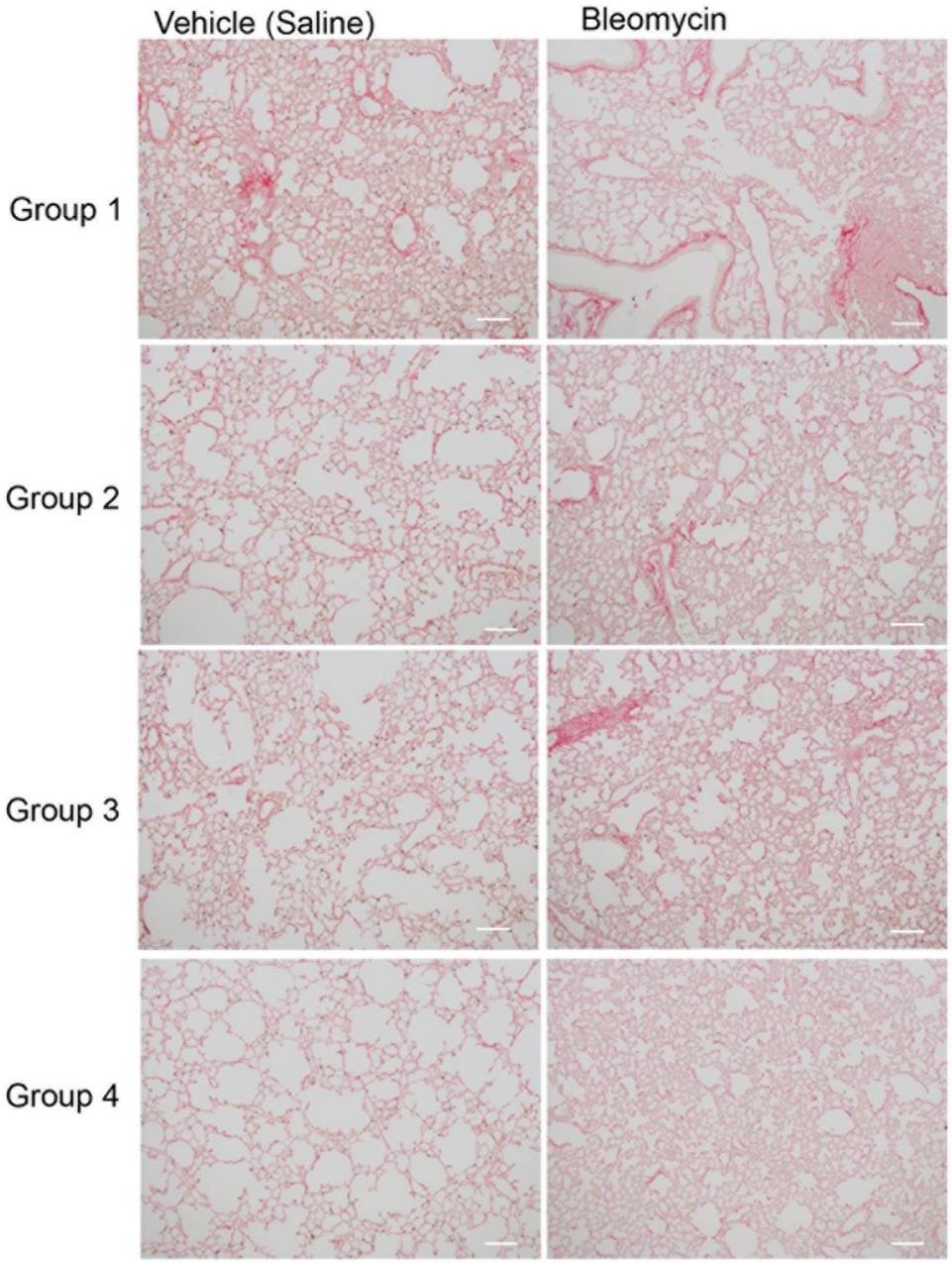

B (ii) Immunohistochemistry relative photographs of bone marrow chimera lungs stained for α-SMA+ve myofibroblasts. Group 1 – WT-WT, Group 2 – WT-KO, Group 3 – KO-WT and Group 4 – KO-KO (Recipient-Donor bone marrow groups), x10 magnification with scale bars representing 100µm.

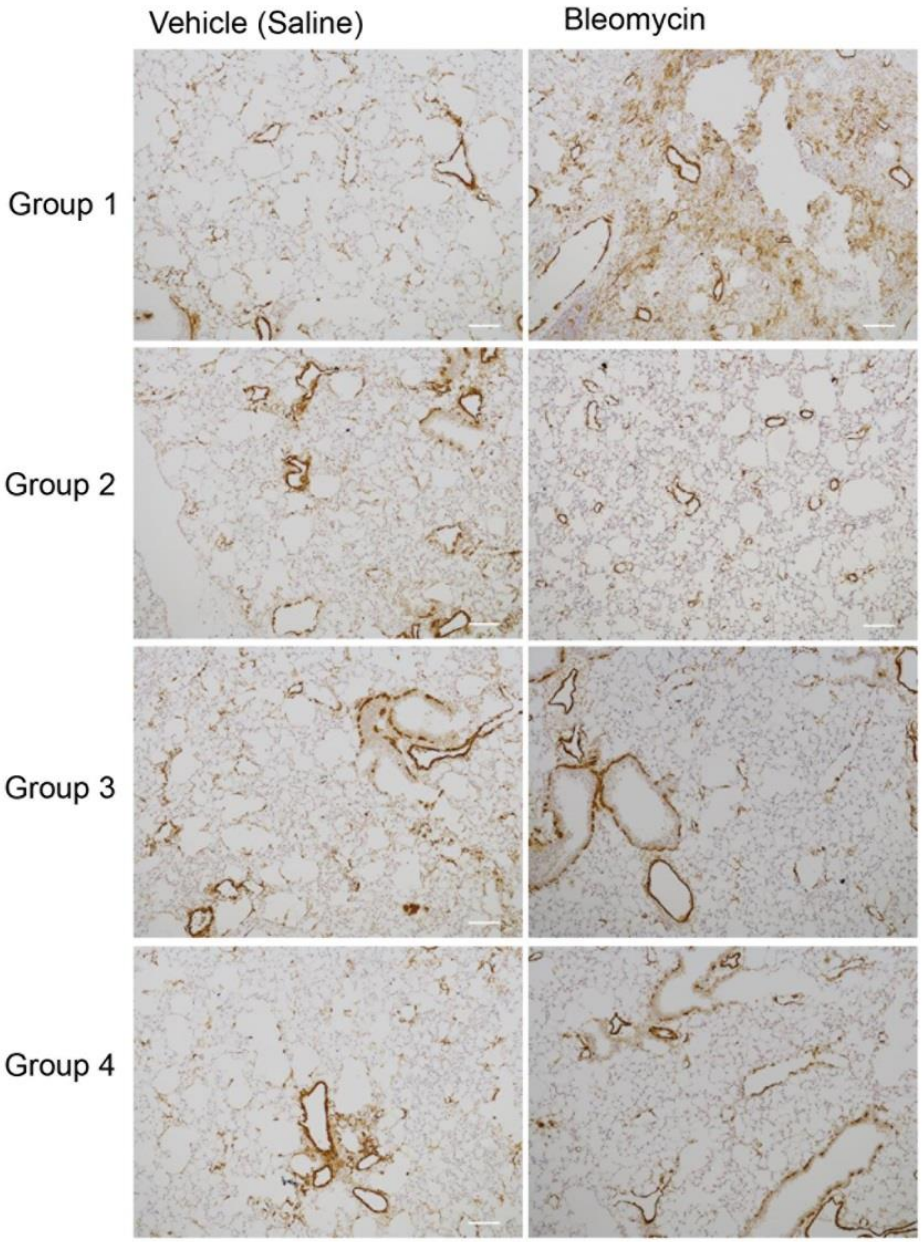

B (iii) Immunohistochemistry relative photographs of bone marrow chimera lungs stained for NIMP+ve neutrophils. Group 1 – WT-WT, Group 2 – WT-KO, Group 3 – KO-WT and Group 4 – KO-KO (Recipient-Donor bone marrow groups), x20 magnification with scale bars representing 100µm.

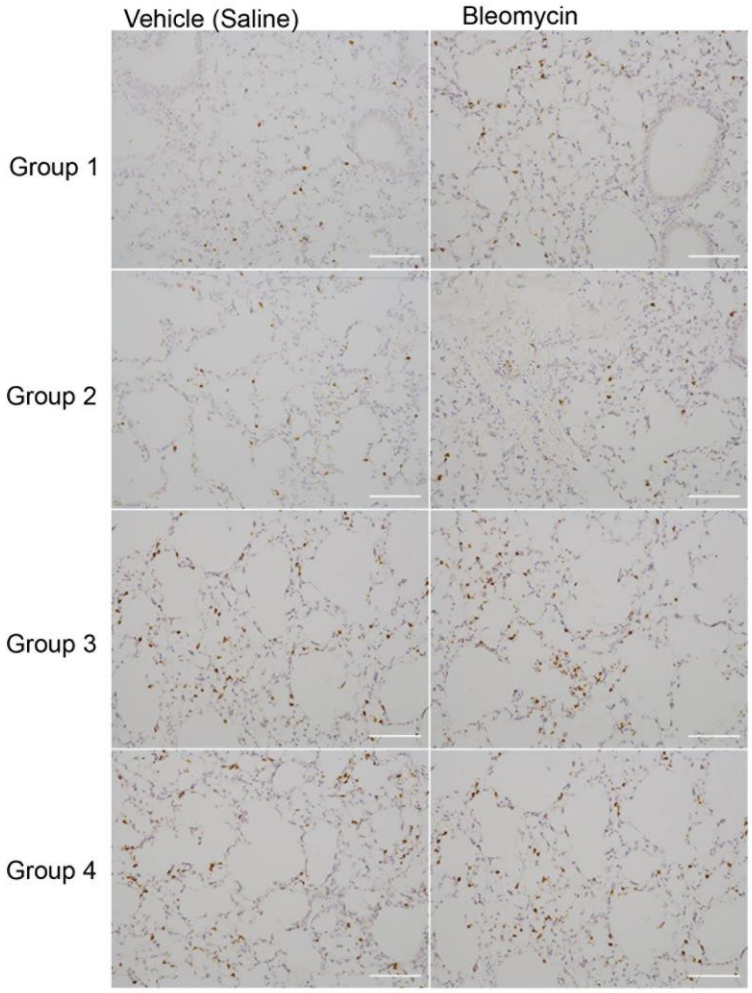

B (iv) Immunohistochemistry relative photographs of bone marrow chimera lungs stained for CD68+ve macrophages. Group 1 – WT-WT, Group 2 – WT-KO, Group 3 – KO-WT and Group 4 – KO-KO (Recipient-Donor bone marrow groups), x20 magnification with scale bars representing 100µm.

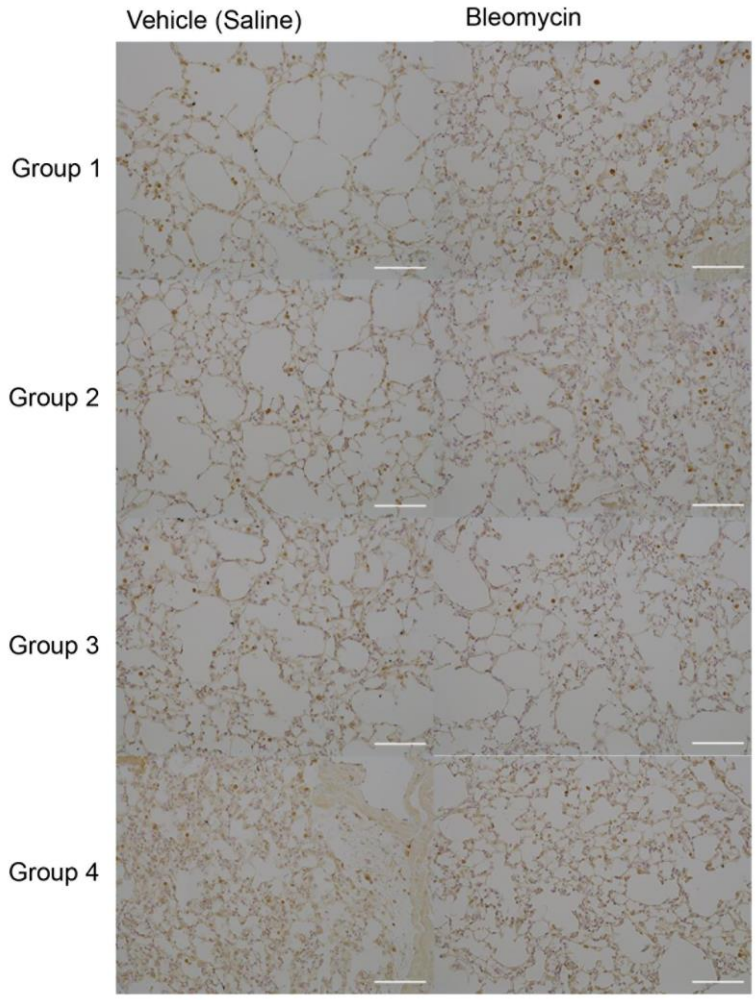

C (i) Relative photographs at x10 magnification of α-SMA levels in livers injured acutely with CCl_4 / olive oil (vehicle), assayed at 24, 48 and 72 hours post-injury. Scale bars represent 100µm,

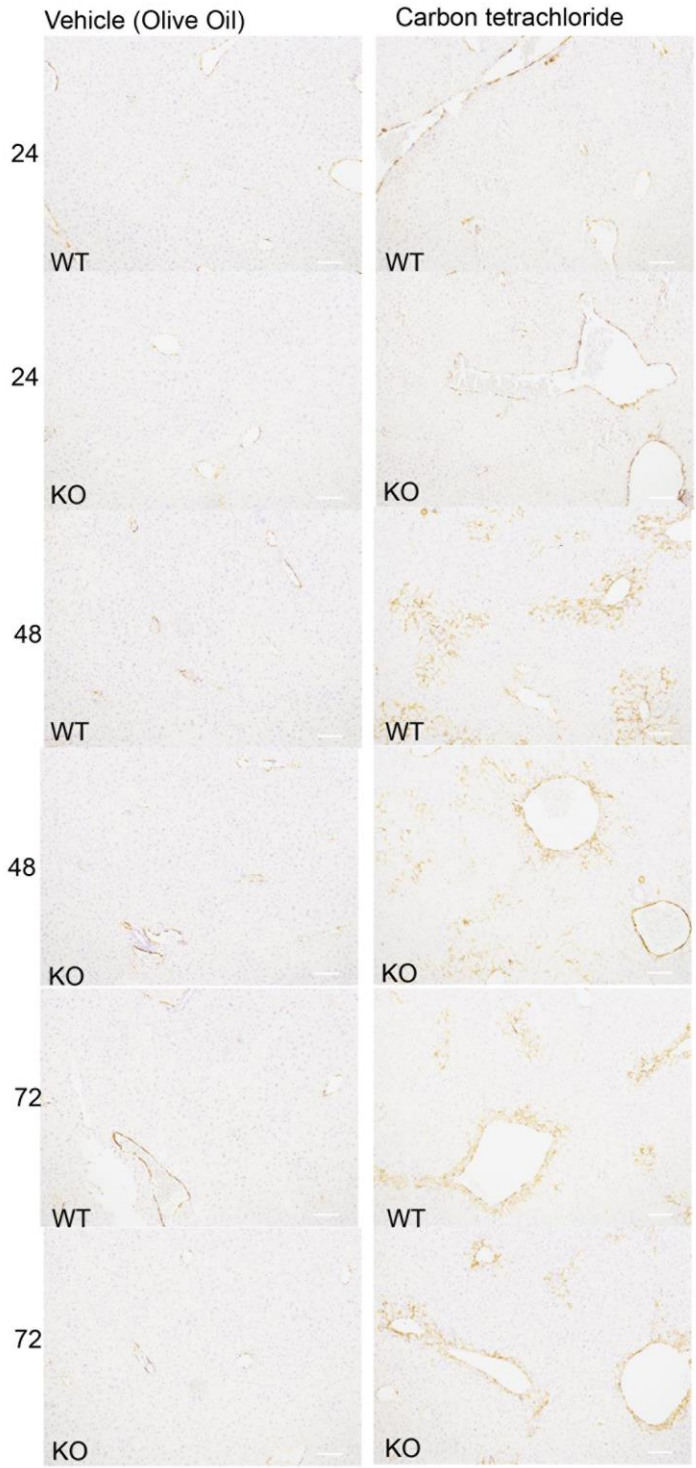

C (ii) Relative photographs at x20 magnification of NIMP+ve neutrophils in livers injured acutely with CCl_4 / olive oil (vehicle), assayed at 24, 48 and 72 hours post-injury. Scale bars represent 100µm,

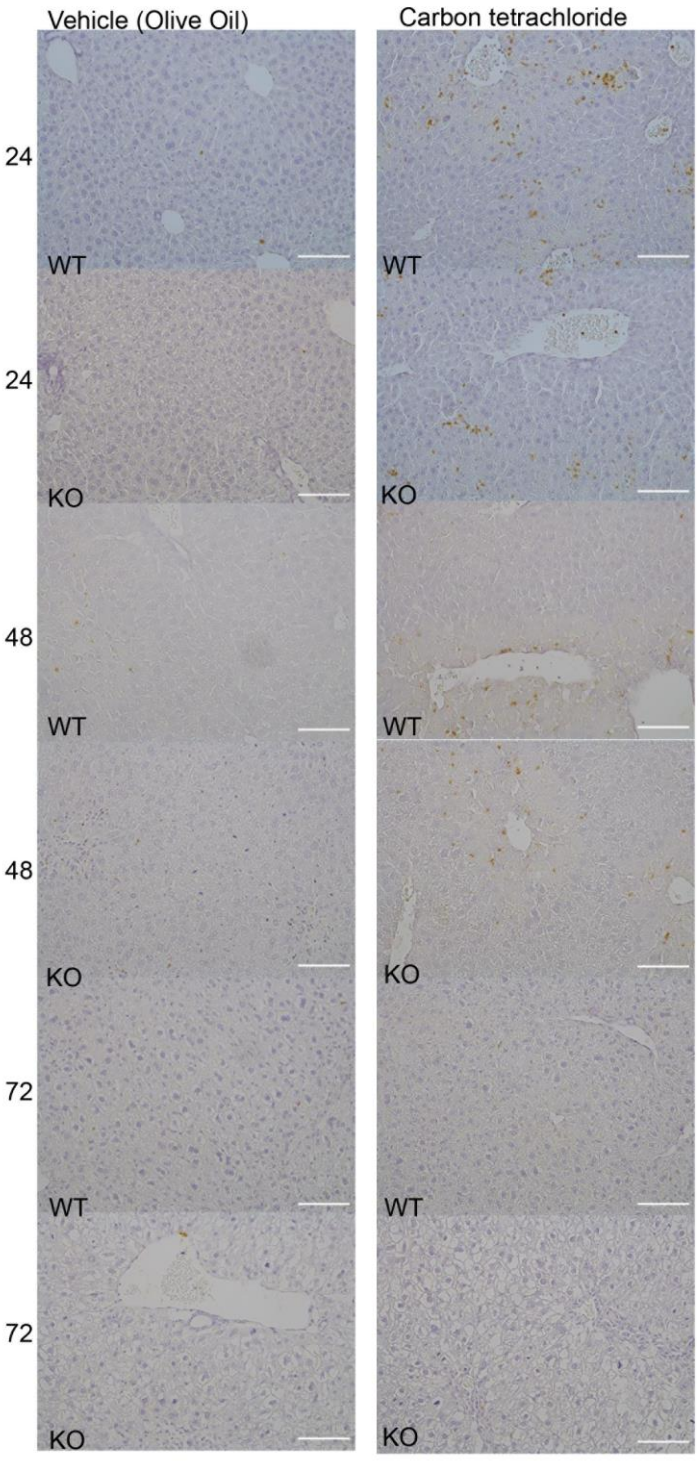

C (iii) Relative photographs at x20magnification of CD68+ve macrophages in livers injured acutely with CCl_4 / olive oil (vehicle), assayed at 24, 48 and 72 hours post-injury. Scale bars represent 100µm,

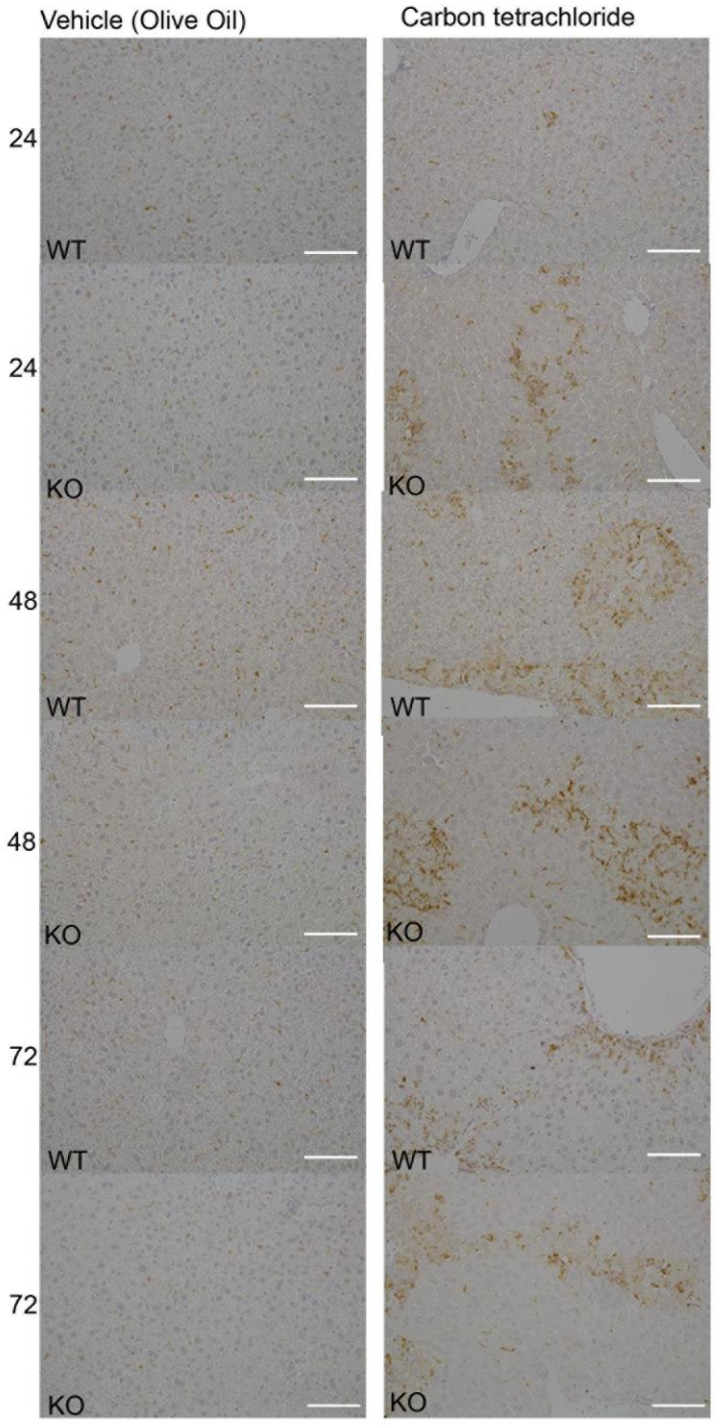

C (iv) Relative photographs at x20magnification of CD3+ve lymphocytes in livers injured acutely with CCl_4 / olive oil (vehicle), assayed at 24, 48 and 72 hours post-injury. Scale bars represent 100µm,

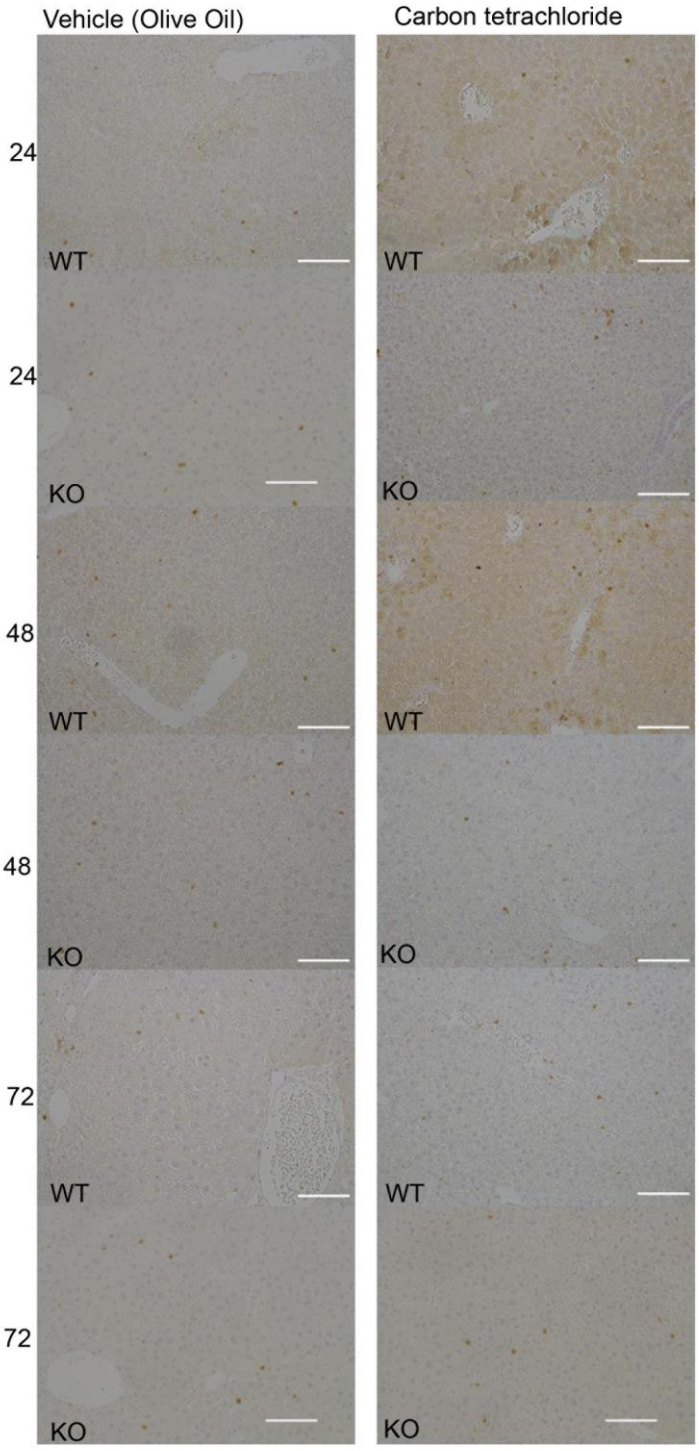

C (iv) Relative photographs at x20 magnification of PCNA+ve proliferating hepatocytes in livers injured acutely with CCl_4 / olive oil (vehicle), assayed at 24, 48 and 72 hours post-injury. Scale bars represent 100µm,

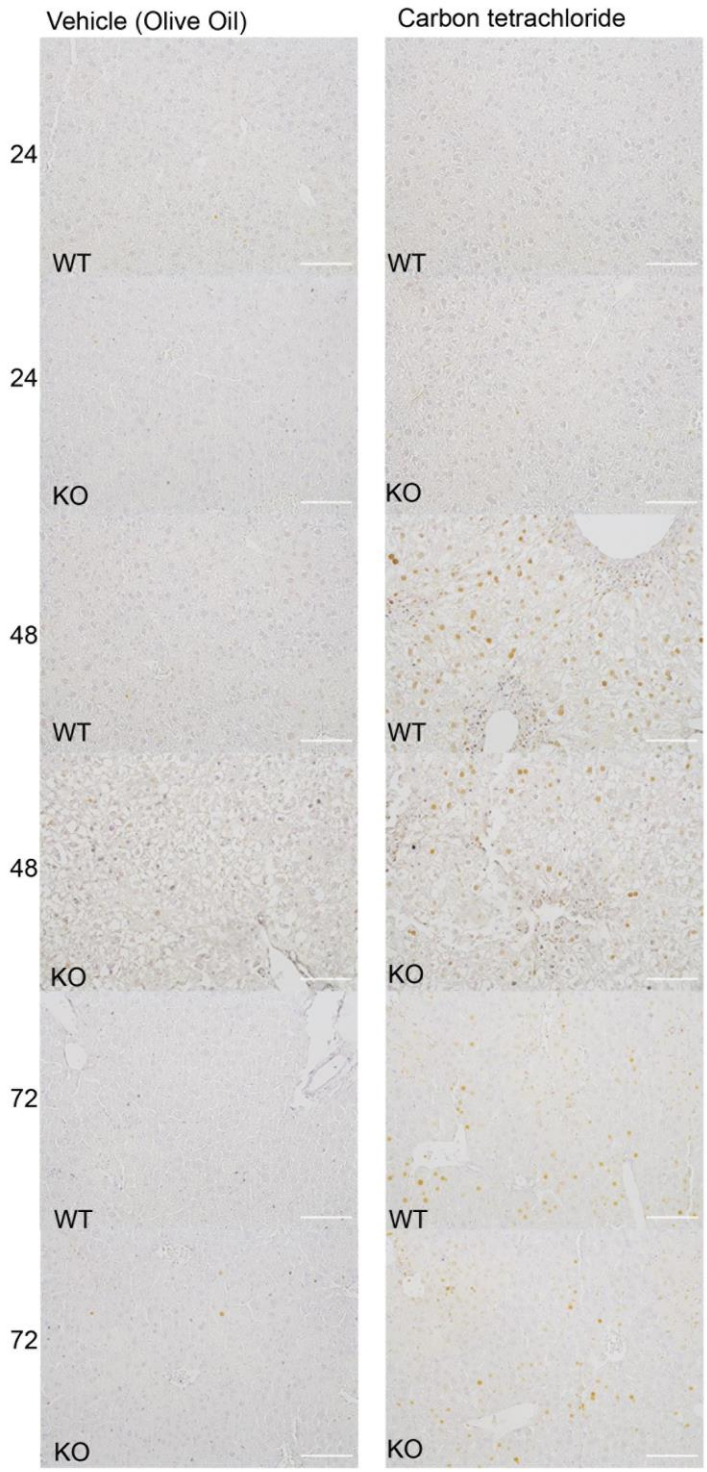

D (i) Relative photographs of negative no primary antibody controls for immunohistochemistry staining in mouse lung tissue for (A) alpha-smooth muscle actin (x10 magnification), (B) NIMP, (C) CD68 and (D) CD3 (x20 magnification).

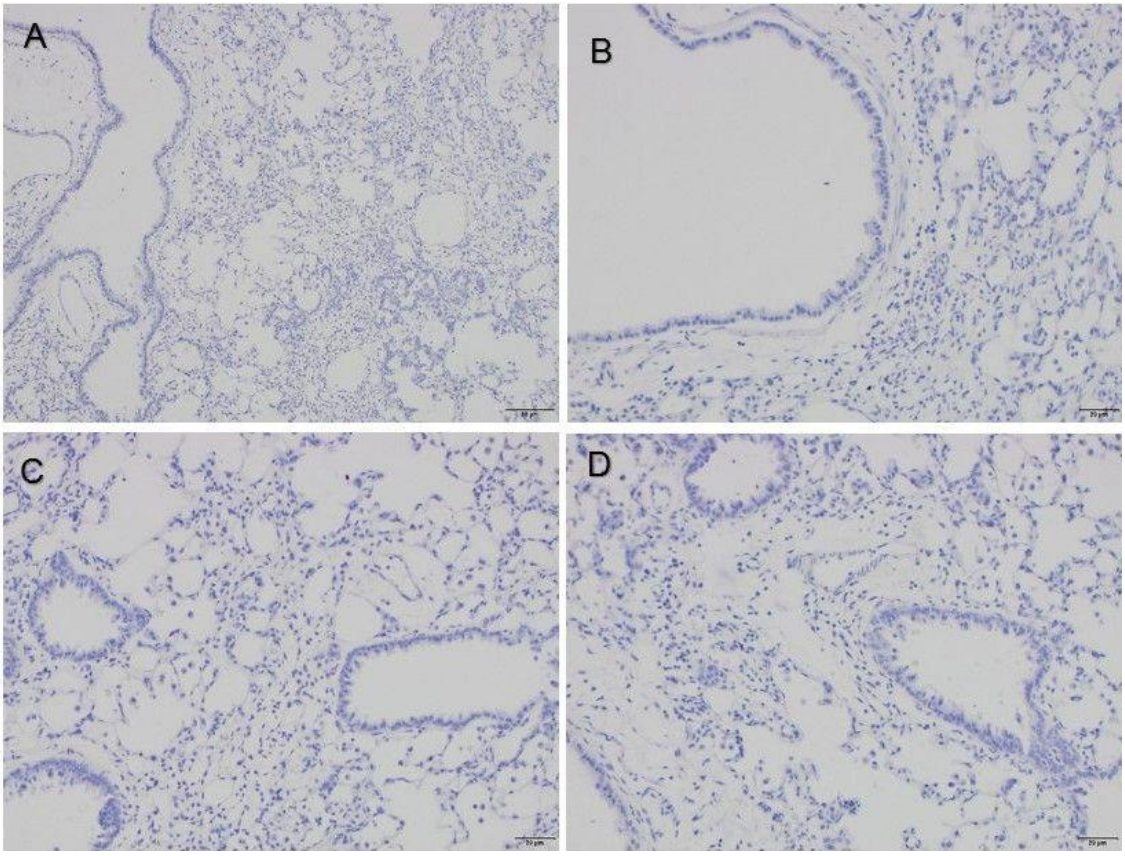

D (ii) Relative photographs of negative no primary antibody controls for immunohistochemistry staining in mouse liver tissue for (A) alpha-smooth muscle actin (x10 magnification), (B) NIMP, (C) CD68 and (D) CD3 and (E) PCNA (x20 magnification).

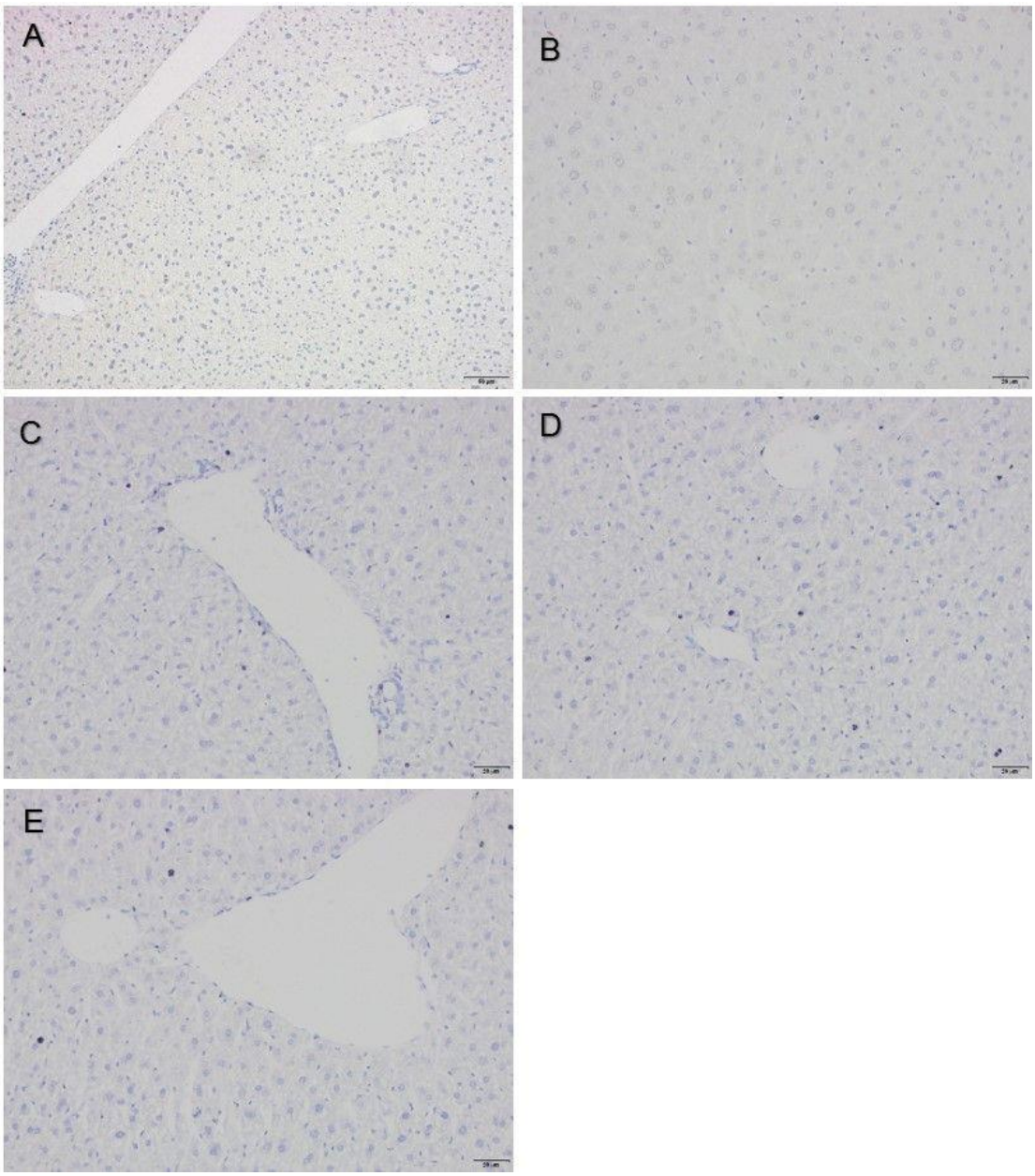

D (iii) Relative photographs of negative no primary antibody controls for immunohistochemistry staining in mouse kidney tissue for (A) alpha-smooth muscle actin (x10 magnification), (B) NIMP, (C) CD68 and (D) CD3 (x20 magnification).